School of Civil and Mechanical Engineering

Development of Novel Metaconcrete to Resist Impulsive Loads

Cheng Xu

0000-0001-8115-8579

The thesis is presented for the degree of

Doctor of Philosophy

of

Curtin University

July 2022

Declaration

To the best of my knowledge and belief, this thesis contains no material previously published by any other person except where due acknowledgment has been made.

This thesis contains no material which has been accepted for the award of any other degree or diploma in any university.

Signature:

Date: 13/07/2022

Abstract

With the rapid urbanization, population and economic growth, the numbers of terrorist attacks, accidental explosions and traffic collisions on transportation infrastructure around the world are rising. Civil infrastructure is prone to suffer damage or failure from impulsive loading, leading to a significant loss in economy and life. Therefore, a safer and more reliable mitigation strategy to protect essential civil engineering structures and facilities is becoming more and more emphatic. Metaconcrete consisting of engineered aggregates (EAs) utilizing the concept of local resonance mechanism may provide a new paradigm to mitigate shock propagation and reduce structural vibration due to its favorable wave attenuation capacity. Although the acoustic performance of metaconcrete structure has been studied in recent years, very limited study has covered the stress wave attenuation performance of metaconcrete structures subjected to impulsive loading. Moreover, very little experimental work has been undertaken to validate the performance of cement-based metaconcrete structure in the mitigation of stress waves induced by impulsive loading. Furthermore, all the studies up to now have focused on investigating the wave mitigation effects of metaconcrete structure, no study has been reported to quantify the static and dynamic mechanical properties of metaconcrete material mixed with different types and volume percentages of EAs, which are essential for the design of metaconcrete structures.

This thesis consists of six main parts. Firstly, the influences of various EA parameters on the frequency bandgaps of metaconcrete unit cell structure are studied so that appropriate EAs having the target frequency bandgap range can be designed to achieve the desired attenuation performance of metaconcrete structures to resist impulsive loading. The key factors such as aggregate shape, size, volume fraction, and material properties on the frequency bandgap associated with the negative effective mass density (NEMD) are investigated by using *Solid mechanics module* in the finite element software *COMSOL Multiphysics.* Then, the influences of different EAs on the stress wave attenuation of an example metaconcrete rod structure are numerically investigated by using hydrocode LS-DYNA. A flowchart to design

EAs with multiple resonant frequencies is proposed. After that, the effectiveness of embedding EAs into metaconcrete structure on mitigation of wave propagation induced by longitudinal impulsive loading is investigated and compared by conducting non-destructive tests and numerical simulations. Experimental and numerical studies are also carried out to investigate the damping properties and stress wave attenuation capacity of metaconcrete structures subjected to transverse impulsive loading. Finally, for practical applications, the static and dynamic mechanical properties of metaconcrete material with different types and volume percentages of EAs are also experimentally tested and quantified.

The thesis consists of 9 chapters. Chapter 1 provides general background, a brief introduction and an outline of this thesis. Chapter 2 conducts an intensive literature review and discussions on the relevant literature and the current research status. Chapter 3 studies the influences and sensitivity of various geometric and material parameters of EA on the frequency bandgaps associated with the NEMD. A three-dimensional (3D) numerical model is established in *COMSOL Multiphysics* to conduct intensive numerical simulations. The influences of various parameters of EA, namely, size, geometry and material properties of the core and soft coating on the frequency bandgap of EA are determined. The results can be used to design EAs for mixing into metaconcrete to achieve the desired stress wave mitigation induced by impulsive loading.

The influences of EA configurations on the stress wave attenuation of metaconcrete rod structure are numerically investigated via hydrocode LS-DYNA considering strain rate effect and material damage in Chapter 4. It is found that the attenuation is more prominent when the metaconcrete with an effective bandgap region coinciding with the primary dominant wave frequency (PDWF) induced by the impulsive loading. A flowchart in designing the EAs is proposed for better attenuation performance of metaconcrete structure.

Chapter 5 reports the experimental tests conducted to investigate the performance of cement-based metaconcrete with conventional EAs (i.e., *rubber-coated steel balls* (RCSBs)) against impulsive loading by considering the effects of inclusion type, volume fraction and effective

bandgap region. Numerical models are also developed to simulate the tests by using LS-DYNA to supplement the experimental tests. With the validated numerical model, a parametric study is carried out to investigate the dynamic performance of metaconcrete structure subjected to various loading cases. The factors of loading profiles such as amplitude and duration on the attenuation performance of metaconcrete structure are discussed.

In Chapter 6, a series of non-destructive impact tests are carried out to study the damping properties and response of metaconcrete structures under transverse impulsive loading. Dynamic responses of metaconcrete beams are compared with those of plain mortar and specimens with non-resonant aggregates in terms of equivalent damping ratio and attenuation performance. The results demonstrate that the metaconcrete structure with resonant aggregates (i.e., EAs) has a larger equivalent damping ratio and superior attenuation capacity as compared with other specimens. The effects of volume fraction, boundary conditions and impact force on the attenuation performance of metaconcrete structures are also revealed and discussed. Furthermore, the bandgap characteristics obtained from the experiment are compared with the prediction using *COMSOL Multiphysics* to verify the existence of bandgap in metaconcrete beam under transverse impulsive loading.

In Chapter 7, to address the issue of strength reduction caused by the soft coating outside the traditional EAs (i.e., RCSBs) whilst maintaining its favorable wave attenuation properties, a new EA by adding a relatively stiff shell named the *rubber-coated steel ball with an enhanced coating* (i.e., ERCSBs) is developed. The static strength and wave attenuation capacity under various impulsive loads are experimentally investigated. It is found that adding a stiffer shell to the conventional EAs can improve the mechanical properties of metaconcrete material while maintaining its good performance in mitigating stress wave propagation under both non-destructive and destructive loads.

In Chapter 8, dynamic compressive properties of metaconcrete material including failure modes, energy absorption capacities and dynamic increase factors (DIFs) are experimentally studied and discussed. Empirical formulae are proposed to estimate the DIFs for dynamic

compressive strength and energy absorption capacity of metaconcrete material.

Chapter 9 concludes this thesis and also gives recommendations for further research needed for practical applications of metaconcrete material in construction for structural protections against impulsive, as well as vibrational loads.

In summary, this thesis provides insight into metaconcrete material and its performance under impulsive loading, the outputs derived from this thesis could provide suggestions and guidance for the design of metaconcrete material and structure against multi-hazardous dynamic loads.

Acknowledgement

First and foremost, I would like to extend my sincerest and deepest gratitude to my supervisor John Curtin Distinguished Professor Hong Hao for the continuous support, great patience, valuable suggestions and invaluable encouragement throughout my PhD study. In addition, I need to extend my heartfelt appreciation to my co-supervisor, A/Prof. Wensu Chen, whose patient guidance and constant encouragement allowed me to complete this thesis.

I would also like to thank other members from the Centre for Infrastructural Monitoring and Protection (CIMP) at Curtin University including Dr. Thong Pham, A/Prof. Kaiming Bi, Dr. Hexin Jin and Dr. Zhijie Huang for their comments and suggestions throughout my PhD study. Special thanks to Mr. Zhixing Li for assisting with sample preparation in the dynamic tests.

Last but not least, I would like to express my deepest gratitude to my family, for their unconditional love and support.

List of published work and work prepared for publication

The list of published papers and work prepared for publications, with the full bibliographic citations in the thesis, are listed below.

Xu C, Chen W, and Hao H. The influence of design parameters of engineered aggregate in metaconcrete on bandgap region. Journal of the Mechanics and Physics of Solids, 2020. 139: 103929.

Xu C, Chen W, Hao H and Jin H., Effect of engineered aggregate configuration and design on stress wave attenuation of metaconcrete rod structure. International Journal of Solids and Structures, 2021. 232: 111182.

Xu C, Chen W, Hao H, Bi K, and Pham TM., Experimental and numerical assessment of stress wave attenuation of metaconcrete rods subjected to impulsive loads. International Journal of Impact Engineering, 2021. 159: 104052.

Xu C, Chen W, Hao H, Pham TM and Bi K., Damping properties and dynamic responses of metaconcrete beam structures subjected to transverse loading. Construction and Building Materials, 2021. 311:125273.

Xu C, Chen W, Hao H, Pham TM, Bi K. Static mechanical properties and stress wave attenuation of metaconcrete subjected to impulsive loading. Engineering Structures. 2022. 263:114382.

Xu C, Chen W, Hao H, Pham TM, Li Z and Jin H., Dynamic compressive properties of metaconcrete materials (Under review)

Statement of contribution

The work presented in this thesis was primarily conducted by the PhD candidate, Cheng Xu, which includes developing numerical simulation, conducting analytical analysis, carrying out the experimental test, analyzing results and preparing the manuscripts. Contributions by others are described as follows. The signed contribution forms are attached in the appendix.

Chapter 3

Prof. Hong Hao and A/Prof. Wensu Chen revised the manuscript and provided intellectual input toward data analysis and discussion of the results. The financial support was provided by the Australian Research Council.

Chapter 4

Prof. Hong Hao, A/Prof. Wensu Chen revised the manuscript and provided intellectual input toward data analysis and discussion of the results. Dr. Hexin Jin assisted with numerical model calibration and provided intellectual input toward the discussion of the results. The financial support was provided by the Australian Research Council.

Chapter 5, Chapter 6 and Chapter 7

Prof. Hong Hao, A/Prof. Wensu Chen, Dr. Thong M. Pham and A/Prof. Kaiming Bi revised the manuscript and provided intellectual input towards data analysis and discussion of the results. The financial support was provided by the Australian Research Council.

Chapter 8

Prof. Hong Hao, A/Prof. Wensu Chen and Dr. Thong M. Pham revised the manuscript and provided intellectual input toward data analysis and discussion of the results. Dr. Hexin Jin and Mr. Zhixing Li provided intellectual input toward data analysis and discussion of the results. The financial support was provided by the Australian Research Council.

Table of Contents

List of Figures

List of Tables

Chapter 1 Introduction

1.1 Background

With the increasing risk and prevalence of extreme events (e.g. accidental or intentional explosions) worldwide, engineering structures during their service life may experience extreme impulsive loading with relatively low probability but disastrous consequences. For instance, blast loading induced by the rapid expansion of explosives could produce a tremendous amount of energy impacting the engineering structures and generate global and local responses associated with different types of failure modes. Concrete is one of the most widely used construction materials for civilian and military facilities, and civilian structures made of concrete (e.g., residential buildings, bridges and industrial facilities) are prone to experience damage under extreme loads induced by accidental or natural hazards such as earthquakes, accidental explosions and vehicle collisions, leading to significant economic losses, as exemplified in Figure 1-1. For instance, the recent devastating Beirut explosion in Lebanon caused tremendous losses. Shockwave propagated approximately 9 kilometers away from the centre of the explosion to damage the terminal buildings at Beirut–Rafic Hariri International Airport [1]. The susceptibility of structures to the threads of multi-hazardous loading has become a widespread issue [2, 3]. Structures designed to resist one type of loading may not be strong to resist another type of loading. For example, most concrete structures designed to be seismic loading resistant may not be able to resist blast and impact loads due to different structural response modes and damage mechanisms under intrinsically different loading conditions regarding amplitudes and frequency contents.

Recently, there has been rapid growth in the field of locally resonant metamaterials (LRMs), which are featured by the favorable wave attenuation properties at the tunable frequency range called "bandgap" [4]. The LRMs have been widely applied to acoustic and vibration isolation systems over the past decade. Unlike periodic composites causing wave dispersion in the mediums or granular crystals through nonlinear Hertzian contacts [5], the LRMs could

generate a prescribed frequency band by adopting the theory of local resonance, the stress wave within the frequency range could be either isolated or suppressed [6-12]. The out-phase motion induced by locally resonant microstructure (resonator) triggers "negative effective properties" overwhelming the entire system against impinging motions [13-17], leading to diverse wave manipulation functionalities [18]. The successful use of this novel concept in mitigating impulsive loading has drawn the attention of the structural community to develop more effective shock mitigation materials, which may bring a promising method of constructing a safer and robust structure [4, 19].
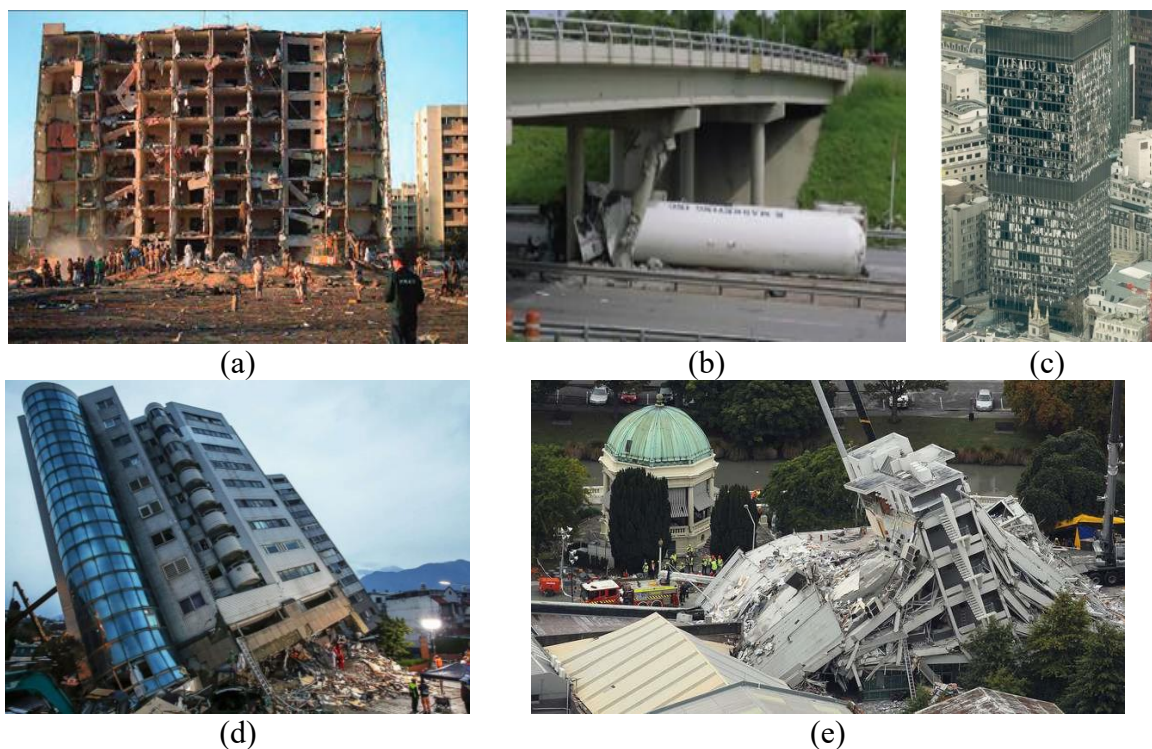
Figure 1-1. Disastrous events of extreme loads on civil structures: (a) The Khobar Towers bombing [20], (b) The Vehicle collision with a highway bridge [21], (c) The Baltic Exchange bombing [22], (d) The Hualien earthquake [23], (e) The Christchurch earthquake [24].

To date, the idea of LRMs provides a novel scheme for achieving tailorable and unconventional wave manipulation properties, which may provide various engineering applications for shock wave mitigation in terms of broadened wave attenuation range and enhanced damage mitigation performance. Inspired by the LRMs, the concept of "negative effective property" has been incorporated into the development of novel concrete material to

resist extreme actions [25-31]. This type of concrete-like metamaterial, termed "metaconcrete", uses the resonant engineered aggregates (EAs) made of heavy core coated with the compliant coating to partially replace the coarse aggregates in conventional concrete. The compliant coating layer is served as an elastic spring allowing the presence of oscillatory motion of the heavy core. By adding EAs in metaconcrete, it could trigger the negative effective mass density (NEMD) of the system interacting with the applied dynamic loading thus attenuating stress wave propagation, when the EAs are tuned. By adjusting the geometry or material property of the engineered aggregate, the metaconcrete could exhibit enhanced wave attenuation performance in the desired range of frequencies. The superior wave attenuation property of metaconcrete structure occurs if the designed resonant frequency of EAs (f_0) is within the frequency spectrum of the applied loading, and therefore the metaconcrete structure can be purposely designed for target loading scenarios to fulfil the specific requirement.

Particular attention is paid to applying metaconcrete material to protect civil engineering structures from multi-hazardous loads such as earthquakes, dynamic impacts and explosions very recently. However, the study on metaconcrete material or structure is still at an early stage, which has only demonstrated the attenuation phenomenon mentioned above. No systematic research has been conducted to evaluate the influence of critical factors on bandgap characteristics and stress wave attenuation performance. Meanwhile, very limited experimental studies have been carried out to verify the attenuation performance of cementitious metaconcrete material or structure subjected to impulsive loading, and there is no experimental study on the static and dynamic mechanical properties of metaconcrete material reported in the open literature. This thesis, therefore, attempts to fill the essential knowledge gap to facilitate the better design of metaconcrete material/structure against extreme loading. In this chapter, the research objective of this thesis is presented to address the identified essential knowledge gap, followed by the outline of this thesis.

1.2 Research objective

The objective of this thesis is to develop novel metaconcrete material against impulsive loading. In addition, metaconcrete with engineered aggregates is designed to have favorable wave attenuation capacity and tunable dynamic property. The objective is fulfilled by implementing the following research tasks:

(1) Identifying the critical design parameters (i.e., geometric & material parameters) of engineered aggregates with respect to their effects on the bandgap characteristics.

(2) Determining the contribution of bandgap characteristics on the stress wave attenuation performance of metaconcrete structure.

(3) Proposing conceptual design flowchart for effectively designing engineered aggregates and metaconcrete structure.

(4) Fabricating engineered aggregates and metaconcrete material, and experimentally validating bandgap and stress wave attenuation performance of metaconcrete structure with fabricated engineered aggregates subjected to longitudinal and transverse impulsive loads.

(5) Improving the mechanical properties of metaconcrete material through retrofitting conventional engineered aggregate design and experimentally investigating its effect on mitigating stress wave propagation,

(6) Studying the static and dynamic compressive properties of metaconcrete material with conventional and retrofitted engineered aggregates.

1.3 Research outline

This thesis comprises nine chapters. A brief research outline is illustrated in Figure 1-2 and the contents of these chapters are described below:

Chapter 1 presents the background, research objective, and research outline.

Chapter 2 presents a comprehensive literature review.

Chapter 3 investigates the influence of the design parameters such as aggregate shape, size, volume fraction, material properties and sensitivity of those parameters on the region of the negative effective mass density (NEMD).

In Chapter 4, influences of geometric and material parameters of engineered aggregates on the bandgap region and contribution of bandgap on the stress wave attenuation and material damage considering strain rate effects are evaluated. A flowchart to design engineered aggregates with broadband attenuation of propagating stress waves is provided.

Chapter 5 presents an experimental and numerical assessment of the design parameters of engineered aggregates on the stress wave attenuation performance. The effectiveness of metaconcrete rod structure with its bandgaps covering or not covering the primary dominant wave frequency (PDWF) on wave propagation mitigation is experimentally verified. The mitigation effect induced by different impulsive loading profiles is numerically studied.

Chapter 6 investigates the damping property and dynamic response of cementitious metaconcrete rod structure with engineered aggregates subjected to transverse impulsive loading. The influence of inclusion types, aggregate size, volume fraction, distribution, loading intensities and boundary conditions are studied. The bandgap characteristics of metaconcrete rod structure under transverse loading are experimentally and numerically assessed.

Chapter 7 presents an experimental investigation of static mechanical properties of metaconcrete materials with conventional and newly proposed engineered aggregates. Then, the dynamic responses of the metaconcrete specimens with different engineered aggregates subjected to non-destructive and destructive impulsive loading are investigated. The failure process and the failure modes of metaconcrete specimens made of conventional and newly proposed engineered aggregates under different loading profiles are compared.

Chapter 8 presents an experimental investigation of the dynamic compressive properties of

metaconcrete materials with conventional and newly proposed engineered aggregates by using the Split Hopkinson Pressure Bar (SHPB) system. Failure process, failure modes, dynamic compressive strength as well as energy absorption capacities under different strain rates are analyzed. Dynamic increase factors (DIF) for compressive strength and energy absorption capacity are derived and their empirical formulae are proposed accordingly.

Chapter 9 presents the main findings from this thesis and recommendations for future studies.
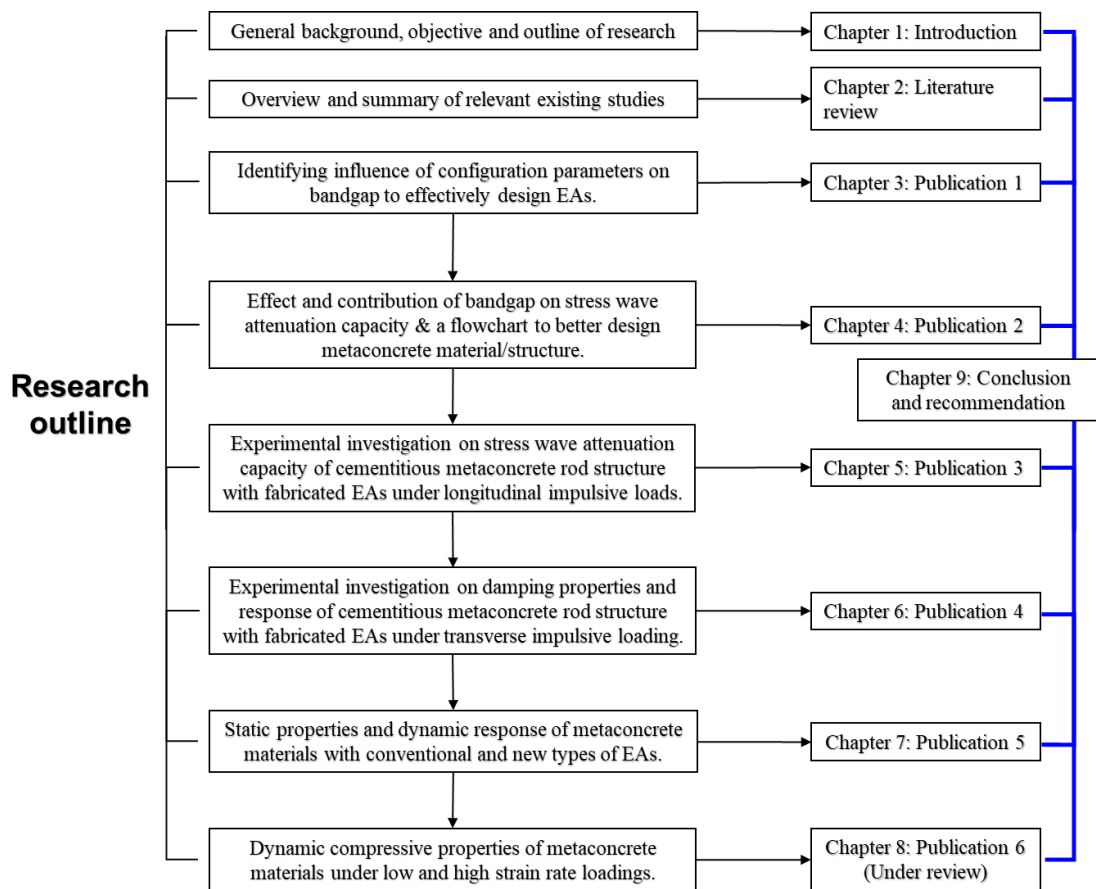
Figure 1-2. Research outline.

Chapter 2 Literature review

2.1 Introduction

As stated in Chapter 1, concrete structures during their service life might experience severe damage under extreme events such as blast and impact loads. Therefore, it is important to gain more insights into the damage mechanism of these structures subjected to hazardous loads and develop more effective protective measures. In this chapter, the concept and current state-of-the-art research of locally resonant metamaterial (LRMs) and metaconcrete material/structure regarding stress wave manipulation are reviewed. Besides, existing analytical and numerical modelling, as well as experimental investigations on the wave attenuation effect of metaconcrete material with various configurations, are presented. The essential research gap in the field of metaconcrete material design and its wave attenuation performance is summarized in this chapter.

2.2 Extreme loading on engineering structures

Impulsive loading could trigger the intensive stress wave propagating through the structural components or the building envelope within a short duration, leading to structural failure or progressive collapse [32-34]. This, therefore, highlights the importance of developing stress wave-resistance materials and effective protective structural systems for the protection of important structures against impulsive loading. Moreover, it is essential to develop concrete material with sound damping properties to attain better attenuation capacity for the safety, serviceability and protection of structures against dynamic loads. However, the majority of protection strategies for existing structures in practice are to enhance the strength and stiffness of the essential structural components. The mitigation measures based on the strengthening of the structural elements do not directly change the amplitude of the stress wave generated in the material when the shock wave acts on the structure. The stress changes due to the wave propagation usually occur in a few microseconds (μs). Brittle materials such as concrete-like materials are prone to experience severe damage in the form of cracking and

7

spalling due to stress wave propagation and stress wave interference (i.e., superposition), even before the occurrence of noticeable deformation of the structure [35], as exemplified in Figure 2-1. Therefore, for effective structural protection, besides the traditional strengthening method, it is important to reduce the peak stresses in concrete structures induced by the shock wave.
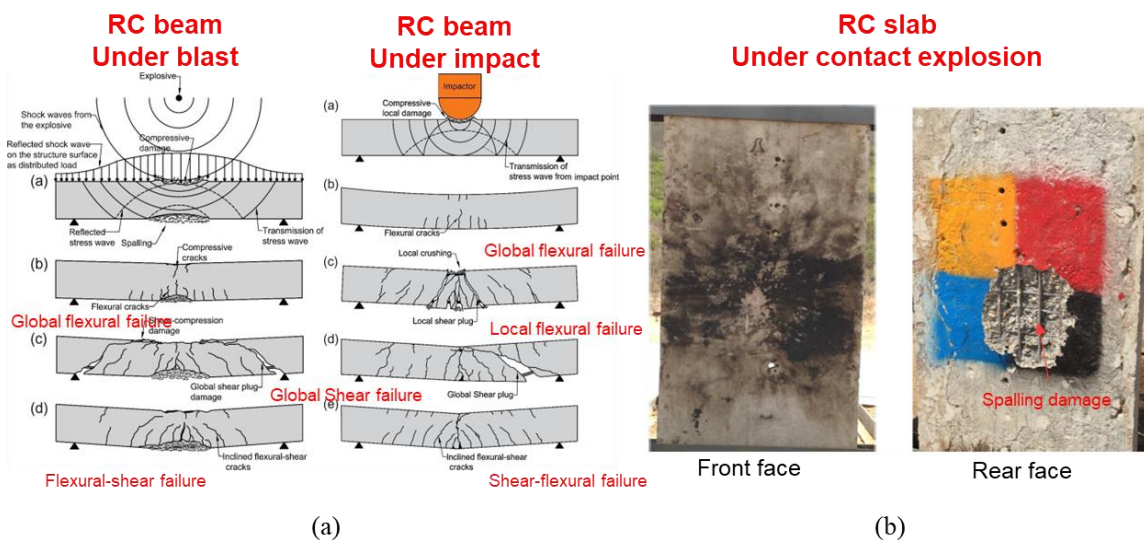
Figure 2-1. Various damage modes due to stress wave propagation: (a) RC beam under blast and impact loads [35], (b) RC slab under contact explosion [36].

In addition, it is well known that structural response under dynamic loads includes two phases: the forced vibration phase and the free vibration phase. When a structure is subjected to dynamic loads with a loading duration much shorter than the structural natural vibration period, there is no sufficient time for the overall structural response to develop in the forced vibration phase. Thus, the maximum global response usually occurs in the free vibration phase. Excessive vibration could cause damage to structural and non-structural components. Therefore, vibration control is often required in designs for structural protection against natural and manmade dynamic loads. Many vibration control technologies and control devices have been developed and applied in practice. As compared to the devices for energy absorption or active vibration control, using the material with enhanced damping properties to construct the structure could achieve a similar or even higher attenuation level [33], and avoid high cost and complexity for construction or maintenance [37]. Additionally, the enhanced damping properties enable the structure to absorb vibration energy substantially

[38]. Recently developed novel metamaterial could be in conjunction with the existing strengthening approaches to develop more effective and efficient protective materials for enhanced damage resistance via attenuating stress wave propagation. Thus, understanding the physical mechanism and potential application of mechanical metamaterial is essential to develop more effective protective measures.

2.3 Mechanical metamaterials and metastructures

Metamaterials are broadly defined as artificial material/structure that exhibits an exotic behavior through the specially designed microstructure configuration [12]. Metamaterials can be categorized into many different groups, and mechanical metamaterial is one of them which has attracted considerable attention as they emerged. The mechanical metamaterial has been used in a wide range of applications to control wave propagation in the fields of acoustics, elastodynamics, seismology and earthquake engineering [39, 40]. Especially, locally resonant metamaterials (LRMs) have seen rapid development by integrating with periodic microstructure and/or locally resonant inclusions to produce superior wave attenuation capacities.

2.3.1 Overview

In recent years, locally resonant metamaterials (LRMs) with the capacity of manipulating wave propagation bring a radically-new way of developing multifunction materials. Tremendous efforts have been put into developing numerical and analytical models of such metamaterials. The physical underpinnings of LRMs showed that the oscillation of resonant inclusions induces out-phase motion in the way of disturbing wave propagation resulting in an apparent spectral gap [41]. In addition, combined with compacted periodic structure, Bragg scattering contributes to mitigating the peak amplitudes [41]. Moreover, Milton and Willis [42] have demonstrated the theory of "negative effective mass density" through mathematical derivation on the two-dimensional "mass-in-mass" model [42]. They revealed the exotic phenomenon in which "negative dynamic effective mass or mass density" presents

when excitation frequency matches the prescribed natural frequency of the inner oscillator. Moreover, the previous study on negative effective properties such as negative effective mass shows that dynamic effective mass could be negative, and therefore, backward acceleration of particle trajectory could be generated depending on the applied perturbation force [43]. To explain the energy transfer mechanisms of LRMs, Huang et al. [44] made a theoretical explanation by adopting a monotonic lattice model that energy from the external force is stored temporarily within inner mass when impinging excitation frequency approaches the resonant frequency of the inclusion. However, the energy is instantly taken out by external force doing negative work in a cyclic manner [16, 45, 46]. Consequently, the energy sequestration and rejection achieved by using local resonators are found to be the mechanism causing energy dissipation [45]. To experimentally expatiate the underpinning mechanism of negative effective mass, Yao et al. [47] conducted the test on a mass-spring system. The experimental results demonstrated that the inner mass at resonance could generate out-of-phase motion interacting with the overall system, leading to the negative effective dynamic mass on the spring-mass structure at the prescribed frequency range. Thus, dynamic responses of the system were mitigated and the wave amplitude transmitted throughout the system was significantly reduced in the prescribed frequency range [17, 48]. Khan et al. [45] further conducted non-destructive pendulum tests on simplified mass-spring structure, which experimentally validated the local resonance effects in mitigating low-frequency impact waves.

In addition, Yin et al. [49] created the 1D acoustic crystals showing that the topological transition phase could affect both bending and longitudinal wave propagation. Baravelli et al. [50] created a novel chiral lattice structure with the insertion of resonant inclusions so that vibration of the structure could be significantly reduced due to tunable high-stiffness and damping properties. Similarly, Manimal et al. [51] and Achaou et al. [52] have numerically demonstrated that the LRMs could bring simultaneous high effective-damping properties and effective stiffness. Bandgap-polarization studied by Ma et al. [53] developed the fluid-like metamaterial termed "meta-rod" which could achieve bandgaps for propagation of

longitudinal, transverse, and torsional waves instantaneously. Fang et al. [54] studied locally resonant nonlinear metamaterial (LRNM) to suppress ultra-low frequency acoustic waves, demonstrating that strong nonlinearity of subwavelength unit cells brings bi-attenuation effects regarding narrowed passbands and expanded stopbands. Moreover, stress wave control by combining the concept of topology and condensed matter physics has gained increasing attention [55].

Furthermore, many strategies have been developed to achieve wave propagation control in LRMs through coupling effects; in return, customizable and tunable frequency-depended properties were appended. For instance, Huang and Sun [15] theoretically studied a novel microstructural model that inhibited the frequency-depended effective Young's modulus showing that the value could be negative in the prescribed frequency range. Besides, other frequency-dependent or "negative effective parameters" have been increasingly gaining attention [49, 56-61]. For example, it has been found that the LRMs composite could generate negative bulk modulus resulting in high resistance to external motion [17]. Moreover, the recent development of Kirigami-based LRMs composed of arrayed folded metal plate with topped masses could effectively control the propagation of the flexural wave at subwavelength scales in three dimensions [14]. Besides, Chen et al. [62] proposed a metamaterial model equipped with broadband attenuation and enhanced damping properties by using viscous material and locally resonant inclusions. Li et al. [46] developed a continuum lattice structure, which could considerably attenuate the stress wave propagation induced by the blast and impact loads. On the other hand, exploiting concepts of locally resonant structures could suppress the wave propagation at the prescribed frequency range or enable the conversion of one type of wave to another [40]. Furthermore, the design and manufacture of effective LRMs suitable for a particular use is noted as a challenge that has received growing research interest.

2.3.2 Wave attenuation mechanisms

The mechanisms of forming such polarized dispersive relations (i.e., bandgap) in LRMs are

attributed to Bragg scattering or local resonance. The primary feature of LRMs is that it contains an artificially designed periodic structure. It is found that the designed periodic structure spaced at a subwavelength scale could induce the rapid and cyclic surface impedance in each different constitutive unit [63]. The scattering and dispersion features associated with this structure could occur along the impedance exchanging with surroundings and causing the concurrence of passband and bandgaps continuously [63]. As a result, the periodicity of structure could filter electromagnetic and/or mechanical waves (e.g., acoustic and elastic stress waves) within the frequency band owing to wave scattering from the surface of the microstructure in conjunction with destructive interference. With frequency contents outside the prescribed band, it is in the natural decay manner. In addition, locally resonant metamaterial relied on the activation of local oscillation of inclusions has brought increased attention to researchers in the last few decades due to its dynamically equivalent negative effective property as shown in Figure 2-2(a) and (b). The benefit of locally resonant structures towards generating desirable wave attenuation properties is that the spatial periodicity of the resonant inclusions sometimes is not compulsory [12]. The example of a frequency-dependent negative effective property is schematically demonstrated in Figure 2-2(c). As shown, the unique tunable behavior occurs only if the designed resonant frequency of embedded locally resonant inclusion is within the frequency range of the applied loading. The out-of-phase motion induced by resonant inclusion could trigger the "negative effective mass or mass density" (NEMD) of the system interacting with the applied dynamic loading and attenuate stress wave propagation according to the anti-momentum principle [62, 64]. Based on the curve of dimensionless ratio between dynamic effective mass (M_{eff}) and static mass (M_{st}) against the dimensionless frequency ratio as shown in Figure 2-2(c), there is a frequency range in which the ratio (i.e., $M_{\text{eff}}/M_{\text{st}}$) becomes negative. Within this frequency range, the stress wave induced by the dynamic loading could be substantially attenuated or suppressed so that this frequency range is termed as bandgap for the mechanical stress wave propagation.

Regarding forced waves, the damping also contributes to the attenuation of waves in both

passbands and stopbands. However, the wave attenuation mechanism becomes more complicated in the nonlinear region. The transmission characteristics within this regime are influenced by the degree of nonlinearity and the presence of defects [12, 63, 65]. The synthetic factors regarding nonlinearity, coupling effects and structural damping could play a critical role in wave attenuation. For nonlinear material, passband properties are also tailorable to control wave propagation whereby achieving chaotic passband [54]. This spectral effect in the finite nonlinear periodic structure could interfere with wave propagation and influence the dispersive relation, which might be useful to retrofit mechanical metamaterial with enhanced properties [12, 63, 65].
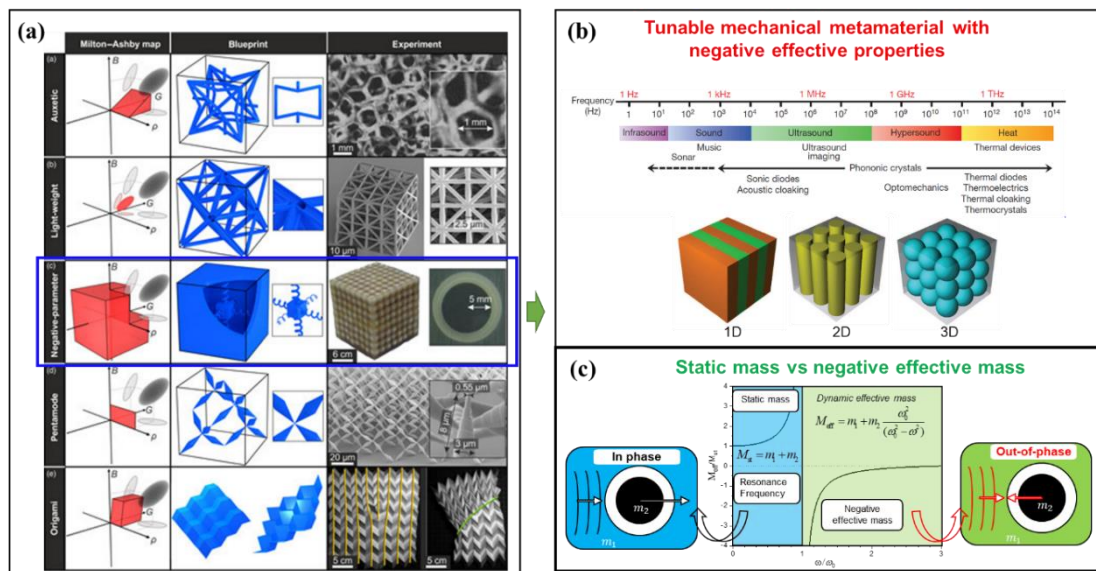
Figure 2-2. Mechanical metamaterials: (a) Classification [13], (b) Mechanical metamaterials with tunable properties [66], (c) Mechanisms of negative effective mass [25].

2.3.3 Application of mechanical metamaterials for structural protections

In recent years, the development of LRMs is driving the progress of enhancement and application to many engineering fields. Apart from manipulating classical waves (i.e. optic and acoustic waves), the concept of LRMs with adjustable frequency-dependent properties has been proposed to control shock waves or transient loading [67]. For example, Tan et al. [64] numerically evaluated the wave attenuation performance of using LRMs incorporating different resonant inclusions to mitigate blast-induced dynamic loading. Since then, several publications have been concentrated on retrofitting LRMs design to enhance attenuation or

mitigation performance [14, 27, 28, 45, 46, 62, 64, 68]. Chen et al. [69] explored the methods of suppressing flexural wave-induced motion on the sandwich composite beam by configuring a spring-mass resonator into the structural foam core. More broadly, the LRMs have been used for a wide range of applications such as seismic isolators/barriers [70], sound insulators [71], mechanical energy absorbers [72], etc. Furthermore, LRMs in various forms such as composite beam [69], composite plate [73], meta-lattices [62, 74-80], woodpile structure [81] and concrete-like metamaterials [25-27, 82, 83] have been developed. In addition, several numerical studies showed that concrete containing periodic local resonators coated by a viscoelastic compliant layer could have the higher energy dissipation capacity [84-86]. To conclude, the current multi-disciplinary research on locally resonant metamaterials have created the unforeseen potential to develop innovative material that could be used to construct a robust and resilient structure in resisting hazardous loading scenarios.

2.4 Metaconcrete

2.4.1 Concept

In 2014, the idea of developing a cementitious composite termed "metaconcrete" against blasting loads was proposed and numerically evaluated by Mitchell et al. [25]. Differing from conventional concrete composed of natural aggregates such as stones or gravels, metaconcrete is padded with artificial aggregates composed of a heavy metal core and more compliant outer material [25], which is designed to activate the local resonance. In the conventional form of engineered aggregates (EAs), it could have tunable dynamic properties through activating oscillatory motion of artificial aggregates about resonance, leading to stress attenuation and damage mitigation. The typical aggregate configuration and ways of disposing of those aggregates including periodic and non-periodic deposition are shown in Figure 2-3. Also, Mitchell et al. [25-28, 31] numerically examined the properties of the proposed cementitious metamaterial to attenuate intensive stress waves and mitigate the structure from damage. They found that metaconcrete structure with purposely designed EAs could exhibit superior wave attenuation and energy dissipation capacity, which could be

potentially used in the construction of structures against blast and impact loading.
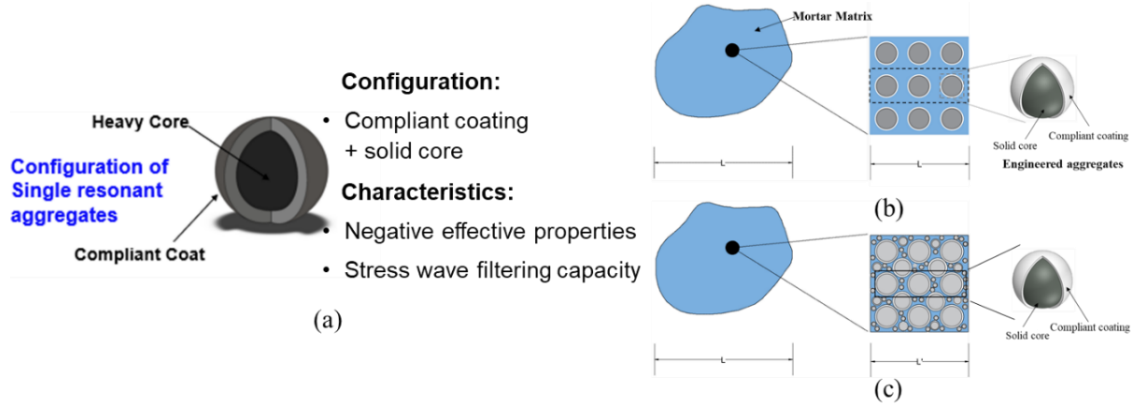
Figure 2-3. Configuration and distribution of engineered aggregates: (a) Configuration, (b) Periodic deposition, (c) Non-periodic deposition.

2.4.2 Analytical study

The physical underpinning of stress wave attenuation of metaconcrete material composed of EAs is achieved due to the negative effective mass or mass density within the bandgap region [25, 26]. Mitchell et al. [25] derived an equation to predict the resonant frequency (f_0 or f_{res}) of the spherical-shaped engineered aggregate. The resonant frequency depends on Young's modulus of coating ($E_{c'}$), coating thickness (t), core radius (R_c) and core density (ρ_c), indicating that the geometric and material parameters influence the locally resonant frequency of the engineered aggregates [25]. The equation can be expressed as:

$$f_0 \ or \ f_{res} = \frac{1}{2\pi} \sqrt{\frac{3E_{c'}}{2R_c t \rho_c}} \tag{2-1}$$

The above equation implies that the geometric parameters and the material selection influence the locally resonant frequency of the engineered aggregates. For instance, using a coating layer with a higher value of Young's modulus ($E_{c'}$) in combination with a small value of the combined parameter ($R_c t$) can achieve higher resonant frequencies.

To quantify the frequency region of the negative effective mass density induced by the resonance features of engineered aggregates, the dimensionless dynamic effective mass (m_{eff}/m_{st}) or dynamic effective mass density (ρ_{eff}/ρ_{st}) can be expressed as follows [25]. It is noted that lower/upper bounds of the NEMD are valid when all the constituents of the

metaconcrete structure remain to be elastic, and the local inclusions are sufficiently tuned.

$$\frac{m_{eff}}{m_{st}} = \frac{\rho_{eff} \cdot V}{\rho_{st} \cdot V} = 1 + \frac{\theta}{1+\theta}\left[\frac{1}{1-(\omega/\omega_0)^2}\right] = 1 + \frac{\theta}{1+\theta}\left[\frac{1}{1-(f/f_0)^2}\right]$$

$$\theta = \frac{m_2}{m_1}, \quad \omega = 2\pi f, \text{ and } \omega_0 = 2\pi f_0$$

(2-2)

where θ is the mass contrast ratio between the aggregate and the matrix, m_{st} and V are the total mass and total volume of the unit cell, respectively. As seen from Eq. (2-2), the normalized dynamic effective mass density (ρ_{eff}/ρ_{st}) becomes negative when f approaches to f_0 and then gradually changes to positive (i.e., $f > f_0\sqrt{1+\theta}$). The associated frequency range where ρ_{eff}/ρ_{st} becomes negative is termed as the bandgap or the region of negative effective mass density (NEMD).
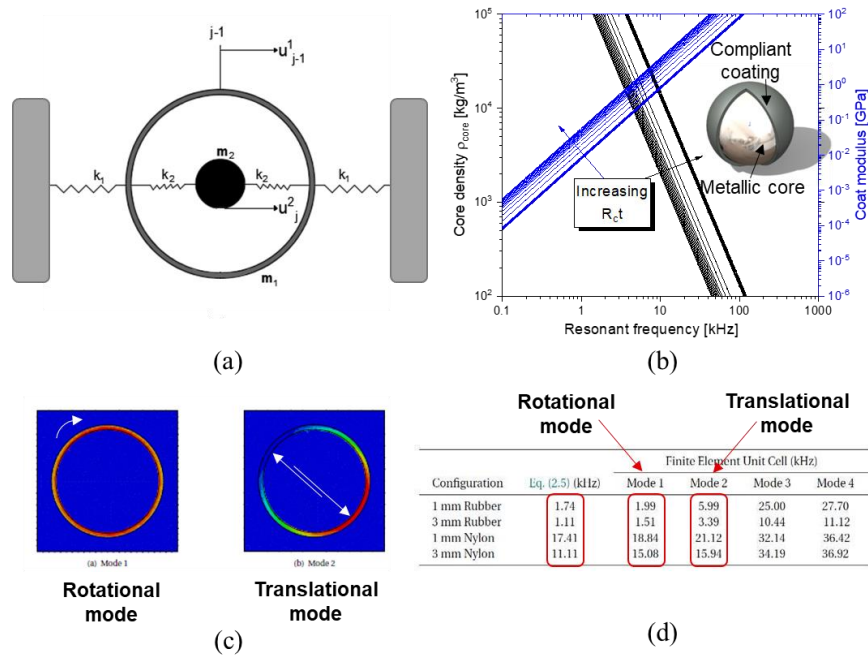
Figure 2-4. Analytical approach to estimate the resonant frequency of engineered aggregates: (a) Equivalent 1D mass-in-mass model, (b) Effect of aggregate parameters on resonant frequencies [25], (c) Translational and rotational mode shapes [25], (d) Comparison of analytical results and numerical predictions [25].

The inner mass (m_2) moves along the out-of-phase direction against the outer mass (m_1), leading to the negative motion of the internal mass within the region of the NEMD. It implies that the wave energy is transferred and stored in the negative motion of the resonant mass, the mechanical wave within this frequency region can be significantly attenuated. The

frequency region of the NEMD is bounded by the resonant frequency (f_0) and the transition frequency where the NEMD is zero. Therefore, the region of the NEMD can be expressed as $[f_0, f_0\sqrt{1+\theta}]$ by letting Eq. (2-2) equal to zero, and either changing the value of θ or f_0 will influence the region of the NEMD. Furthermore, the negative effective properties such as negative effective mass density is triggered by the locally resonant behavior of heavy core only if the resonant frequency or range of bandgap frequencies are within the spectrum of applied loading. Therefore, the resonant frequency of aggregates should specifically fit in the frequency content of the applied loading to enable its frequency-dependent wave mitigation.

On the other hand, it was found that there was an apparent mismatch between analytical results and numerical predictions regarding the estimation of the resonant frequency of engineered aggregates. Specifically, the estimated resonant frequency by using the analytical model was close to 1st modal frequency corresponding to rotational mode as shown in Figure 2-4, while the translational mode is required to activate the local vibration of the core. Namely, the resonant frequency predicted by using an analytical approach may be underestimated. Besides, the wave attenuation properties and negative effective mass density (NEMD) region are dependent on the locally resonant frequency of the engineered aggregates. Thus, it is recommended to conduct a parametric study on the effect of configuration parameters of engineered aggregates on the bandgap characteristics.

2.4.3 Numerical modelling

Apart from the mechanism and analytical study of metaconcrete, numerical verification of the attenuation behavior of metaconcrete structure has been conducted by Mitchell et al. [25]. The numerical results reported in [25, 26, 87] have demonstrated that the maximum longitudinal stress wave amplitude is significantly reduced owing to the existence of periodic resonant inclusions. Specifically, a large proportion of mechanical energy could be absorbed by resonant aggregates thus causing a significant reduction of energy transmission across the slab, which could effectively prevent the matrix from being damaged. Meanwhile, the peak stress amplitude induced by the applied blast load was significantly reduced, so that it could

greatly improve the performance of the material to resist the blast load.

Jin et al. [88] further studied the attenuation performance of metaconcrete rod with fixed-end boundary conditions under blast loading. It shows that the wave mitigation mechanism induced by local vibration of the heavy core could attenuate the stress wave propagation. Also, it has been demonstrated that severe localized damage occurred outside soft coating, as shown in Figure 2-5.
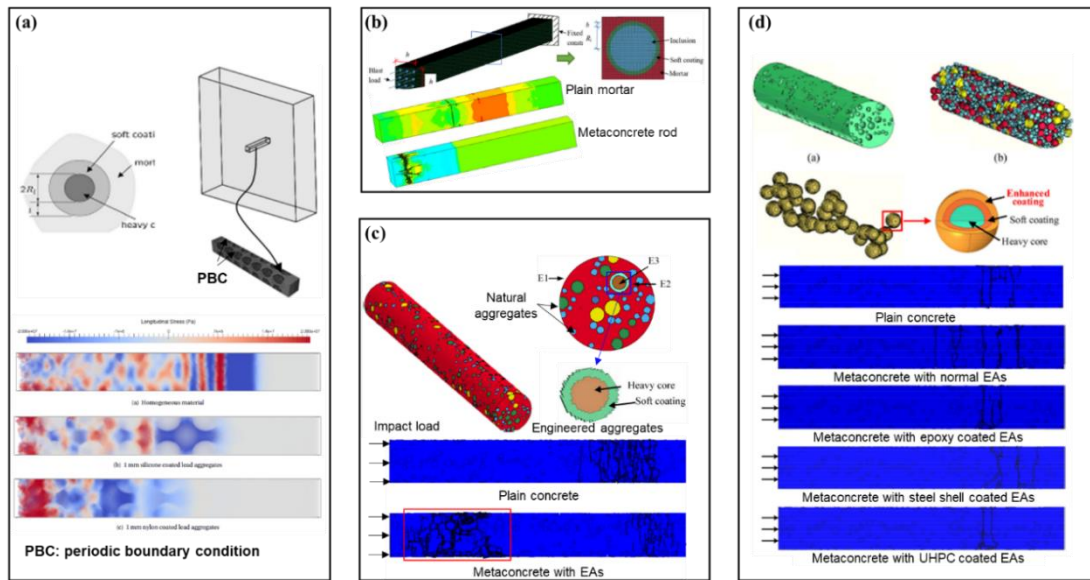
Figure 2-5. Numerical study on metaconcrete structures: (a) Metaconcrete slab under blast load [25], (b) Metaconcrete rod under blast load [88], (c) Mesoscale modelling of Metaconcrete rod under impact load [89], (d) Mesoscale modelling of Metaconcrete rod with enhanced coating [90].

This type of localized damage could be beneficial for absorbing considerable wave energy. However, the geometry and material of the structure should be properly designed and damage needs to be controlled. Subsequently, they further numerically studied the dynamic responses of metaconcrete rod consisting of both natural and conventional engineered aggregates subjected to impulsive loading [89]. They suggested that engineered aggregates with bandgap coinciding with the primary dominant wave frequencies induced by the impulsive loading could be effective in mitigating wave propagation. Besides, it also found that although local vibration of the core could mitigate stress wave propagation, the existence of soft coating reduces the concrete compressive and spalling strength, which might limit the application of

metaconcrete material/structure. To address this issue, the idea of using an enhanced layer outside the conventional engineered aggregates while attempting to maintain the local resonance effect was numerically proposed and verified [90]. Three types of enhanced coating were assessed, and numerical results suggested that enhanced engineered aggregates mixed in metaconcrete rod structure exhibited better attenuation performance and higher impact resistance than metaconcrete rod structure with conventional engineered aggregates. However, the performance of metaconcrete rod structure with enhanced engineered aggregates varied with different coating properties. Therefore, the material for the enhanced coating should be properly selected and designed. Besides, the experimental verification regarding the effect of using the enhanced engineered aggregates is necessary.

2.4.4 Experimental investigation

Various types of specimens, resonators and testing methods summarized in Table 2-1 have been employed in previous experimental investigations to study the stress wave propagation in different LRMs, which were subjected to the impact or vibration excitation at the incident end of the specimen. In order to measure the wave propagation, accelerometers [29, 45, 53, 69, 74, 76] or strain gauges [31, 52, 91] were placed at different locations of the specimen (i.e., incident or transmitted end). The local resonators including soft-coated spherical resonators [4, 28, 29, 31, 53, 92], spring-mass resonators [45, 52, 69, 93] and lattice-like resonators [74] embedded into different matrix materials were investigated. The input stress wave was generated by sonic signal [4, 28], shakers/exciters [29, 53, 69, 74], or impactors [9, 31, 45, 52, 92], representing different loading cases such as sonic wave, vibrational excitations, non-destructive and destructive impulsive loads. The experimental techniques from previous research work on examining stress waves attenuation performance in different LRMs can guide or being used for the experimental design in the present work.

Moreover, regarding the experimental study on metaconcrete material, ultrasonic and vibration tests on wave transmission properties of metaconcrete material were carried out and reported in previous studies [28-30, 83, 94]. The previous experimental studies [28-31, 83]

revealed that adding resonant inclusions into the matrix could improve the mitigation capacity in stress wave propagation by converting the wave energy to kinetic energy through the local vibration of heavy core inside engineered aggregates and thus energy imparted by dynamic loading can be absorbed by the resonant aggregates. When the loading frequency is close to the tunable frequency of resonant inclusions, the resonant inclusions could inhibit the wave propagation throughout the matrix. As a consequence, the sharp transmission dip occurred at the prescribed frequency range, indicating that the underlying physics of the frequency gap was caused by local resonance. Besides, according to previous studies [28-31, 83], another critical feature of metaconcrete material is that the bandgap defined by the tunable frequency range can be customized by changing the configuration of resonant aggregates.
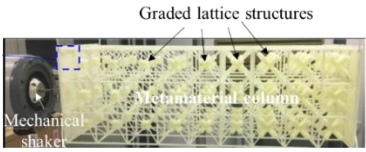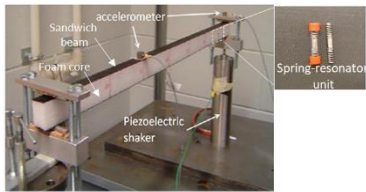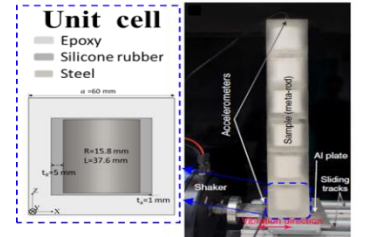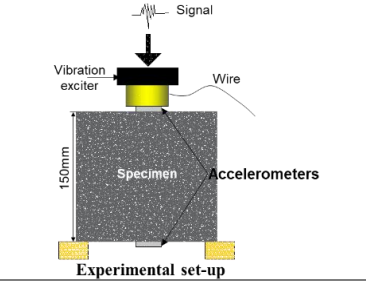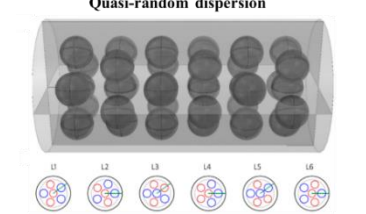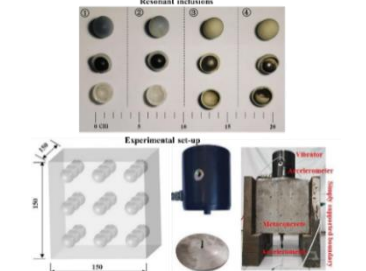
Furthermore, destructive tests on meta-composite made from epoxy rod containing resonant aggregates, which imitates the idea of metaconcrete structure, subjected to high-speed impact were conducted to examine stress wave attenuation properties. A longitudinal strain-based damage criterion was developed to evaluate the performance of the proposed metastructure configuration and examine the validity of underlying physics on stress wave attenuation by local resonance. Impact velocity was arranged in the range of 18 m/s to 100 m/s with plate thickness of impactor from 0.8mm to 25.4mm [31]. The test results showed the reduction of strain magnitude in the estimated bandgap range, in which peak strain was reduced by 72% as compared with homogeneous structure (no inclusions). Although Kettenbeil and Ravichandran [31] explored the dynamic behavior of the rod with resonant aggregates and epoxy resin as matrix subjected to the plate impact, the dynamic response of cementitious metaconcrete material/structure remains to be discovered as the epoxy resin has different mechanical properties from the cementitious material. Meanwhile, very limited studies have been conducted to investigate the dynamic response and damping properties of cementitious metaconcrete structure subjected to transverse impulsive loading. Therefore, it is deemed necessary to perform an experimental study to investigate the performance of structure made by metaconcrete material subjected to impulsive loading and verify its effectiveness in

mitigating stress wave propagation.

Table 2-1. Summary of the experimental setup, resonator and specimen type in previous studies.

No	Ref.	Resonator and Specimen type	Test type	Source/Loading facilities	Schematic illustration
1	[4]	Epoxy-glued 8×8×8 Silicone rubber-coated metallic spheres (SRMS)	Acoustic emission	Sound source	
2	[28]	Cement-mortar with randomly dispersed Polymeric material coated steel mouse balls (PMSMB)	Ultrasound transmission	Digital-signal controlled ultrasound signal producer	
3	[45]	10 spring-attached CMS 25 Smalley springs connected steel plate	Pendulum impact (non-destructive)	Spherical impactor	
4	[76]	DNA-inspired double-helical metamaterials (DDHMs)	Pendulum impact (non-destructive)	Spherical impactor	
5	[52]	Polycarbonate bar with assemblies of Coil-spring resonators and flat spring resonator units	Pendulum impact (non-destructive)	Polycarbonate impactor	
6	[92]	Epoxy matrix with periodically distributed Multilayer rubber-coated dual resonator (RCDR)	Drop Impact (non-destructive)	Metal rod impactor	
7	[93]	Sandwich beam with foam core and Spring- resonators	Hammer impact (non-destructive)	PCB 086C03 impact hammer	
8	[31]	Composite rod made of epoxy matrix and 4 Polyurethane-coated lead ball (PLB)	Plate impact (destructive)	Aluminium plate impactor	

Table 2-1 - (*Continued*)

9	[74]	3×3×9-unit cells of 3D printed composite lattice	Vibration test	Mechanical vibrator	
10	[69]	Sandwich beam with foam core and Spring-resonators	Vibration test	Piezoelectric shaker	
11	[53]	Rod structure casted by epoxy matrix and six Silicone rubber-coated steel cylinders (SRSC)	Vibration test	Electromagnetic Shaker	
12	[29]	Cement-mortar with periodically dispersed polydimetilsyloxhane coated steel sphere (PDMS)	Vibration test	Electro-mechanical mass vibration exciter	
13	[94]	Cement-mortar cylinders with quasi-randomly dispersed PDMS coated or Natural rubber-coated steel sphere	Vibration test	Electro-mechanical mass vibration exciter	
14	[30]	Cement-mortar cylinders with quasi-randomly dispersed PDMS coated + Natural rubber-coated steel sphere (mixed)	Vibration test	Electro-mechanical mass vibration exciter	
15	[83]	Cement-mortar cubes with periodically dispersed Single and dual resonators	Vibration test	Electro-mechanical mass vibration exciter	

2.5 Summary

This chapter presents a comprehensive literature review on different types of mechanical metamaterials and metaconcrete material/structure. The research gaps associated with the study on metaconcrete material/structure are identified as follows.

(1) In the previous studies, it shows that the engineered aggregates with specific configuration could absorb a large proportion of blast energy and reduce the stress transmission in the mortar matrix, which could improve the blast resistance of the concrete structure to a great extent. However, no systematic research has been conducted to evaluate the critical parameters, namely aggregate shape, size, volume fraction, and material properties that influence the bandgap characteristics and wave attenuation performance. In addition, understanding their effects on bandgaps induced by engineered aggregates is essential for a proper design and fabrication of the metaconcrete material and structure for effective structure protection. Besides, the studies on metaconcrete material/structure were limited by the type of resonant modes, in which the transverse resonant mode has not been studied.

(2) Previous numerical works use the elastic or hyper-elastic material model for cement mortar to evaluate the behavior of metaconcrete structure, which can lead to inaccurate predictions on the behavior of concrete-like material subjected to intensive impulsive load. Large impulsive load is likely to induce concrete damage in different modes, which absorbs a large amount of wave energy and also changes the wave frequency, therefore should be considered for a more realistic analysis of wave attenuation characteristics of metaconcrete structure. Parametric studies to understand the effects of different design parameters and configurations of engineered aggregates on the bandgap and stress wave attenuation performance, e.g., energy absorption ratio and stress wave attenuation coefficient, are important but have not been conducted.

(3) No experimental study has been reported in literature yet concerning the performance of

metaconcrete structure made of cementitious material such as mortar subjected to impulsive loading. No experimental verification of the effectiveness of the metaconcrete structure designed with its bandgap covering the primary dominant wave frequency (PDWF) has been reported either.

(4) In the previous studies, the acoustic performance and dynamic response in the longitudinal (i.e., in-plane) mode of metaconcrete structure have been reported. However, the dynamic response of metaconcrete structure subjected to transverse (i.e., out-of-plane) impulsive load has not been examined yet. Also, there is a lack of studies investigating the effect of boundary conditions on the attenuation response of metaconcrete structure subjected to transverse loading. Essentially, the damping properties of metaconcrete structures have not been reported yet.

(5) The recent numerical studies demonstrated that the metaconcrete structure composed of engineered aggregates (EAs) in the conventional form could reduce the compressive and spalling strengths due to the existence of a soft coating layer. This adverse effect of metaconcrete material may limit its wide applications despite its excellent capability in mitigating wave propagations. No experimental study concerning this issue has been reported in literature yet, and a solution to overcome this problem has not yet been developed nor experimentally verified. Moreover, the dynamic compressive properties of metaconcrete material have not been reported, which however is essential for the analysis and design of metaconcrete structure to resist hazardous dynamic loading.

This PhD study tackles the above-identified research gaps and reports the research results. The thesis is a collection of published or unpublished research papers, i.e., manuscripts prepared but are still under review for publication. In each chapter, the information of the relevant paper is also given.

Chapter 3 Influences of engineered aggregate parameters on bandgap of metaconcrete

3.1 Introduction

As reviewed in Chapter 2, the geometric parameters such as the aggregate shape, size, volume fraction, and material properties could influence the bandgap characteristics, i.e., region of the NEMD, but it has not yet been systematically studied. Besides, the frequency range of typical blast scenarios has not been identified but it is essential for designing metaconcrete to resist blast loading. Therefore, this chapter numerically investigates the frequency ranges of different blast scenarios with the scaled distance ranging from 1 $m/kg^{1/3}$ to 10 $m/kg^{1/3}$, which is intended to help design metaconcrete with the desirable attenuation range for structure protection against blast loading. Then, the bandgap characteristics of metaconcrete containing various aggregate configurations are numerically investigated by using a unit-cell study via finite element software *COMSOL Multiphysics*. The numerical model is calibrated first by using the results from a previous study on three-dimensional locally resonant metamaterial. With the calibrated numerical model, the frequency ranges of the negative effective mass density (NEMD) of metaconcrete containing engineered aggregates in four geometric shapes are analyzed. The sensitivity of the factors influencing the region of the NEMD is evaluated and discussed.

The related work in this chapter has been published in Journal of the Mechanics and Physics of Solids.

3.2 Frequency spectrum of blasting wave

When the applied loading frequency (*f*) reaches or exceeds the resonant frequency of the

aggregate (f_0), the negative effective mass density is triggered, which leads to a favorable attenuation performance. Therefore, finding out the targeted frequency range of the applied loading is the primary step for designing engineered aggregates. However, very limited studies on the frequency characteristics of blast loading can be found in the open literature. In this chapter, the frequency characteristics of nine different blasting scenarios are examined in this section to quantify the frequency range. The *LOAD BLAST ENHANCED function in the finite element software LS-DYNA [95], which considers the enhancement of reflected waves, is used to simulate the blast pressure-time history. This function implements the CONWEP (Conventional Weapons Effects Program) empirical model, which is developed based on a report by Randers-Pehrson and Bannister [96]. The CONWEP model given in the code UFC3-340-02 [97] for free air detonation and ground surface detonation has been commonly used to predict the blast pressure due to its efficiency and acceptable accuracy. The overall blast overpressure is predicted by using a characteristic function as follows:

$$P(\tau) = P_r \cos^2 \theta^* + P_i(1 + \cos^2 \theta^* - 2\cos \theta^*) \tag{3-1}$$

where P_i is the incident pressure, P_r is the reflected pressure and θ^* is the angle of incidence. Detailed calculation of P_i and P_r can be found in Kinney and Graham [98] and UFC3-340-02 [97]. In this chapter, free air explosion is applied to the targeted structure, in which the angle of incidence (θ^*) is defined as 0 degree. The peak pressure is characterized by the scaled distance (Z), which is given by $Z = D/\sqrt[3]{W}$, where D is the standoff distance in meter (m), W is the equivalent mass of TNT in kilogram (kg). Different blast scenarios are evaluated by changing the equivalent mass of TNT (W) together with the standoff distance (D) to achieve the specific scaled distance (Z) of 1 and 10 $m/kg^{1/3}$, respectively. The keyword *DATABASE BINARY BLSTFOR is the pre-defined function to retrieve the blast pressure data in LS-DYNA. The time interval between outputs in the numerical simulation is set as 1 μs. The considered explosion cases are given in Table 3-1.

Table 3-1. Parameters for various blasting scenarios.

Standoff distance D (m)	Scaled distance Z ($m/kg^{1/3}$)	TNT equivalency W (kg)
0.1, 1, 10	1	10^{-3}, 1, 10^3
	10	10^{-6}, 10^{-3}, 1
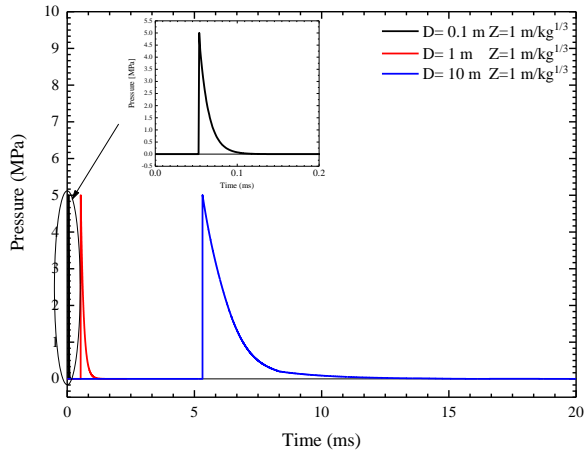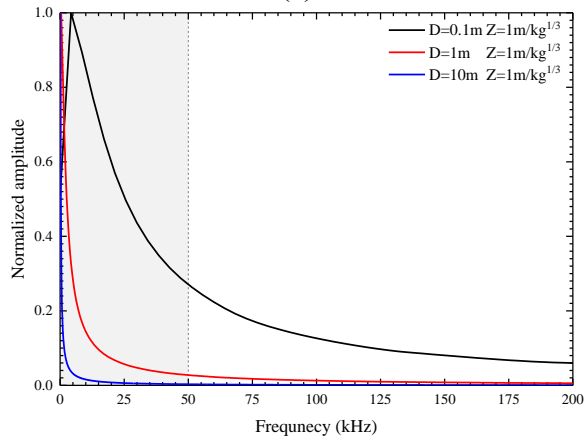
Figure 3-1. Blast load time history and the corresponding frequency spectrum at the scaled distance Z=1 m/kg$^{1/3}$ (a) Time history, (b) Normalized frequency spectra of blast pressure. Shaded area: interested frequency range.
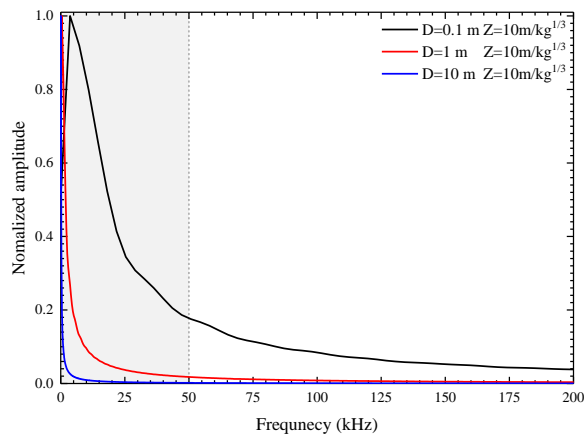
Figure 3-2. Normalized frequency spectra of blast pressure with different standoff distances at scaled distances Z=10 m/kg$^{1/3}$. Shaded area: interested frequency range.

Figure 3-1(a) shows the blast load time histories for the scaled distance of 1 m/kg$^{1/3}$ at different standoff distances (D). To acquire the frequency range, the blast pressure-time

27

history is converted to the frequency domain by using the Fast Fourier Transform (FFT) technique. Figure 3-1(b) depicts the normalized frequency spectra for the scaled distance of 1 m/kg$^{1/3}$ with different standoff distances. The normalized amplitude is defined as the ratio of the pressure amplitude at all frequencies to the peak value of the pressure amplitude. It is found that the frequency range decreases when the standoff distance increases from 0.1 m to 10 m. According to Figure 3-2, the characterized frequency range is sensitive to the standoff distance. The closer standoff distance results in a broader frequency spectrum. However, the mass of TNT has a less significant effect on the range of frequency spectrum than the standoff distance (D). In this chapter, the targeted frequency range for blast mitigation is determined up to 50 kHz and the corresponding amplitude is approximately equal to or less than 30% of the peak amplitude of blast pressure in the frequency domain at the standoff distance of 0.1m.

3.3 Numerical study of dynamic characteristics of metaconcrete unit cell

3.3.1 Model validation

An analytical method has been used to calculate the resonant frequency and bandgap frequencies based on the one-dimensional (1D) spring-mass model. Because of the complexity, most of the existing analytical models consider only a single spherical-shaped engineered aggregate in a 1D spring-mass chain to model the longitudinal wave propagation. Moreover, most of these analytical models are based on single-wave dispersion analysis by solving eigenfrequency problems; no response of engineered aggregates and stress transmission through metaconcrete structure subjected to applied loading are considered. To overcome the limitations mentioned above, numerical simulation is performed to investigate the region of the NEMD for both longitudinal and transverse vibration modes of the unit cell in the matrix based on the frequency response analysis. The proposed numerical model is firstly calibrated with the previous research regarding the characteristics of bandgap frequencies reported in [53]. An experimental study by [53] constructed and tested the three-

dimensional locally resonant metamaterial, which exhibits bandgap-like properties under longitudinal, flexural and torsional excitation. The metamaterial is made up of six locally resonant units. Each unit consists of a silicone-coated steel cylinder and epoxy matrix. It has been reported that this unique structure enables to suppress both longitudinal and flexural vibration under specific frequency region owing to the activation of anisotropic NEMD within the local inclusions [53].

In this chapter, *COMSOL Multiphysics* [99], which has been widely used for analyzing frequency-dependent properties of LRMs in many previous studies [73-75, 77-80], in combination with the theoretical model proposed by [53] is utilized to evaluate the anisotropic effective mass density to the applied frequencies. Figure 3-3(a) shows the configuration of the unit cell in the Z-direction (perpendicular to the top surface), and X, Y-directions (parallel to the top surface). In the simulation, the unit cell is meshed by solid tetrahedral elements with the maximum and minimum element size of 2.5 mm and 0.6 mm, respectively, as shown in Figure 3-3(b). The interfaces within the inclusions and the interfaces between the inclusions and the matrix are assumed to be in perfect contact in the simulation. Thereby the subdomains (i.e., silicone coating and steel rod) are partitioned from the main domain (i.e., unit cell). In addition, periodic boundary conditions (PBC) are applied along the lateral surfaces of the unit cell (i.e., XZ and YZ-plane), and the type of periodicity is set as continuous. The geometric configuration and material parameters used in the simulation are listed in Table 3-2 and Table 3-3, respectively. The equations built-in the model is briefly recalled and adapted from the previous study by [53] as follows.

For a wave propagating in the prescribed direction (i.e., i direction) through the unit cell, the anisotropic dynamic effective mass density (ρ_i^{eff}), effective net force (F_i^{eff}) acting on the unit cell, effective displacement (u_i^{eff}) in i-direction are given in the following equations:

$$\rho_i^{eff} = \frac{m_i^{eff}}{a^3} = \frac{F_i^{eff}}{\ddot{u}_i^{eff} a^3} = \frac{-F_i^{eff}}{\omega^2 u_i^{eff} a^3}, \ i = x, y, \mathrm{z} \tag{3-2}$$

$$u_i^{eff} = \frac{\int u_i djdk \big|_{i,T} + \int u_i djdk \big|_{i,I}}{2a^2} \tag{3-3}$$

$$F_i^{eff} = \int T_{ij} djdk \big|_{i,T} - \int T_{ij} djdk \big|_{i,I}, \quad \begin{matrix} j = x, y, z \\ k = x, y, z \\ i \neq j \neq k \end{matrix} \tag{3-4}$$

where a is the unit cell size, the subscripts i, j, k are the components of the local coordinates system; T_{ij} is the component of stress tensor at the location of the incident and transmitted surface; $\ddot{u}_i^{eff}$ is the effective acceleration of the system; and the subscript I and T stand for the incident and transmitted surfaces, respectively. More in-depth information can be referred to [53].
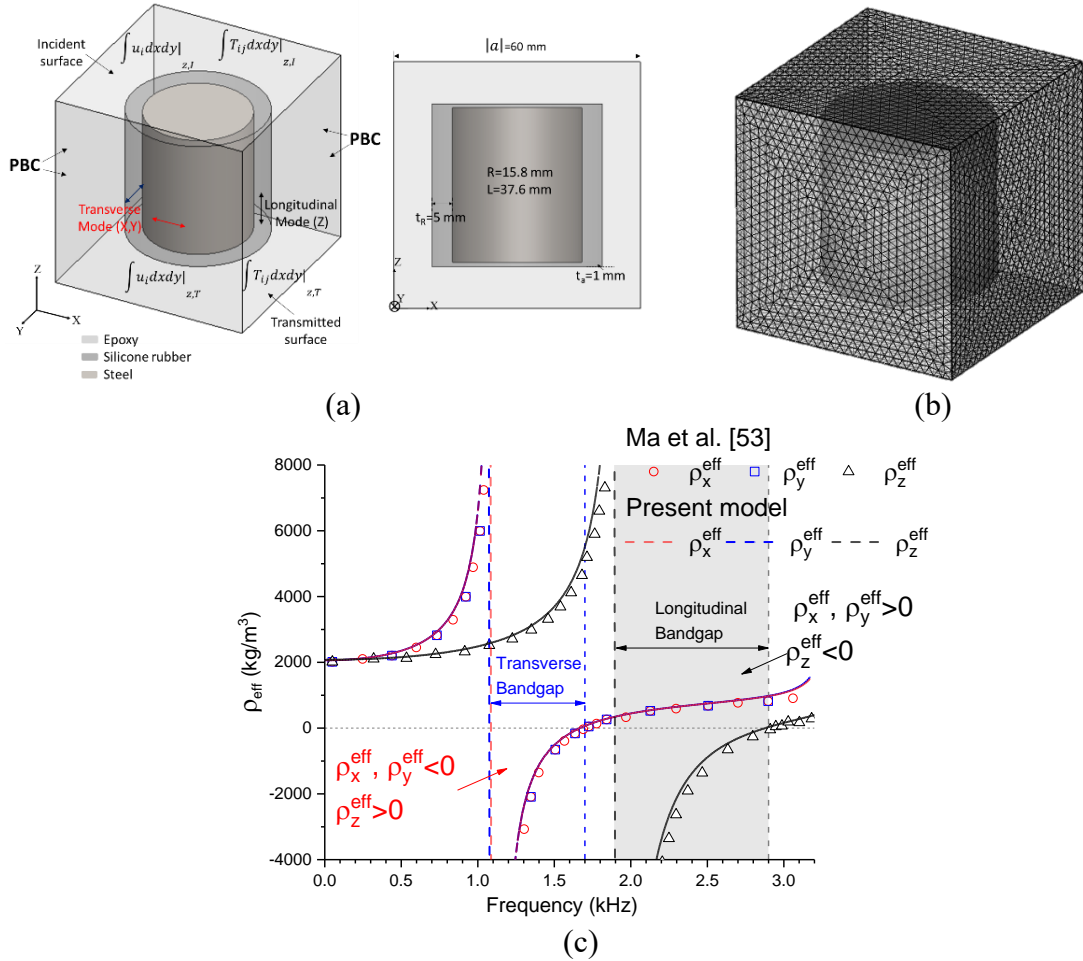
Figure 3-3. (a) Geometry model of the metamaterial unit cell with the radial thickness and axial thickness for the coating proposed by [53], (b) Meshed model, (c) Comparison of the anisotropic effective mass density between the numerical results and the previous results in [53]. Note: PBC means periodic boundary conditions.

With the adopted theoretical model, the dynamic effective mass density (ρ_i^{eff}) is evaluated, in which the results are illustrated in Figure 3-3(c). As shown in Figure 3-3(c), the region for transverse bandgap $\rho_x^{\text{eff}} < 0, \rho_y^{\text{eff}}<0, \rho_z^{\text{eff}}>0$ is about 1.1-1.7 kHz (in blue and red); and the region for longitudinal bandgap $\rho_x^{\text{eff}} > 0, \rho_y^{\text{eff}}>0, \rho_z^{\text{eff}}<0$ is around 1.9-2.9 kHz (in black). Figure 3-3(c) shows a good agreement between the present numerical results and the previous results in [53], which indicates the validity of the present model.

Table 3-2. Geometric parameters of solid elastic metamaterial [53].

Number of the metamaterial unit	Radius of steel R (mm)	Height of steel L (mm)	Axial thickness of silicone rubber t_a (mm)	Radial thickness of silicone rubber t_R (mm)	Unit cell size a (mm)
1	15.8	37.6	1	5	60

Table 3-3. Material parameter of solid elastic metamaterial [53].

Category	Material properties		
	Density ρ (kg/m^3)	Young's modulus E (GPa)	Poisson's ratio v
Epoxy	1130	3.8	0.35
Silicone rubber	1245	3.3×10^{-3}	0.477
Steel	7850	180	0.25

3.3.2 Dynamic behaviors of engineered aggregates with different shapes

Natural aggregates have various shapes including spheres, ellipsoids and polyhedrons [100, 101]. For the sake of simplicity in the analysis, four basic regular shapes containing the sphere, ellipsoid, cylinder and cube (as one of hexahedron) are considered for engineered aggregates to quantify the effect of regular aggregate shapes on the location and region of the NEMD. As explained earlier, the locally resonant behaviors can be attained from different translational resonance modes (i.e., longitudinal or transverse) under dynamic loading. Therefore, it is also worthwhile to explore the region of the NEMD concerning different resonance modes. Table 3-4 illustrates the schematic diagram of the metaconcrete cell occupied by the engineered aggregates of different shapes marked as "S1-S4". The associated geometric and material parameters used in the numerical simulation are listed in Table 3-4, Table 3-5 and Table 3-6, respectively. The periodic boundary condition is assigned along the lateral surfaces of the unit cell (i.e., XZ and YZ-plane). The prescribed displacement is

applied on the top surface of the unit cell, and the bottom surface is left free as shown in Table 3-4. The spherical aggregate, with a core radius of 9 mm and coating thickness of 1 mm, is denoted as "S1". Aggregates with other shapes (i.e., cube, cylinder and ellipsoid) are denoted as "S2-S4", respectively. Moreover, cylindrical aggregate "S3" has two sub-categories. The first one denoted as "$S3_0$" is placed with the axial direction of the cylinder along the Z-direction. The second configuration designated as "$S3_R$" is rotated 90 degrees along the Y-axis, in which the axis of the cylinder is placed along the X-direction. Similarly, two ellipsoidal-shaped aggregates with an aspect ratio (k) of 0.8 denoted as "$S4_0$" and "$S4_R$" are placed along the major axis of the core in the Z and X-direction, respectively. The volume fraction of the core (V_c%) is kept 22% over the total volume of the unit cell for the four shapes. The uniform coating thickness (t) of 1 mm is applied. In this chapter, spherical aggregate is referred to as the benchmark to study the shape effect.

Figure 3-4 summarizes the results of the location (i.e., the lower and upper bound frequencies) and the region of the NEMD. The region of the NEMD is the difference between the upper bound frequency and the lower bound frequency. As shown in Figure 3-4, the aggregates with different shapes produce different bandgap frequencies, indicating that the shape of inclusion affects the bandgap region. This result agrees with the previous findings on locally resonant acoustic metamaterial from Krushynska et al. [102]. On the other hand, although the shape of the engineered aggregate could influence the region of bandgap frequencies, no substantial difference regarding the bandgap width is found for longitudinal and transverse modes as given in Table 3-5. According to Table 3-5 and Figure 3-4, cubic-shaped aggregates could increase the bandgap width by 0.25 kHz in longitudinal mode and 0.75 kHz in the transverse mode as compared to the spherical ones. The directional effect of cylindrical- or ellipsoidal-shaped aggregates on bandgap width is also found. It shows that the cylindrical- or ellipsoidal-shaped aggregates with 0 degree of rotation ($S3_0$ and $S4_0$) could increase the transverse bandgap width by 0.75 kHz and 1 kHz, respectively as compared to the spherical ones. The configuration of $S4_R$ has improved longitudinal bandgap width by 0.5 kHz as compared with spherical-shape aggregate. Since ellipsoidal or cylindrical-shaped aggregates

in 0 and 90 degree behave differently, the loading direction should be considered in the design, which is difficult to control in practice. The spherical-aggregate is selected for the subsequent parametric study. It is found that aggregate in spherical-shape performs consistently regarding the region of the NEMD for both longitudinal and transverse modes. In addition, the spherical aggregate is relatively easy to be fabricated. Therefore, the metaconcrete unit cell containing spherical-aggregate is used for the subsequent parametric study

Table 3-4. Expressions of geometric parameters of aggregates with different shapes.
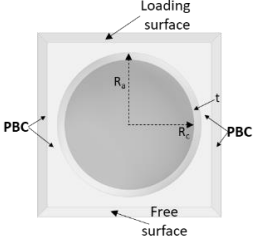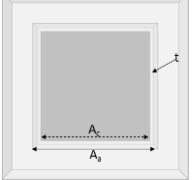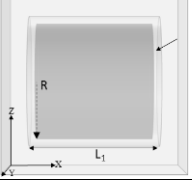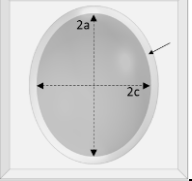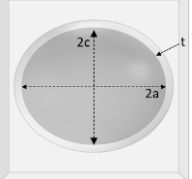
Shape	ID	Schematic diagram	Geometric parameters	Rotation Angle
Sphere	S1		$R_c = 9$ mm $t = 1$ mm $R_a = R_c + t$	-
Cube	S2		$A_c = \alpha_1 R_c$ $\alpha_1 = (\dfrac{3}{4\pi})V_c$ $V_c = \dfrac{4}{3}\pi R_c{}^3$	-
Cylinder	$S3_0$		$L_1 = 2\alpha_2 R_c$ $R = \alpha_2 R_c$ $\alpha_2 = (\dfrac{1}{2\pi}V_c)^{1/3}$	0^0
	$S3_R$			90^0
Ellipsoid	$S4_0$		$a = \alpha_3 R_c$ $\alpha_3 = \dfrac{1}{\sqrt[3]{k}}R_c$ $c = ka$ $k = 0.8$	0^0
	$S4_R$			90^0

Table 3-5. Value of geometric parameters and calculated bandgap frequencies.

Shape	ID	Geometric parameters (mm)				Bandgap frequencies (kHz)	
Sphere	S1				18.0	6.25	7
Cube	S2				14.5	6.5	7.75
Cylinder	$S3_0$	24.1	22	1	15.6	6	7.75
	$S3_R$					6.5	7
Ellipsoid	$S4_0$				19.4	5.75	8
	$S4_R$					6.75	6.75

Table 3-6. Material parameters used in the simulations.

Category	Material	Material parameters		
		Density ρ (kg/m^3)	Young's modulus E (GPa)	Poisson's ration v
Matrix	Mortar [25]	2500	30	0.20
Coating layer	Polyurea [103]	1129	0.0649	0.465
Core	Lead [25]	11400	16	0.44
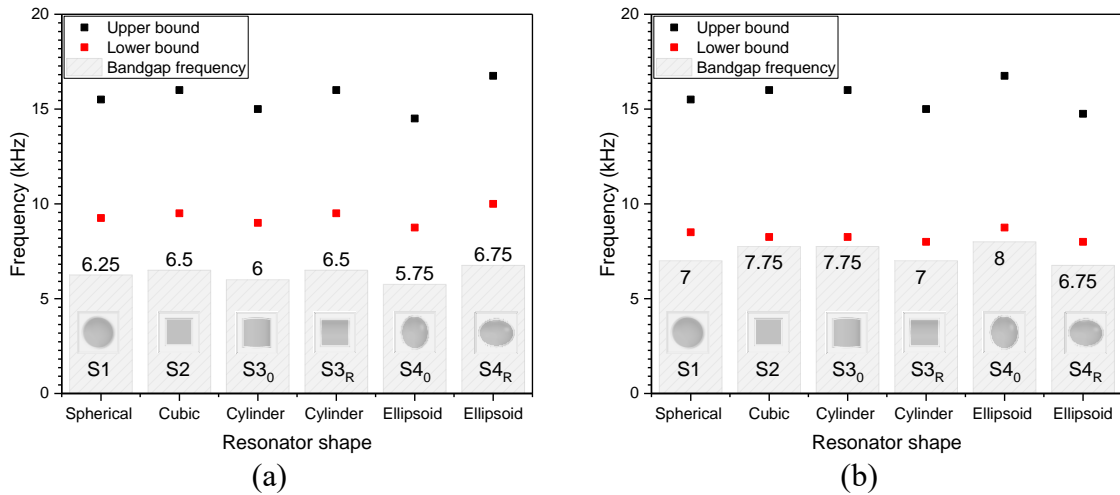
Figure 3-4. Lower/upper bound frequencies and bandgap: (a) Longitudinal mode, (b) Transverse mode.

3.4 Parametric study

To aid in understanding the effect of aggregate configurations on the region of the NEMD, parametric studies are conducted in this section by considering different core sizes, volume fractions and material parameters. Aggregate with the configuration CB2 (in Table 3-7) and the shape "S1" is referred to as the benchmark. The applied loading frequency is set up to 50 kHz to find out the frequency range of the NEMD. In general, the broader region of the NEMD stands for a broader wave attenuation range and allows for enhanced performance. The quantities including the upper bound frequency, lower bound frequency and region of

3.4.1 Effect of aggregate size

Aggregate size ($D_a = D_c + 2t$) consists of two essential components, i.e., the core size (D_c) and coating thickness (t). The effects of D_c and t on the region of the NEMD are evaluated in Sections 3.4.1.2 and 3.4.1.3, respectively. The configuration and material parameters used in the simulations are summarized in Table 3-7.

Table 3-7. Configuration parameters used in the simulations.

	Material		**Parameters**		
	Core material	Coating material	Aggregate size D_a (mm)	Core size D_c (mm)	Coating thickness t (mm)
CB1				19	0.5
CB2				18	1
CB3				16	2
CB4	Lead	Polyurea	20	14	3
CB5				12	4
CB6				10	5
	Core Material	Coating material	Coating thickness t (mm)	Core size D_c (mm)	Mass contrast ratio θ
CS1				10	0.19
CS2	Lead	Polyurea	1	14	0.59
CS3				18	1.46
CS4				22	3.88
	Core material	Coating material	Core size D_c (mm)	t (mm)	
CT1				0.5	
CT2	Lead	Polyurea	18	1	
CT3				2	
CT4				3	
	Core Material	Coating material	Aggregate size D_a (mm)	Volume fraction V_a (%)	Unit cell size L (mm)
VF1				5	43.8
VF2	Lead	Polyurea	20	10	34.7
VF3				30	24.1
VF4				50	20.3

3.4.1.1 Combined effect of various core sizes and coating thickness

In this section, given the unchanged aggregate size ($D_a = D_c + 2t$), the combined effect of simultaneously changing the coating thickness (t) and the core size ($D_c = 2R_c$) is studied. The total aggregate size (D_a) is unchanged as 20 mm for all the scenarios. The coating thickness varies from 0.5 mm to 5 mm and the core size changes from 19 mm to 10 mm accordingly. To visualize the resonance effect, Figure 3-5(a) and (b) show the snapshot of

out-of-phase motion generated by resonant aggregates at the bandgap region with the coating thickness of 1 mm. It shows that the aggregate moves in the opposite direction against the movement of the neighbouring mass triggering the NEMD, which reduces the responses of the surrounding mortar matrix. Figure 3-6(a) and (b) demonstrate the upper and lower bound of the bandgap frequencies concerning different configurations. It proves that increasing coating thickness while reducing the core size leads to the reduction of the region of the NEMD for both longitudinal and transverse modes. The increasing value of coating thickness (t) augments the product of combination parameters ($R_c t$), which causes the reduction of the lower bound of resonant frequency according to one–dimensional metaconcrete model proposed by [87]. In the meantime, the mass of the core drops significantly, which results in a lower mass contrast ratio (θ) between aggregates and the matrix and thereby narrows the region of the NEMD. For instance, the frequency range reduces from 9.3 kHz of CB1 to 1 kHz of CB6 for longitudinal mode with the coating thickness (t) changed from 0.5 mm to 5 mm.

Regarding the transverse mode, Figure 3-6(b) shows an apparent shift of lower bound frequencies when increasing the coating thickness, resulting in a decrease of transverse bandgap frequencies to a greater extent. For example, the frequency range changes from approximately 11.75 kHz of CB1 to 1 kHz of CB6 by increasing the coating thickness from 0.5 mm to 5 mm. Therefore, it can be concluded that increasing the coating thickness while reducing the size of the core causes an adverse effect, leading to reducing the region of the NEMD. On the other hand, increasing the coating thickness might provide more space for the heavy core to vibrate and contribute to the energy absorption to some extent. However, the bandgap width is the main criterion to evaluate the characteristics of metaconcrete unit cell and engineered aggregates in this chapter. The relation between coating thickness and energy absorption could be investigated in future.
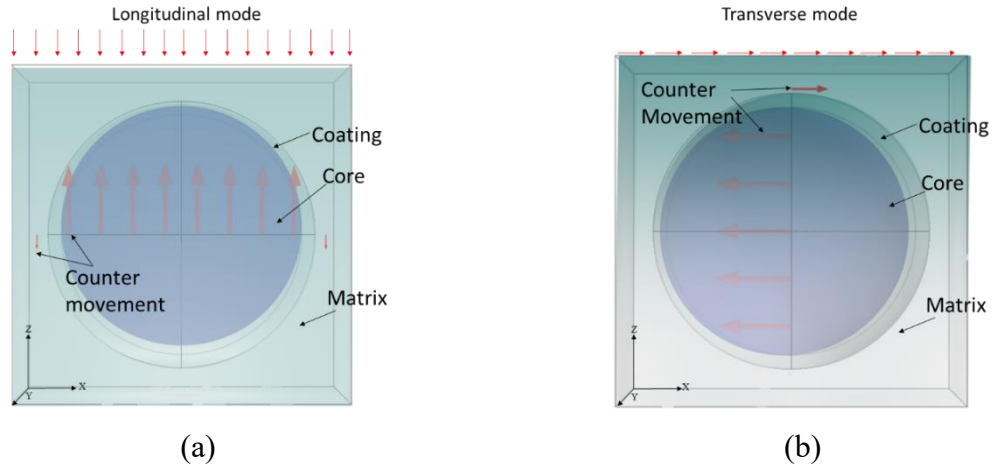
Figure 3-5. Snapshot of negative (out-of-phase) motion of heavy core with coating thickness $t = 1$ mm under the applied loading frequency (f) of 10.251 kHz: (a) Longitudinal mode, (b) Transverse mode.

(a)
(b)
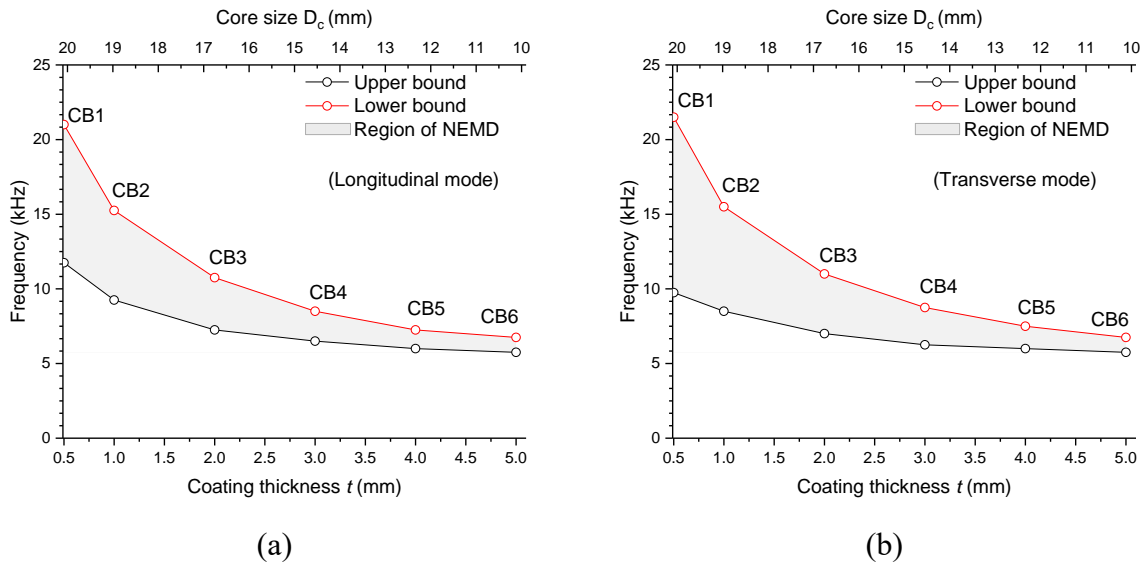
Figure 3-6. Lower and upper bound frequencies and bandgap of combined effects: (a) Longitudinal mode, (b) Transverse mode.

3.4.1.2 Effect of core size

The effect of core size (D_c) on the bandgap is evaluated for both longitudinal and transverse modes. The coating thickness (t) and unit cell size (L) are unchanged as 1 mm and 24.1 mm, respectively. Four cases with the core size (D_c) of 10 mm, 14 mm, 18 mm, and 22 mm are comparatively studied, and only the size of the core is changed to study its effect. As shown in Figure 3-7, the region of the NEMD becomes wider with the rising core size. For instance, the bandgap width changes from 1.5 kHz of CS1 to 10.95 kHz of CS4 for longitudinal mode, while the frequency bandgap width for transverse mode increases from 2 kHz of CS1 to 12 kHz of CS4 with the core size increased from 10 mm to 22 mm. There are two reasons causing

37

changes in the bandgap range. One is that increasing the core size augments the mass of the core while reducing the mass of the surrounding matrix. As a result, the value of mass contrast ratio (θ) significantly increases, resulting in a higher upper bound frequency and a broader range of the NEMD. Another reason is that increasing the core size decreases the equivalent length of the mortar matrix L_m, which increases the matrix spring stiffness according to [87]. To conclude, the bandgap is very sensitive to the variation of core size for both modes as the bandgap increases rapidly with the rising core size when material properties and coating thickness are unchanged.
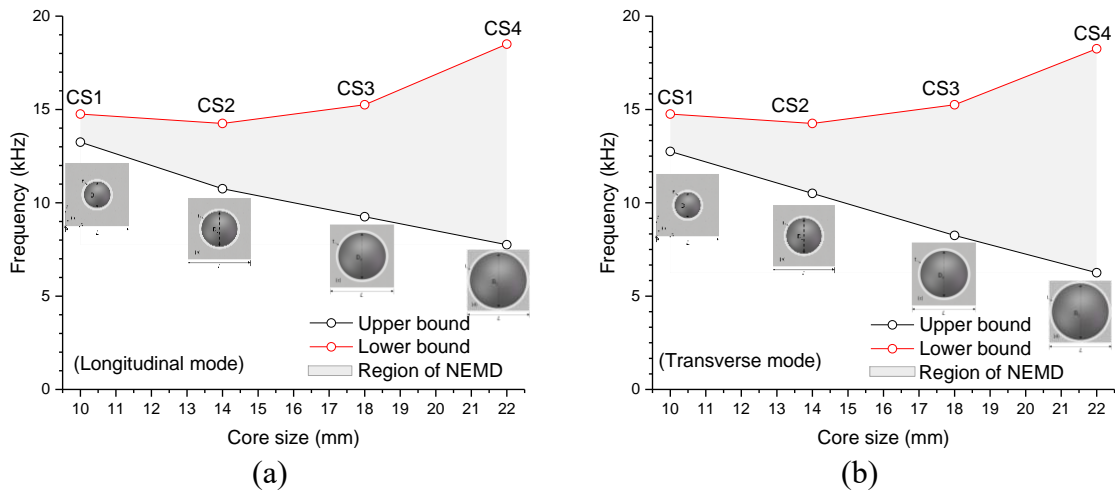
Figure 3-7. Lower and upper bound frequencies and bandgap versus core size: (a) Longitudinal mode, (b) Transverse mode.

3.4.1.3 Effect of coating thickness

The effect of coating thickness (t) on the width of the NEMD is evaluated in this section. The core size and unit cell size are kept constant and similar to the configuration CB2 for the shape "S1". The calculated bandgap for both modes to the coating thickness is presented in Figure 3-8. As the coating thickness increases, the upper bounds of the frequency band for both transverse and longitudinal modes decrease. The upper bound frequency drops faster than the lower bound frequency, causing a narrowing of the bandgap frequencies for both modes. Consequently, there is a shift of the bandgap frequencies to the narrow range for both modes, which implies the adverse effects on bandgap with the rising coating thickness. For instance, the bandgap frequency width changes from approximately 8.25 kHz of CT1 to 4.25

kHz of CT4 for longitudinal mode, while that for transverse mode drops from 10 kHz of CT1 to 4.75 kHz of CT4. There are two reasons causing changes in the bandgap width. Firstly, increasing the coating thickness decreases the stiffness of coating layers, which leads to a decrease in resonant frequency (f_0) by the reciprocal relationship between coating thickness (t) and the resonant frequency. Also, the lower and upper bounds of the NEMD are defined as the range of $[f_0, f_0\sqrt{1+\theta}]$, decreasing the value of ω_0 leads to a reduction of upper bound, causing narrowing of bandgap frequencies. To conclude, the bandgap frequency is less sensitive to the variation of coating thickness as compared to the variation of core size; however, increasing the thickness of the coating layer could trigger an adverse effect on the region of the NEMD for both modes, especially for the transverse mode.
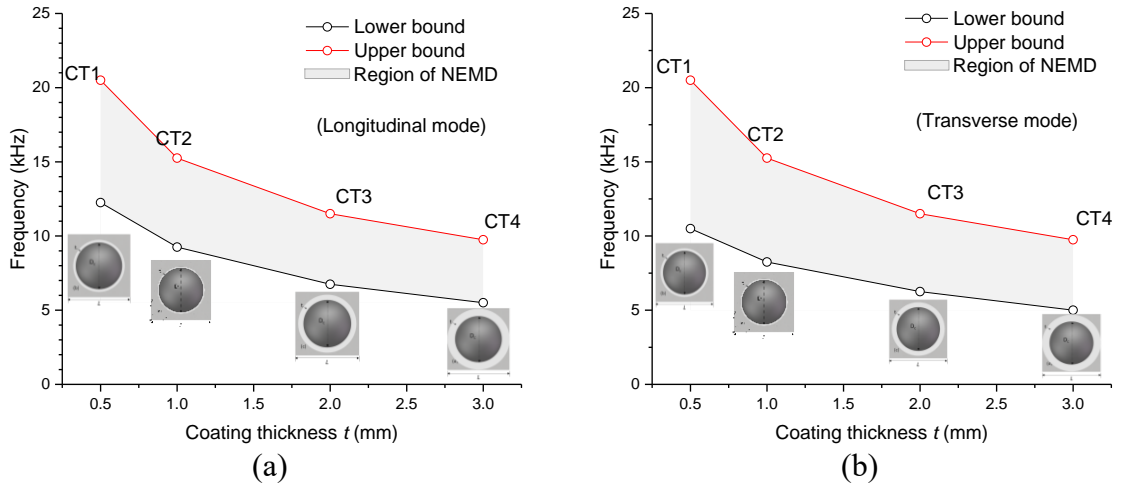
Figure 3-8. Lower and upper bound frequencies and bandgap versus coating thickness: (a) Longitudinal mode, (b) Transverse mode.

3.4.2 Effect of aggregate volume fraction

In this section, the impact of changing aggregate volume fraction ($V_a\%$) on the region of the NEMD is investigated. The volume fraction ($V_a\%$) denotes the ratio of the volume of engineered aggregate over the total volume of the metaconcrete unit cell. The different volume fraction of aggregates is applied by changing the unit cell size only, while the size of the engineered aggregate is fixed. Figure 3-9 presents the calculated results versus aggregate volume fraction for both modes. From Figure 3-9, the upper bound frequency rises quickly when increasing the volume fraction of the engineered aggregates, while the lower bound

frequency remains relatively stable. Consequently, the region of the NEMD becomes wider when increasing the volume fraction of engineered aggregates. For instance, the frequency range increases from approximately 1.25 kHz of VF1 to 10.75 kHz of VF4 for longitudinal mode, and the frequency range for transverse mode increases from 1.75 kHz of VF1 to 12.25 kHz of VF4 with the volume fraction changed from 5% to 50%.
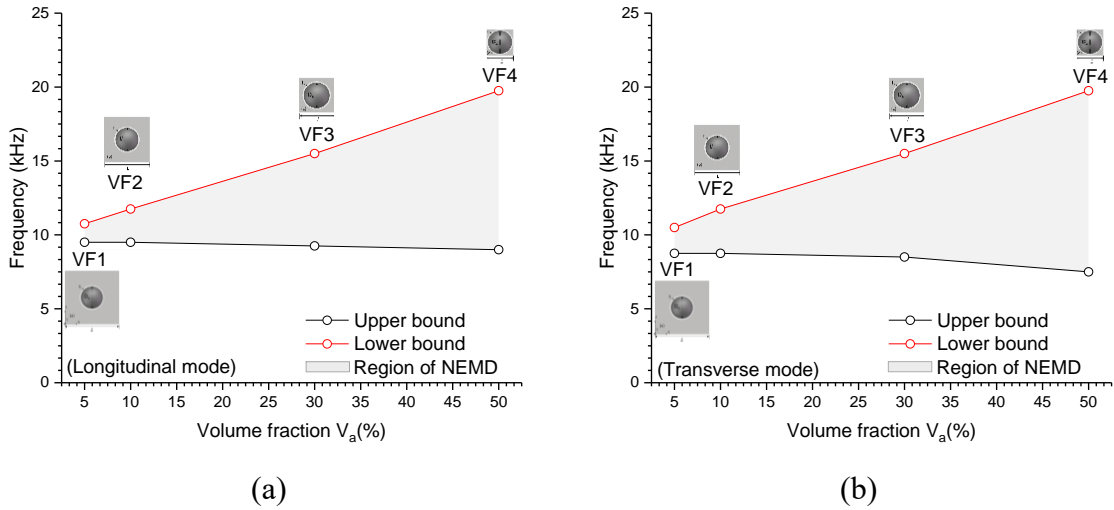
Figure 3-9. Lower and upper bound frequencies and bandgap versus aggregate volume fraction: (a) Longitudinal mode, (b) Transverse mode.

There are two reasons for these observed changes with the volume fraction. One is that increasing the volume fraction of aggregates causes an increase in mass contrast ratio (θ), which results in the broader region of the NEMD. Meanwhile, the equivalent length of the volume of mortar (L_m) reduces when the volume fraction of aggregates grows, leading to the increase of the spring constant of the matrix (k_2). The increasing value of θ combined with the rising value of k_2 produces a wider frequency range of the NEMD. It is concluded that the volume fraction of engineered aggregate plays a vital role in the resonant behavior of metaconcrete unit cell; the region of the NEMD is very sensitive to the changes in volume fraction. Increasing the volume fraction of engineered aggregates increases the bandgap width of frequencies of both modes.

3.4.3 Effect of material properties

The impact of material properties including core density (ρ_c), coating modulus ($E_{c'}$) and Poisson's ratio (ν) on the bandgap is investigated in this section. The normalized parameters

including relative density ratio (α) and relative coating modulus (β) are considered in this chapter. The relative density ratio (i.e., $\alpha = \rho_c/\rho_M$) is defined as the density ratio of the inner core (i.e., lead) over the mortar matrix, and the coating modulus ratio (β) is defined as the ratio of the coating modulus over the elastic modulus of mortar matrix (i.e., $\beta = E_{c'}/E_{matrix}$). The aggregate geometry used in this section is the same as CS3 in Section 3.4.1.2, in which the core size (D_c), coating thickness (t) and unit cell size (L) are unchanged as 18mm, 1 mm and 24.1 mm, respectively.

Table 3-8. Configuration parameters used in the simulations.

	D_c (mm)	t (mm)	V_a (%)	Relative coating modulus β	Coating Poisson's ratio ν	Relative density ratio α
CD1						2
CD2						4.56
CD3	18	1	30	2.16×10^{-3}	0.465	6
CD4						8
CD5						10

	D_c (mm)	t (mm)	V_a (%)	Relative density ratio α	Coating Poisson's ratio ν	Coating modulus ratio β
CM1						10^{-5}
CM2						10^{-4}
CM3	18	1	30	4.56	0.465	10^{-3}
CM4						2.16×10^{-3}
CM5						10^{-2}

	D_c (mm)	t (mm)	V_a (%)	α	β	Coating Poisson's ratio ν
CV1						0.2
CV2						0.3
CV3	18	1	30	4.56	2.16×10^{-3}	0.4
CV4						0.465
CV5						0.49

Note: $\alpha = \rho_c/\rho_M$ and $\beta = E_{c'}/E_{matrix}$

3.4.3.1 Effect of core density

To study the influence of core density (ρ_c) on the bandgap, five density ratios (i.e., $\alpha = 2$, 4.56, 6, 8 and 10) are considered herein. Other parameters, such as coating thicknesses and unit cell size used in the model are given in Table 3-8. Figure 3-10 shows the calculated results of lower and upper bound frequencies and bandgap width for the variation of core

density ratio (α). In general, it is found that the increase in core density leads to a decrease in both lower and upper bound frequencies. In the meantime, limited growth of the bandgap range is obtained with the increasing core density, as shown in Figure 3-10, which agrees with the previous findings regarding locally resonant metamaterials from [79]. For instance, the frequency range changes from approximately 5 kHz of CD1 to 7.25 kHz of CD5 for longitudinal mode, and the frequency range for transverse mode increases from 7.25 kHz of CD1 to 7.75 kHz of CD5 with the relative density ratio (α) changed from 2 to 10.
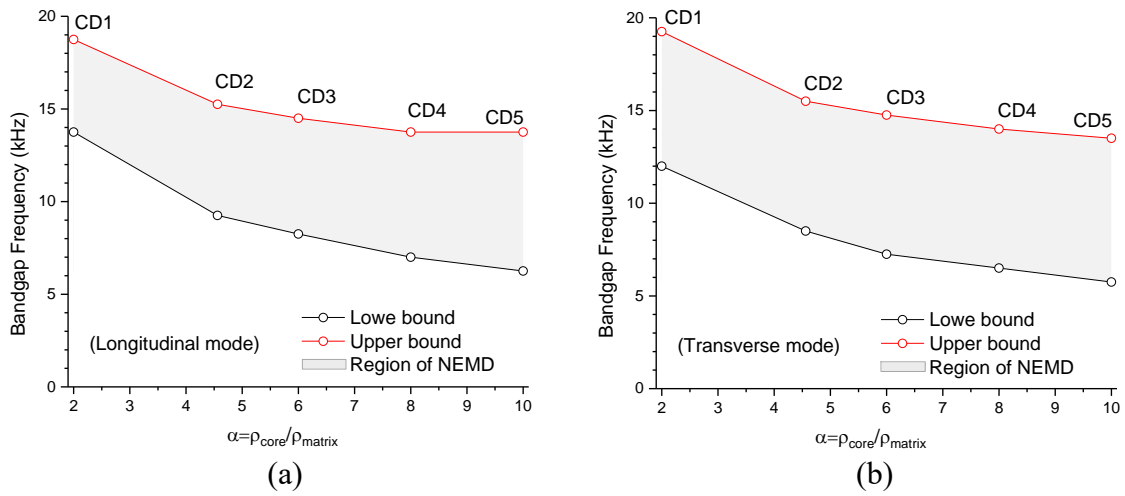
Figure 3-10. Lower and upper bound frequencies and bandgap versus relative density ratio (α): (a) Longitudinal mode, (b) Transverse mode.

These results are related to two factors. One is that the lower bound frequency reflects the resonant frequency of the heavy core and increasing core density triggers the reduction of the resonant frequency of the inner core. Another is that the upper bound frequency decreases at a slower rate than the lower bound frequency with the core density as a result of the increase of mass contrast between engineered aggregate and mortar matrix. Consequently, the region of the NEMD, which is the region between lower bound and upper bound frequency has limited growth. Therefore, it is concluded that the core density has a limited effect on the width of bandgap frequencies for both modes.

3.4.3.2 Effect of coating modulus

Mitchell et al. [25] reported that the modulus value of the coating layer ($E_{c'}$) should be at least an order of magnitude lower than that of matrix material to obtain the desired wave

attenuation function. However, the quantitative relationship between the coating modulus and region of the NEMD for transverse mode has not been investigated yet. Therefore, the correlation between coating modulus and range of the NEMD for two different translational modes is studied in this section. To study the effect, the range of coating modulus is chosen that it can be potentially applied to the coating layer, while Young's modulus of the mortar matrix is unchanged. For instance, the elastomer material has the modulus from 10^{-4} GPa to 10^{-1} GPa [104]. Therefore, five cases of coating modulus ratio (i.e., $\beta =$ $10^{-5}, 10^{-4}, 10^{-3}, 2.16 \times 10^{-3}, 10^{-2}$) are considered herein, where only coating modulus ratios are changed. Figure 3-11 presents the calculated upper/lower bound frequencies and the region of the NEMD with respect to β. The region of the NEMD with a small value of β is very narrow, which can only be observed in the low-frequency region (below kilohertz). However, the region of the NEMD expands when increasing the value of β due to changes in spring stiffness of the coating layer. Moreover, the coating material with lower Young's modulus reduces the equivalent spring stiffness; therefore, the resonance frequency of engineered aggregates shifts to the lower range, leading to the reduction of overall bandgap frequencies. In contrast, increasing coating modulus results in higher resonant frequency and a broader region of the NEMD within the tested range. In general, the region of the NEMD is sensitive to the variation of the coating modulus and increasing the coating stiffness could positively affect the range of longitudinal bandgap frequencies. In addition, the stiffness of the interlayer coating must be compliant with other components to enable the mobility of the heavy core. When aggregate geometry and volume fraction are fixed, it is concluded that using a relatively stiff coating layer by using the material with higher Young's modulus could achieve a broader region of the NEMD in general.
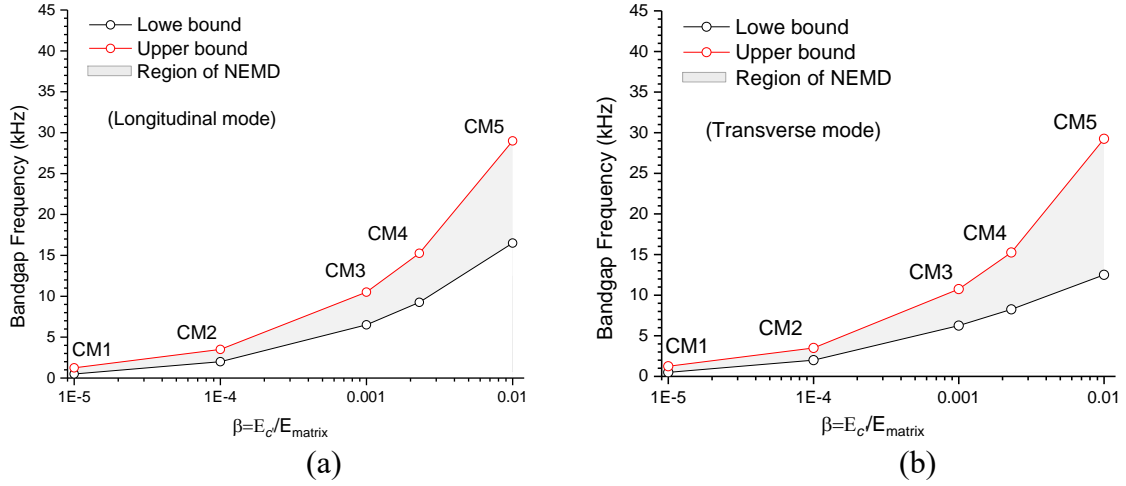
Figure 3-11. Lower and upper bound frequencies and bandgap versus modulus ratio (β): (a) Longitudinal mode, (b) Transverse mode.

3.4.3.3 Effect of coating Poisson's ratio

In this section, five Poisson's ratios (ν) (i.e., ν = 0.2, 0.3, 0.4, 0.465 and 0.49) of the coating are considered. The geometric parameters and other material properties are unchanged. Figure 3-12 presents the calculated results of upper and lower bound frequencies as well as the region of the bandgap. It has been noticed that the bandgap is very sensitive to Poisson's ratio for both modes when ν approaches 0.5. It is because changing the value of ν potentially changes the value of spring stiffness of the coating layer, causing the shift of location and bandgap. Moreover, according to the analytical model proposed by Bo and Li [105], the equivalent stiffness of the coating layer is dependent on Lamé's constants λ_2 and μ_2. The formula for calculating equivalent stiffness of the coating layer is given by Bo and Li [105]:

$$k = -\frac{4}{3}\pi a^2 \left\{ \begin{array}{l} \lambda_2 \left[\left(1-\frac{2}{5K}\right)(T_{31}+T_{32})a + (T_{41}+T_{42})a^{-2} \right] \\ +2\mu_2 \left[\left(1-\frac{1}{2k}\right)(T_{31}+T_{32})a + \left(1+\frac{1}{K}\right)(T_{41}+T_{42})a^{-2} \right] \end{array} \right\}$$ (3-5)

where $\lambda_2 = \frac{E_c\nu}{(1+\nu)(1-2\nu)}$, $\mu_2 = \frac{E_c}{2(1+\nu)}$ and $K = \frac{\mu_2}{\lambda_2+2\mu_2}$; a is the size of the unit cell, and T_{31}, T_{32}, T_{41} and T_{42} are the matrix components.

According to the above analytical model, the variation of Poisson's ratio ν affects the value of equivalent spring stiffness as it could change both Lamé's constants λ_2 and μ_2. It has a

limited effect on spring stiffness when the value of ν is below 0.4. However, the equivalent spring stiffness significantly increases when ν approaches 0.5 due to the rapid rise of first Lamé's constants λ_2. For instance, the bandgap frequency range changes from approximately 3.75 kHz of CV1 to 4.25 kHz of CV4, and then sharply increases to 9.75 kHz of CV5 for the longitudinal mode, and a similar trend is also found in the transverse mode. Higher equivalent spring stiffness results in higher resonant frequency and a broader region of the NEMD, while lower stiffness reduces the part of the NEMD. To further illustrate the phenomenon, a range of value of Poisson's ratios taking small interval value (i.e., 0.01) between 0.4 and 0.49 are studied. The numerical results for the calculated bandgap frequencies are shown in Figure 3-12. It is found that both lower and upper bound frequencies, as well as bandgap frequencies rapidly increase when ν is in the range of 0.4~0.49. Therefore, it is concluded that Poisson's ratio could significantly affect the region of the NEMD when ν approaches the value of 0.5 since the bandgap frequencies shift to a higher frequency region and the frequency range increases considerably.
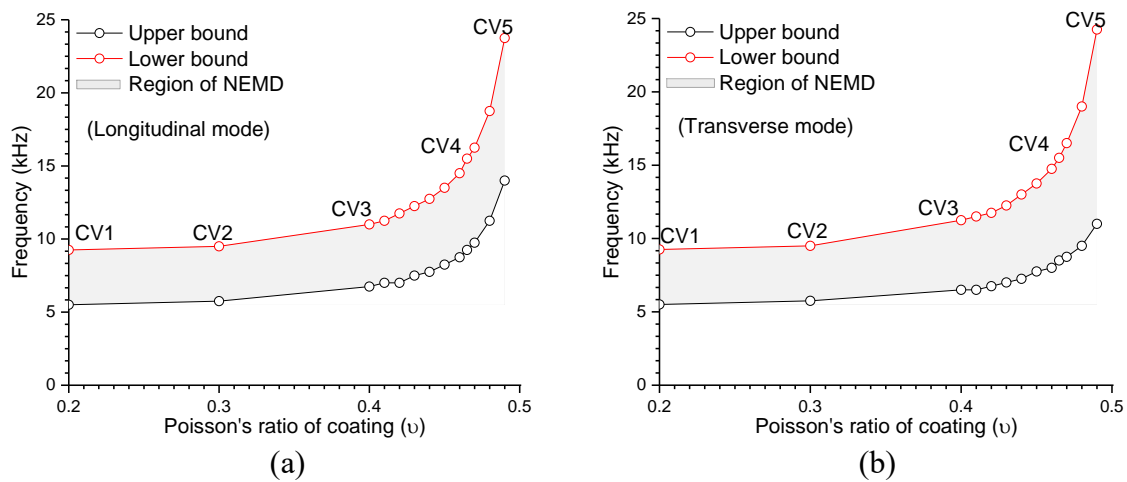
Figure 3-12. Lower and upper bound frequencies and bandgap versus Poisson's ratio of coating layer: (a) Longitudinal mode, (b) Transverse mode.

3.5 Metaconcrete structure subjected to blasting load

The above parametric analyses reveal the influence of various parameters of engineered aggregates on the frequency bandgap. The results can be used in designing the aggregates to meet the requirement for mitigating the propagation of stress wave in a particular frequency

band. In general, the design with significant mass contrast by changing the volume fraction (V_a) and core size (D_c) could enlarge the region of the NEMD. Also, taking a sufficient stiffness contrast between the coating layer and mortar matrix by changing the coating modulus $(E_{c'})$ could help to generate a broader frequency bandgap. However, the width of bandgap frequencies is less sensitive to the variation of core density (ρ_c). Therefore, the spherical aggregate with a relatively large core size (e.g. configuration CS4 in Section 3.4.1.2 is used in this section to obtain the region of the NEMD as wide as possible and to demonstrate the effectiveness of metaconcrete structure with the engineered aggregate against blast loading. The primary objective of this section is to investigate the effectiveness of blasting wave mitigation of metaconcrete structure. The equivalent blasting pressure from 1 g of TNT explosion at 0.1 m of standoff distance is considered and applied onto the incident surface of the structure. The time history of blast loading is shown in Figure 3-13. In the finite element model, the periodic boundary condition (PBC) is assigned to the lateral surface to transmit the movement of the lateral plane, and the end surface is set as free. All the constituents, such as heavy core and matrix are simulated by using solid elements. Four specimens, i.e., homogenized mortar (M-H), mortar matrix with natural aggregate (M-NA), mortar matrix with solid core only (M-SC), and metaconcrete structure with aggregate configuration of CS4 are considered as shown in Figure 3-13. In this chapter, all the constituents of the metaconcrete structure are assumed to remain elastic under the applied blast load. The natural aggregate in the specimen M-NA has Young's modulus E = 40.4 GPa, Poisson ratio ν = 0.16 and mass density ρ = 2750 kg/m^3 based on the previous study by Xu et al. [106]. The geometric and other material parameters used in the simulation are listed in Table 3-6 and Table 3-9. To demonstrate the wave mitigation effect, stress wave attenuation performance is evaluated in this section. The time history curves of transmitted stress at the location of M1 for M-H, M-NA, M-SC and CS4 are shown in Figure 3-14. The transmitted stress-time history curves are attained by plotting the average longitudinal stress (Z direction) at the M1 surface, which is approximately 87.5 mm from the incident surface. The purpose of adding engineered aggregates is to attenuate blast pressure propagating through the

structure. Under blast loading, the engineered aggregates get tuned at their designated frequency exhibiting locally resonant behavior, thus reducing the stress wave transmission in the prescribed frequency range. In this chapter, the peak transmitted stress is selected as the main criterion for the effectiveness of the metaconcrete structure. The peak pressure exerted on the incident surface is around 5 MPa as shown in Figure 3-13.
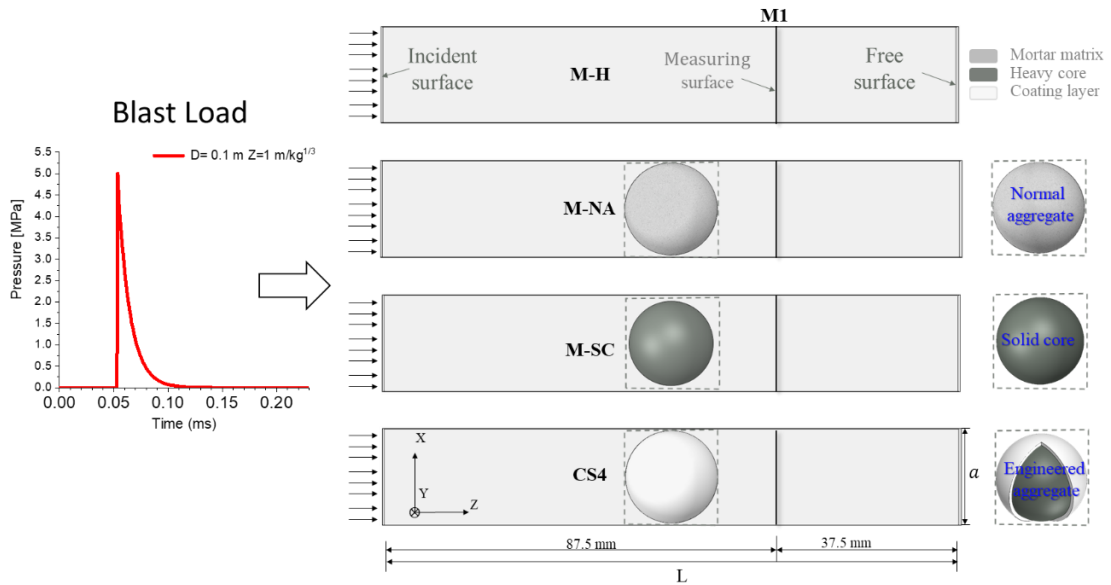
Figure 3-13. Schematic diagram of four specimens subjected to blast loading (lateral view).

Table 3-9. Geometric and material parameters used in the simulation.

ID	Geometric parameters				Material parameters	
	L (mm)	a (mm)	Aggregate size D_a (mm)	Coating thickness t (mm)	Core material	Coating modulus ratio $\beta = E_{coat}/E_{matrix}$
M-H	125	25	-	-	-	-
M-NA	125	25	24	-	Normal aggregate	
M-SC	125	25	22	-	Lead	-
CS4	125	25	24	1	Lead	2.16×10^{-3}

The peak average compressive stress at section M1 presented in Figure 3-14(a) is approximately 4.78 MPa for both H-M, M-NA, 3.58 MPa for M-SC and 3.05 MPa for CS4 measured at M1. Since the parameters (e.g., density, Young's modulus and Poisson's ratio) used for mortar matrix and normal aggregate are comparable, there is no significant difference between H-M and M-NA regarding the amplitude of peak compressive stresses. In the frequency domain, spectrum properties of transmitted stress at section M1 for M-H, M-NA, M-SC and CS4 are illustrated in Figure 3-14(b). For the case of CS4, the peak

amplitude reduction occurs in the prescribed region of the NEMD around 7.7 kHz to 18.5 kHz for longitudinal mode, which agrees with the prediction in Section 3.4.1.2. Since there is no stress reduction for the other three cases (M-H, M-NA, M-SC) within the prescribed NEMD range, it can be inferred that the attenuation effect is achieved by the locally resonant behavior of the engineered aggregate.
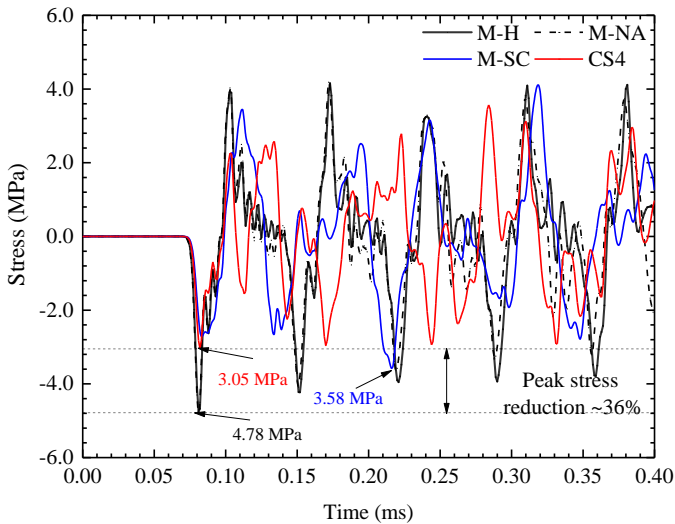
(a)
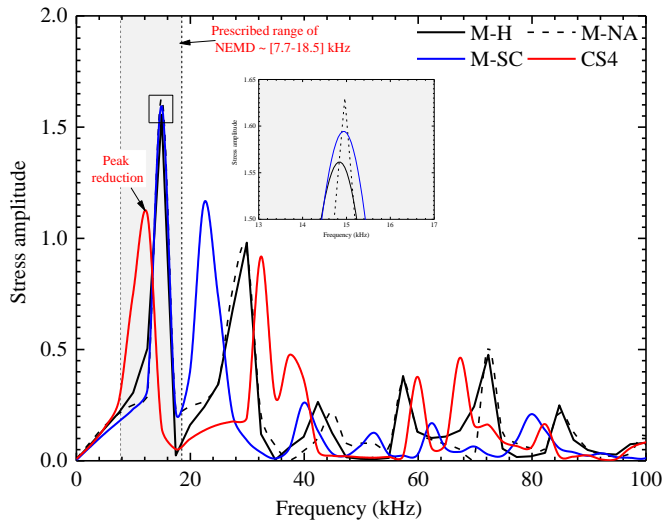
(b)

Figure 3-14. Stress wave at section M1 under blast loading: (a) Transmitted stress-time history, (b) Frequency spectra of the stress wave.

It should be noted that the attenuation effect by locally resonant behavior is not significant since only one unit is employed. Moreover, other peak amplitudes on the stress spectrum outside the prescribed region are due to the higher vibrational modes of the overall structure. To further enhance the attenuation performance, the graded engineered aggregates could be

harnessed to broaden the range of the attenuation region. This aspect is not included in this chapter but could be addressed in future research. In conclusion, the abovementioned results demonstrate that the locations and the range of stress wave reduction are mainly determined by the configuration of engineered aggregate, illustrating the frequency-dependent attenuation behavior of the metaconcrete structure. Besides, the results also show that the aggregate configuration can be purposely designed to attenuate the incoming stress wave at the desired frequencies within the targeted spectrum range.

3.6 Summary

This chapter presents the numerical investigation of the frequency content of blast loading and the critical parameters that affect the bandgap region with different aggregate configurations. Four shapes of aggregates (i.e., sphere, cube, cylinder and ellipsoid) are comparatively studied. The sensitivity of different parameters is numerically explored through parametric analysis by comparing the range of negative effective mass density (NEMD). The main findings from this chapter are summarized as follows.

(1) The frequency contents of blast waves with the scaled distance of 1 m/kg$^{1/3}$ and 10 m/kg$^{1/3}$ have been analyzed, and the targeted design frequency range is found at a maximum of 50 kHz. In addition, the effective range of the frequency spectrum is highly sensitive to the standoff distance. Given the same scaled distance (Z), the broader frequency spectrum is observed when the explosive is placed closer to the exposure surface.

(2) Localized resonant frequency (f_0) of engineered aggregate depends on the geometric parameters ($R_c t$), core density (ρ_c) and coating modulus ($E_c{}'$). Changing the Poisson's ratio (v) of coating material can significantly influence the lower bound resonant frequency (i.e., location of bandgap frequency) when v is between 0.4 and 0.5, in which the location and region of the NEMD are very sensitive to Poisson's ratio. Increasing the volume fraction of engineered aggregate (V_a) has a

limited effect on the lower bound frequency. The bandgap width is less sensitive to the variation of core density (ρ_c).

(3) The location and width of the bandgap frequency are highly sensitive to the variation of the core size (D_c), volume fraction (V_a) and coating modulus (E_c). Increasing core size (D_c), core density (ρ_c), the volume fraction of aggregate (V_a), coating modulus (E_c) and Poisson's ratio could achieve a broader region of the NEMD. The engineered aggregate configuration can be purposely designed to attenuate the stress wave at the desired frequency range.

(4) The effectiveness of structure with engineered aggregates on blast wave mitigation in concrete is demonstrated.

Chapter 4 Effect of engineered aggregate configuration on stress wave attenuation of metaconcrete rod structure

4.1 Introduction

This chapter extends the work from the previous chapter to investigate the effectiveness of using properly designed engineered aggregates to mitigate stress wave propagations in metaconcrete rod structures. Moreover, this chapter investigates bandgap characteristics in metaconcrete rod structures with various configurations of engineered aggregates through frequency domain analysis via software *COMSOL Multiphysics*. In addition, the influences of engineered aggregates configurations on the stress wave attenuation of metaconcrete rod structure equipped with a more realistic concrete material model are numerically investigated by using finite element code LS-DYNA. The effectiveness of properly designing engineered aggregates capable of attenuating impulsive stress at multiple bandgaps coinciding with the primary dominant wave frequencies of stress waves (PDWF) is examined. Subsequently, a flowchart to design engineered aggregates with the integration of multiple resonant frequencies is proposed to enhance the attenuation performance of the metaconcrete rod structure. The results from this chapter could facilitate the design of metaconcrete structures with broader bandgap regions and improve the damage mitigation effectiveness when subjected to impulsive loading.

The related work in this chapter has been published in International Journal of Solids and Structures.

4.2 Bandgap characteristics

4.2.1 Model validation

The frequency response functions, i.e., acceleration ratio, have been commonly used to identify the attenuation behavior and bandgap regions of locally resonant metamaterials (LRMs) by different researchers [53, 74, 107]. In this chapter, *COMSOL Multiphysics* [99] is used to numerically calculate the frequency response function and plot the frequency response curve. The model is firstly calibrated by comparing the response from the present simulation with the available testing data reported in Ma et al. [53]. An experimental investigation by Ma et al. [53] tested the three-dimensional locally resonant metamaterial, which exhibited bandgap-like properties under longitudinal, flexural and torsional excitations. The metamaterial is made of six locally resonant units. Each unit consists of a silicone-coated steel cylinder core and epoxy matrix. It has been reported that this unique mass-in-mass structure enables to suppress both longitudinal and flexural vibrations under the prescribed frequency region, called the bandgap region. To reflect the experimental setup, a numerical model of a rod with six core units of metamaterial placed on the top of the base excitation plate is built, and the analysis is performed using *COMSOL Multiphysics*, the upwards prescribed acceleration (i.e., 1 m/s^2) is applied onto the excitation plate along the longitudinal direction, as in the test. The metamaterial is modelled by six locally resonant unit cells. Each cell consists of a silicone rubber coating and steel core embedded in the epoxy-based cube. In addition, the geometric and material parameters used in the simulation is given in Table 3-2 and Table 3-3. The model is then meshed by solid quadratic tetrahedral elements with a minimum element size of 0.6 mm. More detailed information about model calibration can refer to Chapter 3 in Section 3.3.1.

The response function is obtained by plotting the ratio of acceleration at the top of the rod to that at the bottom (e.g., a_t/a_b) versus the excitation frequencies, as illustrated in Figure 4-1. It shows a frequency dip in acceleration response function at the excitation frequency region from 1.8 kHz to 2.9 kHz (shaded in pink), whereas no frequency dip occurs outside this

region. Therefore, when the excitation frequency is 0.65 kHz outside the bandgap region, the specimen response at the top is not mitigated as shown in Figure 4-1(b), indicating the attenuation performance of the metamaterial structure is not effective outside the bandgap region. In comparison, when the excitation frequency is 2.1 kHz within the bandgap region, the response on the top of the specimen is significantly attenuated. To conclude, a good agreement is achieved between experimental and numerical results. Thus, the numerical model is validated.
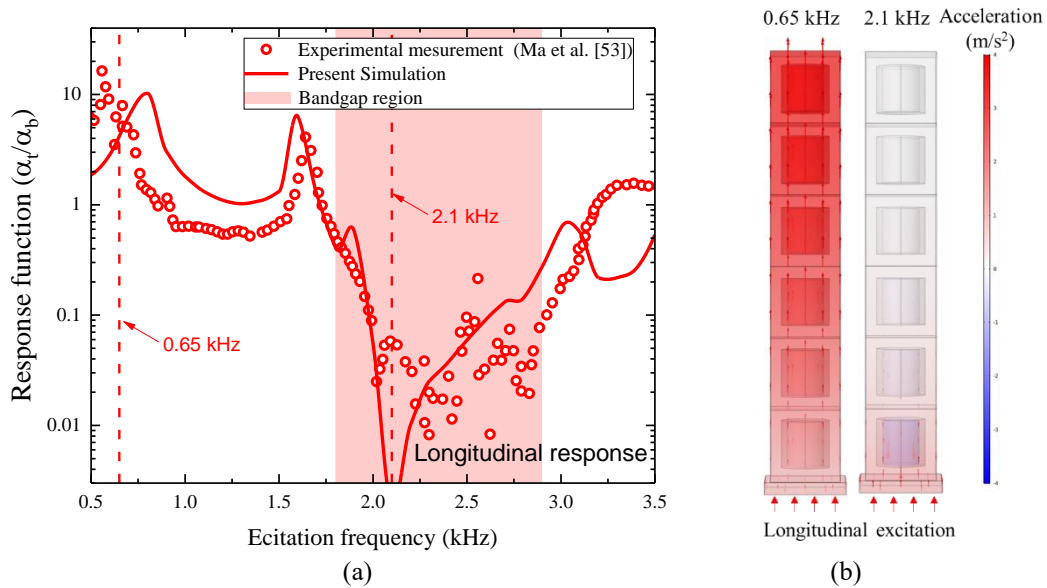
Figure 4-1. (a) Comparison of numerical predictions and experimental results by Ma et al. [53], (b) Acceleration response contour.

4.2.2 Parametric study

With the validated model, parametric studies are conducted to further understand the influence of geometric parameters including core size (D_c), coating thickness (t) and the combination of two parameters (D_c and t) on the bandgap region. In the numerical model, a harmonic excitation with a prescribed acceleration a(t) is applied to the base excitation plate of the specimens with different aggregate configurations, as shown in Figure 4-2. Subsequently, two peak acceleration responses, a_i and a_t along longitudinal directions at the bottom and top of the rod structure are obtained, respectively. The response function is calculated as the ratio of output to input response (i.e., a_t/a_i). All specimens have identical dimensions with the cross-section area and length of the specimens of 30×30 mm² and 240

mm, respectively.

The configurations for all specimens are given in Table 4-1. A series of engineered aggregates with the same coating thickness (t) (e.g., t=2 mm) but different core sizes (D_c) varying from 14 mm to 24 mm, named M-CS1, M-CS2, M-CS3, M-CS4, M-CS5 and M-CS6, are assessed first. In addition, six designs of engineered aggregates with the same core size but different coating thickness (t), named M-CT1, M-CT2, M-CT3, M-CT4, M-CT5 and M-CT6 are studied to investigate the effect of coating thickness on the bandgap region of metaconcrete. To study the influence of the combined geometric parameters (D_c and t) on the bandgap region, engineered aggregates with a fixed diameter ($D_a = D_c + 2t$) of 24 mm but varying coating thicknesses, i.e. the core size is varied accordingly, named M-CB1, M-CB2, M-CB3, M-CB4, M-CB5 and M-CB6 are also included in the simulation. Apart from the geometric parameters, the influences of material properties including core density (ρ_c) and coating modulus ($E_{c'}$) are examined by replacing the material for the solid core and coating layer of engineered aggregates with different materials while keeping the geometric parameters identical. The detailed geometric parameters are listed in Table 4-1. The material parameters used in the simulation for mortar matrix, natural aggregate, coatings and heavy cores are given in Table 4-2.

Table 4-1. Configuration of engineered aggregates in the simulations.

ID	t	D_a	D_c	ID	D_c	D_a	t	ID	D_a	t
M-CS1		18	14	M-CT1		19	0.5	M-CB1		0.5
M-CS2		20	16	M-CT2		20	1	M-CB2		1
M-CS3	2	22	18	M-CT3	18	22	2	M-CB3	24	2
M-CS4		24	20	M-CT4		24	3	M-CB4		3
M-CS5		26	22	M-CT5		26	4	M-CB5		4
M-CS6		28	24	M-CT6		28	5	M-CB6		5

Note: all units in mm.
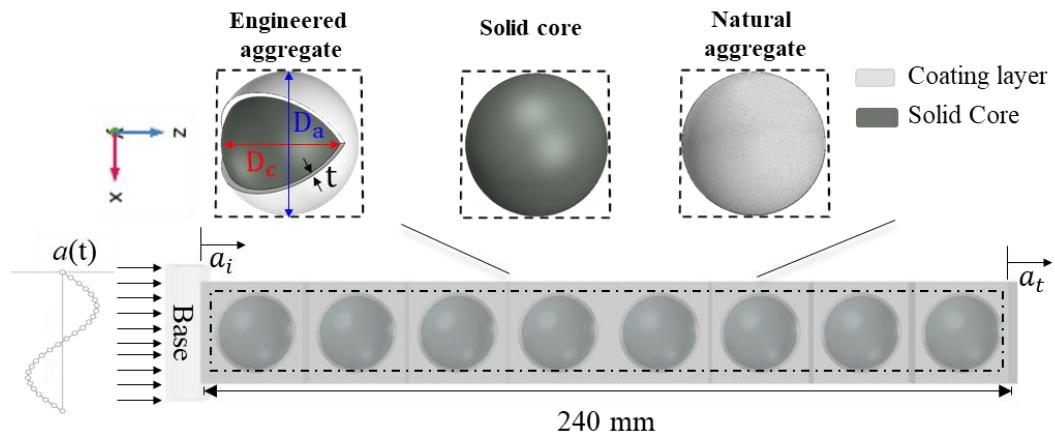
Figure 4-2. Schematic diagram of rod specimens subjected to harmonic excitation. Note: a(t) represents the

applied acceleration in the longitudinal direction.

Table 4-2. Material model and parameters.

Category	Material	Material model and properties		
		*MAT_CONCRETE_DAMAGE_REL3 (*MAT_72_REL3)		
		Density ρ (kg/m^3)	Young's modulus E (GPa)	Poisson's ratio ν	Compressive strength (MPa)
Matrix	Cement mortar [108]	2100	27.6	0.2	34
Inclusions	Natural aggregate [108]	2600	59.87	0.16	160
		*MAT_ELASTIC (*MAT_3)		
		ρ (kg/m^3)	E (GPa)	ν
Coating	Natural rubber [25]	900	0.01	0.49
	Polyurethane [109]	1190	0.0478	0.495
	Compliant polyurea (PU) [103]	1129	0.0649	0.465
	Thermoplastic polyurethane [110]	1200	0.15	0.34
	Stiff polyurea [111]	1120	0.251	0.2
	Nylon [25]	1150	1	0.4
Core	Hematite [112, 113]	5196	162	0.35
	Steel [53]	7850	180	0.3
	Lead [25]	11400	16	0.44
	Tungsten carbide [114]	13800	387.6	0.35
	Tungsten alloy [92]	17500	480	0.28

4.2.3 Results and discussions

As shown in Figure 4-3, no noticeable reduction of acceleration ratio for the mortar with natural aggregate (M-NA) and solid core (M-SC) is observed, while the specimens (e.g., M-CB1 to M-CB6) exhibit the obvious attenuation through the presence of the transmission dip that corresponds to bandgap region.
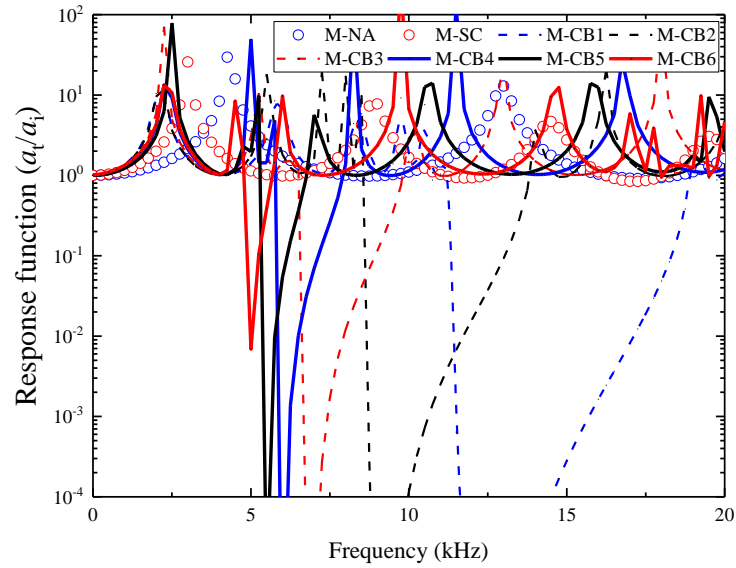
Figure 4-3. Transmission spectra of metaconcrete specimens

To comparatively analyze the influence of design parameters on the bandgap region, Figure 4-4 summarizes the frequency and bandwidths of the bandgap with respect to the design parameters. For instance, Figure 4-4(a) shows that increasing the size of the core (i.e. from M-CS1 to M-CS6) leads to a wider bandgap width. However, increasing the coating thickness (i.e. from M-CT1 to M-CT6) leads to the overall bandgap shifting towards the lower frequency and slightly narrowing the bandgap width as shown in Figure 4-4(b). Moreover, increasing coating thickness while decreasing core size (i.e. from M-CB1 to M-CB6) causes an adverse effect on the transmission properties as the width of the bandgap region becomes narrower, as shown in Figure 4-4(c). The above results agree with the previous findings on metaconcrete structure with a single unit cell reported in Chapter 3, implying a single and multiple identical engineered aggregates generate the same bandgap. In addition, increasing core density results in a much wider bandgap region as shown in Figure 4-4(d), due to the increase of mass contrast ratio as discussed in Section 3.4.3.1 in Chapter 3. Furthermore, the attenuation range is widened and shifts towards the higher frequencies with the increase in coating modulus, as illustrated in Figure 4-4(e). There is a significant change in the bandgap region by using polyurethane as a coating material due to the effect of Poisson's ratio based on the theoretical equation proposed by Bo and Li [105]. According to the theoretical derivation in Section 3.4.3.3, the equivalent coating stiffness sharply increases when

Poisson's ratio of coating material approaches 0.5, causing dramatic changes in lower bound frequency and the bandgap region. In conclusion, the width and location of bandgap regions are sensitive to the core size, coating thickness, combined geometric parameters, core density and coating modulus. The engineered aggregates therefore can be properly designed with the target bandgaps to meet the requirement of stress wave attenuation in the specific frequency range. For example, the prediction of the bandgap region obtained in this section will be used to suppress target frequencies, as illustrated in Section 4.5.
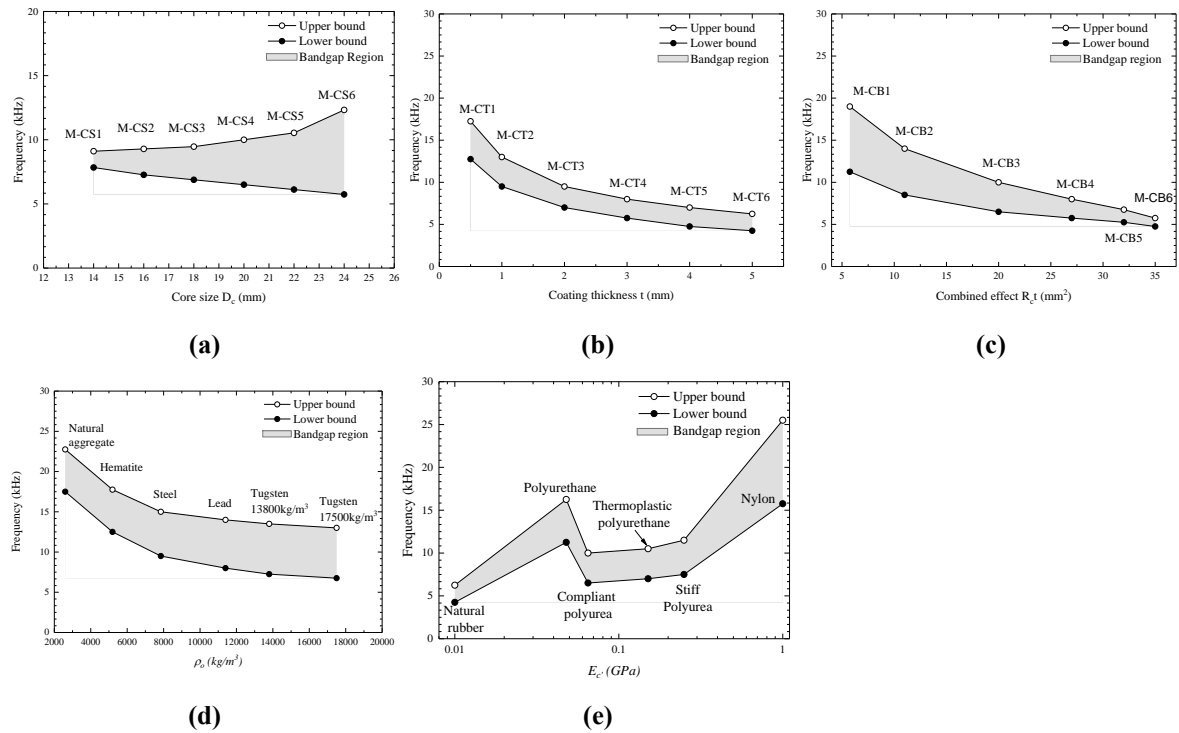
Figure 4-4. Influence of design parameters on the bandgap region: (a) Influence of core size, (b) Influence of coating thickness, (c) Influence of the combination of geometric parameters, (d) Influence of core density, (e) Influence of coating modulus.

4.3 Numerical calibration of concrete mesoscale model

Since there is no experimental work relating to the performance of metaconcrete material/structure subjected to impulsive load yet, the stress wave mitigation performance of conventional concrete with natural coarse aggregates is studied first by using the finite element code LS-DYNA [95]. A three-dimensional (3D) mesoscale model is created by separately modelling the mortar and aggregates. The model is validated by comparing the

numerical predictions with the available testing data from the concrete spalling test conducted by Wu et al. [115] and the numerical simulation reported by Chen et al. [108]. The details of the numerical model, including geometrical and material parameters, are presented in the following sections.

4.3.1 Description of experiment and numerical model

The concrete model consists of two components, including cement mortar and aggregates to simulate the behavior of concrete subjected to impulsive load, in which the dimensions of the specimen and aggregate percentage are given in Table 4-3. Three series of coarse aggregates, namely 4–8 mm, 8–12 mm and 12–16 mm, are considered in the numerical model. The aggregate percentage and size distribution follow Fuller's grading curve, which can be found in [108]. In the present model, a MATLAB-based code is used to generate randomly distributed aggregates by computing coordinates of nodes and element numbers to determine the size and positions of aggregate particles.

Table 4-3. Dimensions and parameters for numerical calibration.

Specimen diameter D (mm)	Specimen length L (mm)	Aggregate size D_a (mm)	Volume fraction of aggregates v_a (%)
74	500	4-8	14.5
		8-12	11.1
		12-16	9.4
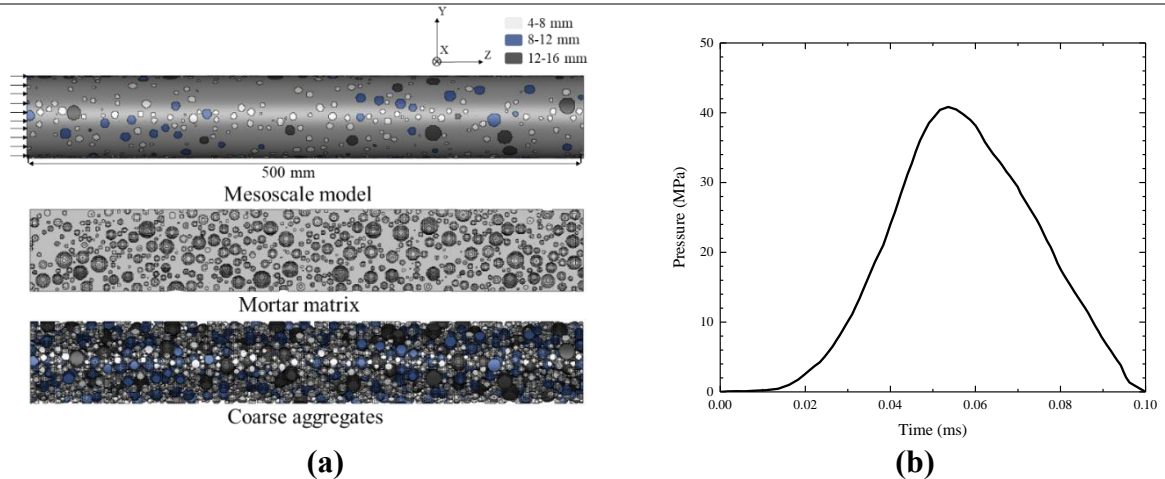
Figure 4-5. (a) Illustration of the mesoscale model of concrete specimen for model calibration, (b) Input impulse [108].

The details of generic algorisms could be found in numerous literature [108, 116, 117]. The process of generic algorisms to generate a 3D mesoscale model in this chapter is briefly

described as follows: (a) generating the entire mesh of specimen; (b) calculating central coordinates and generating distribution of randomly distributed aggregates; (c) checking volume fractions and assigning material properties of each component (e.g., mortar and aggregates). The dimension of the specimen (see Table 4-3) remains the same as that in the literature [108, 115], which has a diameter of 74 mm and a length of 500 mm. Then, the cylindrical specimen is meshed by eight-node solid elements, resulting in a total of 5,471,421 nodes and 5,400,000 elements. The finite element model is subsequently constructed by mapping the meshed elements with the 3D-mesoscale model, as shown in Figure 4-5(a). The operations are checked to avoid the overlapping of neighbouring particles, and the procedures are repeated until the target volume fraction is reached.

4.3.2 Boundary conditions and mesh convergence

The input impulse is applied to the incident surface of the specimen, as shown in Figure 4-5 (b). In the model, the end surface of the specimen is free as in the spalling test [108]. The mesh size is determined by conducting a mesh convergence test to balance the accuracy of the model and the computational cost. Similar to the mesh convergence test in the previous study [108], the mesh size of 1 mm is found to yield accurate predictions regarding strain-time history, damage location and fracture pattern while balancing the computational cost. Therefore, the 1mm mesh size is used in this chapter.

4.3.3 Material model

The commonly used concrete material model MAT_CONCRETE_DAMAGE_REL3 (*MAT_072REL3, named KCC model) in LS-DYNA is adopted for the present simulation. The reliability of this material model in predicting the behavior of concrete-like material under various dynamic loading conditions has been reported in many studies, e.g., [108, 116-119]. KCC model was developed based on plasticity theory and damage theory [120]. This model also considers the strain-rate effect on concrete strength, plasticity and damage softening after failure [121]. In addition, the algorithm MAT_ADD_EROSION is applied to simulate the damage pattern of the specimen under the applied loading. It also helps to avoid

the computational overflow by eliminating elements when it reaches the user-defined failure criteria. The failure criteria in this chapter are determined by the maximum principal strain, in which the values of 0.08 and 0.1 are adopted for the cement mortar and natural aggregates, respectively. Furthermore, the mechanical properties of concrete material under high strain rate loading conditions are significantly different from those under static loading conditions due to the strain rate effect. The ratio between dynamic strength and static strength is defined as the dynamic increase factor (DIF), which is the function of strain rate. In the present simulation, the DIFs of the compressive strength (CDIF) and tensile strength (TDIF) for the concrete are applied by using the following equations [122].

$$CDIF = 0.0419(\log \dot{\varepsilon}_d) + 1.2165 \qquad for \ \dot{\varepsilon}_d \leq 30s^{-1} \qquad (4\text{-}1)$$

$$CDIF = 0.8988(\log \dot{\varepsilon}_d)^2 - 2.8255\log(\log \dot{\varepsilon}_d) + 3.4907 \qquad for \ 30s^{-1} < \dot{\varepsilon}_d \leq 1000s^{-1} \qquad (4\text{-}2)$$

$$TDIF = 0.26(\log \dot{\varepsilon}_d) + 2.06 \qquad for \ \dot{\varepsilon}_d \leq 1s^{-1} \qquad (4\text{-}3)$$

$$TDIF = 2(\log \dot{\varepsilon}_d) + 2.06 \qquad for \ 1s^{-1} < \dot{\varepsilon}_d \leq 2s^{-1} \qquad (4\text{-}4)$$

$$TDIF = 1.4431(\log \dot{\varepsilon}_d) + 2.2276 \qquad for \ 2s^{-1} < \dot{\varepsilon}_d \leq 150s^{-1} \qquad (4\text{-}5)$$

The DIFs for the natural coarse aggregates compressive (CDIF) and tensile (TDIF) strength used in this chapter are given below [123].

$$CDIF = 0.0187(\log \dot{\varepsilon}_d) + 1.2919 \qquad for \ 1s^{-1} \leq \dot{\varepsilon}_d \leq 220s^{-1} \qquad (4\text{-}6)$$

$$CDIF = 1.8547(\log \dot{\varepsilon}_d)^2 - 7.9014\log(\log \dot{\varepsilon}_d) + 9.6674 \ for \ 220s^{-1} < \dot{\varepsilon}_d < 1000s^{-1} \qquad (4\text{-}7)$$

$$TDIF = 0.0598(\log \dot{\varepsilon}_d) + 1.3588 \qquad for \ 10^{-6}s^{-1} \leq \dot{\varepsilon}_d \leq 0.1s^{-1} \qquad (4\text{-}8)$$

$$TDIF = 0.5605(\log \dot{\varepsilon}_d)^2 + 1.3871\log(\log \dot{\varepsilon}_d) + 2.1256 \ for \ 0.1s^{-1} < \dot{\varepsilon}_d < 50s^{-1} \qquad (4\text{-}9)$$

4.3.4 Comparisons between numerical and experimental results

The strain time histories of the element (marked in red) at 150 mm from the incident surface presented in Figure 4-6 are compared. As shown, the current simulation results agree well

with the experimental results by Wu et al. [115] and the numerical results by Chen et al. [108]. In addition, the predicted damage pattern obtained from the present simulation results is also similar to the experimental observation presented by Wu et al. [115], as illustrated in Figure 4-6. Therefore, the present mesoscale numerical model by considering the aggregates and mortar is validated.
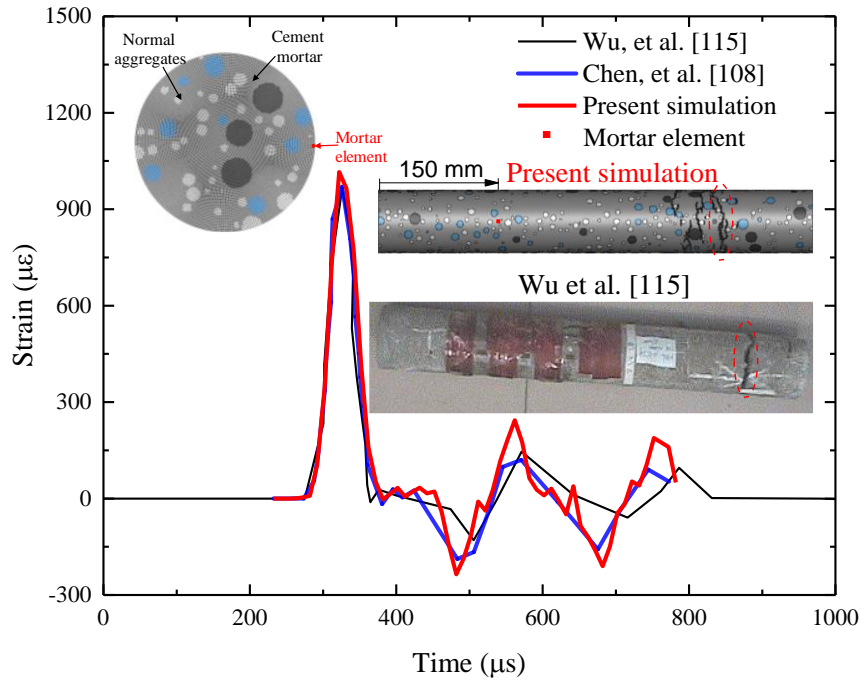
Figure 4-6. Comparison of damage modes and strain time-histories predicted by the present model, and the results reported by Wu et al. [115] and Chen et al. [108].

4.4 Numerical study of metaconcrete structures subjected to impulsive loading

4.4.1 Comparison of wave propagation in metaconcrete structures with different inclusions

4.4.1.1 Model validation and convergence test

With the calibrated numerical model, the performance of rod structures with and without embedding resonant inclusions are comparatively studied in this section by using finite element software LS-DYNA. Figure 4-7 and Table 4-4 provide the configuration and

parameters used in the numerical simulations, respectively. All specimens have identical dimensions and boundary conditions but different types of aggregates. The length (L) and cross-section area of the specimens are 240 mm and 30×30 mm^2. These specimens are subjected to an impulsive load with a peak stress of 5 MPa. The input impulse time history and the corresponding frequency spectrum are shown in Figure 4-7(a) and Figure 4-7(b), respectively. To save the computational cost while achieving reliable numerical results, mesh convergence tests are also conducted with three mesh sizes, namely, 2 mm, 1 mm and 0.5 mm. The mesh convergence is examined by comparing stress-time histories of metaconcrete specimen M-CB3 at cross-section B subjected to the above-defined impulsive load. As shown in Figure 4-8(a), a 1 mm mesh size gives an almost identical prediction to that using a mesh size of 0.5 mm. In contrast, the simulation by using 2 mm element sizes gives slightly different predictions. Considering the balance between accuracy and efficiency in simulation, the mesh size of 1 mm is used in the subsequent simulations. Material model MAT_ CONCRETE_ DAMAGE_ REL3 (*MAT_072REL3,) is adopted to simulate mortar and natural aggregate. Material model MAT_ELASTIC (*MAT_3), the isotropic elastic material model, is adopted to simulate the coating and core and key input parameters are given in Table 4-2. Furthermore, the effect of the possible damping of the system is ignored in the simulation as it has a small contribution on stress wave attenuation compared to that of other effects such as local resonant, wave impedance, etc.

Table 4-4. Specimen configurations.

ID	Description	Material		Geometric parameter	
		Coating material	Core material	D_a (mm)	t (mm)
M-H	Homogenized mortar	-	-	-	-
M-NA	Mortar with natural aggregates	-	Natural aggregate	24	-
M-SC	Mortar with solid cores	-	Lead	22	-
M-CB3	Mortar with engineered aggregates	Polyurea	Lead	24	2
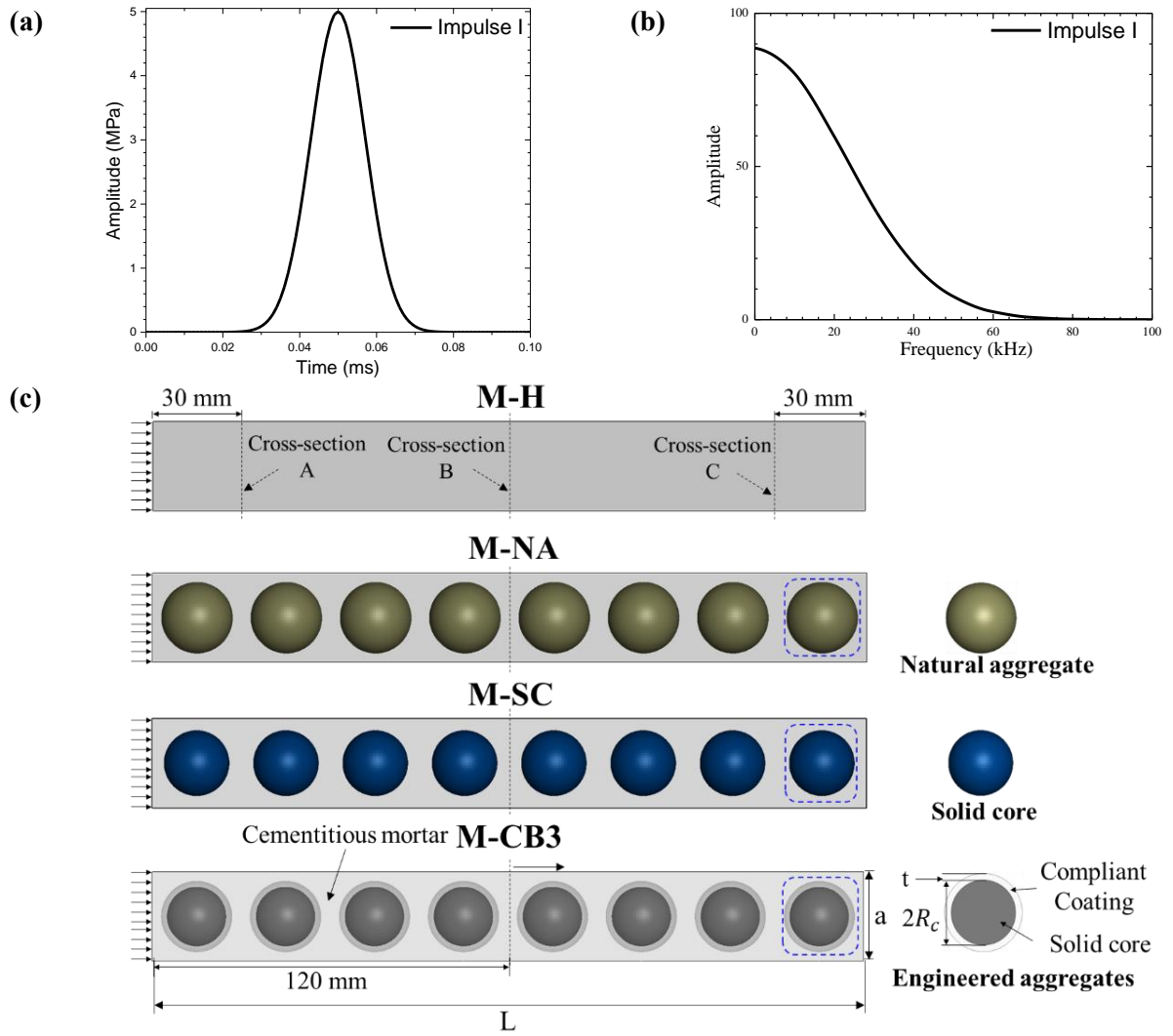
Figure 4-7. (a) Time-history of impulse I, (b) Frequency spectrum, (c) Schematic diagram of specimen M-H, M-NA, M-SC, M-CB3.

To find the dominant wave frequencies of the selected structure under stress wave propagation, M-H (homogeneous, mortar only) specimens with the abovementioned dimension is used as an example for analysis. The same impulsive load profile with peak stress of 5 MPa (see Figure 4-7(a)) is adopted to evaluate the dominant frequencies of stress wave propagating in the selected structure. The average transmitted stress-time histories are extracted from three locations, i.e., cross-sections A, B, and C located at 30 mm, 120 mm and 210 mm from the incident end of the specimen, respectively. The stress-time histories and their corresponding frequency spectra at three designated locations are presented in Figure 4-8(b) and Figure 4-8(c), respectively. As shown in Figure 4-8(c), the dominant wave frequencies of the structure are almost unchanged at three selected locations (A/B/C)

although time delay and some wave attenuations occur when the wave propagates from section A to C. As shown, there are a few dominant wave frequencies, and the first dominant wave frequency in the M-H specimen is 7.96 kHz. To attenuate the stress wave propagation in the specimen, ideally, the engineered aggregates should have a bandgap that covers these dominant frequencies to mitigate the transmissions of the predominant wave energy. In addition, it is interesting to observe that when wave propagates from section A to B, the amplitude corresponding to the first dominant wave frequency increases while the amplitude for the secondary wave frequency decreases. To further examine the effect, average stresses at two additional sections, namely, A1 and A2 (i.e., located at 70 mm and 100 mm from the incident end) in the time and frequency domain are depicted in Figure 4-9. As shown, the amplitude of the wave corresponding to the first dominant frequency increases when the wave propagated from A1 to A2 (highlighted by the yellow box), which might be because the boundary reflection effect from the ends becomes less significant as the wave approaches the middle of the specimen. In the contrast, when the location is closer to the end, the composition of the stress waves becomes more complex due to wave reflection and superposition of incident and reflected waves. Thus, some of the high-frequency components (i.e., second spectral peak) of the stress wave become more prominent (highlighted by the blue box). As shown in Figure 4-4(c), the mortar with engineered aggregates coated by 2 mm thick polyurea (M-CB3) has a bandgap ranging from 6.5 kHz to 10 kHz. To evaluate the effectiveness of using M-CB3 aggregates to mitigate the propagation of wave with the first dominant frequency, specimens with 8 M-CB3 aggregates, 8 natural aggregates (M-NA), 8 solid core (M-SC), together with the homogenized mortar (M-H) as shown in Figure 4-7(c), subjected to impulsive loading are modelled.
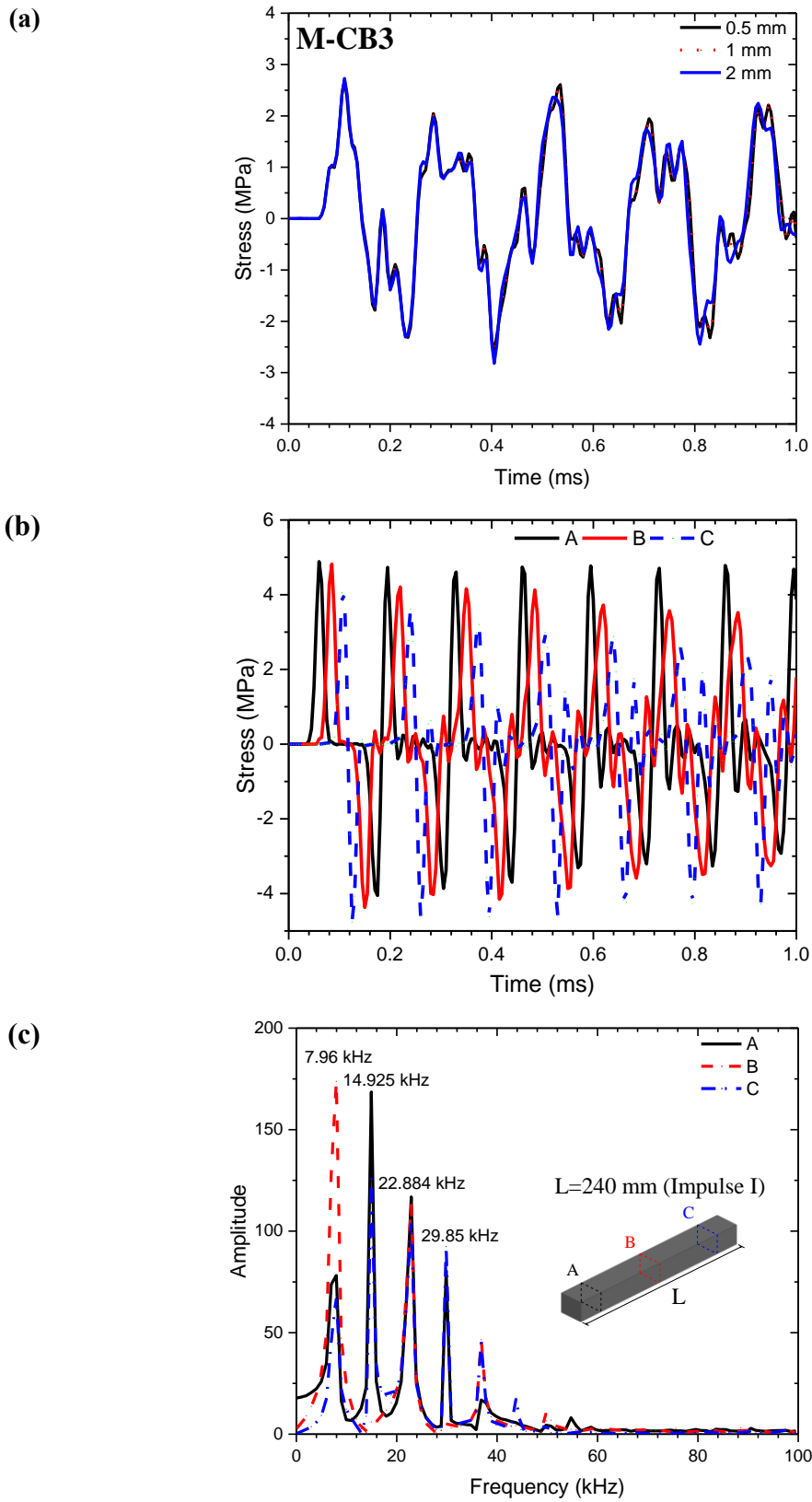
Figure 4-8. (a) Mesh convergence test, (b) Average cross-sectional stress time histories of M-H at three

locations, (c) Frequency spectra of stress at different cross-sections.
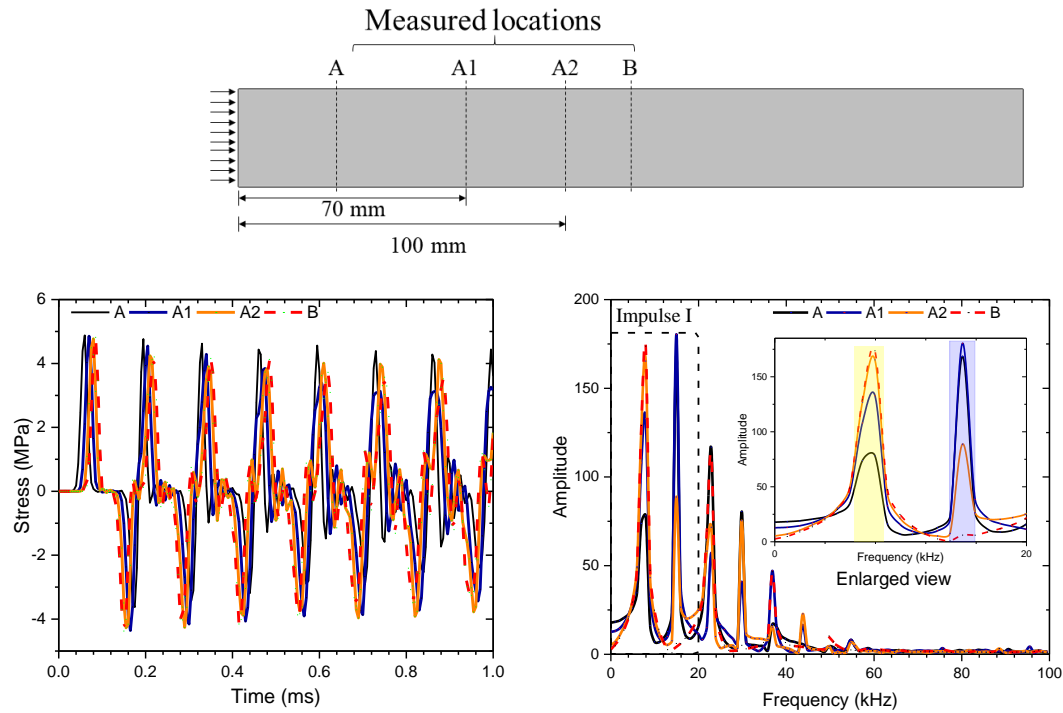
Figure 4-9. Average cross-sectional stresses measured from sections A, A1, A2 and B of specimen M-H in the time and frequency domain.

4.4.1.2 Results and discussion

As shown in Figure 4-8(c), the stress wave at cross-section B (i.e., middle of the specimen as illustrated in Figure 4-7(c)) has the highest amplitude corresponding to the first dominant wave frequency at 7.96 kHz. Therefore, the stress at the cross-section B is selected and analyzed in this section to comparatively investigate the effectiveness of suppressing primary dominant wave frequency on the stress wave attenuation by embedding engineered aggregates. Figure 4-10(a) and Figure 4-10(b) present the average stress at the cross-section B for different rod structures in the time and frequency domains, respectively. As shown in Figure 4-10(a), the initial rise of the stress is due to the transmission of the initial impulse at the designated location. The rising time (t_r) represents the time that the initial peak stress reaches the peak value. The rising time of specimen with engineered aggregates (e.g., M-CB3) is slower as compared to the other three specimens (i.e., M-H, M-NA and M-SC) because of the very different material properties of the engineered aggregates to those of mortar matrix, as well as the local vibration of the solid core. The rising time of M-H and M-NA are almost the same because the material properties that affect the wave propagation,

namely density and modulus or mechanical impedance of mortar and natural aggregates do not vary drastically. Since the lead core material has a very different mechanical impedance from mortar, the rising time of wave in M-SC is also slower than those in M-H and M-NA specimens, but faster than that in the M-CB3 specimen. The changes in wave profiles in the M-CB3 specimen might be influenced by the coating impedance and local vibration of the solid core. After the initial peak, the compressive stress wave propagates in the specimen and reflects at the end surface and becomes a tensile stress wave. The time lag ($t_{l'}$) between initial and second peak compressive stress (positive sign) in M-CB3 is greater than that (t_l) of other specimens. This is because energy trapping in engineered aggregates due to local vibration slows down wave propagation.
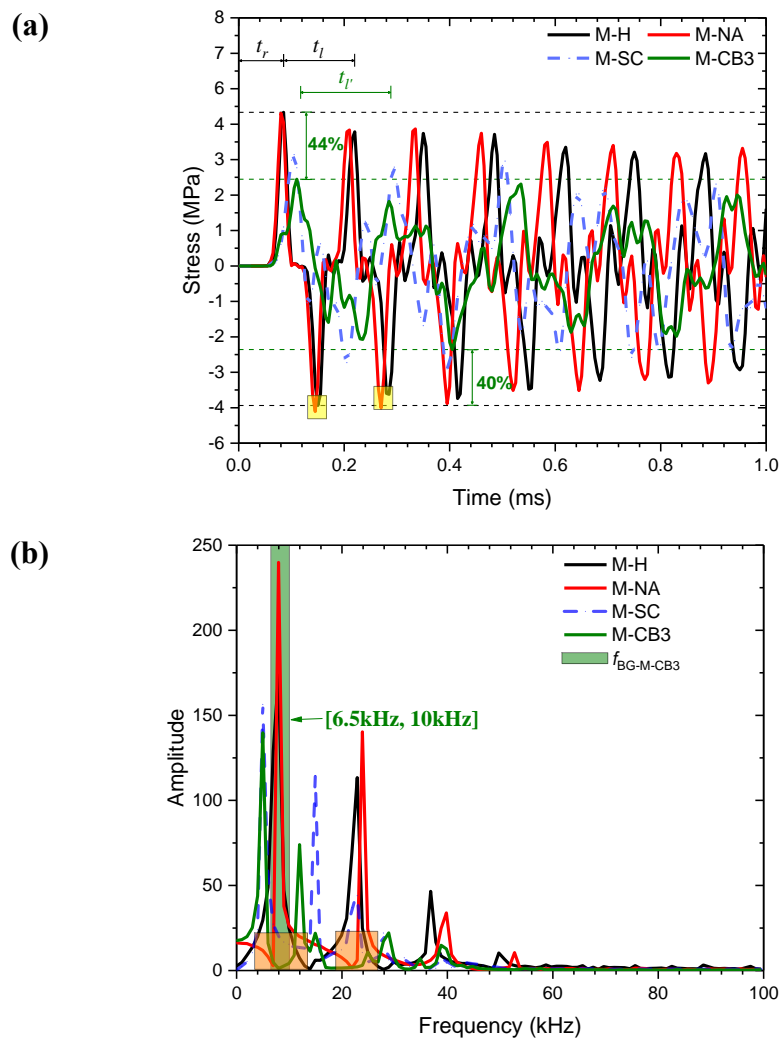
Figure 4-10. Wave propagation in M-H, M-NA, M-SC and M-CB3 subjected to impulsive load: (a) Longitudinal stress time history at cross-section B, (b) Frequency spectra.

As compared with M-H, M-SC also exhibits peak stress reduction because of the wave dispersion due to the wave scattering and interference with the solid aggregates. However, there is no noticeable stress reduction for the specimen with nature aggregates (M-NA) as the natural aggregates have similar physical properties (e.g., density and Young's modulus) to the cementitious mortar. By adding engineered aggregates, specimen M-CB3 shows the highest reductions in the compressive stress by 44% and tensile stress by 40% compared with specimen M-H, as illustrated in Figure 4-10(a). The engineered aggregate embedded in specimen M-CB3 consists of a heavy core and the compliant coating layer, the solid core vibrates within the coating layer interacting with the wave propagation through the specimen. When the heavy cores vibrate, the wave energy is converted to kinetic energy leading to the reduction of peak compressive stress. Thus, using engineered aggregates is effective in attenuating both compressive and tensile stress wave.

To understand the attenuation mechanism, Figure 4-10(b) compares the frequency spectra of stress wave of different specimens. As shown, the peaks can be effectively suppressed at the frequency range of $f_{BG-M-CB3}$ from 6.5 to 10 kHz (shaded in green). This frequency band well agrees with the prediction from Figure 4-4(c). Within the prescribed frequency band as shaded in green, a significant peak stress amplitude reduction is found in specimen M-CB3. This indicates that metaconcrete specimen with specifically designed engineered aggregates can effectively attenuate the stress waves generated by impact load with the frequencies falling in the bandgap of the metaconcrete specimen. However, as shown in Figure 4-10(b), two spectral peaks of the stress wave, one below and one above the bandgap are generated. This observation indicates that although embedding engineered aggregates inhibits wave energy propagating at bandgap frequencies in the metaconcrete structure, some wave energies still pass through at frequencies below and above the bandgap frequencies. In other words, the engineering aggregates change the dominant wave frequency propagating in the specimen. This is probably because the vibrations of hard cores transfer a certain amount of energy through the soft coating to the mortar matrix. For specimen M-SC, the width of the bandgap is nearly negligible. Thus, no obvious wave attenuation is observed. Due to the

increasing mass of the specimen M-SC as compared with specimen M-H, the dominant wave frequencies of the specimen M-SC are also reduced. Because the impedance of the steel core is very different to that of mortar, placing steel cores in mortar matrix also causes wave attenuation as compared to that in the homogenous specimen, but at a less attenuation level as compared that with engineered aggregates. Based on the above result, it can be concluded that mitigation performance found in specimen M-CB3 is mainly attributed to the contribution of the local resonance effect.

4.4.2 Parametric study

The above results show that the use of engineered aggregates in M-CB3 with a bandgap from 6.5 kHz to 10 kHz covers the first frequency range of dominant stress wave, therefore effectively mitigating the wave energy transmission in this range. This observation indicates that if the engineered aggregates are properly designed, they will be effective in mitigating stress wave at the target frequency range. In this section, the influence of geometric parameters (listed in Table 4-1) such as core size (D_c), coating thickness (t) and combined geometric parameter, as well as material properties (listed in Table 4-2) including core density (ρ_c) and coating modulus ($E_{c'}$) on the wave attenuation performance of metaconcrete specimen subjected to impulse I are studied. Under the impulse I with 5 MPa amplitude, all components of rod structures respond in the elastic range as studied above. To compare the performance of the specimen with engineered aggregates of different configurations, two performance metrics, e.g., energy ratio (R_E) and stress attenuation coefficient (C_S) are introduced. R_E is the energy-absorbing effectiveness ratio, which is used to evaluate how effectively engineered aggregates can store the energy applied onto the metaconcrete rod structure subjected to impulsive load. It is mathematically defined as the ratio between the energy absorbed by the engineered aggregates (E_a) and that by the mortar matrix (E_m). In addition, E_a is the energy absorbed by the engineered aggregates which can be expressed as:

$E_a = E_{a,k} + E_{a,i}$, where $E_{a,k}$ is the total kinetic energy of engineered aggregates and $E_{a,i}$ is the total internal energy induced by core and coating deformation. Besides, E_m is the total

energy absorbed by the mortar matrix, which is given by: $E_m = E_{m,k} + E_{m,i}$ where $E_{m,k}$ is the total kinetic energy of mortar matrix and $E_{m,i}$ is the total internal energy of mortar matrix. The expression is given by:

$$R_E = \frac{E_a}{E_m}$$

(4-10)

The stress attenuation coefficient (Cs) in percentage with respect to the homogenized mortar specimen (M-H) at the same location is defined as:

$$C_S = 1 - \frac{\sigma_i^{META}{}_{max}}{\sigma_i^{M-H}{}_{max}} \times 100\%$$

(4-11)

where $\sigma_i^{M-H}{}_{max}$ is the peak stress in the homogenized mortar (*M-H*) at location *i*, $\sigma_i^{META}{}_{max}$ is the peak stress in metaconcrete specimens (*META*) at location *i*. It should be noted that this section investigates the response of engineered aggregates with the specified configurations considered in this chapter. The results demonstrate the effectiveness of properly designing the aggregates to achieve better mitigation of stress wave propagations. The procedure can be applied to structures with other configurations, e.g., beams, slabs, etc., to analyze the predominant or primary dominant wave frequencies and then accordingly design the engineered aggregates. The systematic and generic design approach given in section 4.5 can be used for the design of engineered aggregates for use in different structures.

4.4.2.1 Influence of geometric parameters

Influence of core size

In order to investigate the effect of changing core size (D_c), specimen M-CS1 to M-CS6 with lead core varies from 16 mm to 26 mm under impulse I defined above are investigated. To compare the performance, the elastic responses of the metaconcrete rod structure are considered. The first performance matric R_E of different rod structures are calculated to represent the energy absorption taken by different engineered aggregates with varying core sizes. Another performance metric C_s is derived by taking the ratio of peak stress amplitude

at cross-section B between metaconcrete and homogenized mortar rod structure. Figure 4-11(a) shows the two-performance metrics including the energy ratio (R_E) and stress attenuation coefficient (C_s). As shown, increasing core size from M-CS1 to M-CS6 results in a higher energy ratio and attenuation coefficient, which indicates that increasing the core size of engineered aggregates is favorable for the mechanical performance of metaconcrete rod structures with respect to stress wave mitigation and energy absorption by resonant aggregates. A higher energy ratio implies the mechanical energy stored in the mortar matrix is smaller and that transferred to the engineered aggregates is larger, which reduces the stress wave propagation in the structure. Correlatively, the stress attenuation coefficient (C_s) rises with the increase of core size. It can be concluded that core size is a sensitive parameter affecting wave attenuation performance of metaconcrete rod structure, and the relatively large core size is recommended for the engineered aggregate design because it could store more wave energy and hence mitigate wave propagation.

Influence of coating thickness

To evaluate the effect of the coating thickness (t) on the stress wave attenuation, the energy ratio (R_E) and stress attenuation coefficient (C_S) against the variation of coating thickness are presented in Figure 4-11(b). It is found that the coating thickness has an obvious effect on wave propagation. Increasing the coating layer thickness from 0.5 mm to 2 mm reduces the transmission of the stress wave in the metaconcrete rod structure and achieves better attenuation of peak compressive stress. With respect to energy absorption, increasing coating thickness from 0.5 mm to 2 mm, i.e. from M-CT1 to M-CT3 enhances the energy ratio of engineered aggregates as shown in Figure 4-11(b). It can be inferred that it is easier to experience local vibration with a more compliant coating. Thus, the vibration of aggregates captures more mechanical energy along with the propagation of stress wave. However, further increasing coating thickness from 3 mm to 5 mm, i.e., from M-CT4 to M-CT6 causes an adverse effect. This is because the equivalent coating stiffness of the specimen along the longitudinal direction is not only influenced by coating modulus but also coating thickness.

Increasing coating thickness makes the coating layer over-compliant, and therefore, the energy in mortar cannot be easily transferred to the solid core to activate core vibrations although a thicker coating layer gives the core more space to vibrate, which results in the reduction of the energy ratio (R_E) and lower attenuation coefficient (C_S) as illustrated in Figure 4-11(b). In conclusion, the appropriate stiffness contrast between the coating layer and mortar should be carefully designed to allow the wave energy to be transmitted to the core and induce core vibration, but an over-compliant coating layer due to excessive coating thickness is not recommended, which could reduce the efficiency of using engineered aggregates.

Influence of combined geometric parameters

Two performance metrics (e.g., R_E and C_S) against combined geometric parameters (core radius and coating thickness) are presented in Figure 4-11(c). The product of core radius (R_c) and coating thickness (t) is used to represent each combination case as given in Table 4-1. When the combined value $R_c t$ is greater than 20 mm^2 (e.g., R_c=10 mm, t=2 mm), the performance metrics decrease. The aggregate with a smaller core size but thicker coating could reduce the effectiveness of using engineered aggregates as the coating layer becomes over-compliant, which is not recommended. Also, two performance metrics show a positive correlation to the variation of the bandgap region by comparing with Figure 4-4(c) and Figure 4-11(c). As seen in Figure 4-4(c), a reduction in the bandgap region is observed when the combined value $R_c t$ is greater than 20 mm^2, as a result, the performance metrics including R_E and C_S are reduced. Therefore, it can be concluded that the aggregate with the appropriate geometric combination should be properly designed according to the target impulsive loading and the specimen geometry. For instance, a small core size with an over-compliant coating layer is not recommended for the engineered aggregate design in this chapter.
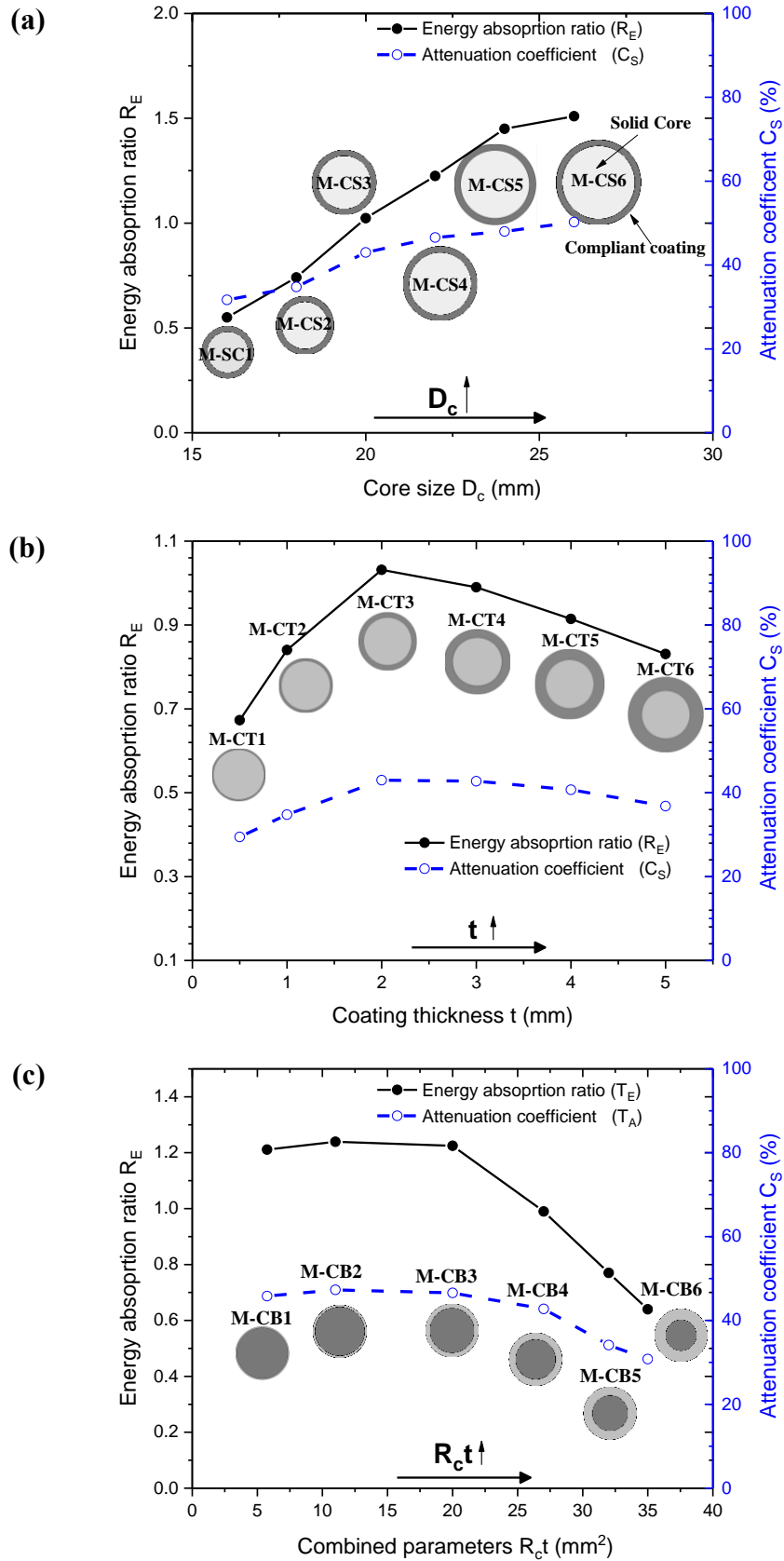
Figure 4-11. Energy ratio and attenuation coefficient vs. geometric parameters: (a) Core size, (b) Coating thickness, (c) Product of core radius and coating thickness.

4.4.2.2 Influence of aggregate material properties

Material properties (e.g., mass density, Young's modulus and Poisson's ratio) could have a substantial effect on the bandgap characteristics of metaconcrete structure as discussed in Section 3.4.3. In this section, twelve representative materials are selected and assigned to the aggregate core and coating layer while keeping the identical aggregate geometries and volume fraction. These commercially available materials are chosen due to their significant differences in density and Young's modulus for core and coating, respectively. The mechanical properties of different materials used in the simulation are listed in Table 4-2. The geometric parameters of the model are kept the same as M-CB3 with a core size of 20 mm and coating thickness of 2 mm, except that the material properties of coating and core are varied. Key findings are summarized in the following sections.

Influence of core material

The energy ratio (R_E) and attenuation coefficient (C_S) of the metaconcrete rod structure vs. core density are presented in Figure 4-12(a). The value of C_S and R_E with the core density less than 11400 kg/m^3 are more sensitive to the change of core density, while the change of core density has no significant effect on the value of C_S and R_E when the core density is over 11400 kg/m^3. With the increase of core density, the total mass of aggregates increases, which provides additional inertia resistance. However, the effectiveness of using engineered aggregates is reduced by having an excessive dense core because the vibration of a very heavy core might not be fully activated. The engineered aggregates with the lead core show the best performance among specimens considered in the analysis. Therefore, the core material should be purposely selected to meet the requirement regarding the bandgap region while avoiding using an excessive dense core.

Influence of coating material

The energy ratio (R_E) and attenuation coefficient (C_S) of the metaconcrete rod structure vs. coating modulus ($E_{c'}$) are presented in Figure 4-12(b). With the increase of coating modulus,

the attenuation coefficient (C_S) slightly increases and the energy ratio (R_E) increases in general. Using compliant polyurea as the coating material provides the highest energy ratio and attenuation coefficient because the first dominant wave frequency is within the prescribed bandgap region.
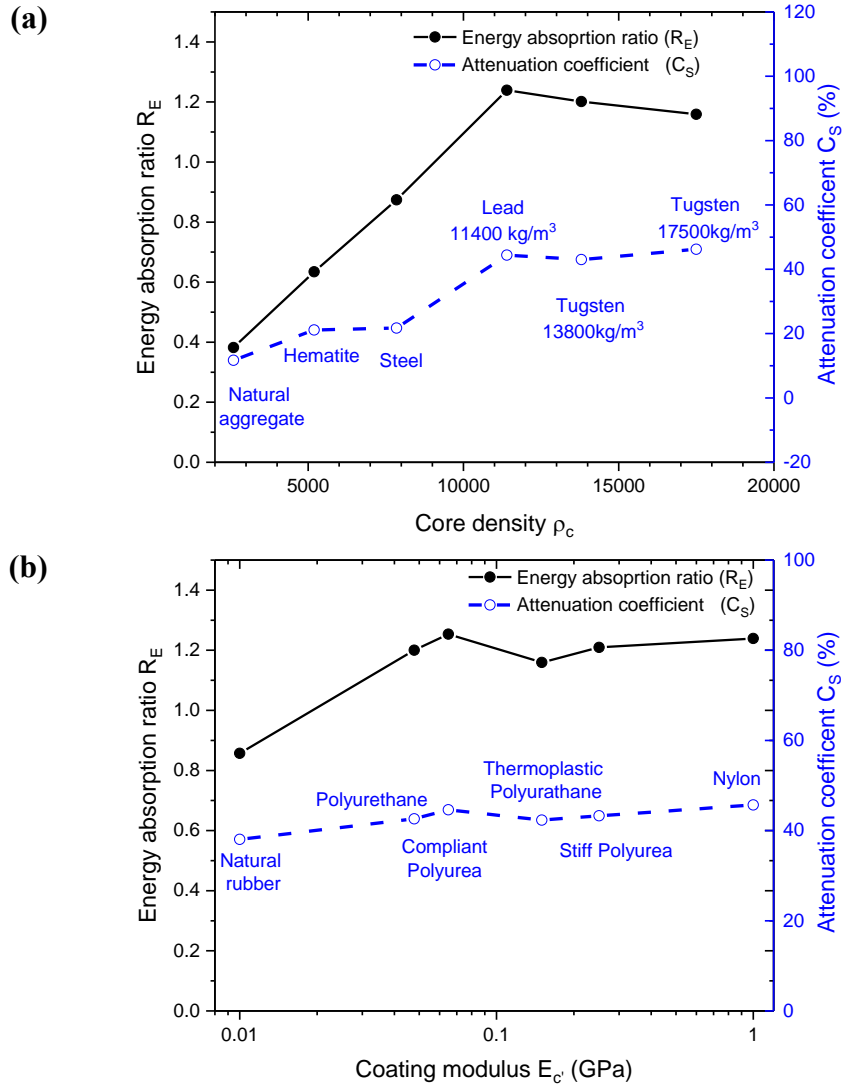
Figure 4-12. Energy ratio and attenuation coefficient vs. material properties: (a) Core density, (b) Coating modulus.

Besides, it is interesting to find that using polyurethane as coating also provides relatively high attenuation performance (i.e., with the second-highest R_E and C_S) as the selected polyurethane has Poisson's ratio of about 0.495, close to 0.50, leading to a wider bandgap region (refer to Section 3.4.3.3), as shown in Figure 4-4(e). Therefore, Poisson's ratio effect should be considered when using hyper-elastic material with Poisson's ratio greater than 0.49

(such as silicone rubber or polyurethane) as it could significantly influence the designed frequencies of engineered aggregates. In addition, the bandgap region is correlated with the equivalent coating stiffness, which depends on the coating thickness (t) and coating modulus ($E_{c'}$). Very soft or over-compliant coating layer (i.e., low coating modulus) cannot transfer much energy from mortar matrix to engineered aggregates although the core is easier to vibrate. On the other hand, using a too stiff coating layer prevents the vibration of the core, which affects the energy ratio and stress wave attenuation efficiency of the engineered aggregates. Thus, the coating material with appropriate Young's modulus as well as Poisson's ratio should be carefully selected to obtain the proper coating stiffness and the desirable bandgap region.

4.5 Design of engineered aggregates with multiple bandgap regions

The influences of configurations, including geometric and material parameters on the stress wave attenuation performance of metaconcrete rod structure, have been studied in section 4.4, which provides the reference for the design of engineered aggregates to generate the desired bandgaps. The effective wave attenuation is achieved by designing the engineered aggregates with their bandgap region to cover the primary dominant wave frequencies. The primary dominant wave frequencies refer to the frequencies at which most wave energy concentrates. It is also expected that wave attenuation performance can be enhanced by designing engineered aggregates in the graded configuration to suppress multiple dominant frequencies of stress wave induced by impulsive loading. The graded aggregates have different resonant frequencies (f_0 or f_{res}), and each f_0 or f_{res} corresponds to a target frequency band for wave attenuation (i.e., target frequencies (f_T)). Because the graded engineered aggregates are designed with the combination of various design parameters (e.g., core size, coating thickness and material properties), each covers a specific frequency bandgap, and the combined bandgap region thus suppresses all target frequencies f_T. It is noted that the attenuation is mainly focused on the longitudinal wave in this chapter. The

flowchart of how to design engineered aggregates for attenuating multiple target frequencies is given below and summarized in Figure 4-13.

i. The workflow starts with the response analysis of the homogenized mortar without aggregate (e.g., M-H) subjected to the applied load. The average transmitted stress-time histories are recorded at two locations as an example, which are close to the end (cross-section A) and away from the end (cross-section B). The frequency spectra are then plotted by using the Fast Fourier Transform (FFT). Each target frequency (f_{Ti}), i.e., primary dominant wave frequency, are identified by extracting the frequencies corresponding to the peak amplitude of the Fourier spectra (referred to Figure 4-8).

ii. The overall bandgap region f_{BG} consists of individually designed bandgap regions $\Delta f_{BGi} = \{\Delta f_{BG1} \cdots \Delta f_{BGn}\}$, where the subscript i indicates different bandgap regions. Therefore, each target frequency (f_{Ti}) corresponding to the different wave frequencies should fall into each Δf_{BGi} (i.e., $\Delta f_{BGi} = \gamma f_{Ti} \in [f_L, f_U]$), where f_L and f_U are the lower and upper bounds of a bandgap, and γ is given by $(f_U - f_L)/f_{Ti}$, respectively. The dimensionless factor γ is used to quantify the bandgap range corresponding to the target frequency, and the larger value of γ represents the wider bandgap. Note that the bandgap region should cover the target frequencies as much as possible to widen the attenuation region.

iii. The target frequencies identified from step i are set as the resonant frequencies (f_0 or f_{res}) of the engineered aggregates. The initial design parameters including geometric parameters (e.g., D_c or R_c and t) and material parameters (e.g., ρ_c and $E_{c'}$) could be estimated by using Eq. (4-12) proposed by Mitchell et al. [25]

$$f_0 \ or \ f_{res} = \frac{1}{2\pi}\sqrt{\frac{2k_i}{m_i}} = \frac{1}{2\pi}\sqrt{\frac{3E_{c'}}{2R_c t\rho_c}} \tag{4-12}$$

Then, different values of η_0, which is defined as the combination of equivalent coating stiffness (k_i) and core mass (m_i), are preliminarily determined in accordance with each target frequency f_{Ti} and individual bandgap Δf_{BGi}.

iv. After the initial estimation of design parameters, the bandgap region is numerically evaluated by using software *COMSOL Multiphysics* through frequency response analysis by applying longitudinal excitation at one side of the structure, which is the commonly used method to assess bandgap properties of the metamaterial by different researchers [29, 53, 74]. Also, each target frequency (f_{Ti}) should satisfy that $\Delta f_{BGi} = \gamma f_{Ti} \in [f_L, f_U]$. If the calculated bandgap regions from the initial estimation meet the above requirement, it shall move to the next step. If not, the trial-and-error processes are required to obtain the appropriate design parameters ensuring that the target frequency f_T is within the designed bandgap region. Finally, given a set of design parameters (e.g., ρ_c and $E_{c'}$), appropriate materials that satisfy the criteria and are commercially available can be selected as the aggregate materials for the solid core and the compliant coating.

As shown in Figure 4-8, the bandgap of using single-resonant aggregate only targets the first dominant wave frequency (i.e., 7.96 kHz), thus it is ineffective for other predominant or primary dominant wave frequencies (e.g., 14.925 kHz, 22.884 kHz and 29.85 kHz). Therefore, the effectiveness of only using a single-resonant type of aggregates is limited. This problem can be tackled by configuring engineered aggregates with graded configurations of multiple aggregates that cover as many dominant wave frequencies as possible through the proposed design steps illustrated in Figure 4-13.

By adopting the proposed design, the aggregates are re-structured to target multiple frequencies through a combination of graded configurations (e.g., M-GEA). For instance, four target frequencies f_T are set as 7.960 kHz, 14.925 kHz, 22.884 kHz and 29.85 kHz concerning dominant wave frequencies illustrated in Figure 4-8(c). To satisfy the requirement, the aggregates are replaced accordingly by specifying the parameters with respect to the four target frequencies f_T mentioned above. The predicted bandgap region for each configuration is referred to Figure 4-4, and structural and material parameters for graded engineered aggregates are listed in Table 4-5. With the designed configuration, the integrated bandgap of metaconcrete rod M-GEA (i.e., $f_{BG\text{-}M\text{-}GEA}$) covers the frequency range from 6.5 kHz to 31

kHz. In addition, the specimen M-CB3 suppressing the first target frequency is adopted to comparatively demonstrate the effect of suppressing multiple target frequencies, and M-H and M-NA are selected as the references. Moreover, two types of impulses (I and II) with a peak amplitude of 5 MPa and 40 MPa are used in the numerical study to further assess the effectiveness, which are illustrated in Figure 4-8(a) and Figure 4-15(a), respectively.
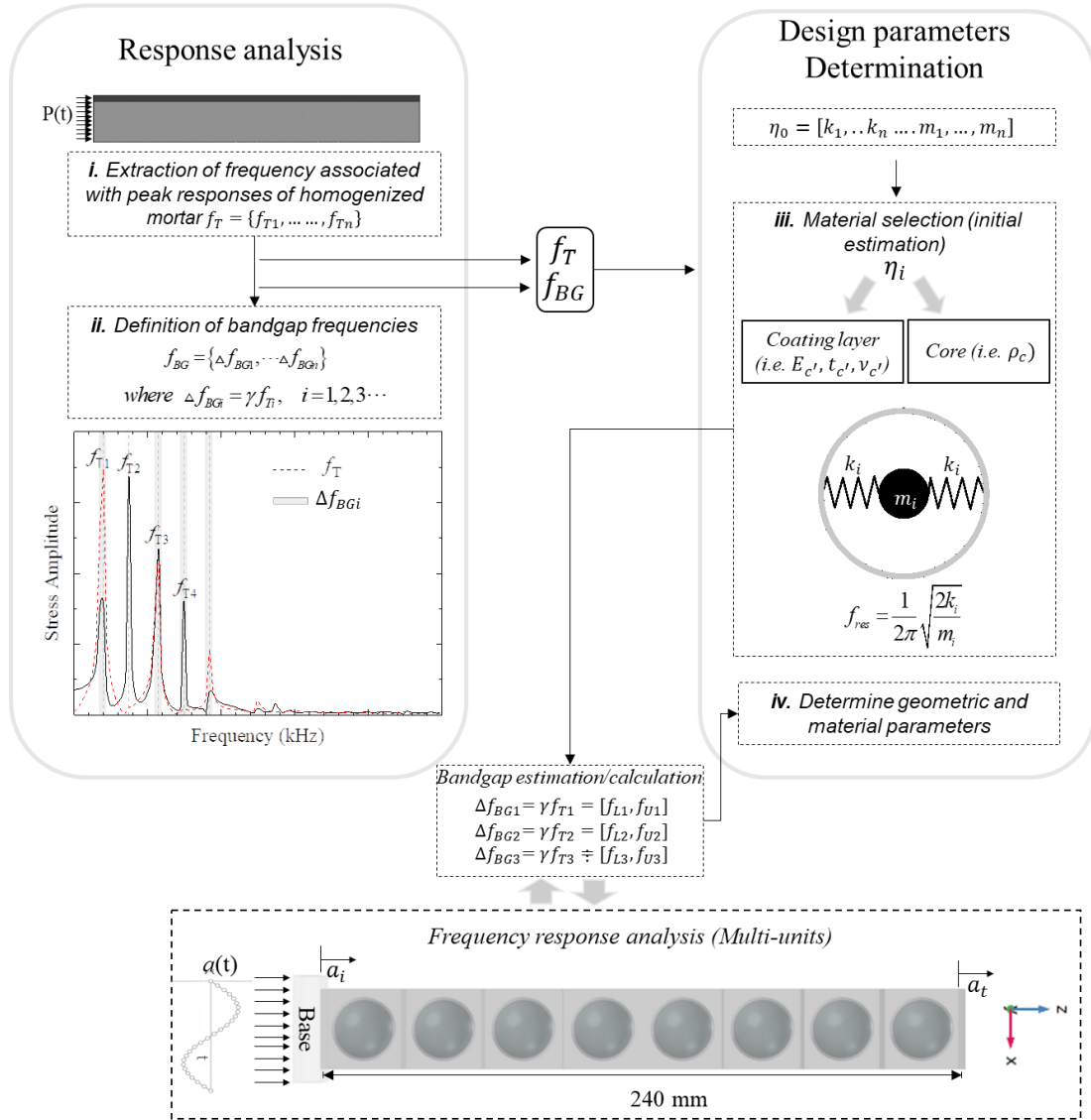
Figure 4-13. Design flowchart. Note: P(t) and a(t) represent the applied loading and the prescribed acceleration, respectively.

The specimens are initially tested under the impulse I to observe the performance within the elastic region. Under the impulse I with 5 MPa amplitude, all materials of rod structures are assumed to remain in the elastic range. To study the influences of inelastic responses and

79

material damage on the effectiveness of mitigating impulsive loading by embedding graded engineered aggregates, impulse II of amplitude 40MPa is adopted in the analysis. In total, four specimens, namely, M-H, M-NA, M-CB3 and M-GEA with 240 mm in length are analyzed under the impulsive loading as shown in Figure 4-8(a) and Figure 4-15(a). To evaluate the performance, Figure 4-14 and Figure 4-15 show average cross-sectional stress at the middle of the specimen (i.e., B) in the time and frequency domain for the four specimens subjected to impulse I and II, respectively. Location B for comparing impulsive mitigation performance is chosen because it allows sufficient distance for wave propagation and attenuation to examine the effectiveness of engineered aggregates.

Table 4-5. Geometric and material parameters used for graded engineered aggregates.

ID	Target frequency f_T	Material		Geometric parameters			Estimated bandgap region f_{BG}
		Coating material	Core material	Core size (mm)	Coating thickness (mm)		

M-CB3   1 2 3 4 5 6 7 8

ID	Target frequency f_T	Coating material	Core material	Core size (mm)	Coating thickness (mm)	Estimated bandgap region f_{BG}
1-8	7.960 kHz	Compliant Polyurea	Lead	20	2	6.5 kHz -10kHz

Replaced aggregates

M-GEA   1 2 3 4 5 6 7 8

ID	Target frequency f_T	Coating material	Core material	Core size (mm)	Coating thickness (mm)	Estimated bandgap region f_{BG}
1, 5-8	7.960 kHz	Compliant Polyurea	Lead	20	2	6.5 kHz -10kHz
2	14.925 kHz	Compliant Polyurea	Steel	20	2	9 kHz -16 kHz
3	22.884 kHz	Polyurethane	Lead	22	1	14 kHz -25 kHz
4	29.850 kHz	Nylon	Lead	22	1	16 kHz -31 kHz

By comparing the stress-time histories for the specimen subjected to impulse I, a noticeable difference in peak compressive and tensile stress is observed in the specimen M-CB3, which is reduced by 44% and 40% compared with the benchmark M-H as shown in Figure 4-14(a). However, as discussed above, placing engineered aggregates changes the wave frequency owing to the local vibrations of the hard cores, therefore two frequency peaks below and above the bandgap of M-CBS are observed. This compromises the effectiveness of wave propagation mitigation because while the transmission of wave energy corresponding to the frequency falling in the bandgap of engineered aggregate is stopped, local vibration of hard

core induces waves at frequencies below and above the bandgap and propagates in the structure. Placing configured engineered aggregates with multiple bandgaps that cover a wide range of target frequencies, the peak compressive and tensile stresses are further reduced by 61% and 51% as compared with the benchmark M-H, and the attenuation percentage are increased by 17% and 11% comparing with M-CB3, respectively as shown in Figure 4-14(a). Comparing the frequency spectra depicted in Figure 4-14(b), the bandgap region $f_{\text{BG-M-GEA}}$ induced by graded engineered aggregates is wider than the bandgap region $f_{\text{BG-M-CB3}}$, which allows suppressing waves in a wider frequency band. In addition, due to the wider frequency bandgap of multiple engineered aggregates, wave energy induced by local hard-core vibration of single-resonant engineered aggregate as observed above could also be mitigated. As shown, several frequency peaks outside the $f_{\text{BG-M-CB3}}$ in M-CB3 do not appear in the specimen M-GEA, and the second spectral peak amplitude of M-GEA moves to a higher frequency band but lower amplitude (highlighted by the yellow box in Figure 4-14 (b)) as compared with M-CB3. Therefore, it indicates the successful suppression of wave propagations at these frequencies by graded engineered aggregates. Thus, it can be concluded that using aggregate in the graded configuration leads to a broader attenuation band and a higher attenuation percentage.

Higher impulsive loading is likely to cause inelastic wave propagation and damage to the structure, which could absorb a certain amount of wave energy and also change the dominant wave frequencies. To assess the inelastic response of specimen subjected to higher amplitude impulse (i.e., impulse II) as shown in Figure 4-15(a), the DIF and erosion criteria for mortar and normal aggregates as specified in Section 4.3 are used in this simulation. Figure 4-15(c) and (d) show the average stress at cross-section B for four specimens in the time and frequency domain, respectively. As presented in Figure 4-15(c), the peak compressive and tensile stresses are considerably reduced by 65% and 37% compared with the benchmark M-H, and it has been further decreased by 16% and 11% with respect to M-CB3. Regarding frequency spectra depicted in Figure 4-15(d), multiple wave bandgaps exist due to the

presence of combined resonant aggregates. Within the prescribed bandgap $f_{BG-M-GEA}$, several peaks in specimen M-GEA have been noticeably attenuated as compared with M-H and M-NA. Comparing the specimen M-CB3 containing a single resonant aggregate, M-GEA can suppress the peak outside the bandgap $f_{BG-M-CB3}$ (highlighted by pink-dotted box), which results in the enhancement of overall attenuation performance.
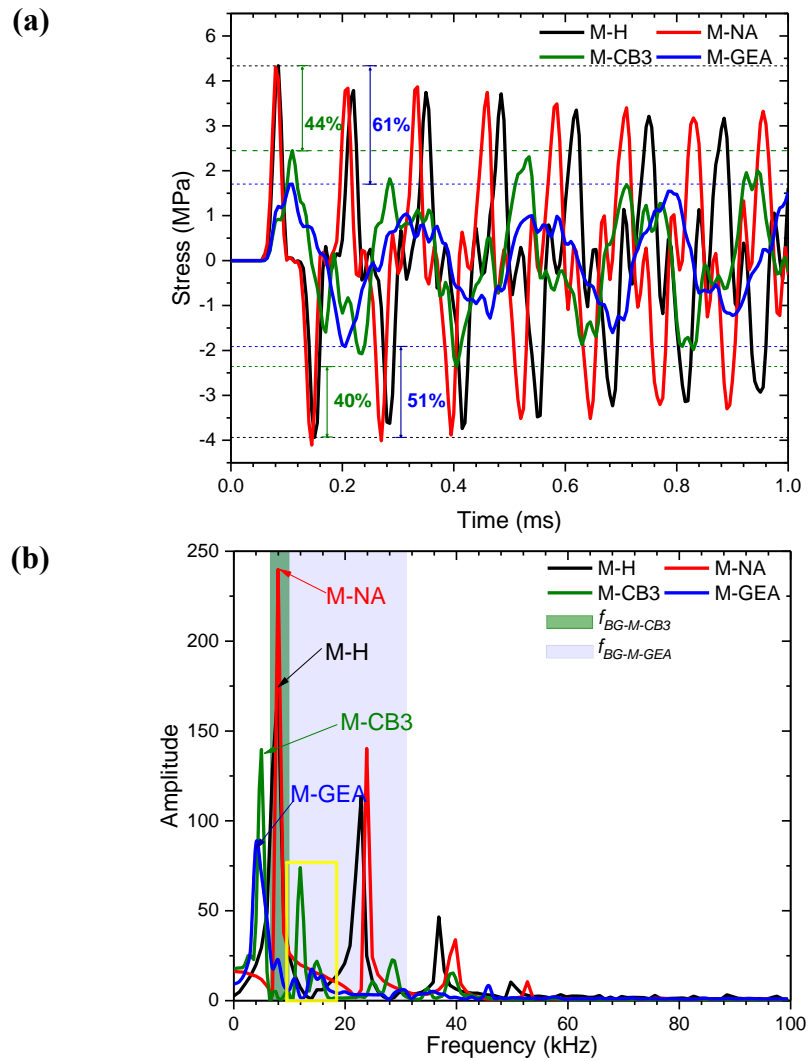
Figure 4-14. (a) Stress time history at cross-section B for M-H, M-NA, M-CB3 and M-GEA subjected to impulse I, (b) Frequency spectra.
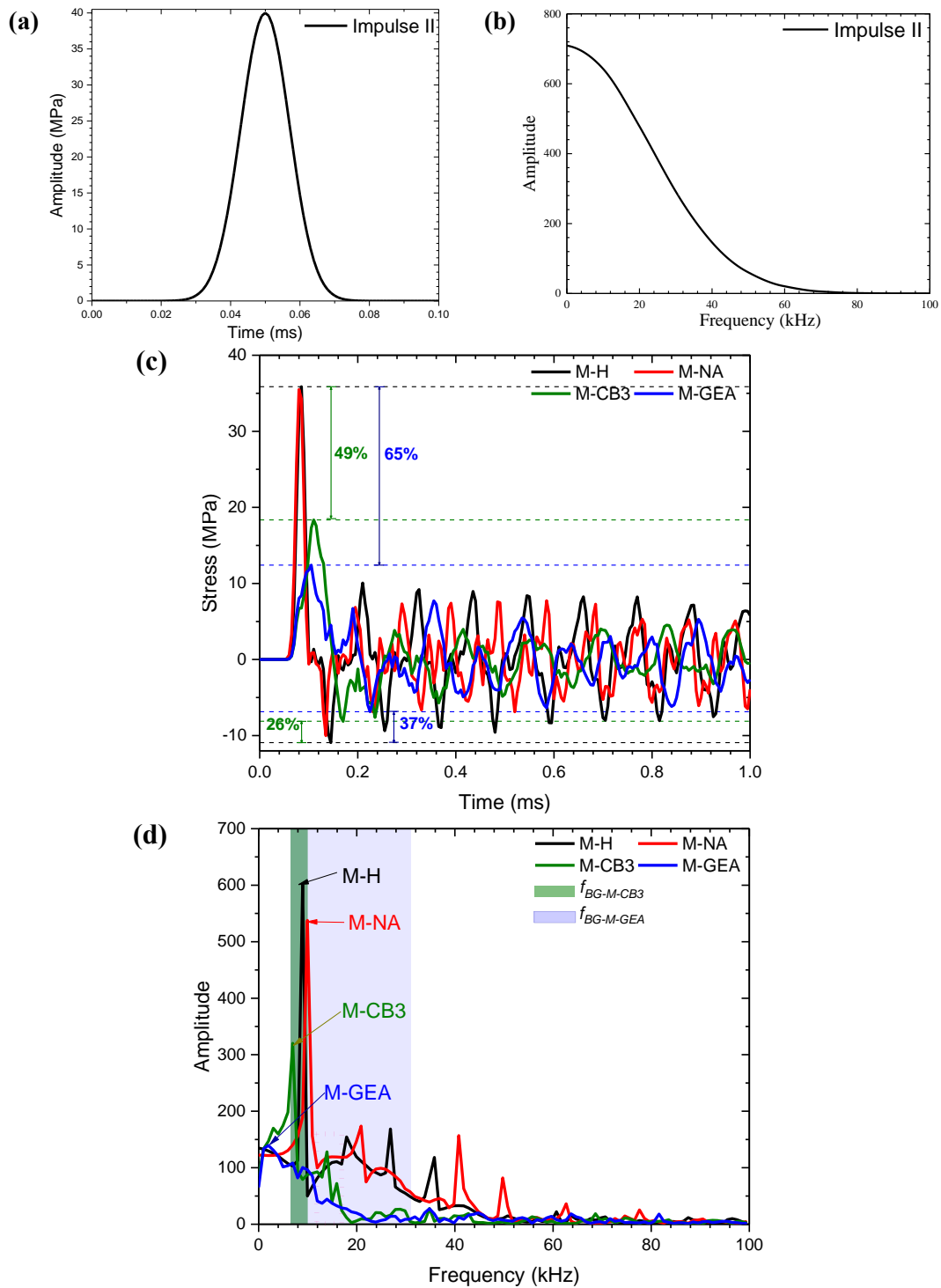
Figure 4-15. (a) Time-history of impulse II, (b) Frequency spectrum, (c) Stress-time histories for M-H, M-NA, M-CB3 and M-GEA subjected to impulse II, (d) Frequency spectra.

With regard to the damage pattern of the specimen, Figure 4-16 displays the effective plastic strain contours of homogenized mortar (M-H) and M-NA, M-CB3 and M-GEA at different time instants. At $t = 0.1$ ms, no element has been eroded in the four specimens. Owing to the existence of engineering aggregates, the time for the wave travelling to the rear end of the

specimen is delayed for the specimen M-CB3 and M-GEA. Moreover, there is a clear stress concentration around the polyurea coating, which potentially leads to localized damage to the mortar matrix surrounding the engineered aggregates. At t = 0.5 ms, Figure 4-16 shows that the specimens M-H, M-NA, M-CB3 and M-GEA experience damage at different levels at various locations. The specimen M-H and M-NA are severely damaged at the location close to the rear end, i.e., the spalling damage commonly observed in spalling tests, which is caused by the superposition of stress waves [108, 115]. As shown, the mortar matrix of the specimens is broken into segments, and new free ends are formed at a broken position. Due to the existence of specimen fracture, the peak values of average stress at cross-section B significantly drop after the initial peak as shown in Figure 4-15(c). On the other side, metaconcrete specimens (i.e., M-CB3 and M-GEA) experience both mortar matrix fracture and localized damage [88] occurring around soft coating, but no obvious spalling damage is observed. In addition, the primary damage location, indicated as broken segment (BS2) in the figure, greatly shifts towards the loading end in specimen M-CB3 and M-GEA as compared with BS1 in specimen M-H and M-NA owing to the existence of engineered aggregates. These results indicate that using engineered aggregates can reduce stress wave propagation, mitigate the associated structure damage and also change the damage mode.

In addition to the mortar fracture, it can be seen from Figure 4-16 that localized damage between cement mortar and soft coating due to stress concentration is found in the specimen M-CB3 and M-GEA. Because of the localized damage, the peak value of average stress at the cross-section is further reduced. This is because material damage could dissipate a substantial amount of energy. Therefore, in addition to the oscillation of heavy core inside the engineered aggregates, the localized damage of the metaconcrete specimen, as shown in Figure 4-16, can also reduce the stress amplitude due to energy dissipation. To conclude, using engineered aggregates with graded configuration (i.e., M-GEA) exhibits better performance in impulsive wave mitigation than the use of single resonant aggregates because a much wider frequency range of dominant wave frequencies are covered by the re-structured

bandgap $f_{\text{BG-M-GEA}}$. The proposed method from the present numerical simulation considering a wider range of frequency bandgap can be used for the design of engineered aggregates.
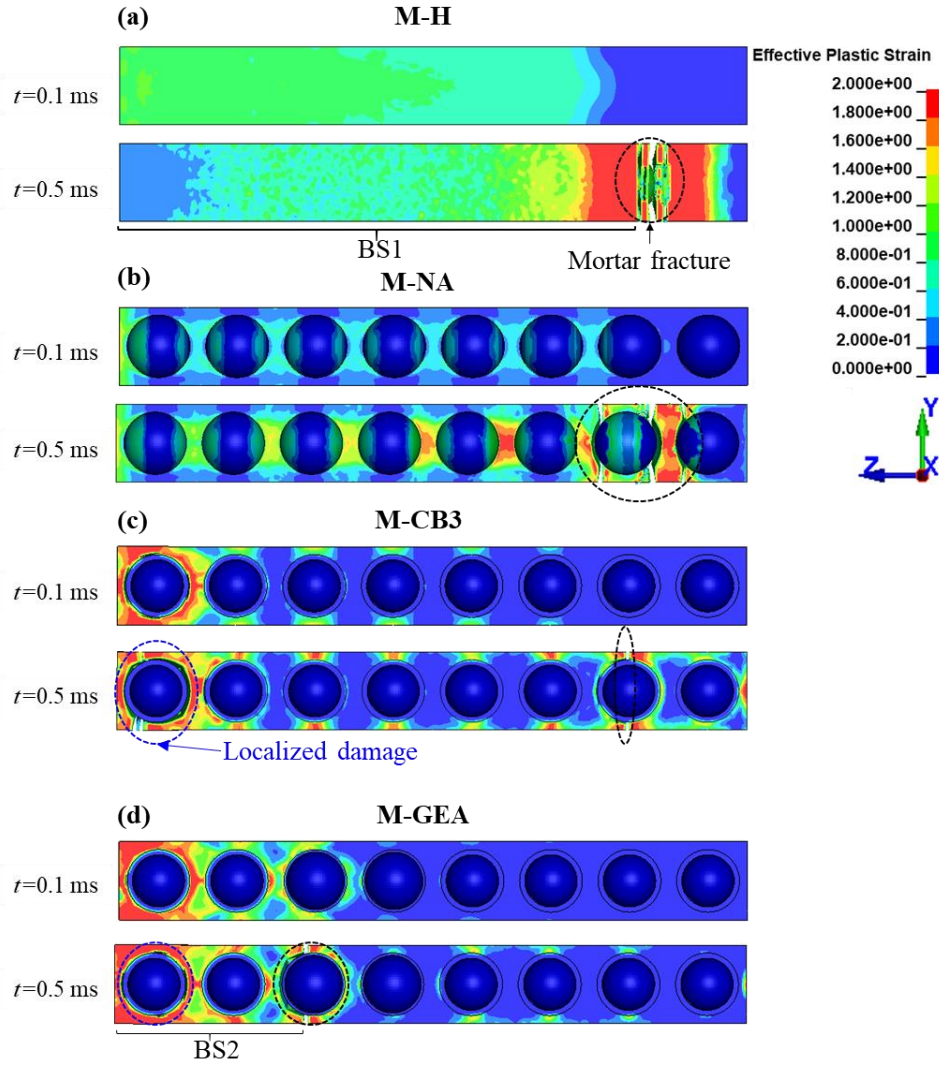
Figure 4-16. Effective plastic strain contours: (a) M-H, (b) M-NA, (c) M-CB3, and (d) M-GEA subjected to impulsive II.

4.6 Summary

This chapter systemically investigates the influence of configurations including core size (D_c), coating thickness (t), combined geometric parameters ($R_c t$), core density (ρ_c) and coating modulus ($E_{c'}$) of engineered aggregates on the bandgap region and the wave mitigation performance of metaconcrete rods subjected to impulsive loading. By studying the frequency response functions, the influence of configuration parameters on the bandgap region is investigated by using *COMSOL Multiphysics*. The influence and sensitivity of design

parameters on the wave mitigation performance of the metaconcrete rod specimens subjected to impulsive load are numerically explored by using LS-DYNA. Furthermore, a new method of designing engineered aggregates with multiple integrated bandgap regions to cover multiple dominant wave frequencies is proposed and validated by numerical simulations. The main findings are summarized as follows.

(1) The bandgap formation is attributed to the mechanism of local resonance. As revealed in Section 4.2, the location and bandgap region are sensitive to the variation of core size (D_c), core density (ρ_c) and coating modulus ($E_{c'}$). Increasing values of D_c, ρ_c, and $E_{c'}$ could achieve a wider bandgap region.

(2) The metaconcrete structure with designed resonant aggregates is more efficient in attenuating stress wave propagation by comparing the specimen with non-resonant inclusions and homogenized mortar.

(3) Energy ratio (R_E) and attenuation coefficient (C_S) are introduced as performance metrics in this chapter. The results from Section 4.4 demonstrate that engineered aggregates with larger core size (D_c) could enhance performance metrics. The performance metrics are sensitive to the change in core density (ρ_c). However, having an over-dense core has no significant improvement on these performance metrics.

(4) The performance metrics are also sensitive to the changes in the equivalent coating stiffness and stiffness contrast between the coating layer and mortar matrix, which are determined by the coating thickness (t), coating modulus ($E_{c'}$) and Poisson's ratio. The coating materials should be carefully selected to obtain the desirable bandgap region.

(5) The design flowchart is given in Section 4.5 for designing engineered aggregates with desired multiple bandgap regions. The effectiveness of using the proposed approach is validated by the numerical simulation. The specimen with multiple resonant aggregates features an enhanced wave mitigation performance than the specimen with single resonant aggregates.

Chapter 5 Experimental and numerical assessment of stress wave attenuation of metaconcrete rods subjected to impulsive loads

5.1 Introduction

In Chapter 4, the effectiveness of using metaconcrete rod structure in mitigating stress wave attenuation is revealed and it is found that PDWF (i.e., the primary dominant wave frequencies) induced by the impulsive loads should coincide with the designed bandgap of the engineered aggregates. In this chapter, the experimental study is carried out to further explore the stress wave attenuation performance of metaconcrete structure subjected to impulsive loads and to verify the numerical findings. The performances of concrete specimens composed of cementitious mortar and different inclusions including natural aggregates, steel balls and resonant aggregates against impulsive load are comparatively studied, in which the resonant aggregates are made of rubber-coated steel balls (RCSBs). In addition, responses of metaconcrete specimens with different ranges of bandgaps that either cover or do not cover PDWF are studied. Furthermore, the experimental results are used to calibrate a developed numerical model in finite element code LS-DYNA. With the validated numerical model, the effectiveness of metaconcrete structure on mitigation of wave propagation induced by different loading profiles is investigated and discussed. The results derived from this chapter could be applied to the design of the metaconcrete structure with targeted bandgaps for resisting specific impulsive loading.

The related work in this chapter has been published in International Journal of Impact Engineering.

5.2 Experimental program

5.2.1 Specimen fabrication

The details of the experimental program, including specimen fabrication and test setup, are described in this section. To fabricate the specimens, high strength mortar is used as the matrix of metaconcrete. The mortar is made of dry-mix Davco Lanko 701 duragrout produced by *Sika Australia Pty Ltd* with the designated compressive strength of 73 MPa after 28 days [124]. The reason for using high strength mortar for specimen preparations is to avoid potential compressive damage under impulsive loading; hence the tests could be focused on the influences of different aggregates on stress wave propagation in the specimen. The mix ratio of cement/sand/water/additives is 1/2/0.5/0.33. To enable the relative movement of the solid core inside the resonant aggregate, Young's modulus of coating should be at least one order of magnitude lower than that of the mortar phase. In this chapter, silicone rubber is selected as the coating layer. Steel balls commercially available and used in a wide range of applications such as bearings, crushing mills and automobiles [125] are selected as the core. Thus, the resonant aggregates are made of steel balls coated with silicone rubber.

With respect to the fabrication process, a schematic diagram of preparing specimen S4 with eight periodically distributed silicone rubber-coated steel balls (RCSBs) is exemplified in Figure 5-1(a). In addition, the silicone rubber-coated steel ball (RCSB) as shown in Figure 5-1(b) is manufactured by a supplier in China. The dome-shape rubber coating is prepared by using the moulding technique. The steel ball is then encapsulated by the upper and lower dome-shape rubber coating, followed by the curing process. As listed in Table 5-1, a total of seven rods (S1-S7) with a length of 270 mm and a cross-sectional area of 30×30 mm^2 are prepared. A plain mortar specimen (S1) without inclusions is prepared as a reference. Besides, S2, S3 and S4 are fabricated by respectively adding natural aggregates with a maximum size of 22 mm, steel ball and RCSBs to evaluate the effect of different embedded inclusions on wave propagation. Three specimens (i.e., S4-S6) are designed to periodically mix the 22 mm RCSBs in mortar matrix with the volume fractions of 18.4%, 9.2% and 22.9% respectively

to explore the influence of volume fraction on wave mitigation. Specimen S7 is mixed with 18 mm RCSBs to study the effect of bandgap on wave mitigation. Detailed information on the specimens and resonator configuration are given in Table 5-1. To ensure the periodic position of specimens S3-S6, three 3D-printed position guides (i.e., G4, G8 and G10) are prepared for the specimens, as illustrated in Figure 5-1(a). During the fabrication process, the first step is to place the bottom layer of mortar in the mould to provide initial cover. After that, the position guide is used for placing aggregates. After the placement, the position guide is removed, and the remaining mortar is poured. Finally, a steel rod is used to ram the specimen to minimize the voids.
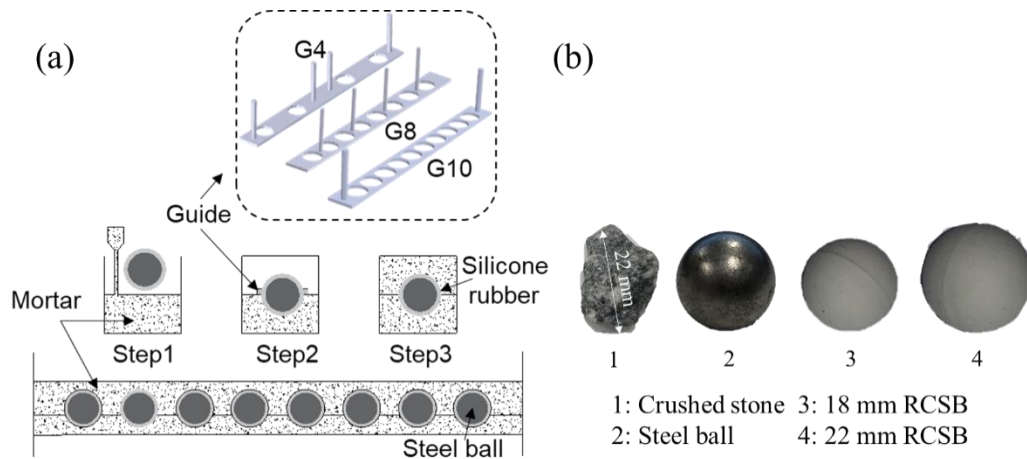
Figure 5-1. (a) Schematic diagram of specimen fabrication, (b) Illustration of different inclusions.

5.2.2 Test setup

As summarized in Table 2-1, metaconcrete specimens made of cementitious mortar in the previous studies [28, 29] were subjected to either ultrasound or vibration excitations, only the specimen made of epoxy resin [31] was tested under plate impact. However, the performance of metaconcrete structure made of cementitious mortar subjected to impulsive loading has not been experimentally examined. In this chapter, the impact test of each specimen is carried out by using a testing system, consisting of a striker, incident bar (bar I) and transmitted bar (bar II), as shown in Figure 5-2. In the test, the specimen is placed between two bars and hanged by two nylon threads. Two nylon threads are tied at one-third of the specimen. The primary function of nylon thread is to hang the specimen and align it to

the testing apparatus. The specimen by using nylon thread instead of using other supports can minimize the interaction between the support and stress wave, which might cause unwanted wave dispersion. The bars are made of stainless steel with the density and Young's modulus of 7800 kg/m^3 and 210 GPa, respectively [126]. The impulsive load of the test is generated by manually sliding the striker bar to impact bar I. Two strain gauges (i.e., SG1 and SG2) with gauge factor of 2.1 are attached at the near front and rear surface of the specimen to record the signal, i.e., 30 mm and 230 mm from the incident surface of the specimen, respectively.
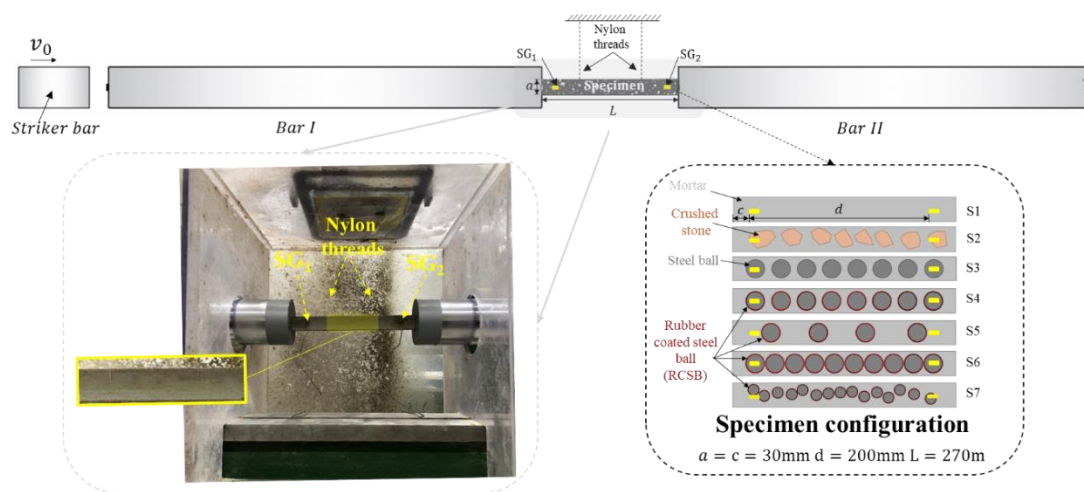
Figure 5-2. Schematic diagram of experimental setup and configuration of tested specimens.

Table 5-1. Configuration parameters and summary of results.

No.	Configuration	Inclusion Type	D_a (mm)	t (mm)	V_a (%)	m_a (%)	R_p	R_s
S1		-	-	-	-	-	0.09	0
S2		Natural aggregate	22	-	18.4	18.7	0.23	0.15
S3		Steel ball	20.5	-	17.0	53.0	0.25	0.18
S4		RCSB	22	1.5	18.4	54.6	0.56	0.52
S5		RCSB	22	1.5	9.2	27.3	0.56	0.52
S6		RCSB	22	1.5	22.9	68.2	0.714	0.69
S7		RCSB	18	1.2	18.9	54.6	0.729	0.71

Note: L is the length of the rod; a is the dimension of the square cross-section; D_a is the diameter of the RCSB; R_p is the peak reduction ratio of the maximum longitudinal strain; R_s is the peak reduction ratio of strain with respect to plain mortar; t is the thickness of rubber coat in RCSB; $V_a\%$ is the volume fraction of RCSB to the overall rod structure, $m_a\%$ is the overall mass fraction; '-' means not applicable.

5.3 Results and discussions

5.3.1 Attenuation effectiveness of specimen containing different types of inclusions

In order to evaluate the wave attenuation effectiveness, four performance metrics [31, 52, 69, 91, 127] are considered in this chapter, which are the peak reduction ratio of the maximum longitudinal strain R_p defined by Eq.(5-1), the peak reduction ratio of strain with respect to plain mortar R_s defined by Eq.(5-2), the normalized longitudinal strain at different time instants $\varepsilon^*(t)$ defined by Eq.(5-3), and the transmission ratio (TR) defined by Eq.(5-4).

$$R_p = 1 - \frac{\varepsilon_2\big|_{peak}}{\varepsilon_1\big|_{peak}} \tag{5-1}$$

$$R_s = 1 - \frac{\varepsilon_{2_{Si}}\big|_{peak}}{\varepsilon_{2_{S1}}\big|_{peak}}, \text{ where } i = 1, 2 \cdots 7 \tag{5-2}$$

$$\varepsilon^*(t) = \frac{\varepsilon_2(t)}{\varepsilon_1\big|_{peak}} \tag{5-3}$$

$$TR = 20 \times \log(\frac{\varepsilon_2(f)}{\varepsilon_1(f)}) \tag{5-4}$$

where ε_1 and ε_2 are the amplitude of longitudinal strain at SG1 and SG2 of the test specimen, respectively; $\varepsilon_1\big|_{peak}$ and $\varepsilon_2\big|_{peak}$ represent the peak value recorded at two strain gauges; $\varepsilon_{2_{Si}}\big|_{peak}$ stands for the peak strain value measured in the different specimens, $\varepsilon_{2_{S1}}\big|_{peak}$ is the peak strain recorded in the plain mortar (specimen S1), and subscript i represents the specimen number; $\varepsilon_1(f)$ is the amplitude of longitudinal strain in the frequency domain recorded by SG1, and $\varepsilon_2(f)$ is the amplitude of longitudinal strain in the frequency domain

recorded by SG2.

R_p is used to quantify the attenuation effectiveness by calculating the ratio of longitudinal strain at the front and rear end of the specimen [31, 52, 91]. R_s is used to comparatively study the influence of added inclusions with respect to the reference specimen as in the previous study [31]. $\varepsilon^*(t)$, the normalized value at different time instants, is the ratio of the strain at the rear end (SG2) to the peak value of the strain at the incident end (SG1) to comparably illustrate the response, which has been adopted in the previous study [52]. Furthermore, the wave frequency filtering effect and the contribution of bandgap corresponded to resonant inclusions can be characterized by the transmission ratio (TR). The transmission ratio (TR) is defined as the ratio of output to input amplitudes in the frequency domain, which has been adopted in previous studies [8, 69, 127]. Note that a negative TR indicates that the response near the end of the specimen is less than the response near the incident end. The shaded frequency band with negative TRs indicates the region of the wave filtering zone or the bandgap.

By using Eq.(5-1), the peak strain reduction R_p of S4 is calculated as 0.56, and the corresponding value for plain mortar (S1), mortar with crushed sandstones (S2) and steel balls (S3) is 0.09, 0.23 and 0.25, respectively, as listed in Table 5-1. These results indicate a peak reduction of 56% in the longitudinal strain for the specimen S4, and the percentage of wave attenuation is much higher than plain mortar and those using natural aggregates and solid core (S1-S3). S4 also shows a higher R_s of 0.52 than 0.15 and 0.18 for S2 and S3, respectively, as calculated by Eq.(5-2). Therefore, specimen S4 with embedded RCSBs confirms more effective in mitigating impact stress waves as compared with other specimens. The performance metric $\varepsilon^*(t)$ regarding the ratio of incident stress wave transmitting through the specimen is shown in Figure 5-3, where the lower peak value means higher attenuation effectiveness and less wave energy transmitted through the specimen. Figure 5-3(a) shows the normalized longitudinal strain at different time instants $\varepsilon^*(t)$ recorded at SG2 for specimens S1, S2, S3 and S4. S4 shows the lowest peak value among the four specimens,

indicating the highest wave attenuation. Specimen S4 with embedded 22 mm RCSBs has better wave attenuation than the specimens with natural and solid inclusions owing to the local resonance mechanism. The above-mentioned attenuation phenomenon by using RCSBs could be inferred from the results in the frequency domain.
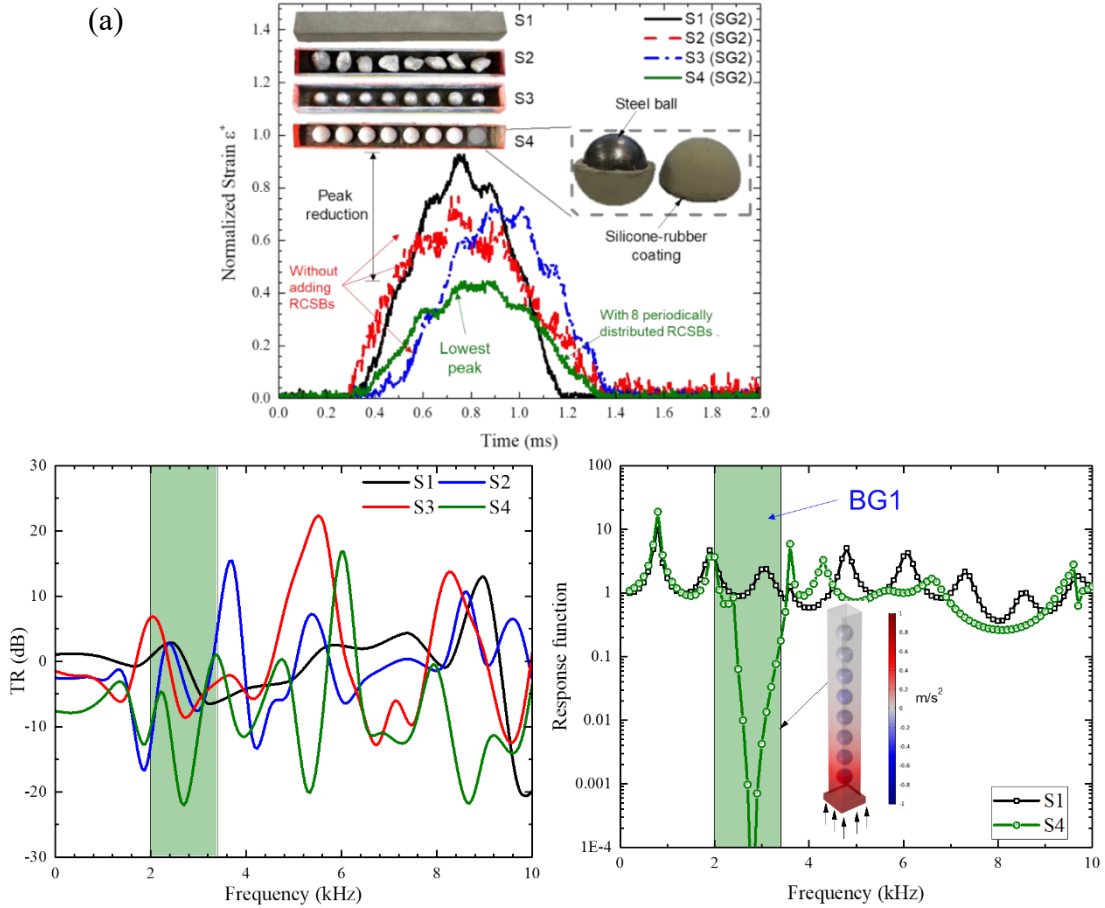
Figure 5-3. Stress wave attenuation performance among specimens S1-S4: (a) Normalized strain-time histories, (b) Frequency spectra (TR: transmission ratio), (c) Predicted bandgap of S4.

To explain the mechanism and evaluate the contribution of the bandgap, TR corresponded to the longitudinal strains are calculated according to Eq. (5-4) and the region of the bandgap is calculated through *COMSOL Multiphysics* [99]. The curves of TR versus frequencies ranging from 0 kHz to 10 kHz for four specimens S1-S4 are presented in Figure 5-3(b). The green shaded zone (i.e., 2 kHz to 3.4 kHz) in the figure represents the estimated frequency range of the bandgap of S4. Figure 5-3(c) shows a numerically calculated response function and the predicted bandgap for S4. The details of the model and the model validation for predicting bandgap have been reported in Chapter 3 and Chapter 4, which are therefore not repeated

herein for brevity. In addition, as shown in Figure 5-3(b), there are no significant changes in TR of the plain mortar (S1) with frequency, especially in the prescribed frequency band, implying no appreciable wave filtering and attenuation in S1. Specimen S2, however, also displays a frequency-dependent attenuation owing to the scattering of the stress wave at the embedded natural aggregates [108, 128]. Similarly, the attenuation phenomenon can be also found in specimen S3 containing eight steel balls, which shows a TR dip of -10 dB at 1.9 kHz.

As compared with specimen S1, both specimens S2 and S3 exhibited the attenuation effect due to the inhomogeneity through adding inclusions. Hence, the attenuation behaviors found in specimens S2 and S3 are attributed to wave scattering and reflection; this trend agrees well with the previous numerical prediction [129]. For specimen S4 with RCSBs, however, besides the wave scattering the predominant wave filtering and attenuation are induced by the local resonance of RCSB. As shown in Figure 5-3(b), apparent frequency dip occurs at the frequency band from 2 kHz to 3.4 kHz, i.e., the bandgap shown in Figure 5-3(c), in which the minimum TR is around -23 dB, indicating that stress wave induced by impulsive loading within this bandgap is substantially suppressed. Within this frequency band, most of the wave energy is transferred to the local resonance of RCSBs, which reduces wave energy transmitted through the cement mortar. Therefore, it can be concluded that adding RCSBs is effective for wave filtering and attenuation, and the existence of local resonance and bandgap can be beneficial for improving the wave attenuation of the specimen subjected to impulsive loading. It should be noted that using steel ball aggregates (S3) leads to slightly more prominent wave attenuation than natural aggregates (S2) because steel material properties are more different from mortar matrix than natural aggregate material. The larger difference in impedance between steel and mortar matrix results in more prominent wave attenuation.

5.3.2 Influence of volume fraction

In this section, responses of specimens S4, S5 and S6 with RCSB volume fractions of 18.4%, 9.2% and 22.9%, respectively are compared to evaluate the influence of the RCSB volume

fraction. Regarding the ability of the peak strain reduction listed in Table 5-1, no difference is observed for the value of R_p between specimens S4 and S5. Kettenbeil and Ravichandran [31] also reported no significant difference regarding the wave attenuation of the metaconcrete structures containing four and eight locally resonant aggregates due to the same configuration of RCSBs. However, R_p increases from 0.56 (S4) to 0.714 (S6), implying that the ability of wave attenuation is greatly improved by increasing the volume fraction of RCSBs from 18.4% to 22.9%. Similarly, there is no difference between specimens S4 and S5 with respect to R_s, while R_s in specimen S6 increases to 0.69 compared to 0.52 for S4. By comparing $\varepsilon^*(t)$ as illustrated in Figure 5-4(a), no significant difference is observed between S4 and S5 as the peak value is almost identical. Nevertheless, the peak value of the normalized longitudinal strain in S6 is 0.296, which is significantly lower than the value of 0.44 in S4.

To understand the mechanism associated with the above observations, Figure 5-4(b) shows the TRs as a function of wave frequency. The shaded zone in the figure indicates the estimated frequency range of the bandgap. Specimens S4, S5 and S6 have similar bandgap induced by local resonant due to the same configuration of RCSBs despite different volume fractions. However, the values of TRs in the predicted bandgap (BG1, as illustrated in Figure 5-4(b) from 2 kHz - 3.4 kHz) are different, which results in a variation in the ability of attenuation. Figure 5-4(b) also displays frequency dips at the higher frequencies in addition to the bandgap (BG1) of RCSB, and these dips might be due to the stress wave reflections by the aggregates. In the frequency bandgap (i.e., 2 kHz-3.4 kHz), specimen S4 has a very close TR value to specimen S5, which leads to similar wave filtering and attenuation behavior. However, the TR value drops to about -30 dB for specimen S6 with ten RCSBs, which causes substantial attenuation. The enhancement of attenuation might be due to the changes in the matrix stiffness between RCSBs. Increasing the volume fraction of RCSBs inevitably narrows the spacing between RCSBs. As shown in Figure 5-4(a), the matrix layer between inclusions for S6 is rather thin, which greatly reduced the stiffness between RCSBs and affected the TR although the bandgap frequency range of engineered aggregate remains the same. The

threshold in this chapter is defined for the volume fraction of RCSBs. The threshold values of volume fraction are determined by comparing the transmission ratios (TR). When the volume fraction is lower than the threshold i.e., S4 (18.4%) In this chapter, changing the volume fraction of RCSBs has little effect on the transmission ratio. When the volume fraction is higher than the threshold, changing the volume fraction of RCSBs has a significant effect on the transmission ratio. A similar observation has also been reported by other researchers [29, 103]. In conclusion, the volume fraction of resonant aggregates is an important design factor, increasing the volume fraction of RCSB could influence the attenuation effectiveness of metaconcrete rod structure subjected to impulsive loading. Further study on the influence of volume fraction of RCSBs is deemed necessary.
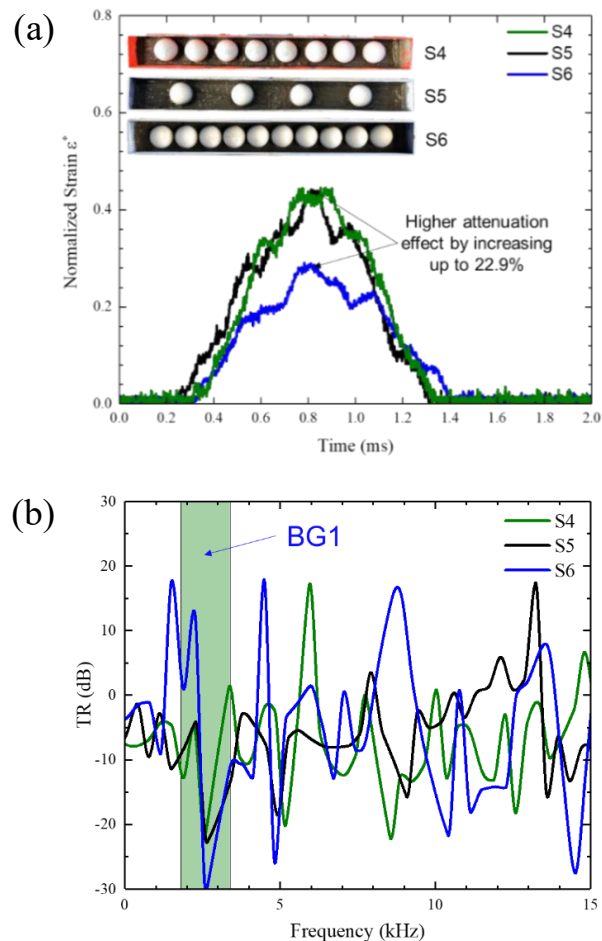
Figure 5-4. Attenuation effect of metaconcrete specimen with different volume fractions (S4-S6): (a) Normalized strain-time histories, (b) Frequency spectra.

5.3.3 Influence of effective bandgap

In the previous studies, metaconcrete material or structure is not designed to achieve the specific effective bandgap based on the frequency band of stress wave in the specimen, instead, the engineered aggregates are arbitrarily configured. When the impulsive load is applied, the metaconcrete structure is very effective to filter and attenuating stress waves with frequency coinciding with the bandgap of the metaconcrete structure. Therefore, the engineered aggregates should be designed to make their bandgaps cover the primary dominant wave frequency (PDWF) for effective wave attenuation. The primary dominant wave frequency (PDWF) refers to the frequency at which most wave energy concentrates. In this chapter, the primary dominant wave frequency (PDWF) of the stress wave propagating in the plain mortar specimen S1 within the elastic range is calculated via LS-DYNA. The average stress-time histories in the middle of the specimen are recorded and the frequency spectrum is then plotted by using the Fast Fourier Transform (FFT). The primary dominant wave frequency is calculated as 6.9652 kHz as shown in Figure 5-5(c), which is the frequency corresponding to the first spectral peak. The bandgap of engineered aggregate can be calculated by the method of determining the response function through *COMSOL Multiphysics* [99]. Based on the *COMSOL Multiphysics* method, the bandgap of 22 mm RCSBs and 18 mm RCSBs are 2 kHz-3.4 kHz and 6.5 kHz-7.5 kHz, respectively, which are denoted as BG1 and BG2 here for easy discussions. Therefore, the bandgap BG2 of specimen S7 with 18 mm RCSBs covers the primary wave frequency PDWF, whereas the PDWF is outside the bandgap BG1 of other specimens with 22 mm RCSBs.

As listed in Table 5-1, specimen S7 with 18 mm diameter RCSBs shows the superior wave attenuation capability with the reduction value R_p of 0.729. Similarly, specimen S7 also has a superior strain reduction R_s of 0.71 compared with S4 (0.52). Hence, specimen S7 is the most effective in suppressing wave propagating through the specimen in this chapter. Moreover, Figure 5-5(a) presents $\varepsilon^*(t)$ of specimens S4, and S7 measured at SG2. The peak value of ε^* of specimens S4 and S7 is 0.44 and 0.296, which are much lower than 0.91 of S1.

These results indicate that if the bandgaps of engineered aggregates cover the PDWF, more effective wave propagation mitigation can be achieved.

To demonstrate the mechanism, TR as a function of wave frequencies for specimens S1, S4 and S7 are plotted in Figure 5-5(b). The bandgaps of S4 and S7 are different, as shown in two shaded areas. Furthermore, the minimum TR value found in S4 is -23 dB located at the frequency band of BG1 (2 kHz-3.4 kHz) shaded in green. The bandgap of specimen S7, namely, BG2 is in the range of 6.5 kHz to 7.5 kHz (colored in light red), which covers the dominant frequency of wave energy. Hence, it is more effective in mitigating wave propagation and leads to a much lower TR value about –45 dB. These results confirm that the design of RCSB with its bandgap covering the PDWF can enhance the ability of metaconcrete structure in attenuating stress wave generated by the impulsive load.
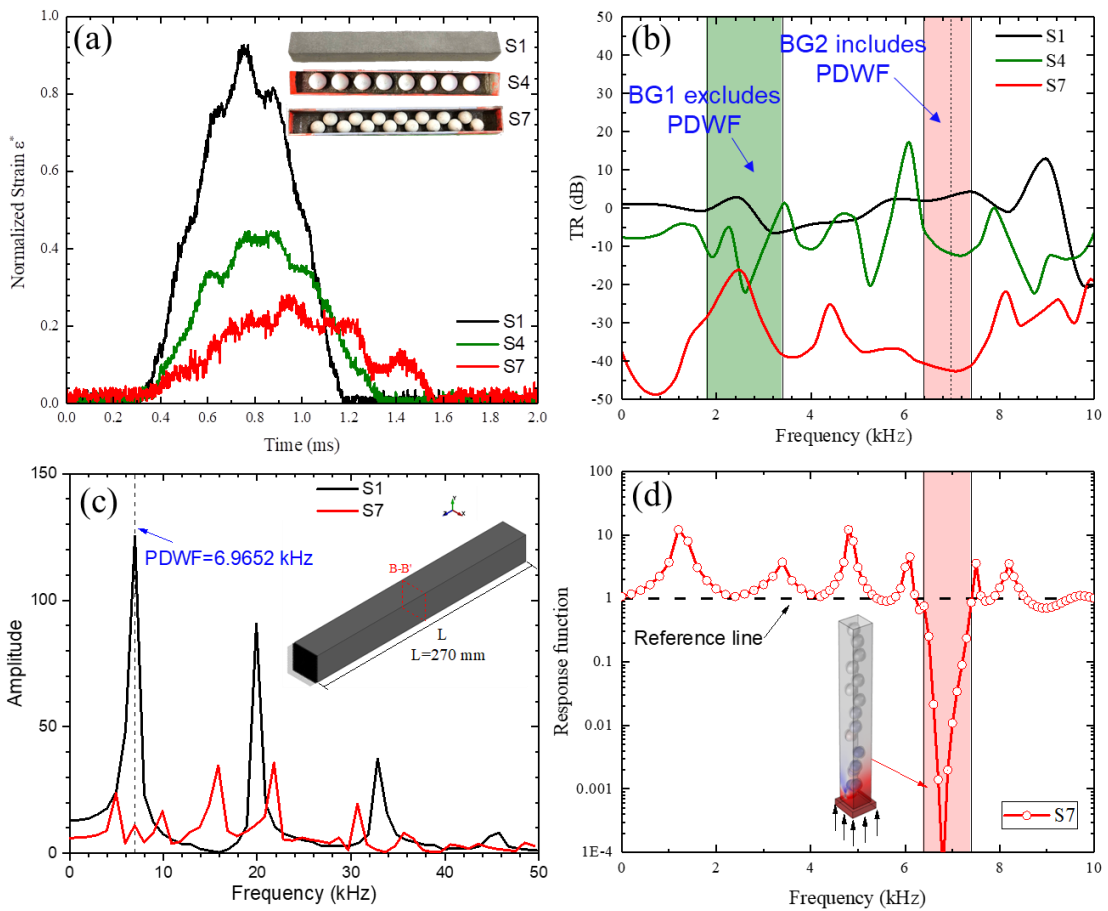
Figure 5-5. Influence of effective bandgap: (a) Normalized strain-time histories, (b) Frequency spectra, (c) Primary dominant wave frequency (PDWF) of plain mortar, and (d) Response function of S7.

5.4 Finite element modelling

5.4.1 Model description and calibration

In order to predict the performance of metaconcrete rod structure subjected to different impulsive loading with different amplitudes and duration, finite element code LS-DYNA is employed in this section to develop numerical models. The numerical model is firstly calibrated with the test data obtained from the above experimental work. The schematic diagram of the numerical model and configuration of specimen S4 as an example is illustrated in Figure 5-6. The geometric and material parameters used in the simulation are listed in Table 5-1 and Table 5-2, respectively. Commonly used concrete material model MAT_CONCRETE_DAMAGE_REL3 (*MAT_072REL3, named KCC model) in LS-DYNA is adopted to simulate mortar material. The accuracy of this model in predicting the behavior of concrete-like material under various dynamic loading conditions has been reported in many previous studies, e.g., [108, 116, 117, 130]. In addition, the dynamic increase factor [122] is also incorporated into the model. Material model MAT_ PIECEWISE_ LINEAR_PLASTICITY is adopted to simulate the steel core. Material model MAT_ MOONEY-RIVLIN_RUBBER is adopted for the rubber coating. The key input parameters required for the present simulation are given in Table 5-2. The strain time histories at 30 mm and 230 mm from the incident surface of the specimen in the numerical model are compared with test data SG1 and SG2, respectively. Three specimens S1, S4 and S7 are selected to calibrate the numerical model. specimen S1 serves as the reference specimen in the study. Since specimens S4 and S7 have different bandgaps, they are used to numerically explore the effectiveness of suppressing wave propagation when achieving the desired bandgap. The comparisons of numerical and experimental results for specimens S1, S4 and S7 are presented in Figure 5-7. In this chapter, each specimen is meshed by the eight-node solid elements in the numerical model, and there are a total of 455,620 elements in each model. The minimum mesh size of 1 mm is adopted for the specimen after conducting a mesh convergence study to obtain reliable results with a reasonable computational cost. The

contacts between the aggregates and mortar are assumed to be the perfect bonding [88].

Table 5-2. Material properties in the numerical model.

Category	Material Model	Parameters	Value
Mortar	*MAT_CONCRETE_DAMAGE_REL3	Mass density	2200 kg/m³
		Unconfined strength	73 MPa
Steel ball	*MAT_PIECEWISE_LINEAR_PLASTICITY	Mass density	7850 kg/m³
		Young's modulus	210 GPa
		Poisson's ratio	0.3
		Yield stress	500 MPa
Rubber [131]	*MAT_MOONEY-RIVLIN_RUBBER	Mass density	1000 kg/m³
		A	0.49755889 MPa
		B	0.10932788 MPa
		Poisson's ratio	0.495

As shown in Figure 5-7(a) and (b), the numerical results match well in general with the experimental results for specimen S1 and S4 despite a slight difference in the peak values and overall duration. Figure 5-7(c) shows some discrepancies in peak strain values for specimen S7 with randomly distributed RCSBs, which might be caused by the imperfection of the sample surface and random locations of RCSBs. The distribution of RCSBs in specimen S7 in the FE model is randomly generated, which may not exactly coincide with those in the tested specimen S7. In conclusion, the overall attenuation behaviors between experimental and numerical results are in good agreement; therefore, the FE model is validated.
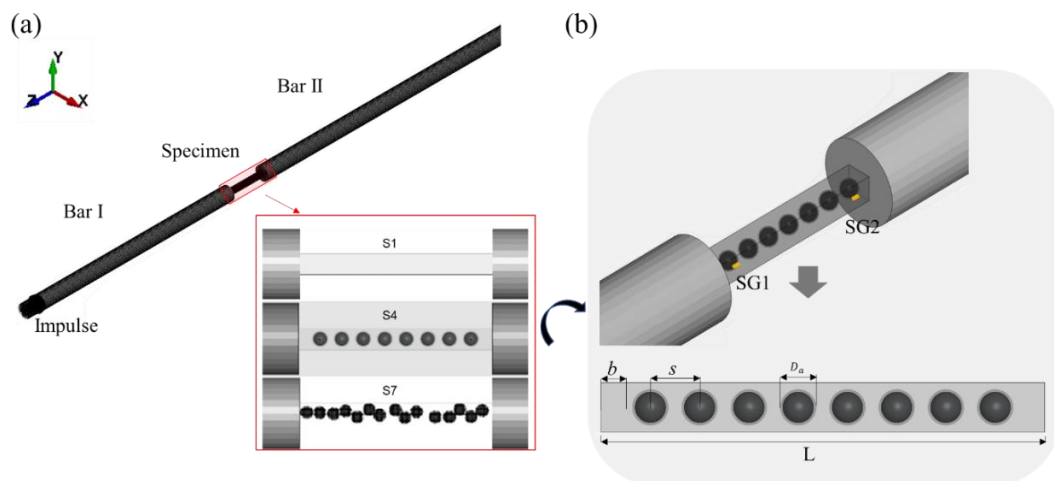
Figure 5-6. (a) Schematic illustration of the numerical model and (b) Configuration of specimen S4.

Note: b=15 mm; s is the spacing between RCSBs; D_a is the diameter of RCSB; L is the length of the specimen.
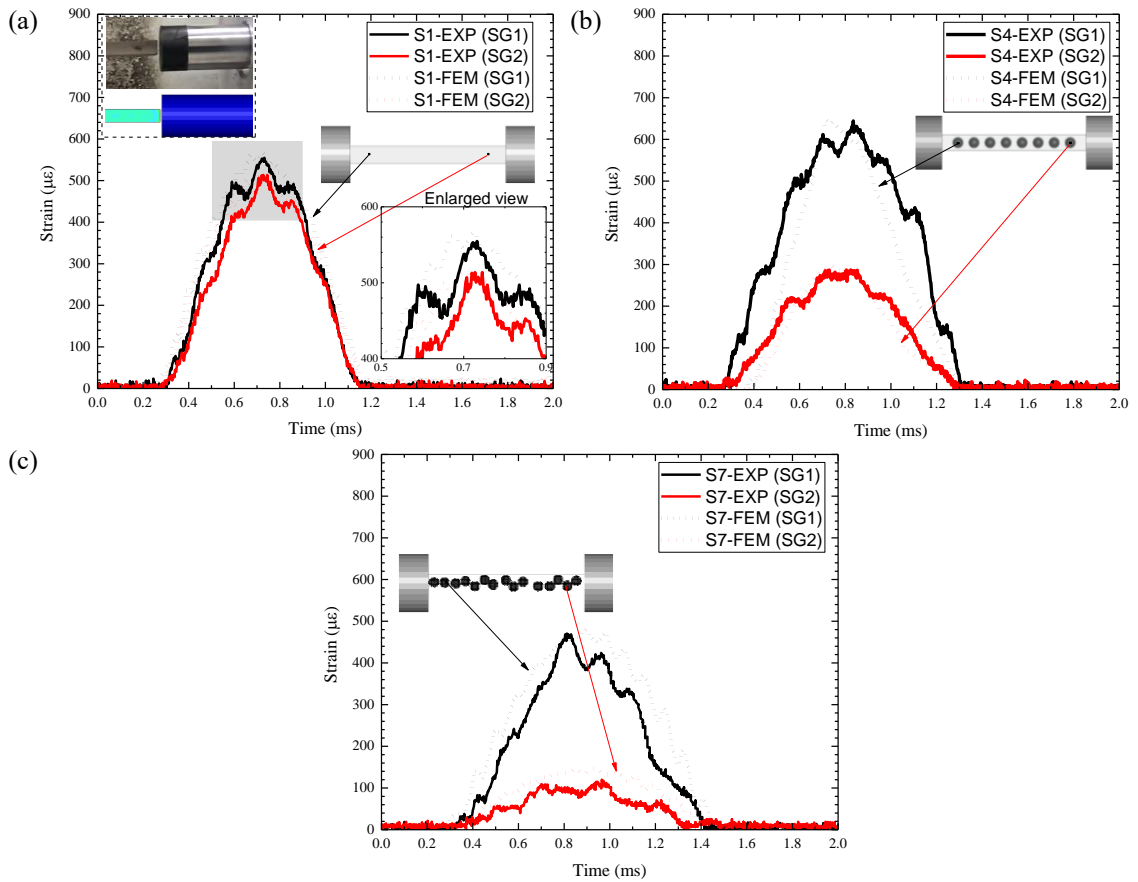
Figure 5-7. Comparisons of numerical prediction and test results of specimens: (a) Comparison of strain time histories in S1, (b) Comparison of strain time histories in S4, and (c) Comparison of strain time histories in S7.

5.4.2 Parametric study

With the validated model, a parametric study is conducted to evaluate the effectiveness of metaconcrete specimens on attenuating waves induced by impulsive loading of different loading parameters. As demonstrated above, metaconcrete structure exhibits significant attenuation behavior of stress waves with dominant wave frequency falling in the bandgap frequency range of locally resonant RCSBs. To assess the ability to attenuate waves generated by impulsive loads with different loading parameters, a series of compressive stress wave profiles with the same amplitude but different duration (i.e., impulse I and II) or with the same duration but different amplitudes (i.e., impulse II, III and IV) shown in Figure 5-8(a) are applied to the incident bar (bar I) as shown in Figure 5-6. Figure 5-8(b) presents the corresponding frequency spectra of selected impulsive loads through FFT. The impulsive

101

loads consist of the single principal impulse of arbitrary form with a short duration [132], e.g., single half-sine impulse, which has been used to study wave propagation in concrete-like material [108, 119]. In this chapter, the single half-sine impulse is also used to assess the attenuation level of stress wave induced by impulsive loads. More specifically, the peak amplitudes of impulse I and II are set as 5 MPa so that it does not result in compressive damage to the concrete specimen during the propagation of the stress wave. The input stress waves with different peak amplitudes (i.e., impulse III and IV) are used to evaluate the ability to attenuate stress waves of different amplitudes. The peak stress amplitudes are set as 2.5 MPa and 10 MPa for Impulse III and IV, respectively. The reduction in the peak strain, i.e., R_p, of specimens S1, S4 and S7 under various loading scenarios are summarized in Table 5-3. Higher reduction ratio R_p value indicates a higher reduction percentage in the maximum longitudinal strain or better mitigation performance. Table 5-3 also gives the peak value of average stress (σ_{ave}) over the cross-section for these three specimens, i.e., $\sigma_{C1,ave}\big|_{peak}$ and $\sigma_{C2,ave}\big|_{peak}$ at two cross-sections C1 and C2 located at 45 mm and 225 mm from the incident surface of the specimen, respectively. To further demonstrate the effectiveness of wave attenuation, the transmitted stress wave profiles at C2 after passing several locally resonant aggregates (i.e., S4 and S7) are compared with that of the plain mortar S1. The stress-time histories at C2 of different specimens and loading scenarios are presented in Figure 5-9.
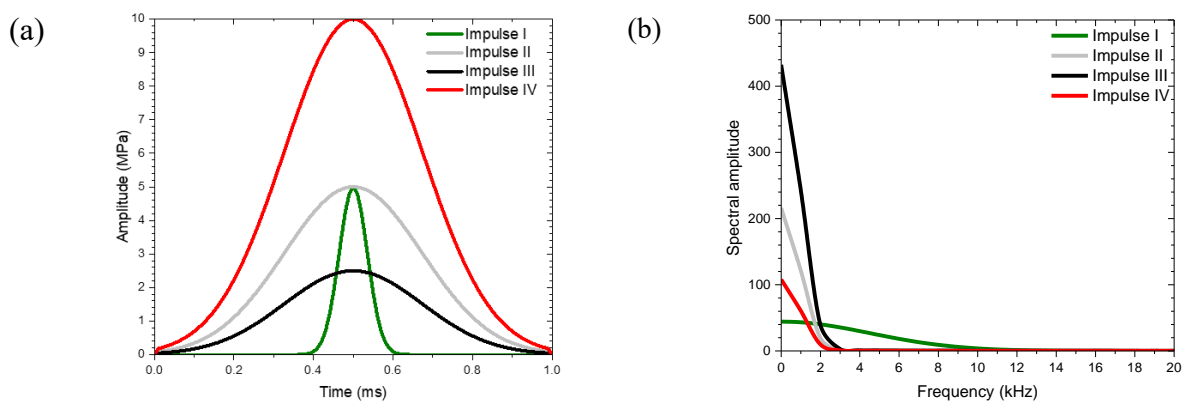
Figure 5-8. (a) Time-histories of input impulsive loads (I, II, III, IV), (b) Frequency spectra.

As illustrated in Table 5-3, the specimen with RCSBs generally shows a higher reduction ratio (i.e., R_p) than the plain mortar in all loading cases. Higher reduction ratio indicates

higher reduction percentage of the maximum longitudinal strain after passing serval RCSBs, implying better performance on wave propagation mitigation as compared to the one without RCSBs. Moreover, the value of R_p for metaconcrete specimens under impulse I is slightly higher than that under impulse II with a larger duration, i.e., the wave propagation mitigation (i.e., R_p value) slightly decreases with the increase in loading duration. This is because increasing the loading duration makes its energy concentrate in a narrower frequency band. Hence, the wave attenuation of metaconcrete specimens is less effective, especially when the wave energy is in a frequency band outside the bandgap of the metaconcrete structure.

Table 5-3. Reduction in the peak strain, the peak value of average stresses at cross-sections C1and C2 under various input impulses.

| Specimen No. | Impulse | | | $R_p = 1 - \dfrac{\varepsilon_2\big|_{peak}}{\varepsilon_1\big|_{peak}}$ | $\sigma_{C1,ave}\big|_{peak}$ (MPa) | $\sigma_{C2,ave}\big|_{peak}$ (MPa) |
	No.	Duration (ms)	Peak amplitude (MPa)			
S1	I	0.2	5	0.093	5.11	4.65
	II	1	5	0.080	17.12	15.58
	III	1	2.5	0.079	8.42	6.98
	IV	1	10	0.081	33.99	30.76
S4	I	0.2	5	0.586	5.12	2.02
	II	1	5	0.551	14.76	6.41
	III	1	2.5	0.533	7.76	3.46
	IV	1	10	0.581	27.85	11.79
S7	I	0.2	5	0.733	5.43	1.48
	II	1	5	0.707	13.92	4.13
	III	1	2.5	0.695	7.10	2.16
	IV	1	10	0.739	27.29	7.63

This observation agrees with the testing results reported in Kettenbeil and Ravichandran [31]. In addition, wave propagation mitigation is more effective when the specimen is subjected to the impulse with higher loading amplitude. This is because higher loading amplitude induces larger local vibrations of the hard core inside the engineered aggregate. Thus, more wave energy is absorbed by the engineered aggregates hence resulting in more effective mitigation of wave propagations. This result also agrees with the findings from [31], who conducted the plate impact experiment with varying impact velocities. Furthermore, the strain reduction is found to be more pronounced in specimen S7 where R_p of 0.695 and 0.739 under impulse III and IV is observed. Thus, it demonstrates again that RCSBs designed with the effective bandgap (i.e., S7) that covers the primary dominant wave frequency (PDWF) is more

effective in mitigating stress wave propagations. To conclude, the wave mitigation efficiency of the metaconcrete specimen is less prominent if the impulsive load has a long duration or narrow frequency band and the frequency band is outside the bandgap of the metaconcrete specimen (e.g., S4 and S7). Therefore, it is important to properly design the engineered aggregates to have their bandgaps cover the primary dominant frequency bands of expected stress waves. It is interesting to note that the mortar specimen S1 has a slightly larger reduction value R_p when the loading intensity is higher. Since specimen S1 is homogeneous and the response is within the elastic range, the only mechanism to dissipate wave energy and attenuate wave is geometric attenuation, as mentioned in [133, 134]. Yuan et al. [133] stated that the spatial attenuation coefficient of rock specimen increases when subjected to more intensive loading owing to the geometric attenuation, indicating the geometric attenuation is wave amplitude-dependent, more geometric attenuation is expected if propagating wave has a higher amplitude. A similar characteristic of sandstone specimens under dynamic loading is reported by Cheng et al. [134]. Moreover, the Poisson effect might be another reason to cause higher attenuations in this chapter. A larger longitudinal wave in a rod is also associated with a larger lateral expansion owing to the Poisson effect, which also attracts some wave energy during propagation.

Furthermore, it is also interesting to note that the average stress over the cross-section C1 on the input side corresponding to impulse I of S7 is the highest, followed by S4 and that of the homogenous mortar specimen S1 is the smallest. This is because of the wave reflection on the surface of the aggregates. When the impulse is applied onto the specimen, it generates the stress wave propagating inside the specimen. On the input side, while the local vibration of the engineered aggregates is not fully activated yet, the wave reflection by the aggregates slightly increased the stress over the cross-section C1. The opposite, i.e., the largest average stress over cross-section C1 occurs in specimen S1, followed by S4 and the smallest average stress occurs in S7, however, is observed for input impulses II, III and IV. This is probably because the duration of these impulses is longer, implying more energies for these impulses to activate the local vibrations of the first aggregate in S4 and the first three aggregates in S7,

which attenuate the stress waves. Moreover, longer impulse duration means a narrower frequency band and lower primary frequency of the input, which makes the wavelength longer, leading to less wave reflection by the aggregates.
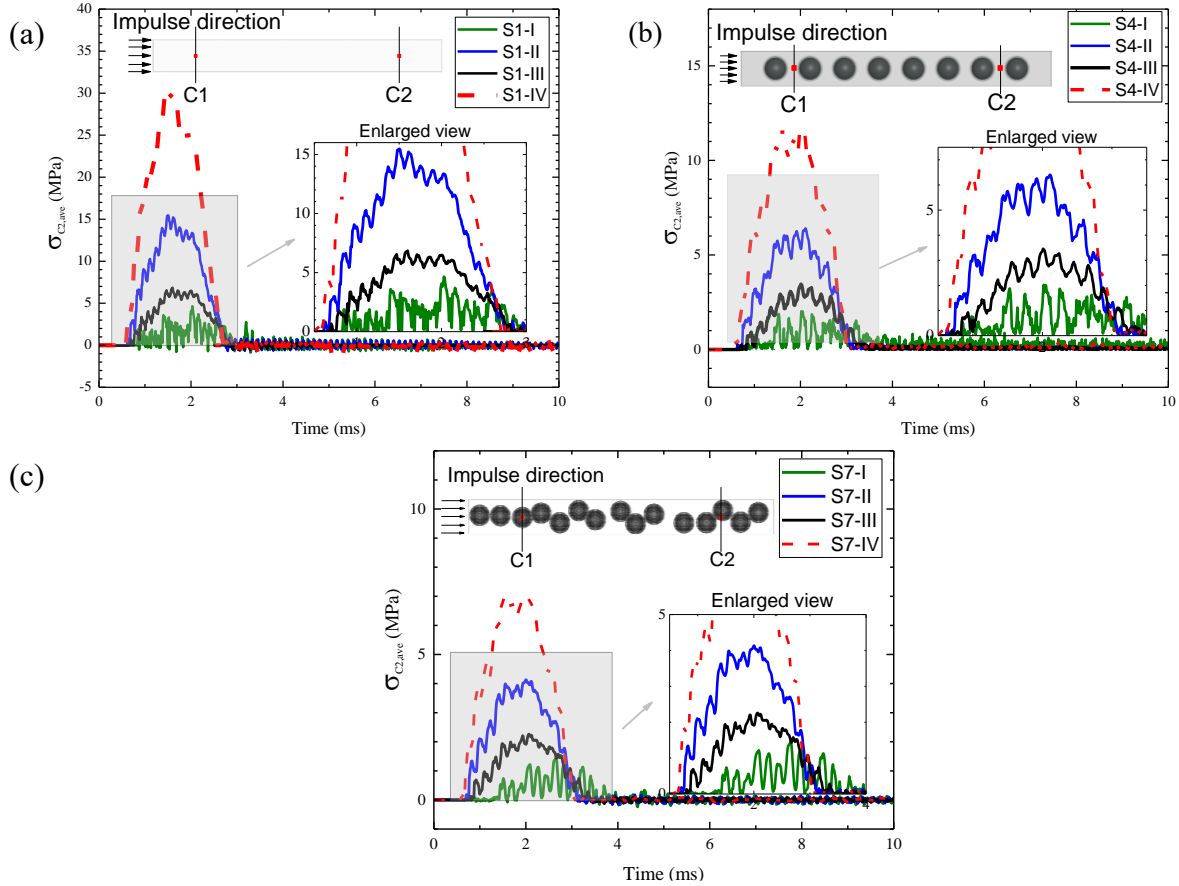
Figure 5-9. Plot of average stresses transmitted at cross-sections C2 of specimen S1, S4 and S7 subjected to different impulses, (a) S1, (b) S4, (c) S7.

To study the stress wave propagation in different rod structures, Figure 5-9 plots the average stress transmitted at cross-section C2 for specimens S1, S4 and S7. As shown in Figure 5-9 (a), (b) and (c), the specimen with RCSBs has a lower peak value of transmitted stress (i.e., higher attenuation performance) than plain mortar (S1) under different loading scenarios. By comparing specimen S4 with S7 from Figure 5-9(b) and (c), it can be observed that specimen S7 gives the lowest average value of transmitted stress at cross-section C2 during all loading scenarios. In other words, it has better performance in wave mitigation than the plain mortar and the specimen with its bandgap excluding PDWF (e.g., S4) due to the mechanism of the bandgap. In general, by comparing the reduction ratio (i.e., R_p) of the maximum longitudinal strain and the transmitted average stress, it can be concluded that the presence of resonant

RCSBs can effectively improve the stress attenuation performance, and the properly designed RCSBs with the effective bandgap show better performance in stress wave attenuation.

5.5 Summary

In this chapter, the effectiveness of using resonant aggregates named RCSBs to mitigate stress wave is explored experimentally and numerically. The experiment has investigated the influences of different types of inclusions, volume fractions and bandgaps on the stress wave attenuation of rod structures subjected to impulsive loading. The effectiveness of metaconcrete structure on mitigation of wave propagation induced by different impulsive loading profiles is numerically investigated. The main findings are summarized as follows.

(1) The experiment demonstrates that the presence of RCSBs in metaconcrete rod structure could attenuate stress wave more effectively than plain mortar, mortar with natural aggregates and mortar with steel balls. The favorable stress wave attenuation performance in the specimen with RCSBs is attributed to the formation of the bandgap.

(2) The volume fraction of RCSBs is an important factor affecting the wave attenuation performance under impulsive loads. More prominent wave mitigation capacity can be obtained if the volume fraction of RCSB reaches a threshold.

(3) Metaconcrete with RCSBs has superior wave attenuation performance than plain mortar under various loading scenarios. Wave mitigation performance in metaconcrete specimen can be enhanced when subjected to the input impulse with a shorter duration or higher amplitude.

(4) A newly proposed design method for resonant aggregates with an effective bandgap to cover the primary dominant wave frequency (PDWF) of plain mortar is experimentally verified. The PDWF of plain mortar structure can be used to design the resonant aggregates (e.g., RCSBs) of metaconcrete structure for better wave mitigation performance.

Chapter 6 Damping properties and dynamic responses of metaconcrete beam structures subjected to transverse loading

6.1 Introduction

In Chapter 5, the dynamic response of metaconcrete rod structure subjected to longitudinal impulsive loading is revealed. This chapter then investigates the damping property and dynamic response of cementitious metaconcrete beam with resonant aggregates made of rubber-coated steel balls (RCSB) subjected to transverse impulsive loading. A total of nine beam specimens are prepared, made of plain mortar, mortar with non-resonant inclusions and metaconcrete beam with various volume fractions of RCSBs (i.e., 9.2%, 18.4% and 22.9%) and different sizes of RCSBs (i.e., 22 mm, 18 mm and 15 mm). Two boundary conditions (i.e., cantilevered and clamped support) are adopted in the tests. The influence of periodic and non-periodic RCSB distributions is also analyzed. The effectiveness of the metaconcrete beam on the response attenuation subjected to different transverse impulsive loading intensities is examined. Furthermore, the bandgap characteristics obtained from the experiment are compared with the numerical prediction using *COMSOL Multiphysics* to verify the existence of bandgap in metaconcrete beam and understand the attenuation mechanism of the metaconcrete beam specimens under transverse impulsive load.

The related work in this chapter has been published in Construction and Building Materials.

6.2 Dynamic response of metaconcrete beam subjected to transverse loading

Many models are available to analyze the vibration response of periodic composite structures. Lougou et al. [135] proposed the double scale asymptotic method (DSAM) suitable for periodically supported sandwich beam and Hamdaoui et al. [136] further analyzed the damped response of sandwich beam via the adjoint method. Besides, the Euler-Bernoulli beam model has been often used for studying wave propagation in continuous periodic structures [137], flexural wave propagation in the beam with periodic masses [138, 139], and flexural response of a beam with mass-springs subsystems [140-142]. Without losing generality, the dynamic response of a metaconcrete beam specimen subjected to transverse non-destructive impulsive load is determined by using the Euler-Bernoulli beam theory. According to the Euler-Bernoulli beam theory [143, 144], the governing equation of motion can be simplified as:

$$EI\frac{\partial^4 u}{\partial x^4} + \rho A \frac{\partial^2 u}{\partial t^2} = P(x,t) \tag{6-1}$$

where E, I, ρ, A and u are Young's modulus, the moment of inertia, density, cross-sectional area and displacement of the beam, respectively, $P(x,t)$ is the equivalently distributed load per unit length. When the impulsive load $P(t)$ is applied at the tip of the cantilevered beam ($x=L$), the equivalent distributed force per unit length can be expressed as $P(x,t) = P(t)\,\delta(x\text{-}L)$, where $\delta(x)$ is the Dirac delta function [144].

In addition to the concrete matrix, the metaconcrete beam specimen has distributed RCSBs consisting of solid core and soft coating, as shown in Figure 6-1(a), which can be treated as the equivalent spring-mass system. When the cantilevered beam is subjected to an impulsive load (i.e., impulsive load $P(t)$), the local resonators (RCSB) tend to vibrate and dissipate energy. The metaconcrete beam with resonators can be simplified as the combination of an equivalent mass-spring system with an internal core connected by springs, as depicted in

Figure 6-1(b) and the concrete matrix. The equivalent mass-spring system (i.e., highlighted by red box) can mitigate the dynamic response of the beam induced by external dynamic loads, such as impulsive load.
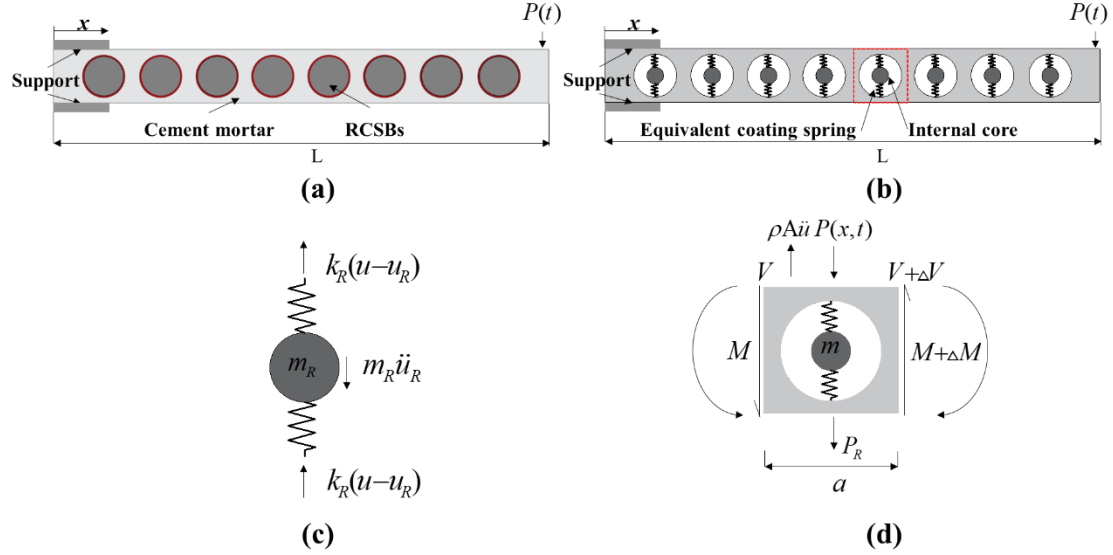
Figure 6-1. (a) Metaconcrete beam with RCSBs, (b) Simplified equivalent mass-spring model, (c) Free-body diagram of local resonator (i.e., RCSB), and (d) Representative segment.

Since the elastic response is assumed, the overall structure can be divided into representative segments, as shown in Figure 6-1(b). Figure 6-1(c) and (d) respectively illustrate the free body diagram of the local resonator and representative segment. When the core starts to vibrate, the impulsive energy is transferred to the internal resonators (i.e., RCSBs), therefore mitigating the response of the beam structure.

Based on the assumption of the Euler-Bernoulli beam and free body diagram shown in Figure 6-1(d), three coupled equations of motion for the metaconcrete beam segment can be expressed as:

$$\begin{cases} EI \dfrac{\partial^4 u}{\partial x^4} + \rho A \dfrac{\partial^2 u}{\partial t^2} = P(x,t) \\ m_R \ddot{u}_R + 2k_R(u_R - u) = 0 \\ P_R a = 2k_R(u_R - u) \end{cases} \tag{6-2}$$

where a, k_R, m_R, u and u_R are the segment length, equivalent spring stiffness, the mass of RCSBs, displacements of segment and RCSBs, respectively. P_R represents the equivalent

uniformly distributed force acting on the segment generated by resonators. Let:

$$\bar{k}_R = \frac{k_R}{a}, \bar{m}_R = \frac{m_R}{a}, \omega_R = \sqrt{\frac{2\bar{k}_R}{\bar{m}_R}} \tag{6-3}$$

where $\bar{k}_R$ and $\bar{m}_R$ are the normalized equivalent spring stiffness and mass, respectively, ω_R is the resonant frequency of RCSBs (rad/s). Eq. (6-2) with considering Eq. (6-3) can be expressed as:

$$\begin{cases} EI\dfrac{\partial^4 u}{\partial x^4} + \rho A\dfrac{\partial^2 u}{\partial t^2} - 2\bar{k}_R(u_R - u) = 0 \\ \bar{m}_R \ddot{u}_R + 2\bar{k}_R(u_R - u) = 0 \end{cases} \tag{6-4}$$

Introducing the general displacement solution for beam segment and local resonator [25, 145], it can be written as:

$$\begin{cases} u = U(x)e^{i\omega t} \\ u_R = U_R(x)e^{i\omega t} \end{cases} \tag{6-5}$$

where $U(x)$ and $U_R(x)$ stand for the displacement solution for beam segment and local resonator at location x [145], respectively. Substituting Eq. (6-5) into Eq. (6-4), the equations of motion can be expressed as:

$$\begin{cases} U_R = \dfrac{2\bar{k}_R}{2\bar{k}_R - \bar{m}_R\,\omega^2}U \\ EI\dfrac{\partial^4 U}{\partial x^4} - \left(\rho A - \dfrac{2\bar{m}_R\,\bar{k}_R}{2\bar{k}_R - \bar{m}_R\,\omega^2}\right)\omega^2 U = 0 \end{cases} \tag{6-6}$$

As seen from Eq. (6-6), the ratio of displacement amplitude (U_R/U) between the local resonator and beam segment is related to the resonant frequency of resonator (ω_R), or RCSB in this chapter. It is found that when $2\bar{k}_R - \bar{m}_R\,\omega^2$ is close to zero or the loading frequency approaches resonant frequency, i.e., $\omega \to \omega_R$, the vibration amplitude of RCSB approaches

infinity theoretically. Hence, the impulsive energy is greatly dissipated via converting into kinetic energy of RCSBs. Similar to the theoretical explanation as mentioned in Section 2.4.2, the frequency band where displacement ratio (U_R/U) theoretically approaches infinity is termed as bandgap, indicating that the internal core of the local resonator moves out-of-phase against the matrix. Thus, the stress wave induced by the impulsive load within the bandgap is suppressed, leading to the mitigation of dynamic responses.

6.3 Experimental program
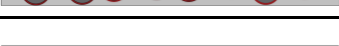
6.3.1 Specimen fabrication

This chapter is aimed to investigate the influences of different parameters on the dynamic response of the specimen subjected to the transverse impulsive load. High strength mortar is used as the matrix of the metaconcrete specimen to avoid damage during the test. The mortar is made of dry-mix Davco Lanko 701 duragrout produced by *Sika Australia Pty Ltd* with the designated compressive strength of 73 MPa after 28 days [124]. The mix ratio of cement/sand/water/additives is 1/2/0.5/0.33. In addition, the casting method for specimens with periodically placed RCSBs in a mortar matrix is schematically depicted in Figure 6-2(a). Besides, five types of inclusions are used to fabricate the specimens, as depicted in Figure 6-2(b). In addition, the silicone rubber-coated steel balls (RCSBs) as shown in Figure 6-2(b) are fabricated by encapsulating steel ball with rubber coating, followed by a curing process.

Detailed information on the specimens and the configuration of inclusions are listed in Table 6-1. As shown, a total of nine specimens (i.e., S1-S9) with a length of 270 mm and a cross-sectional area of 30×30 mm are prepared. A plain mortar beam (S1) without inclusion is prepared as a reference specimen. Besides, S2, S3 and S4 are fabricated by respectively adding natural aggregates, steel balls and RCSBs to evaluate the effect of inclusion type. Three specimens labelled as S4, S5 and S6 are designed to periodically mix the different number of 22 mm-diameter RCSBs in metaconcrete specimen. Giving the RCSB volume fraction of 9.2%, 18.4% and 22.9% in metaconcrete specimen, it could explore the influence

of the volume fraction of engineered aggregates. S8 has the same number of aggregates as S4, but they are randomly distributed in a mortar matrix to study the influences of randomly distributed vs periodically distributed engineered aggregates on the behavior of metaconcrete beam structure. RCSBs with different sizes, namely, 22 mm, 18 mm and 15 mm in diameter as illustrated in Figure 6-2(b), are used to fabricate the S4, S7 and S9 to study the effect of aggregate size. To ensure the periodic position of S3, S4, S5 and S6, three 3D-printed position guides are prepared for the specimen fabrications. During the fabrication process as illustrated in Figure 6-2(a), the first step is to place the bottom layer of mortar in the mould to provide the initial cover. After that, the position guide is used for placing aggregates and then the position guide is removed. For S7, S8 and S9, the RCSBSs are randomly placed on top of the initial layer. Sequentially, the remaining mortar is poured. Finally, a steel rod is used to ram the specimen to minimize the voids.

Table 6-1. Summary of specimen configuration and parameters.

No	Configuration	Type	Distribution	D_a (mm)	t (mm)	V_a (%)	LBF (kHz)	UBF (kHz)
S1		-	-	-	-	-	-	-
S2		Natural aggregates	Periodic	22	-	18.4	-	-
S3		Steel balls	Periodic	20.5	-	17	-	-
S4		RCSB	Periodic	22	1.5	18.4	2.4	3.4
S5		RCSB	Periodic	22	1.5	9.2	2.4	3.4
S6		RCSB	Periodic	22	1.5	22.9	2.4	3.4
S7		RCSB	Random	18	1.2	18.9	6.88	7.6
S8		RCSB	Random	22	1.5	18.4	2.4	3.4
S9		RCSB	Random	15	1.2	18.6	8.38	9.1
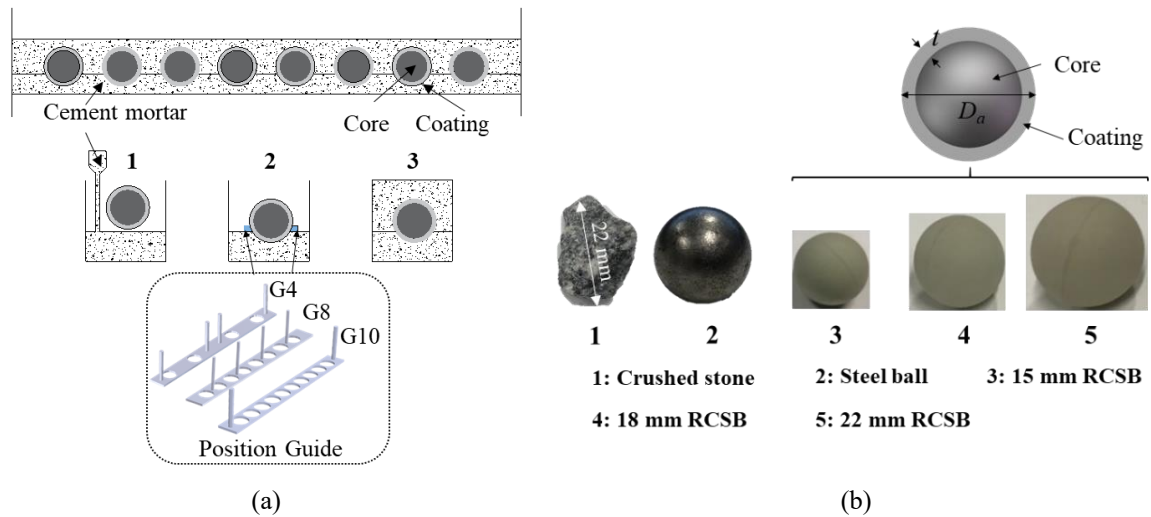
Figure 6-2. Schematic diagram: (a) Casting method of the specimen, (b) Different inclusions.

6.3.2 Test setup

The hammer excitation technique has been commonly used in vibration tests to study the damping properties and dynamic response. In the previous studies [28, 29], only the longitudinal (in-plane) response of the metaconcrete structure was studied. The out-of-plane dynamic response of metaconcrete beam under non-destructive impulsive loading is further explored herein. For the test setup, accelerometers are usually placed near and away from the impact location to measure the wave propagating through local resonators under different excitations [29, 45, 53, 69, 74, 76]. One accelerometer (i.e., accelerometer #1 (a_1)) is adhered underneath the impact location to record the input acceleration using a Quantum X universal data acquisition system (DAQ) with a sampling rate of 19.2 kHz. Another accelerometer (i.e., accelerometer #2 (a_2)) is installed near the support to measure the output acceleration. A Dytran® 5800B3 impulse hammer equipped with a soft polyurethane tip (6250PS) is used to impact the specimen at the prescribed location and the hammer force is also recorded by DAQ. Moreover, concrete specimens with identical geometrical size (i.e., 30×30×270 mm) and mortar strength but two different boundary conditions, i.e., cantilevered (labelled as B1) and clamped support (labelled as B2) are tested. For the cantilevered beam, all specimens are fixed at one support and excited at its free end to evaluate the damping and out-of-plane dynamic responses, while the beam specimens with clamped boundary are impacted at mid-

113

span. The attenuation properties of nine specimens with cantilevered and clamped boundary conditions are comparatively studied to evaluate the effect of boundary conditions. The schematic diagram of the experimental setup is illustrated in Figure 6-3.
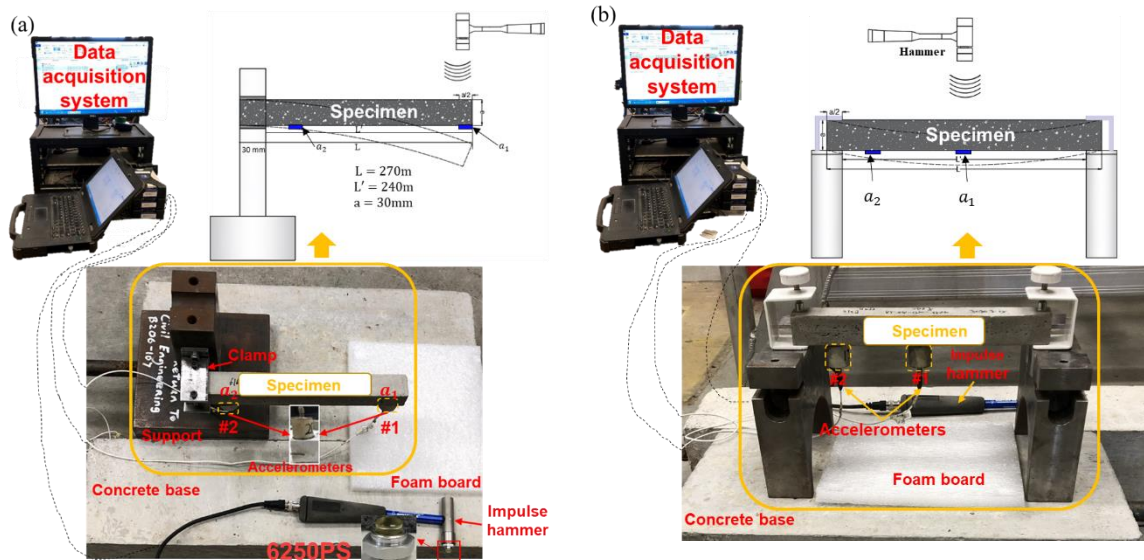
Figure 6-3. Schematic diagram of the experimental setup with two boundary conditions: (a) Cantilevered support, (b) Clamped support.

6.4 Experimental results and discussions

6.4.1 Damping

Damping includes viscous damping, friction damping, and solid damping [146]. In this chapter, nine cantilevered specimens described above are studied by conducting a forced vibration test with an instrumented impact hammer. The equivalent damping ratio is extracted from the testing data to represent the damping of the structure. The free vibration phase of cantilevered structures under hammer impact is used to evaluate the equivalent damping ratio. Without losing the generality, testing data from specimen $S1_{B1}$ are used to illustrate the procedure to derive the equivalent damping ratios of the beam specimen. Figure 6-4(a) shows a typical hammer impact force profile with two peaks recorded during the impact test on specimen $S1_{B1}$. At the end of the impulse, the specimen starts vibrating freely. In this chapter, the free vibration response in the time region from 0.0228s to 1s (shaded area) as shown in Figure 6-4 (b) is selected for analysis. The equivalent damping ratio can be determined by

using the exponential fitting method [146-148]. Specifically, Figure 6-4(c) illustrates the acceleration time history recorded by accelerometer #2, and the equivalent damping ratio (ξ) is determined using the equation depicted in Figure 6-4(c). Figure 6-4(d) shows the fast Fourier transform (FFT) spectrum, from which the corresponding fundamental frequency can be obtained. For brevity, the details of the method are not presented herein but can refer to [147].
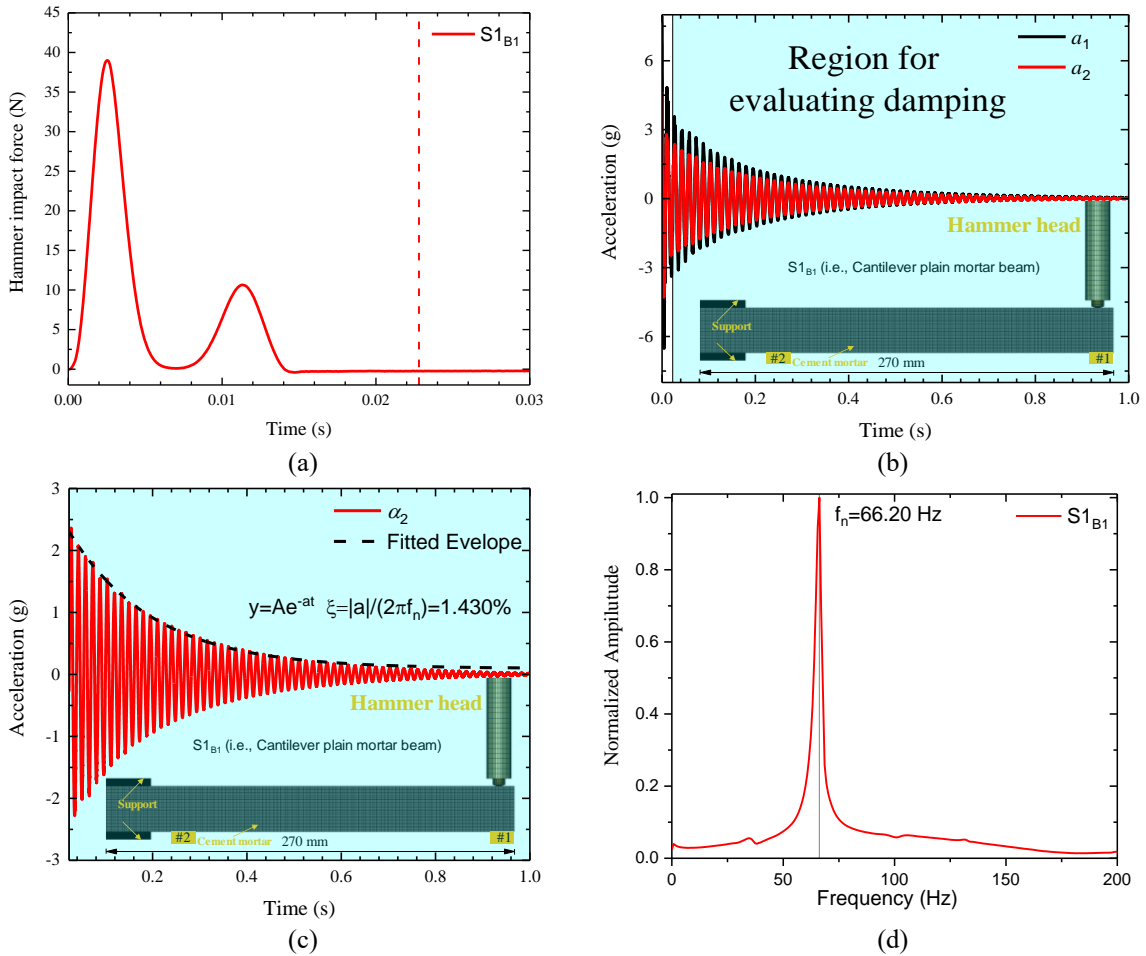
Figure 6-4. Evaluation of damping: (a) Hammer impact force-time histories, (b) Corresponding acceleration time histories and free-vibration region for evaluating damping, (c) Illustration to calculate equivalent damping ratio through the exponential fitting, (d) FFT spectrum and fundamental frequency.

Each specimen is impacted by the hammer at least three times, and a total of 27 acceleration-time histories are analyzed to derive the equivalent damping ratio, the results and average equivalent damping ratio for each specimen from the test are summarized in Table 6-2. In addition, the average equivalent damping ratios of $S1_{B1}$-$S9_{B1}$ are summarized in Figure 6-5.

As shown, the specimens with RCSBs (i.e., S4$_{B1}$-S9$_{B1}$) have much higher equivalent damping ratio than the specimens without RCSBs (i.e., S1$_{B1}$-S3$_{B1}$). For instance, the equivalent damping ratio for the beam with eight RCSBs (i.e., S4$_{B1}$) has an equivalent damping ratio of 2.683%, which is much higher than S1$_{B1}$ of 1.355%, S2$_{B1}$ of 1.366% and S3$_{B1}$ of 1.946%. It is worth noting that the equivalent damping ratio of metaconcrete specimen S4$_{B1}$ is 96% higher as compared to that of S2$_{B1}$ (normal concrete). The enhancement of the equivalent damping ratio is attributed to the existence of RCSBs because some vibration energy is absorbed by the local vibrations of steel cores. Moreover, the volume fraction of RCSBs provides a favorable effect on the equivalent damping ratio. It is found that the average equivalent damping ratio increased from 2.524% in S5$_{B1}$ (9.2% volume fraction) to 3.052% in S6$_{B1}$ (22.9% volume fraction). This is because the larger amount of viscoelastic rubber coating and more local vibrations of RCSBs lead to more energy dissipations. Thus, damping ratios of the metaconcrete specimen are positively correlated to the volume fraction or the number of RCSBs in the metaconcrete mix.

Table 6-2. Summary of equivalent damping ratio of cantilevered specimens.

ξ (%) Specimens No.	Test no.			Average value	Standard derivation
	T1	T2	T3		
S1$_{B1}$	1.430	1.370	1.204	1.335	0.166
S2$_{B1}$	1.269	1.461	1.369	1.366	0.136
S3$_{B1}$	1.979	1.955	1.905	1.946	0.053
S4$_{B1}$	2.739	2.637	2.672	2.683	0.073
S5$_{B1}$	2.506	2.450	2.615	2.524	0.119
S6$_{B1}$	2.989	3.215	2.953	3.052	0.201
S7$_{B1}$	2.757	2.952	2.994	2.901	0.179
S8$_{B1}$	2.647	2.847	3.039	2.844	0.277
S9$_{B1}$	2.708	2.913	3.109	2.910	0.284

Besides, the equivalent damping ratio varies slightly for the specimens with different aggregate sizes (S7$_{B1}$, S8$_{B1}$, S9$_{B1}$) but similar volume fractions of RCSBs. Given a similar volume fraction of RCSBs, S7$_{B1}$ with 18 mm RCSBs has the average equivalent damping ratio of 2.901%, and S9$_{B1}$ with 15 mm RCSBs presents an average equivalent damping ratio

of 2.910%, which is slightly different from that of S8$_{B1}$ with 22 mm engineered aggregates. Moreover, the aggregate distribution slightly affects the damping properties by comparing the equivalent damping ratios of S4$_{B1}$ and S8$_{B1}$. These results demonstrate that the metaconcrete specimens with RCSBs can achieve a much higher equivalent damping ratio than the normal concrete specimen, which can effectively reduce the dynamic response.
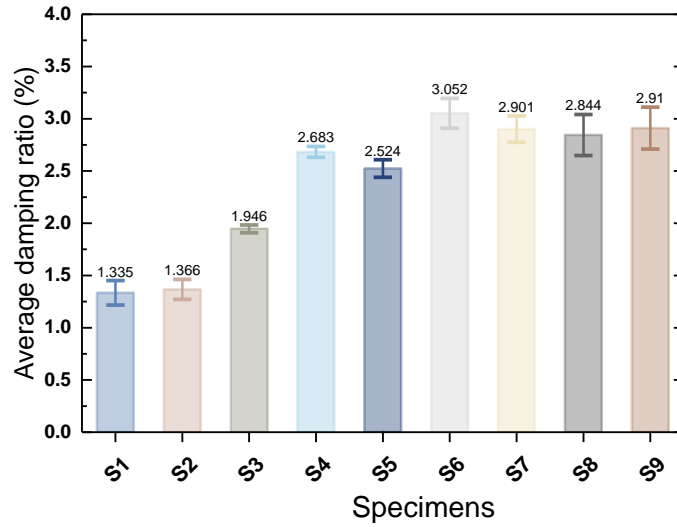
Figure 6-5. Average equivalent damping ratio for cantilevered specimens.

6.4.2 Dynamic responses under transverse impulsive loads

In this chapter, two performance indexes as defined in [31, 52, 91] are adopted to examine the attenuation effectiveness of each specimen. First, the attenuation ratio R_a, the ratio between input and output acceleration response, is adopted as a primary performance index. In this chapter, two acceleration responses refer to the accelerations recorded near and away from the impact location, i.e., location #1 and # 2, respectively as illustrated in Figure 6-3. Besides, taking S1 (plain mortar specimen) with no inclusions as a reference, the index R_m, i.e., the ratio of the acceleration recorded at location #2 normalized by the corresponding peak hammer force in each test for metaconcrete specimen (Si) to that of S1 is used as another performance index. The equations to calculate these two performance indices [31, 52, 91] are given by:

$$R_{a-B1} \text{ or } R_{a-B2} = 1 - \frac{a_2|_{max}}{a_1|_{max}} \times 100\% \tag{6-7}$$

$$R_{m-B1} \, or \, R_{m-B2} = (1 - \frac{a_2',_{Si}|_{max}}{a_2',_{S1}|_{max}}) \times 100\% \,, \text{ where } a_2',_{Si}|_{max} = \frac{a_{2,Si}|_{max}}{F_{peak}}, \quad i=1,2\cdots 9 \qquad (6\text{-}8)$$

where subscripts B1 and B2 refer to the two boundary conditions; a_1 and a_2 are the amplitude of acceleration recorded by two accelerometers at locations #1 and #2 of the test specimens, respectively, $a_1|_{max}$ and $a_2|_{max}$ are the maximum values recorded by the two accelerometers; $a_{2,Si}|_{max}$ is the normalized maximum acceleration by the corresponding peak hammer force F_{peak} (highlighted by the red box in Figure 6-4) for each specimen (S_i). The letter i represents the specimen number. For example, $a_2',_{S1}|_{max}$ is the maximum acceleration at location #2 of the specimen S1 normalized by the corresponding peak hammer force (F_{peak}), as tabulated in Table 6-3 and Table 6-4. More specifically, R_{a-B1} and R_{a-B2} are used to quantify the effect of RCSBs on impact mitigation throughout the specimens [45, 76]. Indexes R_{m-B1} and R_{m-B2} for the two boundary conditions are used to compare the attenuation performance of the metaconcrete specimen with respect to the plain mortar specimen S1, as used in the previous study [31]. The typical hammer force profiles of the nine specimens with similar maximum amplitudes under two boundary conditions are shown in Figure 6-6.
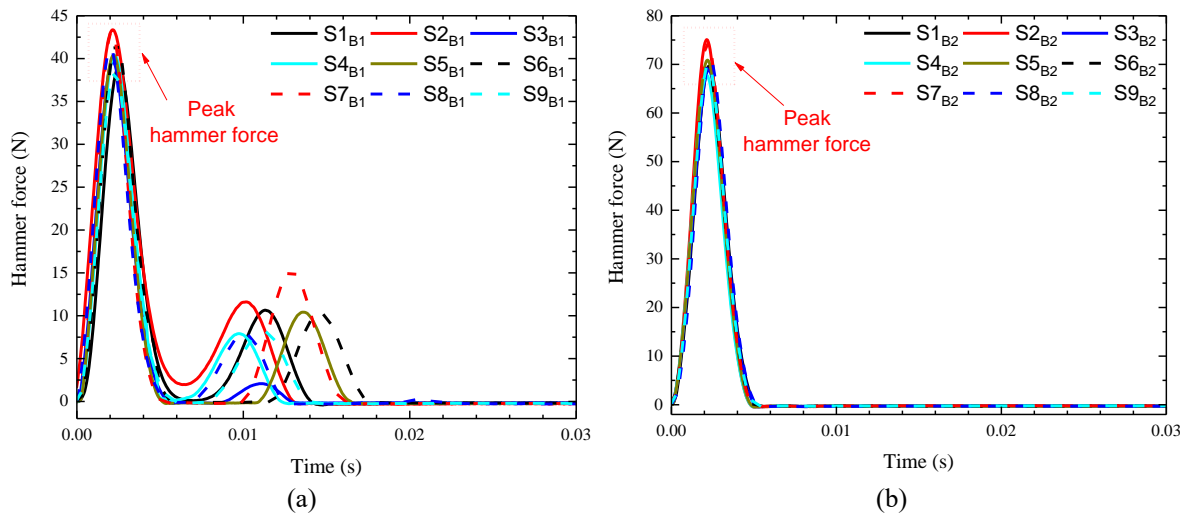
Figure 6-6. Illustration of the typical recorded hammer impact force profiles for nine specimens under two boundary conditions: (a) B1- cantilevered support, (b) B2-clamped support.

As observed, the force profile for the cantilevered boundary condition has a second peak

while the force profile for clamped boundary condition has no obvious second peak, which might be due to the relatively larger rebound vibration causing a second impact of specimens with B1 boundary condition during the tests. It should be noted that this second impact does not affect the evaluation of the vibration, damping and wave attenuation characteristics of the tested specimens.

Table 6-3. Test results for cantilevered specimens.
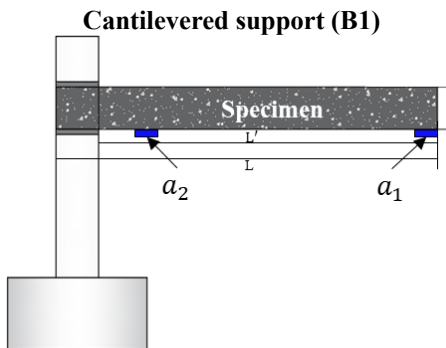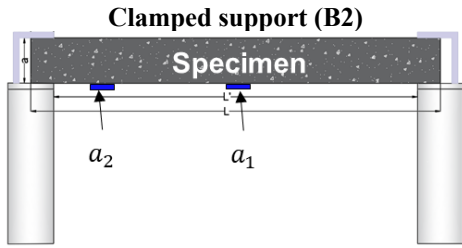
Boundary condition	No.	F_{peak} (N)	$a_1\big|_{max}$ (g)	$a_2\big|_{max}$ (g)	$R_{a\text{-}B1}$	$R_{m\text{-}B1}$
	$S1_{B1}$	39	7.95	4.86	39%	-
	$S2_{B1}$	43.4	10.19	5.29	48%	2.1%
Cantilevered support (B1)	$S3_{B1}$	40	3.85	1.80	53%	73%
	$S4_{B1}$	40.4	3.72	1.60	57%	77%
	$S5_{B1}$	40.2	9.55	4.20	56%	40%
	$S6_{B1}$	41.9	4.32	1.45	66%	82%
	$S7_{B1}$	43	4.26	1.53	64%	81%
	$S8_{B1}$	41	4.64	1.84	60%	75%
	$S9_{B1}$	40.5	4.07	1.58	61%	79%

Table 6-4. Summarized test results for clamp-support specimen.

Boundary condition	No.	F_{peak} (N)	$a_1\big|_{max}$ (g)	$a_2\big|_{max}$ (g)	$R_{a\text{-}B1}$	$R_{m\text{-}B2}$
	$S1_{B2}$	69	5.06	4	21%	-
	$S2_{B2}$	73	5.40	3.90	28%	27%
Clamped support (B2)	$S3_{B2}$	68.8	3.08	2.23	28%	58%
	$S4_{B2}$	69	3.43	1.96	43%	76%
	$S5_{B2}$	70	4.38	2.63	40%	65%
	$S6_{B2}$	69	3.42	1.50	56%	86%
	$S7_{B2}$	74	4.10	2.83	31%	52%
	$S8_{B2}$	71	5.19	2.68	48%	71%
	$S9_{B2}$	70	3.89	1.95	50%	80%

Note: F_{peak} is the peak hammer force; $a_1\big|_{max}$ is the maximum acceleration amplitude recorded by accelerometer #1; $a_2\big|_{max}$ is the maximum acceleration amplitude recorded by accelerometer #2; $a_2'_{,Si}\big|_{max}$ is the maximum acceleration normalized by peak hammer force (i.e., F_{peak}).
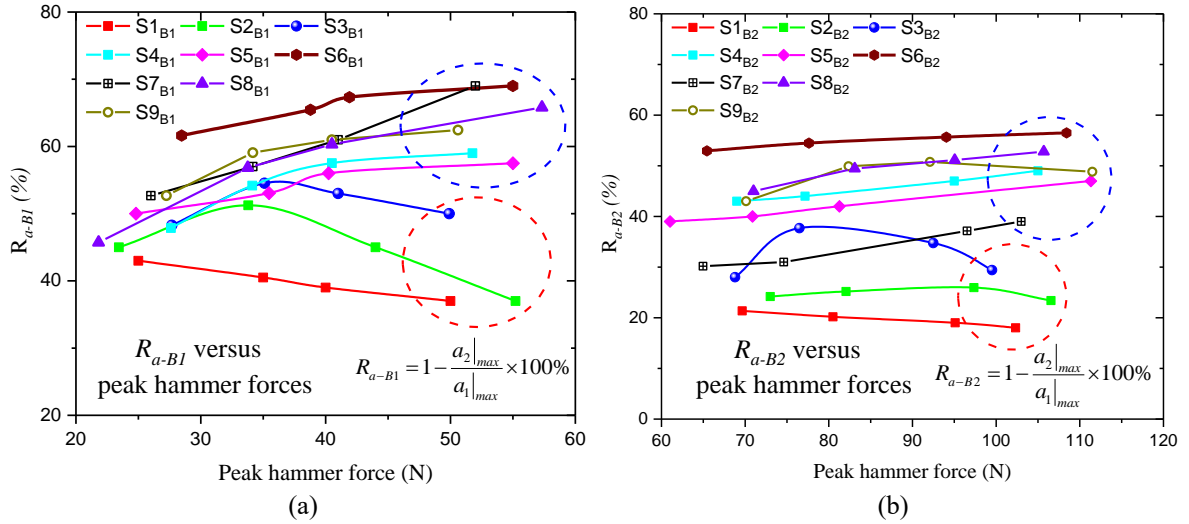
Figure 6-7. (a) Acceleration attenuation ratio (R_{a-B1}) of the cantilevered specimen with respect to peak hammer forces of different amplitudes, (b) Acceleration attenuation ratio (R_{a-B2}) of clamped boundary specimen with respect to peak hammer forces of different amplitudes.

6.4.2.1 Dynamic responses of cantilevered specimens

Influence of different types of inclusions

Four specimens, namely, $S1_{B1}$, $S2_{B1}$, $S3_{B1}$ and $S4_{B1}$ are compared to examine the influence of different inclusions on the cantilever beam. By using Eq. (6-7), the attenuation ratio R_{a-B1} of $S4_{B1}$ is calculated as 57%, as compared to 39%, 48% and 53% of plain mortar beam ($S1_{B1}$), mortar with crushed stones ($S2_{B1}$) and steel balls ($S3_{B1}$), respectively, as tabulated in Table 6-3. Besides, $S4_{B1}$ also is attained the highest R_{m-B1} of 77%, compared to 2.1% and 73% for $S2_{B1}$ and $S3_{B1}$, respectively. It is interesting to note that $S3_{B1}$ with periodic steel balls is only a few percentages lower than $S4_{B1}$ with RCSBs, this is because Bragg scattering and destructive interference existed in the structure took the effect due to periodic changes of the impedance [149]. Because of the co-existence of high wave impedance and wave destructive interference in $S3_{B1}$, the attenuation level found in $S4_{B1}$ is not considerably higher than $S3_{B1}$ subjected to transverse loading with similar amplitudes. To conclude, the $S4_{B1}$ with RCSBs exhibited better vibration and wave mitigation performance than the specimens with non-resonant inclusions such as natural aggregate and steel ball, as the local resonance of RCSBs inside $S4_{B1}$ interacted with the incident waves to mitigate the dynamic response.

Influence of volume fraction

In this section, the performance of specimens with 9.2% (S5$_{B1}$), 18.4% (S4$_{B1}$) and 22.9% (S6$_{B1}$) volume fraction of RCSBs are compared to evaluate the effect of volume fraction. As shown in Table 6-3, the attenuation ratio R_{a-B1} of S4$_{B1}$ is 1% higher than that of S5$_{B1}$, i.e., increasing the volume fraction of RCSBs from 9.2% (S5$_{B1}$) to 18.4% (S4$_{B1}$) only slightly increases the attenuation ratio by 1%. However, R_{a-B1} is increased from 57% to 66% by increasing the volume fraction of RCSBs from 18.4% (S4$_{B1}$) to 22.9% (S6$_{B1}$). These results indicate that attenuation ability is positively correlated to the volume fraction of RCSBs. Similarly, as shown in Table 6-3, increasing the volume fraction of engineered aggregates increases the attenuation performance index R_{m-B1}. The performance index R_{m-B1} are 40%, 77% and 82% respectively for S5$_{B1}$ with a volume fraction of RCSBs of 9.2%, S4$_{B1}$ with a volume fraction of 18.4%, and S6$_{B1}$ with a volume fraction of 22.9%. These results indicate that the attenuation efficiency can be substantially improved when doubling the volume faction of RCSBs as compared to the reference structure (S1$_{B1}$). It is because the mitigation performance is enhanced via waves propagating through more RCSBs when increasing their volume fraction. In conclusion, the out-of-plane vibration attenuation performance can be enhanced by increasing the RCSBs' volume fraction.

Influence of aggregate size

In order to study the effect of aggregate size on the attenuation performance, the attenuation performance of three cantilevered specimens with randomly distributed RCBSs of the same volume fraction but different engineered aggregate sizes, namely S7$_{B1}$ (18 mm-diameter RCSBs), S8$_{B1}$ (22 mm-diameter RCSBs) and S9$_{B1}$ (15 mm-diameter RCSBs), are compared. Among the three specimens, S7$_{B1}$ shows a slightly higher R_{a-B1} value of 64% as compared with that of S8$_{B1}$ of 60% and S9$_{B1}$ of 61%, as tabulated in Table 6-3. In addition, S4$_{B1}$ and S8$_{B1}$ have the same volume fraction of 22 mm-diameter RCSB but the aggregates in S8$_{B1}$ are randomly distributed while they are periodically distributed in S4$_{B1}$. As given in Table 6-3, R_{a-B1} for S8$_{B1}$ is about 3% higher than that for S4$_{B1}$. This is because wave scattering and

reflection in the longitudinal and transverse mode is affected by the distributed aggregates. Other distribution patterns would slightly change the attenuation performances. Moreover, S7$_{B1}$ has a R_{m-B1} value of 81%, which is higher than S4$_{B1}$, S8$_{B1}$ and S9$_{B1}$. It is worth noting that S7$_{B1}$ demonstrates the best attenuation performance while its RCSB size is not the smallest among them. These results indicate that although reducing the size of engineered aggregates while keeping the volume fraction unchanged, i.e., increasing the number of engineered aggregates, enhances the vibration mitigation efficiency, if the aggregate size is smaller than a certain size, further reducing the aggregate size is detrimental to its attenuation efficiency. This is because reducing the RCSB size inevitably reduces the size of the steel core; a small steel core has less ability to trap sufficient wave energy, leading to the reduction in attenuation efficiency [88]. For instance, the RCSBs of S9$_{B1}$ might not be fully activated as they are over-compacted, which made the attenuation effectiveness less prominent. Further study on the influence of RCSB size and optimal volume percentage of RCSBs is deemed necessary. To conclude, the attenuation capacity of the specimen is generally enhanced when adding more numbers of RCSBs with smaller size when the RCSB size is not smaller than an optimal value; when the aggregate size is smaller than the optimal value, further reducing the size of RCSBs has a negative effect on vibration mitigation efficiency.

Influence of hammer force

As reported in the previous study [31], a metaconcrete beam specimen is more effective in mitigating the longitudinal stress wave propagation when subjected to impulsive loading with higher intensity because high-intensity loading can more effectively activate the local vibrations of the hard cores of engineered aggregates, hence convert more loading energy to kinetic energy of local vibrations. Besides attenuation of longitudinal stress wave propagations, the dynamic response of metaconcrete structures under different transverse loading intensities has not been investigated. To investigate the influences of engineered aggregates on dynamic responses, experimental tests with the peak hammer forces ranging from 20N-60N are conducted. The R_{a-B1} values for S1$_{B1}$-S9$_{B1}$ versus different loading

intensities are presented in Figure 6-6(a). As shown, the metaconcrete cantilever specimen with RCSBs (i.e., $S4_{B1}$-$S9_{B1}$) achieves more significant attenuation in terms of acceleration responses than the cantilevered beam with other aggregates, especially when the hammer force is relatively large. Moreover, the attenuation ratio of the metaconcrete cantilever specimen increases with peak hammer impact force while the cantilever with other types of aggregates may decrease as shown in Figure 6-7(a) (highlighted by the blue circle). This is because the local resonance effect depends on the relative motion between the resonant inclusion (i.e., steel core) and the mortar matrix. Increasing loading intensity causes larger deformation of the beam and enlarged the relative movement of RCSBs. Hence, a higher proportion of mechanical energy in the system is transferred to the kinetic energy of the steel core inside RCSBs as well as the internal energy of rubber coating. Therefore, the percentage in response reduction of metaconcrete cantilever specimen is higher under the higher intensity of traverse loading, which is similar to the performance of metaconcrete structure in mitigating longitudinal stress wave propagations reported in the previous study [31]. In contrast, the attenuation performance generally weakened for $S1_{B1}$ with the rising loading intensity. This is because $S1_{B1}$ is a uniform specimen that there is no other mechanism to attenuate energy other than geometric attenuation, therefore, the attenuation percentage is smaller when the input energy is higher. The attenuation level of $S2_{B1}$ and $S3_{B1}$ increased first but reduced after reaching a certain loading threshold, as highlighted by the red circle in Figure 6-7(a). The initial rising of attenuation percentage may be because of wave scattering and reflection. To conclude, the cantilevered metaconcrete specimens illustrate an enhanced attenuation performance when increasing the loading intensity.

6.4.2.2 Dynamic responses of clamp-supported specimens

Influence of different types of inclusions

The damping and dynamic response of the cantilevered specimen have been presented in Sections 6.4.1 and 6.4.2.1. In a previous study, Guo et al. [150] numerically investigated the effect of boundary conditions on wave propagation in a periodic compound plate and reported

that the attenuation of wave propagation is sensitive to the boundary conditions as well as the number of locally resonant cells in the structure. Likewise, Raghavan and Phani [149] revealed the effect of boundary conditions on the Timoshenko beam with periodic masses and resonators. However, no experimental study investigating the effect of boundary conditions on the response of metaconcrete beam structure with locally resonant aggregates subjected to transverse loading has been reported in the literature yet. To investigate the influences of different boundary conditions on dynamic responses of metaconcrete beam specimens, the beam specimens with clamped boundary conditions are impact tested. As shown in Figure 6-3(b), the specimen is clamped at two ends and impacted at the mid-span. Four clamp-supported specimens $S1_{B2}$, $S2_{B2}$, $S3_{B2}$ and $S4_{B2}$, are compared to examine the influence of specimen containing different inclusions. As shown in Table 6-4, $S4_{B2}$ has the attenuation ratio R_{a-B2} of 43%, which is higher than $S1_{B2}$ of 21%, $S2_{B2}$ of 28% and $S3_{B2}$ of 28%. Similarly, $S4_{B2}$ exhibited the highest value of R_{m-B2} of about 76%, which is much higher than $S3_{B2}$ (58%) and $S2_{B2}$ (27%). $S4_{B2}$ shows the highest reduction percentage of the acceleration responses among these four specimens with the same boundary condition subjected to the similar peak hammer force input (i.e., F_{peak}).

Comparing R_{a-B1} and R_{a-B2} in Table 6-3 and Table 6-4, it shows that the value of R_{a-B2} is, in general, lower than the value of R_{a-B1}, indicating a lower attenuation level for a clamp-supported specimen than the cantilevered specimen. The primary reason is that the effective distance (i.e., the distance between the two measurement locations) in a clamp-supported specimen is much shorter than that of a cantilevered one, hence, the number of RCSBs between the two locations are less excited compared to that between the two locations in the cantilevered specimen, therefore, leading to less effective attenuation performance. A more detailed discussion about the influence of boundary conditions is summarized in Section 6.4.3. In conclusion, $S4_{B2}$ with RCSBs under clamp-supported condition demonstrates a better attenuation performance than the specimens with non-resonant inclusions in the same boundary condition.

Influence of volume fraction

In this section, the performances of specimens with three-volume fractions of RCSBs, namely, 9.2% ($S5_{B2}$), 18.4% ($S4_{B2}$) and 22.9% ($S6_{B2}$) with the clamp-supported condition are compared. As given in Table 6-4, R_{a-B2} increases from 40% ($S5_{B2}$) to 56% ($S6_{B2}$) with the increasing volume fraction. $S6_{B2}$ also has the highest R_{m-B2} value of 86% as it contains the highest volume fraction of RCSBs among the three specimens. Thus, a higher volume fraction of RCSBs can enhance the attenuation magnitude of metaconcrete beam with clamped boundary condition. As shown in Table 6-4, $S6_{B2}$ presents the highest reduction percentage of acceleration responses, indicating a better mitigation capacity. Besides, it is observed that the clamp-supported specimen has less significant attenuation performance (i.e., R_{a-B2}) than the respective cantilevered specimen (i.e., R_{a-B1}). In conclusion, increasing the volume fraction of RCSBs could positively influence the attenuation capacity of the metaconcrete specimen.

Influence of aggregate size

To determine the effect of aggregate size, four clamp-supported specimens, namely, $S4_{B2}$, $S7_{B2}$, $S8_{B2}$ and $S9_{B2}$ subjected to similar peak hammer forces are compared. As presented in Table 6-4, R_{a-B2} increases from 43% for $S4_{B2}$ to 50% for $S9_{B2}$. Regarding the R_{m-B2}, $S9_{B2}$ has the highest value of 80% among the four specimens as $S9_{B2}$ has the highest volume fraction of RCSBs despite the aggregate size being the smallest. It is interesting to observe that $S7_{B2}$ has a lower reduction percentage than $S4_{B2}$, which illustrates a different trend from the cantilevered specimens. This might be caused by the insufficient number of 18 mm RCSBs between the two measurement locations in $S7_{B2}$. Compared to the cantilevered specimen, the distance between the two accelerometers in the clamp-supported specimen is much shorter. In other words, the number of RCSBs to interact with the incident waves within the distance between the two measurement locations is less. As a result, only a smaller number of RCSBs could absorb loading energy between the two measurement locations, thereby being detrimental to the attenuation effect.

Influence of hammer force

In this section, hammer forces with an intensity ranging from 60N-120N are applied to the clamp-supported specimens. It is noted that the flexural stiffness of the clamp-supported beam specimen is much higher than that of the cantilevered one; therefore, a higher intensity of hammer force is required to excite the specimen. R_{a-B2} values for nine specimens versus different loading intensities are depicted in Figure 6-7(b). The attenuation ratio (i.e., R_{a-B2}) of metaconcrete specimens increases slightly when increasing hammer force as shown in Figure 6-7(b) and highlighted by the blue circle. The local resonance of RCSBs could help to reduce the response of specimens under higher intensity loading, which is similar to the observations discussed in Section 6.4.2.1. On the other side, attenuation level decreases for $S1_{B2}$ and $S2_{B2}$ as highlighted in Figure 6-7(b) by the red circle because there is no existence of RCSBs or local resonance effect within those specimens. It is interesting to note that the attenuation percentage for $S3_{B2}$ increased initially and then decreased when further increasing the loading intensities. This might be because the periodic distribution enabled steel ball to effectively interact with incident wave due to wave scattering and wave impedance. Due to the lack of viscoelastic coating layer, and no local resonance effect, the attenuation is only attributed to the geometric spreading as discussed above and thereby leading to the reduction in attenuation percentage when the hammer force increased to a higher level. To conclude, the clamp-supported metaconcrete beam with RCSBs generally achieved a better attenuation performance with the increased loading intensity, but due to the absolute attenuation value associated only with geometric spreading remains almost unchanged, the opposite observation on the attenuation percentage can be drawn for the specimens without RCSBs.

6.4.3 Influences of boundary conditions on the attenuation performance

Metaconcrete beam specimens with the two considered boundary conditions in this chapter show the same attenuation trend, but different attenuation levels as presented in Section 6.4.2. As shown in Figure 6-7(a) and (b), the clamp-supported specimens have generally lower attenuation percentages than the respective cantilevered specimens, i.e., $R_{a-B2} < R_{a-B1}$. Two

reasons are accounted for this observation. Firstly, the activation of local resonance of RCSBs relies on the relative motion between the cement matrix and RCSBs. The clamp-supported specimen is harder to be excited due to its higher flexural stiffness than the cantilevered specimen, resulting in lower relative motion and less effectiveness in using RCSBs. Secondly, Guo et al. [150] found that the effect of the bandgap on wave propagation depended on the number of local resonators. In this chapter, the distance between two accelerometers for the clamp-supported specimen is shorter than that of the cantilevered one, which indicates waves passing less number of RCSBs, leading to a lower attenuation level. Therefore, the attenuation efficiency of the metaconcrete specimen depends on the vibration level of the specimen, which in turn depends on the boundary condition of the structure, and the volume fractions of engineered aggregates.

6.5 Bandgap characteristics

In the previous studies [25, 30, 31, 83], the bandgap characteristics of metaconcrete structure for longitudinal wave propagations are reported, while its bandgap characteristics for transverse wave propagations have not been investigated yet. In addition, the influences and contributions of bandgaps on the out-of-plane responses of the metaconcrete structure are unknown. Since bandgap characteristics are related to the wave filtering and attenuation mechanism of the metaconcrete structure, it is essential to understand the bandgap characteristics for a better explanation of the experimental observations. In this section, the bandgap characteristics of the tested specimens are investigated through numerical simulations by using *COMSOL Multiphysics*.

6.5.1 Model calibration

The numerical model is built by using *COMSOL Multiphysics* and calibrated with the available testing data reported by Ma et al. [53]. Ma et al. [53] tested the three-dimensional locally resonant metamaterial, which is made of six locally resonant units. Each unit consisted of a silicone-coated steel cylinder core and epoxy matrix. It has been reported that

this epoxy-based meta-rod structure is capable of suppressing flexural wave propagation within the bandgap. A numerical model of the specimen tested by Ma et al. [53] is built, which is a meta-rod consisting of six units of a steel core with a silicone rubber coating in the epoxy matrix. The rod is placed on top of the excitation plate. The transverse excitation (inwards prescribed acceleration of amplitude 1 m/s^2) is applied onto the excitation plate along the transverse direction. Table 3-2 and Table 3-3 present more information about the geometric and material parameters used in the simulation. The model is meshed by solid quadratic tetrahedral elements with a minimum element size of 0.6 mm after conducting a mesh convergence test. More detailed information about model calibration can refer to the study conducted in Chapter 3 and Chapter 4, which investigates the bandgap properties of meta-rod structure under longitudinal excitations.
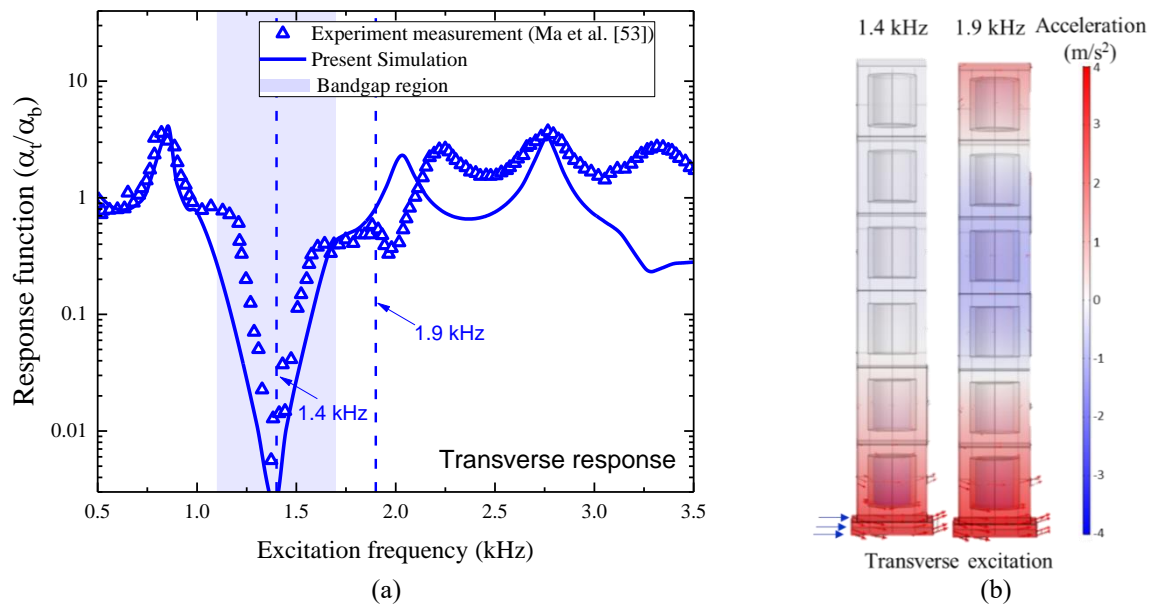
Figure 6-8. (a) Comparison of numerical predictions and experimental results by Ma et al. [53], (b) Acceleration response contour.

The response function as illustrated in Figure 6-8(a) is gained by plotting the ratio of acceleration at the top of the rod to that at the bottom (e.g., a_t/a_b) versus the excitation frequencies. It demonstrates an obvious response dip at the frequency range from 1.1 kHz to 1.7 kHz (shaded area), whereas no response dip occurs outside this frequency region. Therefore, when the excitation frequency is 1.4 kHz within the bandgap region, the response

on the top of the specimen is significantly attenuated, as shown in Figure 6-8(b) (left). In contrast, the specimen response at the top is not effectively mitigated, i.e., Figure 6-8(b) (right) when the excitation frequency is 1.9 kHz outside the bandgap region. Although there are some noted discrepancies between the numerical and the experimental results possibly due to the slightly different supporting conditions between simulation and experiments, the results obtained from the numerical model can reasonably predict the transverse responses of meta-rod structure and derive the bandgap for transverse responses.

6.5.2 Modelling bandgap characteristics of metaconcrete specimen

With the calibrated model, bandgap characteristics of four specimens (i.e., $S1_{B1}$, $S4_{B1}$, $S7_{B1}$ and $S9_{B1}$) are numerically studied. The geometric and material parameters used in the simulation are tabulated in Table 6-1 and Table 6-5, respectively. Similar to the numerical modelling in Chapter 3 and Chapter 4, the response function, defined as the ratio of the top to the bottom lateral acceleration responses, versus sweeping frequencies up to 9.6 kHz are computed for the four specimens. It is noted that $S1_{B1}$ served as the reference for comparison, which is expected to have no bandgap. Due to different configurations of RCSBs embedded in $S4_{B1}$, $S7_{B1}$ and $S9_{B1}$, different bandgap widths or the attenuation zone in the frequency domain are expected. It is worth noting that there have been two commonly used methods to obtain the bandgap of LRMs i.e., dispersion relation analysis (wave dispersion property in the medium) and wave transmission ratio/coefficient or response function (wave attenuation performance) [31, 44, 53, 74], where later method is adopted in the present numerical study. Figure 6-9 shows the schematic configuration of the finite element (FE) model. To reveal the bandgap characteristics, the model can be simplified by placing mortar and metaconcrete specimens on the excitation plate with the prescribed acceleration input along the transverse direction, as illustrated in Figure 6-9. This method by considering wave attenuation performance has been applied in other studies [74, 107]. Moreover, the distributions of RCSBs for specimens such as $S7_{B1}$ and $S9_{B1}$ in the FE model are randomly generated by keeping the identical dimension and volume fraction, but the exact locations of RCSBs may

not be the same as those in the tested specimens.
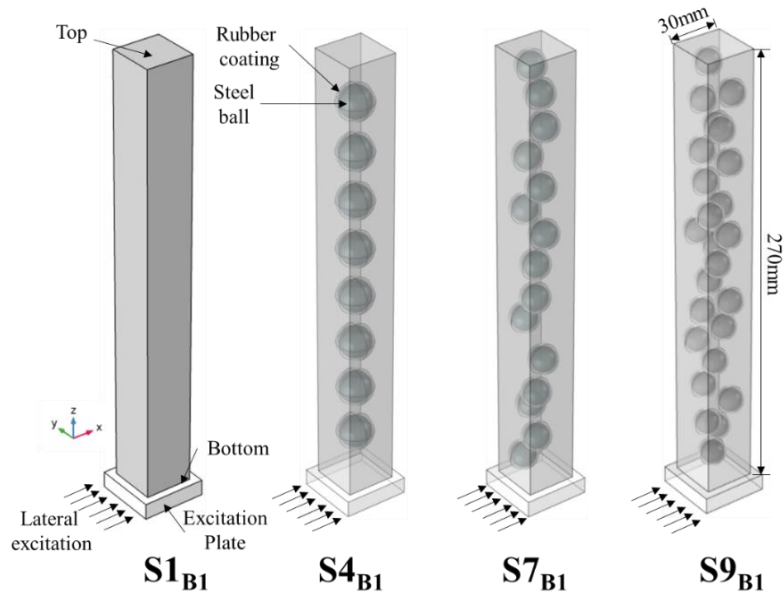
Figure 6-9. Finite element models of S1$_{B1}$, S4$_{B1}$, S7$_{B1}$ and S9$_{B1}$ under transverse excitation.

Table 6-5. Material properties in the numerical model.

Material	Parameters	Value
Mortar	Mass density	2,200 kg/m^3
	Young's modulus	29.6 GPa
	Poisson's ratio	0.2
Steel ball	Mass density	7,850 kg/m^3
	Young's modulus	210 GPa
	Poisson's ratio	0.3
Rubber [131]	Mass density	1,000 kg/m^3
	A	0.49755889 MPa
	B	0.10932788 MPa
	Poisson's ratio	0.495

6.5.3 Results and discussions

In this section, the amplitude ratio (AR) spectrum of the metaconcrete specimens and mortar specimen are derived from the test data and compared to study the attenuation mechanism. AR spectrum is defined as the ratio between output and input signals, such as acceleration responses in the frequency domain, which is often used to interpret the attenuation mechanism [29, 83]. Moreover, two steps are involved in computing the AR spectrum. The first step is to transform the time-domain acceleration responses obtained from two accelerometers into the frequency domain (i.e., $a_1(f)$ and $a_2(f)$) by using FFT. Then, the AR spectrum can be computed by Eq. (6-9) [29, 83].

$$AR = 20 \times \log(\frac{a_2(f)}{a_1(f)})$$

<div align="right">(6-9)</div>

It is worth noting that the AR spectrum is used to evaluate the attenuation performance in the frequency domain as well as to study the local resonance mechanism; it is different from the performance parameter $R_{a\text{-}B1}$ concerning attenuation in the time-domain response. Besides, the shaded region labelled in the AR spectrum (e.g., Figure 6-10(a), Figure 6-11(a) and Figure 6-11(b)) representing the bandgap or the attenuation zone are derived from the test data. A negative AR value in the frequency band indicates significant attenuation due to the local resonance effect.

The AR spectrum based on Eq. (6-9) is calculated to find the attenuation band by using the experimental results. The AR spectrum in the frequency range from 0 kHz to 9.6 kHz are plotted. It is noted that the spectrum range derived from the FFT method is correlated to the sampling rate in the test. As the sampling rate in the test is 19.2 kHz, half of the sampling rate is adopted for the AR spectrum's frequency range [144]. The shaded parts in the figures represent the estimated bandgap or the attenuation band as shown in Figure 6-10 and Figure 6-11. In comparison with the reference structure $S1_{B1}$, it can be found that the response of metaconcrete specimens ($S4_{B1}$, $S7_{B1}$ and $S9_{B1}$) are attenuated within the prescribed bandgap, as shown in Figure 6-10 and Figure 6-11. Moreover, when the frequency is outside the bandgap, there is no apparent response dip or sudden drop of spectral amplitude in the metaconcrete specimens. In addition, Figure 6-10(a) presents the comparison of AR spectra for $S1_{B1}$ and $S4_{B1}$ based on experimental results. An apparent response dip of the AR curve only appeared in $S4_{B1}$ (colored in green), whereas it did not occur in $S1_{B1}$ (colored in red). Additionally, there is an apparent frequency band between 2.4 kHz and 3.4 kHz corresponding to the large dip in numerical response function as shown in Figure 6-10(b), which confirmed an attenuation occurred at the predicted bandgap region.
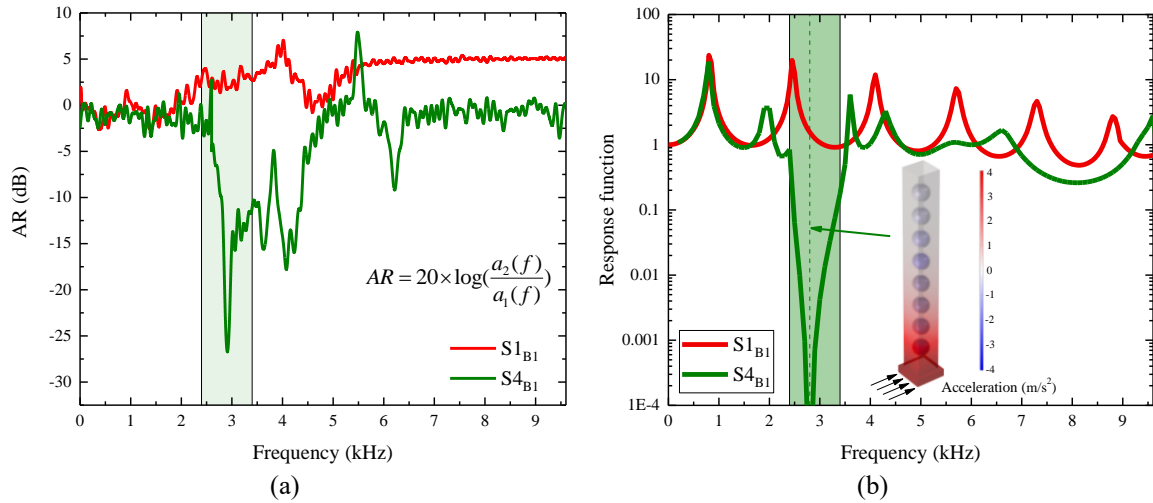
Figure 6-10. Comparison of bandgap region between test results and numerical prediction for S1$_{B1}$ and S4$_{B1}$: (a) AR spectrum for S1$_{B1}$ and S4$_{B1}$, (b) Comparison of the numerical response function of S1$_{B1}$ and S4$_{B1}$.

Likewise, the bandgap for S7$_{B1}$ has a frequency range from 6.88 kHz to 7.6 kHz, as shown by the red shaded region in Figure 6-11(a) and (c), where the bandgap derived from experimental results matched well with the numerical response function. Figure 6-11(b) and (d) show the identical bandgap of S9$_{B1}$ ranging from 8.38 kHz to 9.1 kHz in the blue shaded region. Moreover, the response contours at frequency bandgap for S4$_{B1}$, S7$_{B1}$ and S9$_{B1}$ are respectively depicted in Figure 6-10(b), Figure 6-11(c) and Figure 6-11(d). As shown, when the excitation frequency is within the bandgap region, particularly at the response dip, the response at the top of specimens is significantly attenuated, which confirmed the contribution of the bandgap to the attenuation. In conclusion, the response dips are observed at the prescribed bandgap for the specimen with RCSBs according to the calculated AR spectrum (i.e., Figure 6-10(a), Figure 6-11(a) and Figure 6-11(b)), and spectral amplitude is substantially reduced in the corresponding bandgap. The bandgap predicted from the numerical model is in good agreement with the attenuation band from experimental results. The numerical results verify the existence of such bandgaps, as shown in Figure 6-10 and Figure 6-11 for transverse responses. Thus, it can be concluded that the effectiveness of adding RCSBs to the vibration attenuation of structures can be attributed to the local resonance.
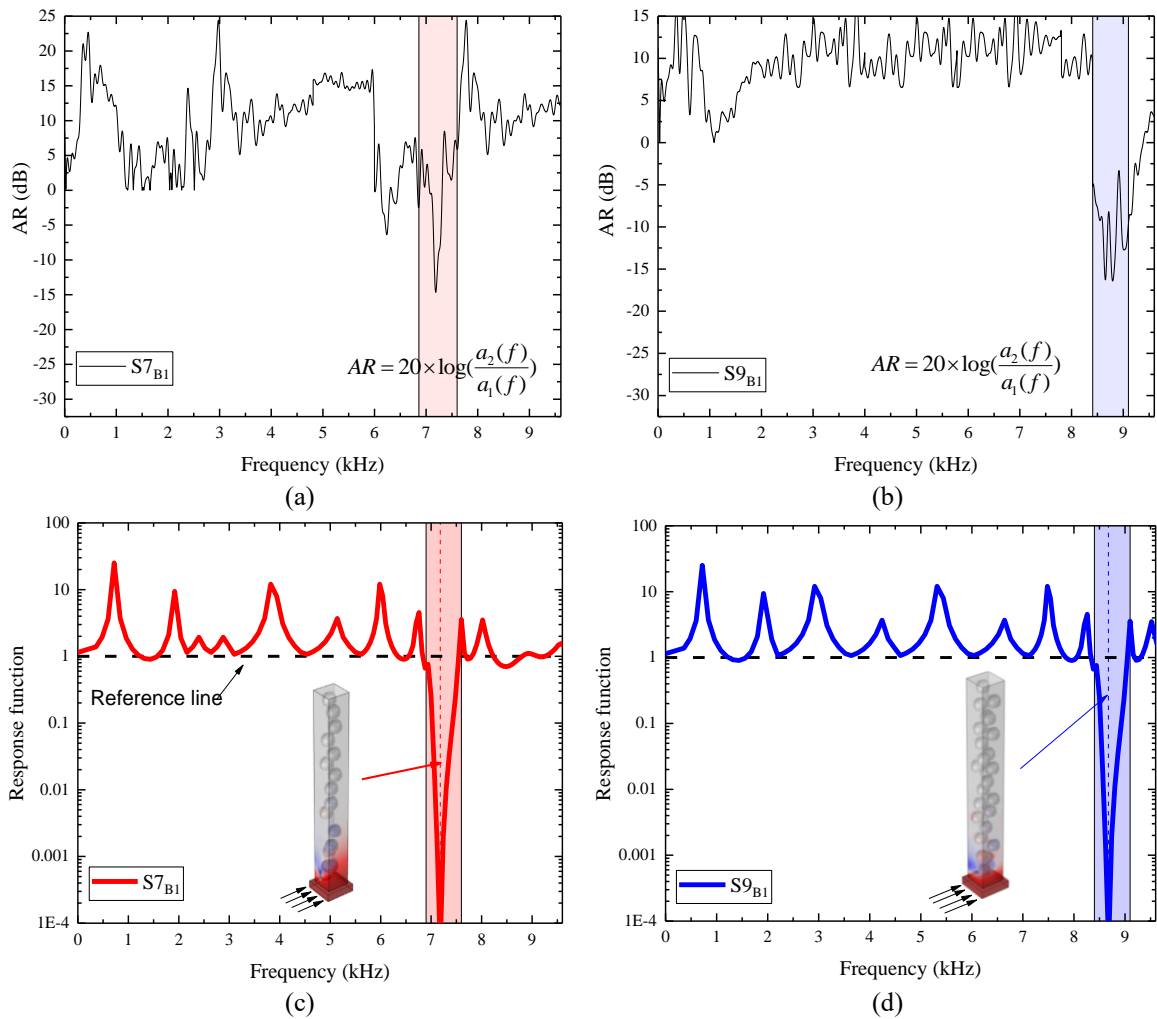
Figure 6-11. Comparison of bandgap region between test results and numerical predictions for $S7_{B1}$ and $S9_{B1}$: (a) AR spectrum for $S7_{B1}$, (b) AR spectrum for $S9_{B1}$, (c) Numerical response function of $S7_{B1}$, (d) Numerical response function of $S9_{B1}$.

6.6 Summary

This chapter investigates the damping properties and out-of-plane dynamic responses of cementitious metaconcrete specimens with resonant RCSBs. For comparison, similar specimens with non-resonant inclusions of natural and steel ball aggregates are also studied. The metaconcrete specimens with different aggregate configurations by considering three volume fractions of RCSBs (i.e., 9.2%, 18.4% and 22.9%), three sizes of RCSBs (i.e., 22 mm, 18 mm and 15 mm) and two boundary conditions are prepared and tested. The following conclusions can be drawn.

(1) Specimen with resonant aggregates (i.e., RCSBs) has a higher equivalent damping ratio and better attenuation capacity than plain mortar specimen and specimen with non-resonant inclusions (e.g., natural aggregates and steel balls). The equivalent damping ratio of metaconcrete specimen can substantially increase up to 96% as compared with the normal concrete structure in this chapter.

(2) The increasing volume fraction of RCSBs leads to a higher attenuation percentage and a higher equivalent damping ratio. The equivalent damping ratio could increase by 20.9% when the RCSBs volume fraction increased from 9.2% to 22.9%.

(3) Specimens with similar RCSB volume fractions but the smaller aggregate size and more numbers of RCSBs are more effective for the attenuation of dynamic response.

(4) The attenuation level of the metaconcrete specimen is more prominent as the intensity of excitation force is increased because it could more effectively activate the local vibrations of solid cores in RCSBs.

(5) The attenuation performance of the metaconcrete specimen is sensitive to the boundary condition. The cantilevered specimen shows better attenuation performance than the clamp-supported one owing to the relatively larger responses of the cantilever specimen which induced larger local vibrations of RCSBs, and also because of less number of RCSBs within the effective distance between the two response measurement locations for the clamp-support specimens than the cantilevered specimens in the present tests.

(6) The bandgap characteristics of metaconcrete specimens are derived experimentally and numerically. Both experimental and numerical simulation results verify the existence of the bandgap and the contributions of local resonance to the attenuation of the dynamic response of metaconcrete structures under transverse loading.

Chapter 7 Static mechanical properties and stress wave attenuation of metaconcrete subjected to impulsive loading

7.1 Introduction

Previous numerical studies [89] have demonstrated that metaconcrete structure composed of a conventional configuration of engineered aggregates (EAs) could reduce the compressive and spalling strengths due to the existence of soft coating despite its excellent capability in mitigating wave propagations [151-153]. To enhance the strength of metaconcrete specimens whilst keeping its wave-filtering capability, engineered aggregates with a relatively stiff layer outside the soft coating are developed. Three types of inclusions including rubber-coated steel balls (RCSBs), 18 mm rubber-coated steel balls with the enhanced coating (ERCSBs/18) and 15 mm rubber-coated steel balls with enhanced coating ERCSBs/15 are fabricated, and they are randomly dispersed in cementitious mortar to fabricate metaconcrete specimens. Mechanical properties of plain mortar, concrete and metaconcrete specimens with EAs (i.e., RCSBs and ERCSBs) under quasi-static loading and their dynamic responses under destructive and non-destructive tests are examined and reported. Meanwhile, the influences of adding an enhanced layer outside RCSBs on the performance of metaconcrete specimens are assessed. The frequency spectra obtained from the non-destructive test data are processed to verify the existence of frequency-dependent wave-filtering capacity of metaconcrete specimens. After that, the attenuation mechanism of the metaconcrete specimens with newly proposed ERCSBs is revealed. Furthermore, the effectiveness of the metaconcrete specimens in mitigating stress wave propagations induced by different impulsive loading profiles is investigated. The failure process and failure modes for all configurations under destructive tests are compared and discussed.

The related work in this chapter has been published in Engineering Structures.

7.2 Experimental program

7.2.1 Specimen preparation

In the experiment, all specimens can be classified into two groups: mortar-based and concrete-based specimens, the configuration of specimens is schematically illustrated in Figure 7-1. S-S1 is made by plain mortar only. S-S2, S-S3 and S-S4 are made of cementitious mortar with 10.6% volume fraction of engineered aggregates (EAs). S-S5 is composed of cementitious mortar and natural aggregates (NAs) of 41.8% in volume. S-S6 and S-S7 consisted of mortar, natural and engineered aggregates. S-S6 contains 31.2% of NAs together with 10.6% of ERCSBs/18. S-S7 includes 31.2% of NAs and 10.6% of ERCSBs/15. Namely, the total volume percentage of aggregates (including NAs and EAs) remains 41.8%, while a proportion of natural aggregates (10.6% in total volume) are replaced by respective EAs. To fabricate mortar-based specimens, high strength mortar is utilized as the matrix of metaconcrete specimens. The mortar consisted of Portland cement, fine sand and additives (calcium alumina-sulphate) [124]. The use of high-strength mortar is to provide sufficient strength and avoid potential damage under non-destructive impulsive loading; hence the enhancement of stress wave attenuation as compared with the plain mortar is mainly due to the local resonance mechanism instead of material damage. The mix ratio of cement/sand/water/additives is 1/2/0.5/0.33. The mix proportions are detailed in Table 7-1. Natural aggregates with a maximum size of 10 mm and bulk density around 1522 kg/m^3 (in accordance with [154]) are used in the plain concrete mix. Natural aggregates in combination with engineered aggregates are adopted for concrete-based metaconcrete specimens. When the diameter of a cylindrical specimen is at least three times the maximum size of the natural aggregate, the heterogeneity owing to the existence of aggregates can be neglected in

dynamic impact tests [155]. In this chapter, the diameter of the specimen (i.e., 100 mm) is five times the maximum aggregates size (i.e., 20 mm EAs), therefore the heterogeneity effect under dynamic tests can be neglected.
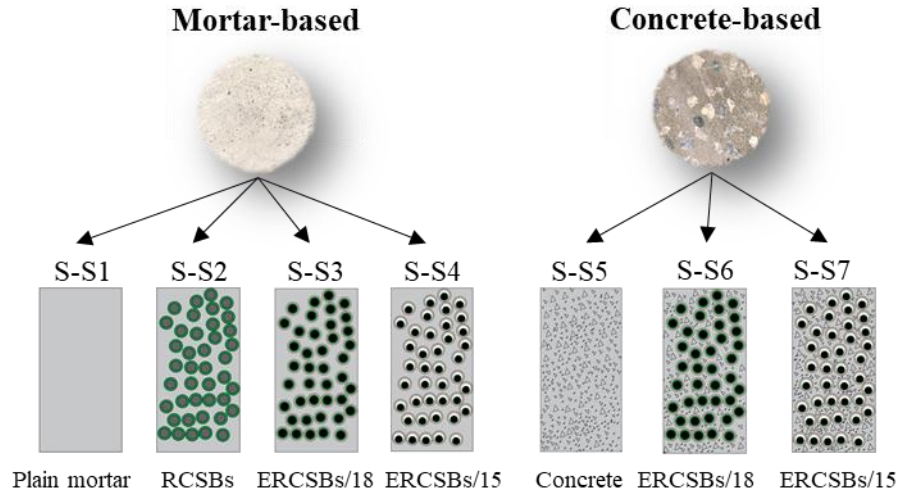
Figure 7-1. Specimen classification.

Three types of engineered aggregates (EAs) are utilized to cast metaconcrete specimens including RCSBs (rubber-coated steel balls) and two types of ERCSBs (RCSBs enclosed in a steel shell), i.e., ERCSBs/18 and ERCSBs/15. All EAs are designed to have an identical overall size of 20 mm in diameter. The configuration details of EAs, namely RCSBs and ERCSBs are given in Table 7-2. Conventional RCSBs are made of steel balls coated with silicone rubber. The dome-shaped rubber coating is prepared by using the moulding technique [151]. The steel ball is then encapsulated by the upper and lower dome-shaped rubber coating, followed by a curing process to form RCSBs. ERCSBs is made by enclosing RCSB with steel shell. Lazar-welding is used to seal steel shell for each ERCSB. Specifically, ERCSBs/18 is made of 18 mm RCSBs with an additional 1 mm-thick steel shell. Besides, inspired by the granular dampers [156-158] and nonlinear spherical pendulum resonator [159], ERCSBs/15 is made by enclosing the RCSB inside a larger steel shell with a gap clearance, i.e., 15 mm diameter RCSB enclosed inside a 20 mm-diameter steel shell. Since the thickness of the steel shell is 1 mm for ERCSBs/15, there is a 3 mm clearance between the steel shell and the RCSB. Under dynamic loading, the RCSB can move inside the steel

shell, which also could attract a certain amount of energy induced by the dynamics loading, besides the oscillation of the steel core in conventional EA. Therefore, this type of EA is expected to dissipate the considerable amount of energy via the combination of the motion-caused collisions, sliding and rolling between the inner inclusions and shell walls as well as local vibration of the solid core.

The metaconcrete specimens are cast in accordance with ASTM C192/C192M-19 [160] using different inclusions such as RCSBs, ERCSBs/18 and ERCSBs/15. Besides, the attenuation mechanism of metaconcrete mainly relies on the local resonance effects of EAs instead of Bragg scattering. Since metaconcrete material with randomly distributed EAs tends to be more practical in engineering applications [29], all inclusions (e.g., RCSBs and ERCSBs) are dispersed randomly rather than regular deposition in the cementitious mortar when casting. As listed in Table 7-3, a total of forty-two cylinders (i.e., six cylinders per configuration) with a height of 200 mm and a diameter of 100 mm are prepared. Plain mortar specimen (S-S1) with 0% EAs is regarded as the reference. In addition, S-S2, S-S3 and S-S4 are fabricated to evaluate the effect of different embedded inclusions on the performance of metaconcrete specimens. Concrete-based specimens (i.e., S-S5 to S-S7) are designed to mix EAs in combination with natural aggregates. Detailed information on the mix proportions, specimens and configuration of EAs is given in Table 7-2 and Table 7-3, respectively. A steel rod is used to ram the specimen to minimize the voids during casting. ASTM C192/C192M-19 [160] is followed for the specimen curing.

Table 7-1. Mix proportions.

Type	Water (kg/m³)	Cement (kg/m³)	Sand (kg/m³)	NA[b] (<10mm) (kg/m³)	EA[c] (kg/m³)	Additive[d] (kg/m³)
Mortar	204	408	816	-	-	136
Plain concrete	204	408	816	863	0	136
Metaconcrete [a]	204	408	816	554	637	136

Note: ^a: concrete-based metaconcrete specimens; ^b: 41.8% volume fraction of natural aggregates (NAs) in plain concrete; ^c: NAs (10.6% in total volume) are replaced by EAs in concrete-based metaconcrete specimens. ^d: Calcium alumina-sulphate is used as the additive.

7.2.2 Test setup

7.2.2.1 Quasi-static test

The quasi-static compressive test is conducted by using a MATEST testing machine. The test setup is shown in Figure 7-2. For the compressive test, three $\emptyset 100 \times 200$ mm surface-grinded cylinders per configuration are tested with a loading rate of 0.33 MPa/min following the ASTM C39/C39M-21 guide [161] with the equivalent strain rate of $10^{-4}\,\text{s}^{-1}$.

Figure 7-2. Quasi-static compression test setup (SG: strain gauge).

Modulus of elasticity and Poisson's ratio are determined based on the guidelines [162]. The longitudinal strain is measured by using the longitudinal strain gauge SG1 attached to the specimen, as shown in Figure 7-2. To measure the transverse strain, another strain gauge SG2 with a length of 50 mm is attached perpendicularly to the direction of compression at the middle of the specimen. The reported results are the mean values of three identical specimens. The values of modulus of elasticity and Poisson's ratio can be calculated as follows [162]:

$$E = (S_2 - S_1) / (\varepsilon_2 - 0.000050) \qquad (7\text{-}1)$$

where E is chord modulus of elasticity in MPa; S_2 is the stress corresponding to 40% of ultimate load; S_1 is the stress in MPa corresponding to a longitudinal strain ε_1 of 0.000050

and ε_2 is the longitudinal strain produced by stress S_2.

$$\mu = (\varepsilon_{t2} - \varepsilon_{t1}) / (\varepsilon_2 - 0.000050) \qquad (7\text{-}2)$$

where μ is Poisson's ratio; ε_{t2} is the transverse strain at mid-height of the specimen produced by stress S_2, and ε_{t1} is the transverse strain at mid-height of the specimen produced by stress S_1.

7.2.2.2 Dynamic test

In this chapter, two types of dynamic tests including non-destructive Figure 7-3(a)) and destructive tests (Figure 7-3 (b)) are carried out. All the dynamic tests are conducted as consistently as possible by using a testing apparatus composed of striker bar, bar I, bar II and bar III with a diameter of 100 mm as well as the buffer system, as shown in Figure 7-3. The bars are made of stainless steel with Young's modulus (E_{bar}) of 210 GPa [126]. It is worth noting that the purpose of using this apparatus is not to obtain dynamic material properties, instead, it is to examine the effectiveness in mitigating stress wave propagation of the metaconcrete specimens.

Under the non-destructive test, the impulsive load of the test is generated by manually sliding bar III as a striker to impact bar II, as demonstrated in Figure 7-3(a). Two 5 mm strain gauges (i.e., SG2 and SG3) are installed near the front and rear surface of the specimen to record the signal, i.e., 30 mm and 170 mm from the incident surface of the specimen, respectively. It is worth noting that when measuring the mechanical properties (e.g., compressive strength) the strain gauge should be long enough. However, the dynamic test conducted in this Chapter intends to investigate the stress wave propagation in the designed specimens rather than its mechanical properties. Long strain gauge is not required and the strain gauge with similar gauge lengths to the study of concrete materials [108] and metamaterials [31] have been applied to investigate stress wave propagation. Besides, in this study, the strain gauges are located as far as possible to allow stress waves to propagate through sufficient numbers of engineered aggregates. Thus, strain gauges with short gauge lengths are used. The destructive test setup is shown in Figure 7-3(b). The striker bar for the destructive test is launched by a

pressure vessel to generate intensive dynamic load in order to examine the inelastic response of the specimen. The signal recorded on bar I is used to determine the input impulsive loading.

A high-speed camera as illustrated in Figure 7-3(c) with a frame rate of 12500 frames per second (FPS) is employed to measure the failure process of all specimens under destructive tests. During the destructive tests, rubber pulse shapers with a diameter of 20 mm and thickness of 3 mm are applied to eliminate the high-frequency oscillation as suggested by the previous study [126]. It is worth noting that the specimen is placed between two bars and hanged by two nylon ropes in the actual test setup Figure 7-3(c)). Two nylon ropes are tied near two ends of the specimen. The purpose of using nylon rope is to hold the specimen and align it to the testing apparatus. The specimen using nylon ropes instead of using other supports can minimize unwanted wave dispersion caused by the interaction between the support and stress wave [151].

(a) Non-destructive test (NDT)
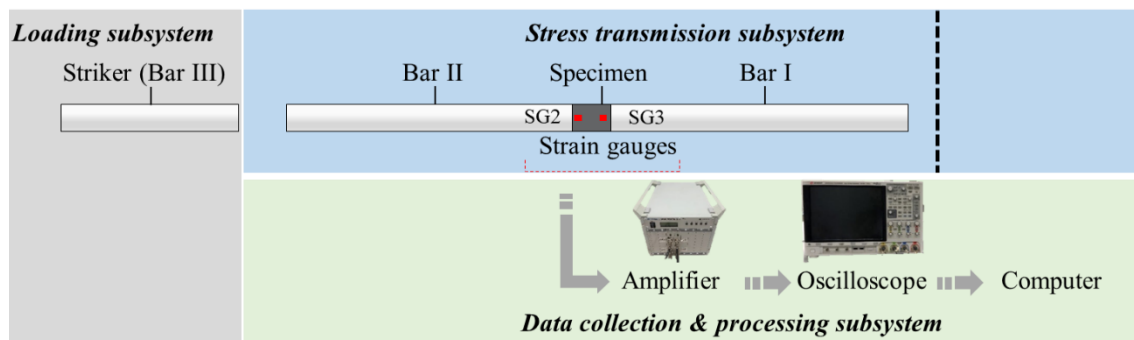
(b) Destructive test (DT)
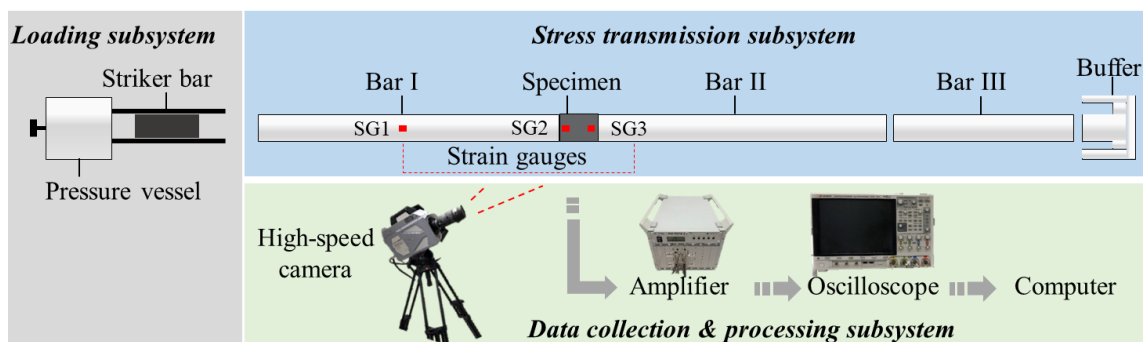
(c) Actual setup
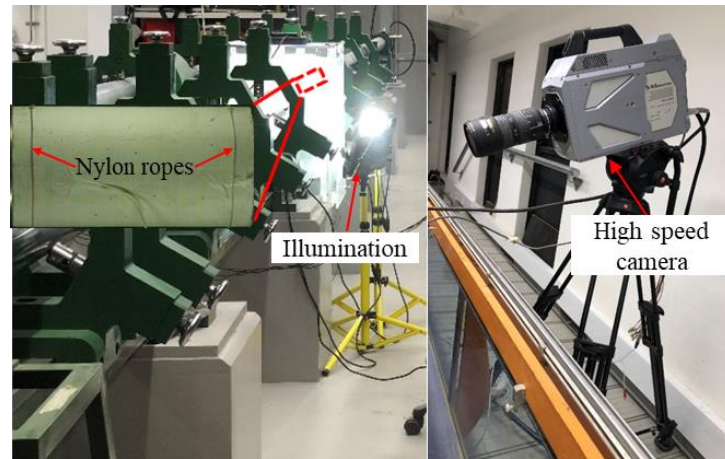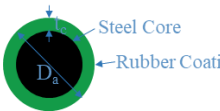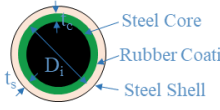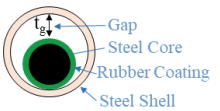
Figure 7-3. Dynamic test setup.

Table 7-2. Configuration of engineered aggregates (EAs).

Type	Illustration	Configuration	Dimension	Advantages	Disadvantages
RCSB		Steel Core — Rubber Coati — D_a	D_a=20 mm t_c=2.3 mm	Local resonance effect	Low stiffness Strength reduction due to the soft coating
ERCSB/18 (no gap)		t_c — Steel Core — Rubber Coati — D_i — Steel Shell t_s	D_a=20 mm D_i=18 mm t_c=1.5 mm t_s=1 mm	Stiffer Local resonance effect	Insufficient bonding due to smooth surface
ERCSB/15 (with a gap)		t_g — Gap — Steel Core — Rubber Coating — Steel Shell	D_a=20 mm D_i=15 mm t_c=1.3 mm t_s=1 mm t_g=3 mm	Stiffer Lighter Local resonance effect Rocking effect	Insufficient bonding due to smooth surface

Note: D_a is the diameter of engineered aggregate; D_i is the diameter of inner inclusion; t_c is the thickness of

coating; t_s is the thickness of steel shell; t_g is the thickness of gap.

Table 7-3. Specimen configurations and test results under non-destructive test (NDT).

Name	Inclusion types	V_{NA}%	V_{EA}%	size (mm)	ρ_{ave} (kg/m³)	R_{p-NDT}	R_{s-NDT}
S-S1		-	0	-	0	2183.8	-27%	0%
S-S2		RCSBs	0	10.6%	20	2477.5	79%	396%

Table 7-3 - (*Continued*)

			$V_{NA}\%$	$V_{EA}\%$		ρ_{ave}	R_{p-NDT}	R_{s-NDT}
S-S3		ERCSBs/18	0	10.6%	20	2504.9	86%	422%
S-S4		ERCSBs/15	0	10.6%	20	2325.3	62%	332%
S-S5		Natural gravel aggregates (NAs)	41.8%	0	-	2285.7	-0.4%	98%
S-S6		NAs+ ERCSBs/18	31.2%	10.6%	20	2658.9	71%	365%
S-S7		NAs+ ERCSBs/15	31.2%	10.6%	20	2463.9	68%	354%

Note: $V_{NA}\%$ is the volume fraction of natural aggregate; $V_{EA}\%$ is the volume fraction of engineered aggregate; ρ_{ave} is the average density; R_{p-NDT} is the peak reduction ratio of maximum longitudinal strain; R_{s-NDT} is the specific reduction ratio of strain with respect to plain mortar (reference). The negative value of the peak reduction ratio means the magnification of amplitude; "-" means reference specimen (S-S1).

7.3 Results and discussions

7.3.1 Quasi-static test and results

Figure 7-4 shows the failure modes of different specimens under quasi-static compression. Cracks usually are initiated at weak locations (e.g., the interface between cement mortar and aggregates, ITZ) and extend into the mortar matrix under quasi-static loading, leading to the brittle failure of the cementitious matrix [163]. Thus, the induced cracks associated with static loading are usually long and have an arbitrary path. The specimen with 0% NAs or EAs (i.e., mortar specimen S-S1) shows a columnar cracking pattern since the specimen is observed to fail into pieces on the external surfaces of the cylinder with brittle collapse, as shown in Figure 7-4(a). The failure mode of metaconcrete specimens with 10.6% RCSBs is characterized as a combination of shear and split. Cracks initiating at the top are propagated towards the bottom of the specimen and circumferential cracks are bifurcated from a major columnar crack, as highlighted by red circles in Figure 7-4(b). Also, there is localized damage

around RCSBs as highlighted by the red box in Figure 7-4 (b) due to the dissimilarity of modulus and deformation between the rubber layer and mortar matrix. Besides, the failure mode of S-S3 is similar to S-S4 with different types of ERCSBs, as shown in Figure 7-4(c) and (d). Both S-S3 and S-S4 show the diagonal shear cracks together with several columnar cracks and failed into more pieces, indicating more severely brittle failure. Meanwhile, columnar vertical cracking through both ends is observed in S-S5 (Figure 7-4(e)), and the specimen is broken into pieces. As shown in Figure 7-4(f) and (g), the concrete-based metaconcrete specimens (S-S6 and S-S7) have similar failure characteristics as mortar-based metaconcrete specimens. More cracks appear at the interface between ERCSBs and matrix resulting in localized damage, which might be due to the stress concentration at the interfacial transition zone between ERCSBs and the surrounding matrix.
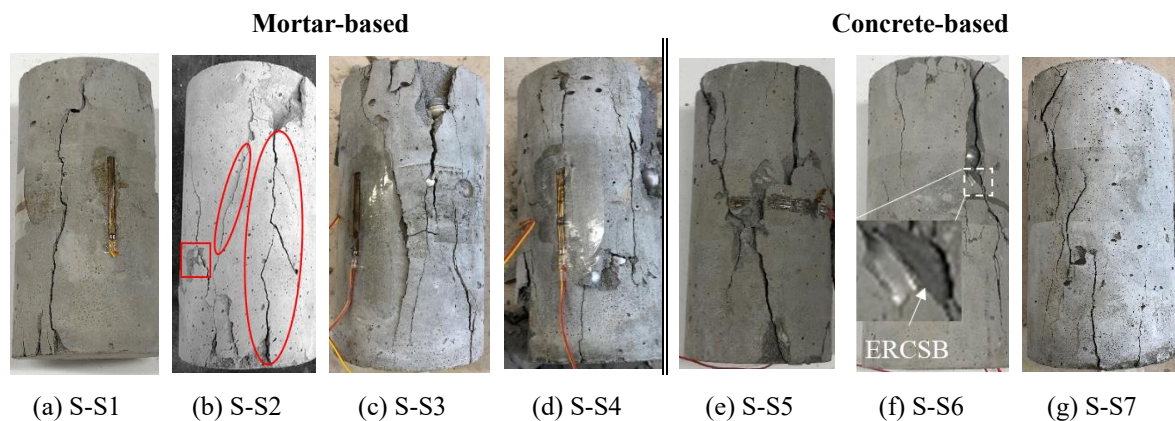
Figure 7-4. Failure modes of specimens under quasi-static loading.

Figure 7-5 shows compressive stress-strain curves for all the specimens under quasi-static tests. All curves show a similar trend and brittle failure after reaching the peak stress. As shown in Figure 7-5(a), the plain mortar S-S1 is failed at the average ultimate stress of 67.49 MPa and the average strain at the peak stress is around 0.380%. The plain concrete (S-S5) has an average ultimate strength of 67.92 MPa and the average strain at the peak stress is around 0.352%, as shown in Figure 7-5(e). Figure 7-5(b), (c), (d), (f) and (g) show the stress-strain curves of metaconcrete specimens. The average strain at the peak stress of metaconcrete specimens S-S2, S-S3, S-S4, S-S6 and S-S7 are about 0.267%, 0.272%, 0.230%, 0.255% and 0.278%, respectively. As observed in Figure 7-5, the compressive strength of the

metaconcrete specimen is considerably improved by using ERCSBs as compared to the metaconcrete specimen with RCSBs (S-S2). These results indicate that adding EAs into the concrete mix could reduce the concrete strength and deformation ability.

(a) S-S1

(b) S-S2

(c) S-S3

(d) S-S4

(e) S-S5

(f) S-S6

(g) S-S7
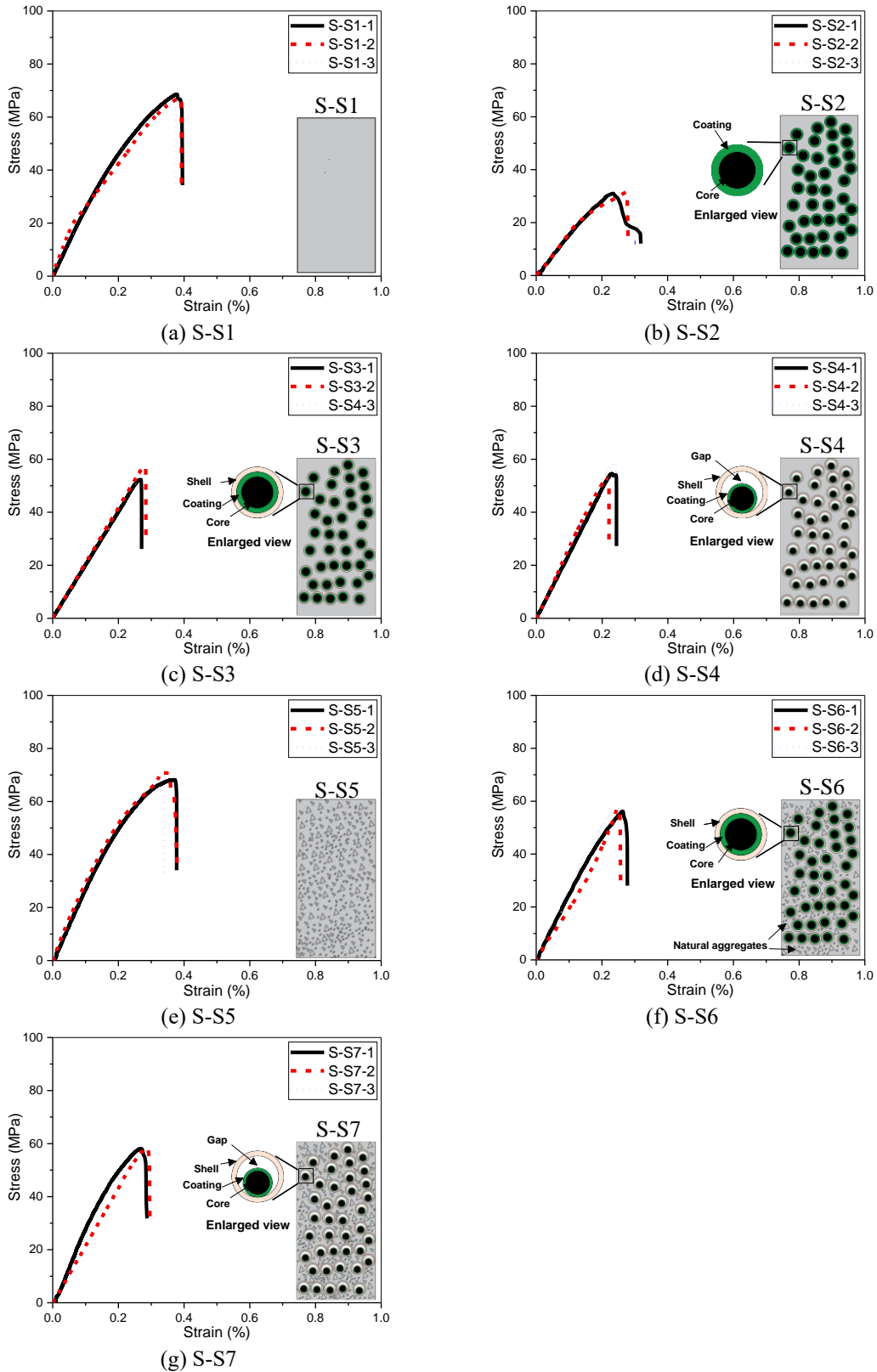
Figure 7-5. Stress-strain curves of specimens.

The mean compressive strength of mortar and metaconcrete specimens with different aggregate configurations is illustrated in Figure 7-6(a). The average compressive strength of S-S1 is 67.49 MPa. However, the compressive strength greatly decreases to 29.98 MPa when adding RCSBs in S-S2. Namely, the reduction in the compressive strength of metaconcrete specimen by adding 10.6% volume percentage of RCSBs is around 55.6% in comparison with S-S1. This result is consistent with that obtained from the detailed numerical modelling [89], i.e., adding RCSBs into the concrete mix could reduce the concrete strength although the local vibrations of the core in RCSBs could mitigate stress wave propagation. The reasons for the adverse effect of mixing RCSBs into the mortar on the compressive strength of metaconcrete specimens are attributed to: a) a soft coating with low stiffness is prone to deform while the surrounding mortar is brittle, causing damage to the mortar matrix; b) the mismatch of the elastic modulus and deformation capacity made the surrounding matrix vulnerable to be damaged. As shown, adding a hard steel shell can improve the average compressive strength of metaconcrete specimens to 54.97 MPa and 55.57 MPa for S-S3 and S-S4, which increase around 80.3% and 85.4% as compared to S-S2, respectively, but are still lower than the mortar specimen (S-S1). The reason for the compressive strengths of S-S3 and S-S4 being lower than S-S1 is because of the insufficient bonding between the steel shell surface and the surrounding mortar matrix, evidenced by the debonding failure between ERCSBs and mortar matrix shown in Figure 7-4. Nevertheless, adding the steel shell to the conventional EAs significantly improves the compressive strength of metaconcrete specimens mixed with the conventional EAs. Similar observations can be drawn on the concrete-based specimens, i.e., S5, S6 and S7. The respective average compressive strength is 67.92 MPa, 56.19 MPa, and 56.81 MPa. The strength of metaconcrete specimens with enhanced EAs is still slightly lower than the concrete specimen (S-S5). Therefore, further improvement is deemed necessary to enhance the bonding strength between the EAs and cementitious matrix so that the strength of the metaconcrete specimen is not compromised while having the excellent capability of wave propagation mitigation.

The mean modulus of elasticity (E) of the tested specimens is compared in Figure 7-6(b) and

Table 7-4, the average value and standard deviation (SD) are listed in Figure 7-6. The elastic modulus of metaconcrete specimens with conventional EAs is substantially smaller than that of the reference specimen. For instance, the elastic modulus of S-S2 is 15.34 GPa, which is 39.4% lower than that of plain mortar (25.42 GPa). This is again because the soft coating of the conventional EA caused the reduction of the elastic modulus of the metaconcrete specimens. In contrast, the specimens with the enhanced EAs have a comparable or even slightly higher modulus of elasticity than the reference specimen. For instance, by replacing NAs with ERCSBs (i.e., 10.6% in total volume) in S-S3, S-S4, S-S6 and S-S7, the higher modulus of elasticity, i.e., 26.44, 26.59, 26.91 and 26.24 GPa can be obtained, respectively. It is because the steel shell is much stiffer than the surrounding cementitious matrix (i.e., $E_{\text{shell}} \gg E_{\text{matrix}}$) and adding a stiff steel shell on the conventional EA overcomes the problem of softening the metaconcrete materials. However, the overall modulus of elasticity of metaconcrete specimens with ERCSBs is not changed significantly, implying the elastic modulus is still governed by the mortar matrix.

The mean Poisson's ratio (μ) of the tested specimens is also depicted in Figure 7-6(b) and Table 7-4. As shown, the mean Poisson's ratio has an opposite variation trend to the modulus of elasticity. All the specimens, except metaconcrete specimens made of conventional EAs, has a similar Poisson's ratio. The Poisson's ratio of the conventional metaconcrete specimen (S-S2) is slightly higher than other specimens. This is because the coating layer outside conventional EAs is made of hyper-elastic material (silicone rubber), which has a higher Poisson's ratio than cementitious mortar.

Table 7-4 also gives the failure strain (ε_f) and specific fracture energy (G_f) of the specimens. It is found that metaconcrete specimen has lower failure strain and specific fracture energy than plain mortar and concrete in general as metaconcrete specimen has lower deformation capacity and compressive strength due to weak bonding at the EAs-matrix interfaces. Hence, it is essential to enhance the bonding strength between EAs and mortar matrix for improving the performance of metaconcrete specimens. It should be noted that the bonding strength can

be improved by using mechanical or chemical treatment such as roughing EAs' surface or adding bonding additives (e.g., epoxy resin) outside the EAs. Alternatively, the steel shell can be replaced by cementitious materials with superior mechanical properties to the surrounding matrix.
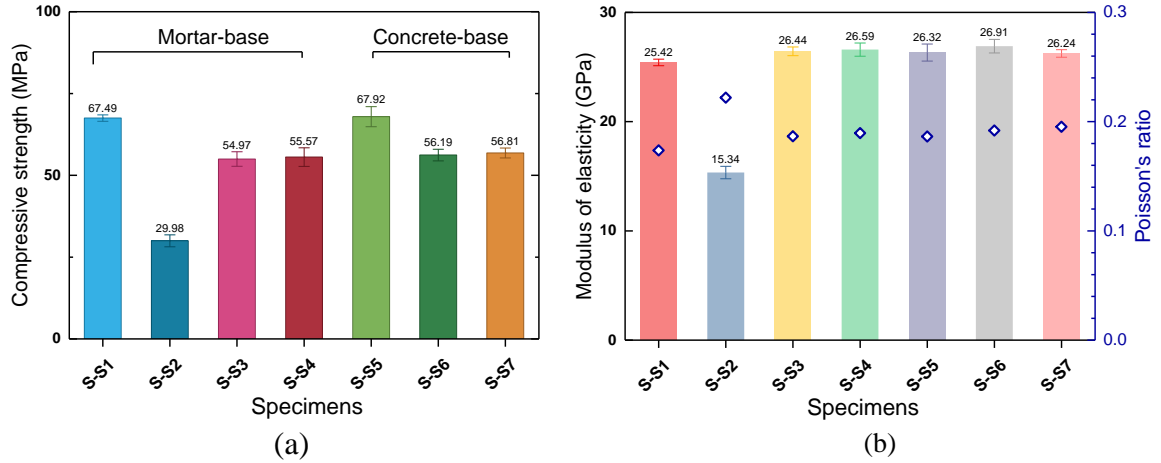
Figure 7-6. Comparisons of: (a) Compressive strength, (b) Modulus of elasticity and Poisson's ratio.

Table 7-4. Mechanical properties of mortar, concrete and metaconcrete specimens.

Specimen No.	f'_c [a] (MPa)	SD	E [a] (GPa)	SD	μ [a]	SD	ε_f [a] (%)	SD	G_f [a] (kJ/m³)	SD
S-S1	67.49	0.99	25.42	1.01	0.173	0.004	0.380	0.0067	131.02	6.00
S-S2	29.98	1.81	15.34	1.91	0.222	0.003	0.267	0.0241	45.91	1.96
S-S3	54.97	2.22	26.44	1.33	0.187	0.007	0.272	0.0081	81.70	4.36
S-S4	55.57	2.83	26.59	2.00	0.190	0.009	0.230	0.0073	77.50	5.50
S-S5	67.92	3.06	26.32	2.61	0.186	0.005	0.352	0.0142	135.78	9.92
S-S6	56.19	1.78	26.91	2.07	0.192	0.005	0.255	0.0069	82.57	9.40
S-S7	56.81	1.52	26.24	1.17	0.195	0.006	0.278	0.0062	90.01	13.55

Note: [a] is the 28-days mean value; f'_c is compressive strength; E is the modulus of elasticity; μ is Poisson's ratio; ε_f is failure strain; G_f is specific fracture energy, i.e., the enclosed area under the stress-strain curve, in kJ/m³; SD is standard derivation.

7.3.2 Dynamic test results and discussion

To quantify the effectiveness of wave propagation mitigation of specimens, three groups of performance metrics are considered in this chapter. The definition of each performance metric is specified as follows.

(i) $R_{p\text{-}NDT}$ or $R_{p\text{-}DT}$ is defined as the peak reduction ratio of maximum longitudinal strain given

by Eq. (7-3), corresponding to the non-destructive (NDT) or destructive (DT) test. Specifically, it is used to quantify the effectiveness in mitigating stress wave propagation by calculating the ratio of peak strain at the front and rear end of the specimen (i.e., SG2 and SG3), as shown in Figure 7-3(a) and (b).

$$R_{p-NDT} \text{ or } R_{p-DT} = (1 - \frac{\varepsilon_3|_{peak}}{\varepsilon_2|_{peak}}) \times 100\%$$

(7-3)

(ii) R_{s-NDT} or R_{s-DT}, the specific reduction ratio of strain at SG3 with respect to the reference (S-S1), is computed by Eq. (7-4).

$$R_{s-NDT} \text{ or } R_{s-DT} = (1 - \frac{\varepsilon_{2_{S-Si}}|_{peak} / \varepsilon_{3_{S-Si}}|_{peak}}{\varepsilon_{2_{S-S1}}|_{peak} / \varepsilon_{3_{S-S1}}|_{peak}}) \times 100\% \quad where \ i = 1, 2 \cdots 7$$

(7-4)

(iii) Transmission ratio (TR) is defined as the ratio of output (SG3) to input (SG2) amplitudes in the frequency domain within the specimen by using Eq. (7-5), which has been used in the previous studies [8, 151]. The negative TR value indicates that the response near the rear end of the specimen is less than the response near the loading end of the specimen.

$$TR = 20 \times \log(\frac{\varepsilon_3(f)}{\varepsilon_2(f)})$$

(7-5)

Where $\varepsilon_2(f)$ and $\varepsilon_3(f)$ are the longitudinal strain at SG2 and SG3 of the tested specimens, respectively; $\varepsilon_1|_{peak}$, $\varepsilon_2|_{peak}$ and $\varepsilon_3|_{peak}$ represent the peak strain value recorded by the attached three gauges, as shown in Figure 7-3(b). $\varepsilon_{S1}|_{peak}$ is the peak strain recorded in the plain mortar (S-S1) as the reference, and subscript i represents the specimen number for each configuration, as shown in Figure 7-1; $\varepsilon_2(f)$ is the amplitude of longitudinal strain in the frequency domain recorded by SG2, and $\varepsilon_3(f)$ is the amplitude of longitudinal strain in the frequency domain recorded by SG3.

7.3.2.1 Response of specimen under non-destructive test (NDT)

The specimens are subsequently investigated under non-destructive tests with the relatively low-amplitude impulses generated by manually striking bar III to bar II (shown in Figure

7-3(a)). When the specimen is impacted, the stress waves are generated at the impactor-specimen interface and propagated through the specimen. The primary or longitudinal stress waves then propagated along the loading direction [164]. In order to examine the wave attenuation in the specimens, wave signals near the loading and rear ends are recorded (i.e., $\varepsilon_2(t)$ and $\varepsilon_3(t)$). Figure 7-7 shows the strain time histories of $\varepsilon_2(t)$ and $\varepsilon_3(t)$ for seven specimens subjected to non-destructive loading. As shown in Figure 7-7(a), there is no apparent wave attenuation in terms of peak strain reduction in S-S1, instead, the strain peak is enlarged. Amplification of the stress is caused by wave interaction (i.e., superposition) between the incident and the reflected wave near the end of the specimen. As shown in Figure 7-7(b), the apparent peak stain reduction (i.e., $\varepsilon_3\big|_{peak} < \varepsilon_2\big|_{peak}$) is found in S-S2, indicating that the elastic stress waves are attenuated greatly when the waves passed through the RCSBs. Similarly, the value of $\varepsilon_3\big|_{peak}$ is greatly reduced in S-S3 (Figure 7-7(c)) and S-S4 (Figure 7-7 (d)), demonstrating the metaconcrete specimens consisting of ERCSBs also exhibits favorable wave attenuation properties. Figure 7-7(e) shows the strain time histories of plain concrete (i.e., S-S5). It is observed that the value of $\varepsilon_3\big|_{peak}$ is also higher than $\varepsilon_2\big|_{peak}$ due to the wave interaction (i.e., superposition). As observed in Figure 7-7(f) and (g), the values of $\varepsilon_3\big|_{peak}$, however, are greatly reduced in S-S6 and S-S7. It can be concluded that all specimens with ERCSBs are capable of mitigating the propagation of elastic stress waves.
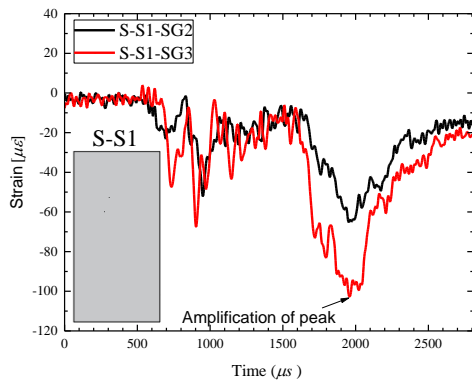
(a) S-S1
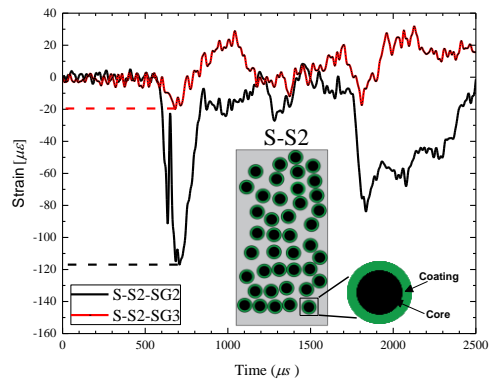
(b) S-S2
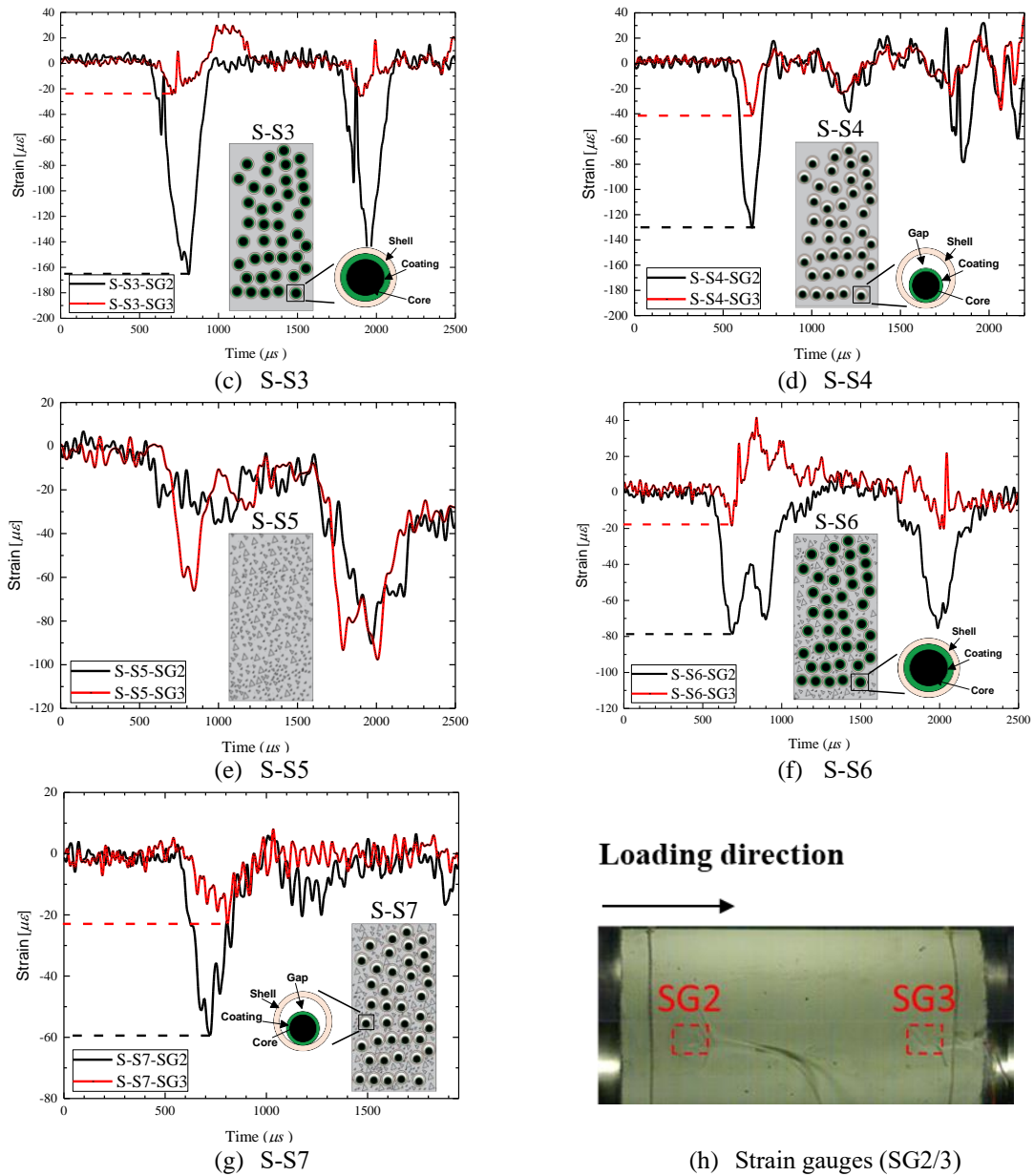
Figure 7-7. Strain-time histories of all specimens under non-destructive tests. Note: SG2 and SG3 represent the input and output strain.

Moreover, the performance metric $R_{p\text{-}NDT}$, i.e., peak strain reduction ratio, is summarized in Table 7-3, where the higher value means superior capacity in attenuating stress wave propagations. By using Eq. (7-3), the peak strain reduction $R_{p\text{-}NDT}$ of S-S1 is calculated as -27%. The negative value of $R_{p\text{-}NDT}$ signifies the magnification of amplitude owing to the superposition of incident and reflected waves. The corresponding one for metaconcrete specimen with RCSBs (S-S2), mortar with ERCSBs/18 (S-S3) and ERCSBs/15 (S-S4) is 79%, 86% and 62%, respectively, as listed in Table 7-3. S-S3 shows a higher $R_{p\text{-}NDT}$ than S-S2 owing to the more pronounced difference of wave impedances between steel shell and

151

mortar matrix as compared to that between rubber coating and mortar matrix. When an elastic wave approaches the interface between steel shell and cementitious matrix with different impedances, the incident stress wave partially reflects and the rest refracts into other material [165]. As a result, more stress wave attenuation can be achieved. S-S3 also presents a higher value of $R_{p\text{-}NDT}$ than S-S4 because the steel core inside ERCSBs/18 is larger than that inside ERCSBs/15. S-S3 also displayed a higher $R_{s\text{-}NDT}$ (i.e., the specific reduction ratio of strain with respect to plain mortar) of 422% than 396% of S-S2 and 332% of S-S4, as calculated by Eq. (7-4). Table 7-3 tabulates the values of $R_{p\text{-}NDT}$ and $R_{s\text{-}NDT}$ for S-S5, S-S6 and S-S7. Among concrete-based specimens, S-S6 has the highest reduction value of 71% ($R_{p\text{-}NDT}$) and 365% ($R_{s\text{-}NDT}$), which are greater than S-S5 of -0.4% and 98% as well as S-S7 of 68% and 354%, respectively. Based on the above results, it can be concluded that using the enhanced EAs proposed in this chapter can achieve comparable or even slightly better wave propagation attenuation than the conventional EAs, and the design of ERCSB/18 performed better than ERCSB/15, indicating the idea of allowing RCSB sliding inside the steel shell did not lead to better energy absorption probably because the steel core vibration in RCSB is less excited.

Furthermore, the wave attenuation mechanism associated with the above observation could be inferred from the frequency domain analysis, which has been widely used in previous studies [30, 31, 94]. The transmission ratio (TR) with respect to the longitudinal strain is calculated by Eq. (7-5). The curves of TR versus frequencies ranged from 0 kHz to 15 kHz for S-S1 to S-S4 are presented in Figure 7-8. As shown in Figure 7-8(a), there is no significant drop in spectral amplitudes in the TR curve of the plain mortar (S-S1), implying that no noticeable wave filtering effect is found. S-S2 with randomly dispersed RCSBs displays a frequency-dependent attenuation, in which a minimum TR value of -32.8 dB at 3.6 kHz (i.e., frequency dip) is observed. Therefore, the local resonance effect plays an important role in mitigating stress wave propagation. As the loading frequency approaches the resonant frequency of RCSBs, a large proportion of wave energy is transferred to the local vibration of the cores, which reduces the wave energy transmitting across the mortar matrix. This

attenuation phenomenon is consistent with the experimental results reported in the previous studies [28-30, 94].

(a) mortar-based specimens   (b) concrete-based specimens
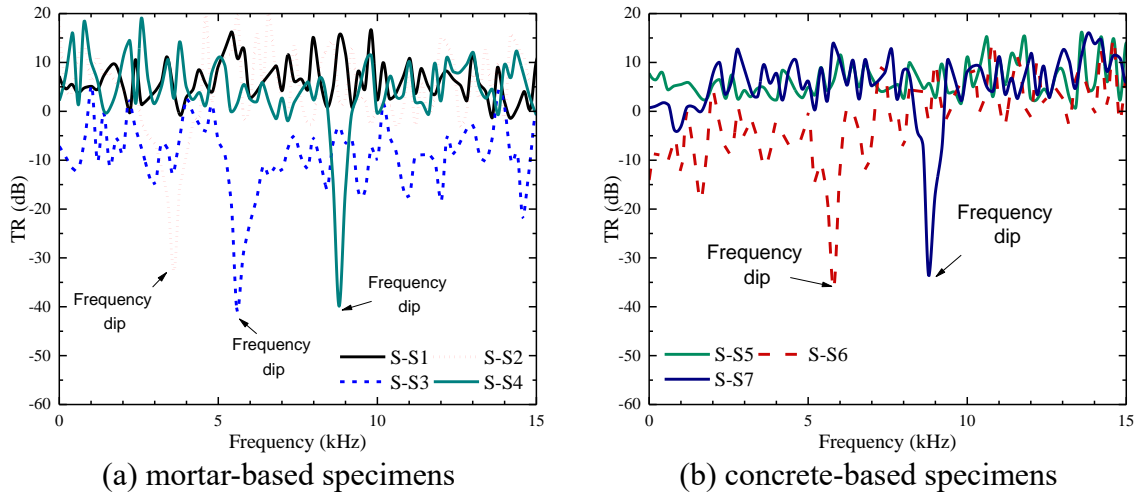
Figure 7-8. Comparisons of transmission ratio (TR) of different specimens.

As compared to S-S2, both S-S3 and S-S4 exhibit analogous frequency-depended attenuation effects. For S-S3 with ERCSBs/18, an apparent frequency dip occurs at 5.6 kHz as shown in Figure 7-8(a), in which the minimum TR is around -41.0 dB. Similar to S-S2, the local resonance of the core inside ERCSBs could dissipate wave energy, resulting in favorable wave attenuation performance. In addition, S-S4 displays a less significant attenuation effect in which the minimum TR is around -39.9 dB at 8.8 kHz. The frequency-dependent wave-filtering capacity and attenuation behaviors found in S-S3 and S-S4 with ERCSBs, as well as in S-S2, can be attributed to the local resonance effect. Likewise, the frequency spectra for concrete-based specimens are shown in Figure 7-8(b). There is no substantial reduction in spectral amplitude of plain concrete (S-S5) owing to the nonexistence of local resonant aggregates. In contrast, apparent frequency dips are observed in S-S6 and S-S7, in which the minimum TR is around -36.5 dB at 5.8 kHz and -33.6 dB at 8.9 kHz, respectively. Again, the metaconcrete specimens consisting of both conventional (i.e., RCSBs) and enhanced EAs (i.e., ERCSBs) shows the frequency-dependent wave-filtering effect within the prescribed frequency range or bandgap. Specifically, the EAs are tuned within the prescribed bandgap leading to an out-of-phase vibration of the inner metal core. This local vibration of the core could interact with stress waves induced by impulsive loading, hence mitigating the stress

wave propagation throughout the matrix. The details of deriving the prescribed frequency range are not presented herein but can refer to Chapter 3 and Chapter 4 as well as previous studies [151-153]. In conclusion, adding ERCSBs is effective for elastic wave propagation attenuation under the non-destructive impulsive load.

7.3.2.2 Response of specimens under destructive test (DT)

Figure 7-3(b) shows the setup of the destructive test. It is worth mentioning that this experiment mainly focuses on the effectiveness in mitigating stress wave propagation of each specimen rather than its dynamic material properties. Stress equilibrium condition [166] is thus not required for this test. Besides, three loading cases with different peak incident stress (i.e., impulses I, II and III as shown in Figure 7-9 by varying striker velocities through changing air pressure in the pressure vessel) are utilized to examine the dynamic responses of each specimen.
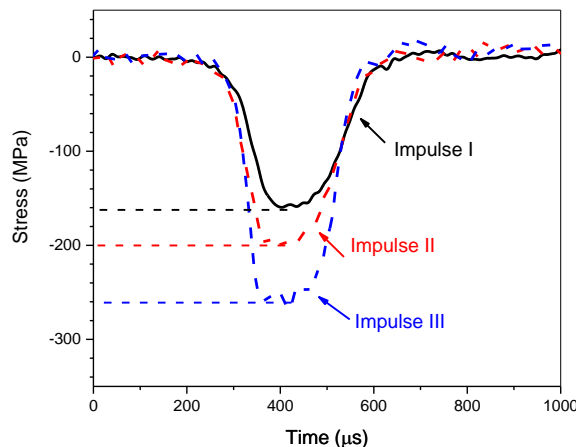
Figure 7-9. Typical input impulses I, II and III.

Failure process and failure modes

The typical failure process of all the specimens under intermediate impulsive loading (impulse II) is shown in Figure 7-10(a) and (b) captured by using a high-speed camera. For impulse I, specimens experience less severe damage while specimens are rapidly pulverized into fragments under impulsive III. To better demonstrate the damage initiation and development before the specimens completely failed, the failure processes subjected to impulse II are demonstrated herein. 0 µs represented the moment when the specimen is

initially stressed. For plain mortar (S-S1), cracks are initiated from the loading side of the specimens and developed into the mid-region. Afterwards, more cracks are initiated within the mid-region and developed further. As shown in Figure 7-10(a), S-S1 is experienced spall damage, i.e., clear tensile damage, owing to the reflected stress wave. This damage mode of plain mortar is consistent with the experimental results reported in the previous study [166, 167]. Metaconcrete specimen with RCSBs develops cracks earlier than the plain mortar due to its lower compressive strength, i.e., S-S2 shows severe cracks in the middle region at 320 μs, while only a minor crack is found on the S-S1 at 320 μs. In addition, the metaconcrete specimen with RCSBs is suffered severe failure as shown in Figure 7-10(a), the cracks are parallel to the loading direction concentrated in the middle region, showing a splitting failure mode. S-S2 at 640 μs shows more cracks than S-S1 at the same time instant. At 640 μs, two major cracks are nearly parallel to the loading direction together with numerous minor cracks extended from arbitrary directions as observed in Figure 7-10(a). Severe diagonal fractures are observed in S-S2 at 960 μs owing to its low compressive strength.

For the metaconcrete specimen with ERCSBs/18 (S-S3), the cracks are initiated at the loading surface of the specimen and propagated to the middle region at 320 μs. Besides, the number of cracks at all-time instants for S-S3 is less than that of the metaconcrete specimen with RCSBs (S-S2) owing to the higher compressive strength of S-S3. S-S4 also is experienced fewer cracks than S-S2 at all-time instants due to the existence of hard steel shells. The previous study [27, 31] reported that the effect of local oscillation of heavy cores may lead to a reduction in the crack development as the local vibration of EAs could dissipate a certain amount of wave energy. However, S-S2 displays lower resistance and less mitigation capacity due to early damage to the matrix. By adding steel shells, the mitigation capacity and damage resistance are improved as compared to metaconcrete specimen with RCSBs (S-S2). Eventually, both S-S1 and S-S2 are shattered into small pieces because of the brittle nature of the mortar matrix as shown in Figure 7-10(a). In contrast, the majority part of metaconcrete specimens with ERCSBs (i.e., S-S3 and S-S4) remained intact. It is also noted that no tensile crack is observed in S-S3 and S-S4, implying the ERCSBs reduced the stress wave amplitude

such that the reflected tensile stress wave is small to cause tensile failure in S-S3 and S-S4.
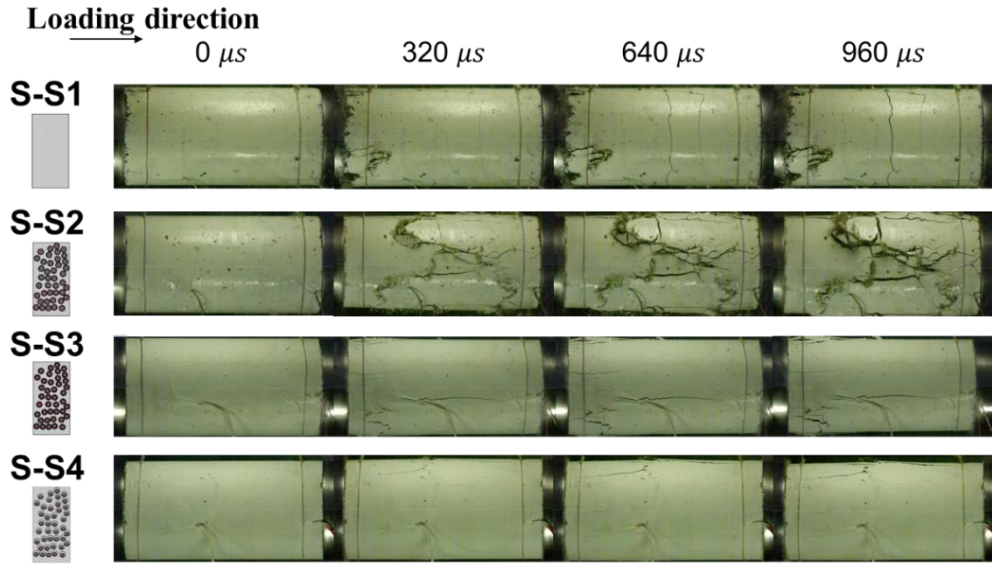
(a) Mortar-based specimen
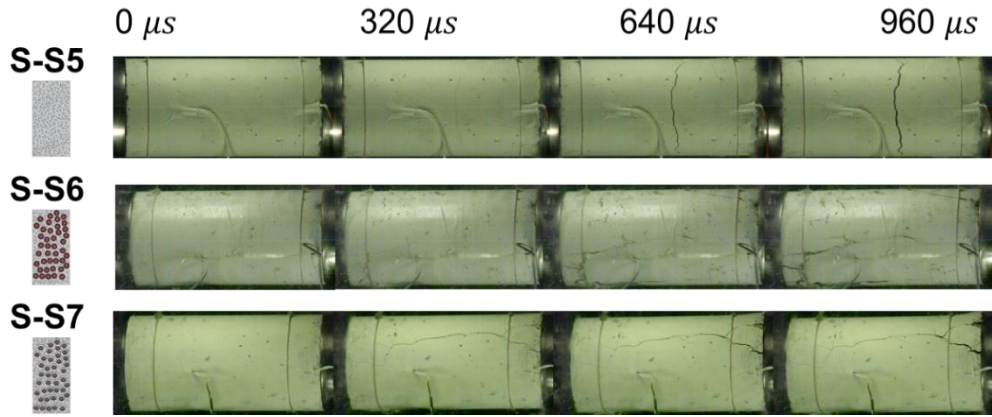
(b) Concrete-based specimen

(c) Failure process comparison of S-S5 and S-S6 under impulse II

Figure 7-10. Failure process of specimens subjected to impulse II.

The fracture pattern observed in the plain concrete (i.e., S-S5) is similar to S-S1 under impulse II. As shown in Figure 7-10(b) and (c), the plain concrete specimen is broken into two parts owing to tensile failure. This damage mode of plain concrete is consistent with the experimental results reported in the previous study [115, 166, 168]. For metaconcrete specimens (i.e., S-S6 and S-S7), however, it is experienced brittle crushing damage on the loading end as shown in Figure 7-10(c). It is noteworthy that cracks in specimens are usually initiated at weak sections (i.e., ITZ or air voids) and then are extended. For metaconcrete

specimens with ERCSBs, the induced cracks in the specimens associated with impulsive loading are originated from the interface between ERCSBs and the surrounding matrix and then propagated either parallel (i.e., longitudinal cack) or perpendicular (i.e., transverse crack) to the loading direction. As shown in Figure 7-10(c), S-S5 is experienced dynamic fracture (i.e., spalling) in the middle at the time instant of 53920 µs and S-S6 is experienced severe crushing at the loading end at the same moment, which could absorb a significant amount of energy and result in less amount of wave energy transmitting to the remaining part of the specimen. Based on the above observations, it can be concluded that mixing EAs with a stiff shell in metaconcrete specimens can greatly enhance the structural capacity to resist impulsive loading.

Figure 7-11 shows the final failure modes of the specimens with various configurations under different input loading (impulses I, II and III). As observed, plain mortar (S-S1) and plain concrete (S-S5) are experienced significant dynamic fracture (i.e., spalling) and they are disintegrated into two parts under impulse I owing to insufficient tensile strength. These failure modes of plain mortar and concrete are consistent with the experimental results reported in the previous studies [115, 166, 167], and the fracture profile agreed with the results reported by Klepaczko and Brara [168]. Metaconcrete specimen with RCSBs (S-S2) experienced columnar cracking through both ends, and severe localized damage is found in the middle region due to stress concentration at the interfacial area around RCSBs. This damage mode is also consistent with the results reported in the previous studies [31, 88, 89]. Besides, metaconcrete specimens with both types of ERCSBs (i.e., S-S3, S-S4, S-S6 and S-S7) are experienced localized damage and only several cracks appeared near the loading end under impulse I, as illustrated in Figure 7-11(a) and (b). Based on the above results, metaconcrete specimen with ERCSBs demonstrates better impulsive loading resistance as compared to metaconcrete specimen with RCSBs (S-S2) as well as plain specimens (S1-S1 and S-S5) under impulse I.

With the applied load increased to impulse II, plain mortar (S-S1) is shattered into several

fragments as shown in Figure 7-11(a). Metaconcrete specimen with RCSBs (S-S2) exhibits unsatisfactory loading resistance, in which the diagonal fracture with several cracks through the rear ends is observed and the front part is crushed into numerous pieces owing to its lower compressive strength. For S-S3 under impulse II, it is experienced damage in the middle region and an obvious crack is observed perpendicular to the loading direction but the overall specimen is still intact. For S-S4, a relatively large piece at the mid-section of the specimen is fell off while the rest of the part is intact. Thus, metaconcrete specimens with ERCSBs/18 and ERCSBs/15 has higher loading resistance as compared to other specimens (S-S1 and S-S2) under impulse II as these specimens are shattered into small pieces. Plain concrete (S-S5) is broken into two disconnected parts under impulse II owing to the reflected tensile stress wave. As shown in Figure 7-11(b), approximately 1/3 of S-S6 on the loading side is crushed but the remaining part of the specimen is kept its integrity with some peel-off damage on the specimen surface. S-S7 is also experienced local damage near the loading end. Peel-off damage to specimen appears more severe in S-S3, S-S4, S-S6 and S-S7. This could be attributed to poor bonding between steel shell and mortar matrix. Under axial impact loading, the specimens expand laterally owing to Poisson's ratio effect, poor bonding between mortar and EAs causes the specimen more vulnerable to peel-off damage. Therefore, improving the bonding strength between EA and mortar matrix is important. Moreover, peel-off damage may be caused by the wave impedance mismatch between steel shell and cementitious matrix, so that significant wave reflection is induced leading to serious interfacial failure. Hence, the enhanced coating material with wave impedance closed to the matrix material is suggested to ensure smooth transmission of stress waves inside the engineered aggregate, which could potentially reduce the interfacial failure.

Higher loading intensity greatly affects the failure mode of metaconcrete specimens. Under impulses I and II, a certain level of specimen integrity is maintained. When a more intensive load (i.e., impulse III) is applied, all the specimens are shattered into smaller pieces. For instance, S-S1 is crushed into chunks, while metaconcrete specimen with RCSBs, ERCSBs/18 and ERCSBs/15 are broken into various pieces, as shown in Figure 7-11(a) and

(b). Smaller fragments (broken pieces) are generated in metaconcrete specimens than in plain specimens owing to the insufficient interfacial strength between EAs and cementitious matrix. Based on the above results, metaconcrete specimens consisting of EAs with the enhanced coating (i.e., ERCSBs) shows a higher loading resistance capacity than metaconcrete specimen with RCSBs in all loading cases.
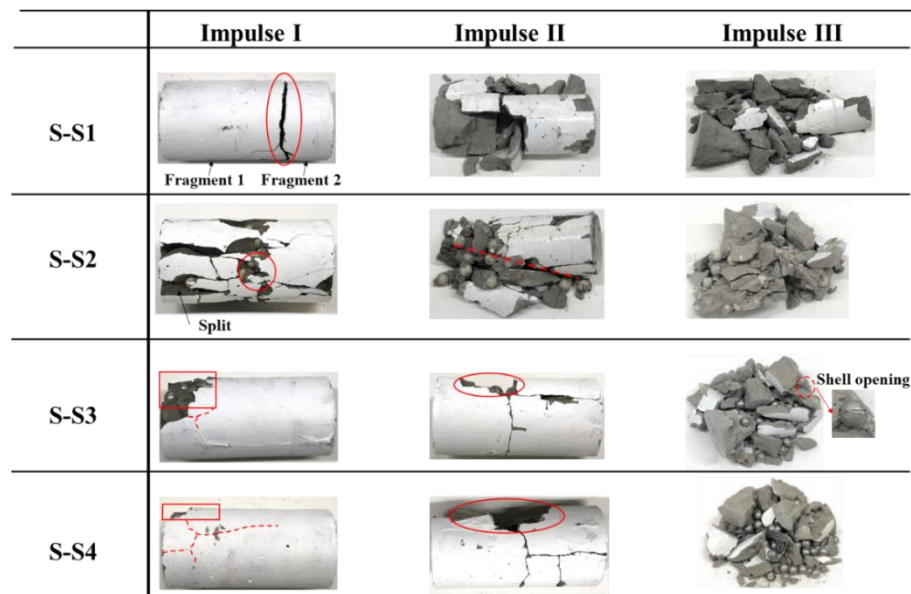
(a) Mortar-based specimen
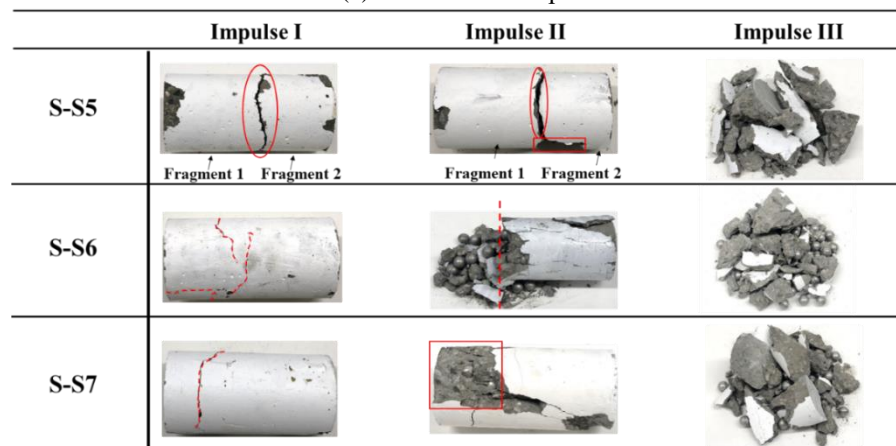
(b) Concrete-based specimen

Figure 7-11. Failure modes of specimens subjected to impulses I, II and III.

Comparison of stress wave attenuation performance

To further examine the effectiveness of wave attenuation in metaconcrete and plain specimens, strain-time histories for all the specimens subjected to impulses I, II and III are compared in Figure 7-12. S-S2 has the highest value of $\varepsilon_2\big|_{peak}$ owing to its lowest modulus

of elasticity or stiffness of the material, as shown in Figure 7-12(b). Meanwhile, the strain gauge near the loading end (i.e., SG2) is broken at an early stage because of the specimen damage (see Figure 7-12(a)), which is due to its lower compressive strength when subjected to impulses I, II and III. As shown in Figure 7-12(c) and (d), S-S3 and S-S4 have smaller values of $\varepsilon_2\big|_{peak}$ as compared to S-S1 owing to their higher modulus of elasticity. It is worth noting that the stress wave propagating along the specimen is inhibited if a substantial reduction in the transmitted peak strain (i.e., SG3) is obtained. No significant peak strain reduction indicates that there is no noticeable stress wave attenuation effect, whereas a noticeable reduction of peak transmitted strain ($\varepsilon_3\big|_{peak}$) indicates the wave propagation mitigation. As shown in Figure 7-12(a), S-S1 exhibits no significant wave attenuation effect as the reduction of transmitted peak strain is not obvious for each loading scenario. In contrast, noticeable peak strain reduction is found in S-S2 (see Figure 7-12(b)), implying that the stress wave is attenuated after passing through the conventional RCSBs owing to the local resonance effect, in which this attenuation phenomenon is consistent with the experimental observation reported in the previous study [31]. Besides, considerable peak strain reduction is also observed in S-S3 and S-S4 (see Figure 7-12(c) and (d)), demonstrating the addition of the hard shell does not significantly affect the wave mitigation performance of the engineered aggregates. In fact, ERCSB could provide a comparable or even better wave mitigation effect than conventional RCSB. For plain concrete (S-S5), the value of peak transmitted strain ($\varepsilon_3\big|_{peak}$) is close to the peak incident value ($\varepsilon_2\big|_{peak}$), namely, there is no noticeable wave propagating attenuation, as observed in Figure 7-12(e). In contrast, the values of $\varepsilon_3\big|_{peak}$ for S-S6 and S-S7, as displayed in Figure 7-12(f) and (g), are considerably reduced, indicating the specimens with ERCSBs achieves enhanced stress wave attenuation performance than plain concrete due to the local resonance of engineered aggregates. To conclude, metaconcrete specimens consisting of enhanced EAs proposed in this chapter can improve the strength of metaconcrete specimens and also maintain its stress wave attenuation capacity.

(a) S-S1

(b) S-S2

(c) S-S3

(d) S-S4

(e) S-S5

(f) S-S6

(g) S-S7
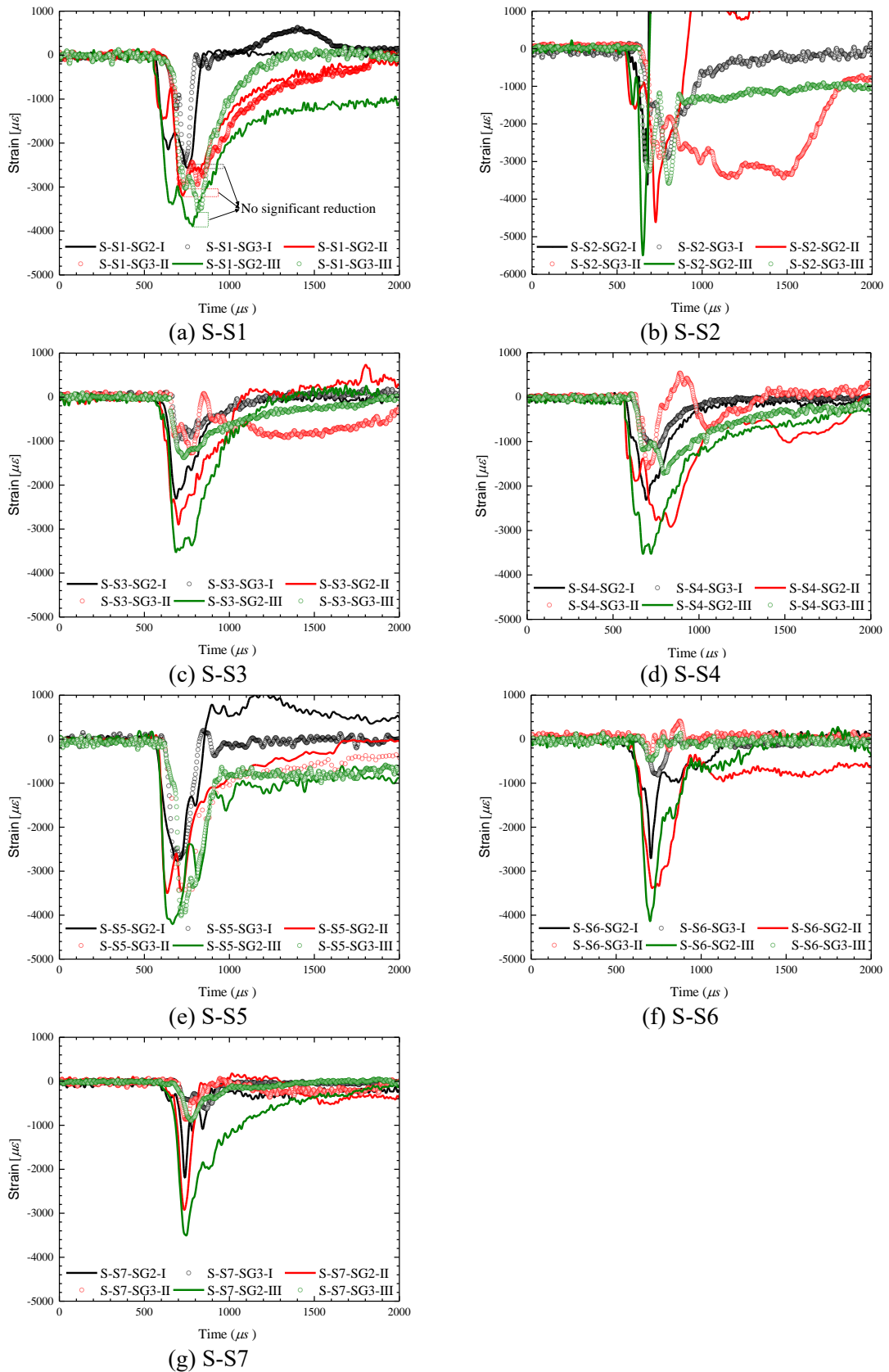
Figure 7-12. Comparison of strain-time histories of specimens subjected to impulses I, II and III.

Moreover, the peak reduction ratios of the maximum longitudinal strain ($R_{p\text{-}DT}$) derived by using Eq. (7-3) are summarized in Table 7-5 to qualitatively compare the performance of

wave propagation mitigation. A higher value of $R_{p\text{-}DT}$ means a greater reduction in the maximum longitudinal strain within the specimen, namely, better wave propagation mitigation performance. As shown in Table 7-5, the specimen with RCSBs generally has a greater value of $R_{p\text{-}DT}$ than the plain specimens (e.g., S-S1) in all loading cases. For instance, $R_{p\text{-}DT}$ under impulses I, II and III in S-S2 is 20%, 26% and 35%, which are greater than S-S1 of 5%, 6% and 8%, respectively. This is because the local resonance of the core can attenuate the stress waves propagating through the specimen. However, owing to the lower strength of metaconcrete specimen with RCSBs, S-S2 is experienced severe damage to the surrounding matrix at an early stage, which limits the local resonance effectiveness. This observation is consistent with those reported in the previous numerical studies [88, 152]. Thus, its wave propagation attenuation effect is not significant as compared to metaconcrete specimens with ERCSBs. By adding a steel shell, metaconcrete specimens with ERCSBs show a higher reduction value. For instance, $R_{p\text{-}DT}$ of S-S3 under impulses I, II and III are 52%, 57% and 61%, which are greater than S-S2 of 20%, 26% and 35%, respectively, as given in Table 7-5. This is because metaconcrete specimen with ERCSBs has higher strength, which can prolong the local resonance effect and lead to an improved mitigation performance. Besides, S-S3 generally has a higher $R_{p\text{-}DT}$ value than S-S4. This is because ERCSBs/18 with a larger steel core than ERCSBs/15 results in a more prominent local resonance effect, and the gap between RCSB and steel shell in ERCSB/15 might also lead to the less activated steel core vibration as discussed above. In addition, as shown in Table 7-5, localized matrix material damage could also dissipate energy and a lower proportion of input energy are transmitted to the rest part of the specimen. For instance, the front parts of S-S6 and S-S7 are significantly crushed and the rest parts experienced less damage. The failure of the front part dissipated a large amount of energy, which results in a lower proportion of energy being transmitted to the rest part. Therefore, the energy dissipation is contributed by the matrix fracture damage and the local resonance effect. As given in Table 7-5, $R_{p\text{-}DT}$ is 70%, 89% and 90% for S-S6, and 60%, 70% and 75% for S-S7, which are substantially greater than 1.7%, 2% and 5% of S-S5 (i.e., plain concrete). Furthermore, with the increase in loading intensity (i.e., from impulse I to

III), $R_{p\text{-}DT}$ gradually increases for metaconcrete specimens with ERCSBs. It can be explained as follows: a) higher loading amplitude induces larger local vibrations of hard core inside engineered aggregate so that more wave energy is absorbed by the engineered aggregates [151, 152]; b) more severe matrix material damage with the rising loading intensity could dissipate substantial amounts of energy; c) damage of steel shell (e.g., shell opening) outside the ERCSBs (see Table 7-5) could also absorb considerable amounts of wave energy leading to more effective mitigation effect.

As given in Table 7-5, $R_{s\text{-}DT}$ (i.e., the specific reduction ratio of strain with respect to plain mortar) slightly varies for metaconcrete specimens with ERCSBs under different loading scenarios. Metaconcrete specimens with ERCSBs has a higher value of $R_{s\text{-}DT}$ than metaconcrete specimens with RCSBs and followed by plain mortar and plain concrete. For instance, by using Eq. (7-4), a similar trend for the value of $R_{s\text{-}DT}$ is observed in all specimens. Especially, when it is subjected to impulse II, S-S6 has the highest $R_{s\text{-}DT}$ of 93%, followed by S-S7 of 91%, S-S3 of 89% and S-S4 of 87%. $R_{s\text{-}DT}$ of S-S5 is calculated as -200%, indicating S-S5 ($R_{p\text{-}DT} = 2\%$) has a lower mitigation capacity of stress wave propagation than S-S1 ($R_{p\text{-}DT} = 6\%$) as given in Table 7-5. It should be noted that the negative value of $R_{s\text{-}DT}$ indicates that the level of stress wave propagation mitigation in the specific specimen is less than that in the reference specimen (S-S1).

Table 7-5. Summary of destructive testing (DT) results under impulses I, II and III.

No.	Specimen	$R_{p\text{-}DT}$			$R_{s\text{-}DT}$		
		I	II	III	I	II	III
S-S1	Plain mortar	5%	6%	8%	-	-	-
S-S2	Mortar with RCSBs	20%	26%	35%	73%	77%	75%
S-S3	Mortar with ERCSBs/18	52%	57%	61%	90%	89%	86%
S-S4	Mortar with ERCSBs/15	40%	47%	52%	87%	87%	84%
S-S5	Plain concrete	1.7%	2%	5%	-174%	-200%	-73%
S-S6	Concrete with ERCSBs/18	70%	89%	90%	92%	93%	91%
S-S7	Concrete with ERCSBs/15	60%	70%	75%	91%	91%	89%

7.4 Summary

In this chapter, a new kind of engineered aggregate (ERCSB) is proposed to enhance the mechanical properties of conventional metaconcrete material. Quasi-static mechanical properties and dynamic responses of plain mortar, normal concrete and metaconcrete materials with RCSBs or ERCSBs under destructive and non-destructive dynamic loading are experimentally investigated. The experimental results confirm the effectiveness of using ERCSBs in metaconcrete material in enhancing the compressive strength while preserving the wave attenuation ability in comparison with metaconcrete material with conventional RCSBs. The main findings are summarized as follows.

(1) Metaconcrete specimen with randomly dispersed RCSBs could exhibit frequency-dependent attenuation properties, which can mitigate elastic and inelastic stress wave propagation owing to the local resonance effect.

(2) The quasi-static compressive property of metaconcrete specimen with RCSBs is reduced due to the soft coating of conventional EAs (RCSBs). It can be addressed by adding a hard shell outside RCSBs to form ERCSBs, which can increase compressive strength by 80.3 % and modulus of elasticity by 72.3% as compared to the metaconcrete specimen with RCSBs.

(3) Metaconcrete specimen with ERCSBs also exhibits frequency-dependent wave filtering capacity, resulting in favorable wave attenuation performance. The specimens with both types of ERCSBs (without/with a gap between the external shell and RCSB) are effective in mitigating stress wave propagation induced by non-destructive and destructive dynamic loading.

(4) Insufficient bonding between the matrix and EAs negatively impacts both the static mechanical properties and dynamic responses of metaconcrete material. To improve the performance of metaconcrete material, mechanical or chemical treatment on ERCSBs' outer layer is recommended to improve its bonding strength.

Chapter 8 Dynamic compressive properties of metaconcrete materials

8.1 Introduction

The responses of metaconcrete structures subjected to vibration and impulsive loading and their stress wave attenuation performances have been discussed in Chapter 3 to Chapter 6. Metaconcrete materials, therefore, have great potential for application in the construction of engineering structures against multi-hazardous loading such as earthquakes, dynamic impacts and explosions. In Chapter 7, static mechanical properties of metaconcrete materials with different types of engineered aggregates have been studied. For the practical application of metaconcrete material in construction, the dynamic material properties need to be defined for structural designs, however, it has not been reported yet in the literature. The dynamic compressive properties of metaconcrete materials containing three types of engineered aggregates are therefore examined and reported in this chapter. Dynamic compression tests on the mortar-based and concrete-based metaconcrete materials are conducted by using the Split Hopkinson Pressure Bar (SHPB) system. Failure process, failure modes, dynamic compressive strength as well as energy absorption capacities at different strain rates of metaconcrete specimens are obtained. Using the static material properties obtained in Chapter 7 as a reference, dynamic increase factor (DIF) for compressive strength and energy absorption capacity of metaconcrete materials are derived and the corresponding empirical formulae are proposed. The results can be used to model the dynamic properties of metaconcrete materials in structural designs to resist dynamic loads.

The related work in this chapter has been submitted to a journal for review.

8.2 Experimental program

8.2.1 Specimen preparation

As introduced above, in this chapter, three types of engineered aggregates (EAs) are used to cast metaconcrete specimens, they are rubber-coated steel balls (RCSBs) and two types of RCSBs with an enhanced coating (i.e., ERCSBs). Specifically, RCSBs are made of steel balls coated with silicone rubber. The dome-shaped rubber coating is prepared by using the moulding technique. The steel ball is subsequently encapsulated by the upper and lower dome-shaped rubber coating, followed by a curing process. ERCSBs are made by adding a steel shell outside the RCSB. ERCSB/18 is made by adding a 1 mm-thick steel shell directly on the 18 mm RCSB, while ERCSBs/15 is made by adding the same 18 mm internal diameter steel shell on the 15 mm RCSB, which therefore leaves a 3 mm clearance between RCSB and the external steel shell wall as shown in Figure 8-1.

All specimens can be classified into two groups, namely mortar-based and concrete-based specimens, as illustrated in Figure 8-1. There are no natural aggregates (NAs) in the mortar-based specimens. High strength mortar is used as the matrix of all specimens. The mortar is produced by *Sika Australia Pty Ltd* consisted of Portland cement, fine sand and additives (calcium alumina-sulphate) [124]. The mix ratio of cement/sand/water/additives is 1/2/0.5/0.33. D-S1 is made of plain mortar only. D-S2 is made of plain mortar and RCSBs. D-S3 and D-S4 with two kinds of ERCSBs are fabricated to evaluate the effect of different embedded inclusions on the dynamic behaviors of mortar-based metaconcrete specimens. The volume percentages of the EAs in D-S2, DS-3 and DS-4 are all 10.6%. DS-5 is a normal or plain concrete specimen with 41.8% volume fraction of natural aggregates. DS-6 is a metaconcrete specimen made by replacing 10.6% volume fraction of natural aggregates in DS-5 by ERCSBs/18, while DS-7 is made by replacing 10.6% natural aggregates in DS-5 by ERCSBs/15. In another word, concrete-based metaconcrete specimens consisted of 10.6% of engineered aggregates in combination with 31.2% of natural aggregates. The maximum size of natural aggregates (NAs) is 10 mm and that of EAs, including RCSBs and ERCSBs, are

all 20 mm. The mix proportions are listed in Table 7-1 in Chapter 7. It is worth noting that the heterogeneity effect of aggregates can be ignored when the diameter of the specimen is at least three times the maximum size of coarse aggregate, as reported in [155]. In this chapter, the diameter of the specimens is 5 times the size of the maximum aggregate (i.e., 20 mm), therefore, the heterogeneity effect can be neglected. The disc-like specimens with a height of 50 mm and a diameter of 100 mm (see Figure 8-2(a)-(c)) for the dynamic test are prepared by using the moulding technique. In total, 84 discs ($\emptyset 100 \times 50 \mathrm{~mm}$) for dynamic compression tests are prepared. A plain mortar specimen (D-S1) without aggregates is regarded as the reference. RCSBs and/or ERCSBs are randomly mixed with a mortar or concrete matrix by using a 70L pan mixer. The average density for each specimen is determined in accordance with [154] and listed in Table 8-1. More detailed information on the specimen configuration is also presented in Table 8-1.
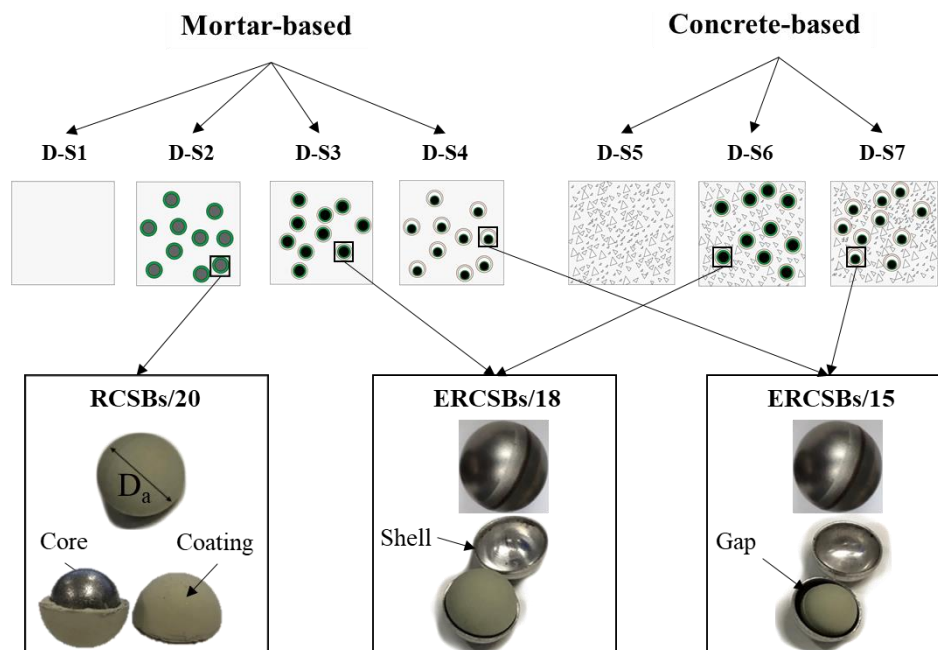
Figure 8-1. Configuration of specimens and engineered aggregates.
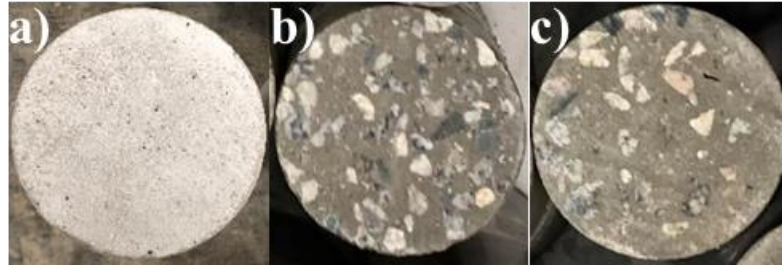
Figure 8-2. Illustration of specimens after surface-grinding: (a) Mortar-based specimen, (b) Plain concrete, (c) concrete-based metaconcrete specimens.

Table 8-1. Summary of specimen configuration.

Specimen	Description	Inclusions	V_{NA}%	V_{EA}%	ρ_{ave} (kg/m³)
D-S1	Plain mortar	-	0	-	2183.8
D-S2	Mortar with RCSBs	Rubber-coated steel balls (RCSBs)	0	10.6%	2477.5
D-S3	Mortar with ERCSBs/18	18 mm rubber-coated steel balls with enhanced coating (ERCSBs/18)	0	10.6%	2504.9
D-S4	Mortar with ERCSBs/15	15 mm rubber-coated steel balls with an enhanced coating (ERCSBs/15)	0	10.6%	2325.3
D-S5	Plain concrete	Natural aggregates (NAs)	41.8%	0	2285.7
D-S6	Concrete with ERCSBs/18	NAs + ERCSBs/18	31.2%	10.6%	2658.9
D-S7	Concrete with ERCSBs/15	NAs + ERCSBs/15	31.2%	10.6%	2463.9

Note: V_{NA}% is the volume fraction of natural aggregates; V_{EA}% is the volume fraction of engineered aggregates, ρ_{ave} is the average density.

8.2.2 Dynamic compression test setup

Dynamic compression tests are conducted by using the Split Hopkinson pressure bar (SHPB) system, which has been widely used to determine the dynamic properties of concrete-like materials [126, 169-174]. As illustrated in Figure 8-3, the SHPB system with a diameter of 100 mm consisted of a cylindrical striker, incident and transmitted bars together with absorption bar with the length of 600 mm, 5500 mm, 3000 mm, and 1000 mm, respectively. A total of 84 disc-like specimens are tested. For each configuration, three specimens are repetitively tested under a similar strain rate as close as possible. Stress wave signals are recorded from the strain gauges attached to the incident and transmitted bars. To minimize the effect of end friction, the grease is attempted to apply to the interfaces between specimens

and bars. Moreover, a 3 mm-thick Ø20 mm rubber pulse shaper as shown in Figure 8-3(b) is used to facilitate stress equilibrium [175]. The failure progress of each specimen is recorded by using a high-speed camera.

(a)

(b)
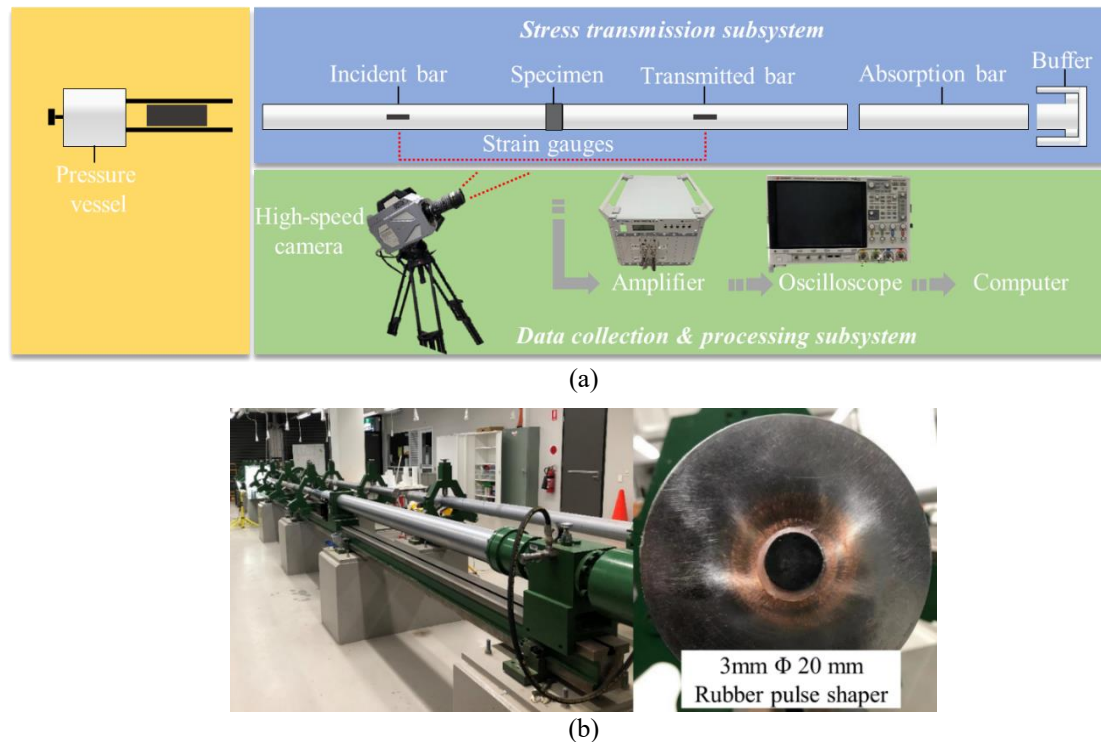
Figure 8-3. Experimental set-up: (a) Schematic illustration, (b) Photograph.

8.3 Results and discussions

8.3.1 Quasi-static test results

Quasi-static tests are conducted in Chapter 7 and the results are presented in Section 7.3.1. A total of 21 Ø100 × 200 mm cylindrical specimens are fabricated in accordance with ASTM C192/C192M-19 [160] and the quasi-static compression test on these specimens is conducted with a loading rate of 0.33 MPa/min (the equivalent strain rate of $10^{-4}\,s^{-1}$) according to ASTM C39-18 [161]. The results from the quasi-static test reported in Section 7.3.1. are presented in Figure 8-4 for comparison. As shown, the quasi-static compressive strength is decreased when adding RCSBs. Specifically, the compressive strength of plain mortar (D-S1) is 67.49 MPa. As compared to D-S1, the compressive strength of D-S2 is decreased by 55.6% to 29.98 MPa, which is due to the existence of a soft coating layer of RCSB. As compared to the mortar-based metaconcrete specimens with RCSBs, the compressive strength of

metaconcrete specimens D-S3 and D-S4 are increased by 80.3% and 85.4% to 54.97 MPa and 55.57 MPa in comparison with D-S2 by replacing 10.6% RCSBs with ERCSBs/18 and ERCSBs/15, respectively in the mortar matrix. Moreover, the compressive strengths of concrete-based specimens are 67.92 MPa (D-S5), 56.19 MPa (D-S6) and 56.81 MPa (D-S7). It is observed that although the quasi-static compressive strength of metaconcrete material is substantially improved by adding a relatively stiff layer outside the conventional RCSBs, metaconcrete specimens with ERCSBs still have lower compressive strength than the respective plain mortar (D-S1) and plain concrete (D-S5) owing to the poor bonding between ERCSBs and the surrounding matrix at the interfacial transition zone (ITZ) because of the smooth surface outside the steel shell of ERCSBs. The effect of poor bonding between inclusions and cementitious matrix on the reduction of compressive strength has been reported and discussed in previous studies [126, 169]. As a consequence, it is suggested that the bonding between ERCSBs and cementitious matrix needs to be enhanced through a mechanical or chemical treatment to improve its mechanical strength. A more detailed discussion about the quasi-static mechanical properties of metaconcrete materials can refer to Chapter 7 in Section 7.3.1.
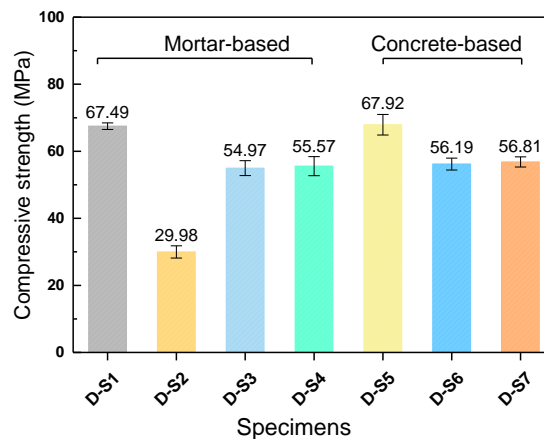
Figure 8-4. Summary of quasi-static compressive strengths of plain mortar, concrete and metaconcrete specimens.

8.3.2 Validity and strain rate determination of SHPB dynamic tests

Figure 8-5 shows the typical recorded signals at the incident and transmitted bars. One-dimensional wave propagation theory is applied. The stress (σ), strain (ε) and strain rate ($\dot{\varepsilon}$)

of the specimens can be derived from Eq. (8-1) ~ Eq. (8-3), respectively [170, 171, 176-178].

$$\sigma_t = E_b\left(\frac{A_b}{A_s}\right)\varepsilon_T(t) \tag{8-1}$$

$$\dot{\varepsilon}(t) = -\frac{2C_0}{L}\varepsilon_R(t) \tag{8-2}$$

$$\varepsilon(t) = \int_0^T \dot{\varepsilon}(t)\,dt \tag{8-3}$$

where E_b, A_b and C_0 respectively denote the modulus of elasticity, cross-section area and wave velocity of the pressure bars; A_s and L represent the cross-section area and length of the specimen, respectively; $\varepsilon_T(t)$ and $\varepsilon_R(t)$ are the time-dependent transmitted and reflected strain, respectively.
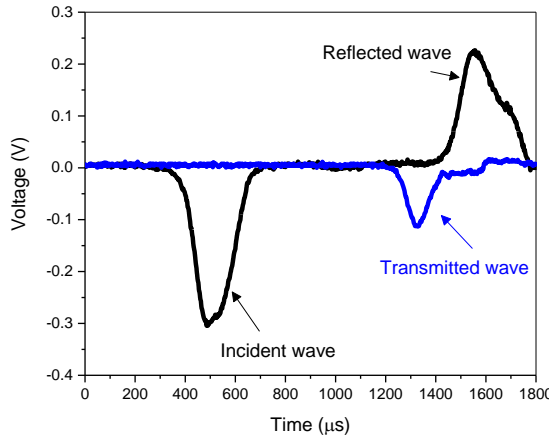
Figure 8-5. Typical signals recorded at the incident and transmitted bars.

Stress equilibrium must be achieved to ensure the validity of the SHPB test data. Hence, stress equilibrium is checked for each test data by comparing the sum of the incident and reflected stress waves with the transmitted wave. For strain rate determination, two frequently used approaches to determine the strain rate are reported in the previous studies [126, 169, 171, 178, 179]. One method is based on the peak dynamic compressive stress at which the corresponding strain rate is determined. Another method adopted the averaged strain rate values from the plateau of the strain rate curve. In this chapter, the strain rate is determined based on the peak compressive stress, as exemplified in Figure 8-6. Subsequently, stress equilibrium in all testing samples is assessed and verified by applying the abovementioned method. All the reported data are from those specimens that achieved the stress equilibrium while invalid data are discarded. The stress equilibrium of representative plain mortar, concrete and metaconcrete specimens is demonstrated in

Figure 8-7. As shown, the incident + reflected and transmitted waves match well from the beginning to the peak value, indicating that the stress equilibrium is achieved until the peak stress. After the peak stress, the deviation between transmitted and incident + reflected waves in all the specimens is observed, especially at higher strain rates. It is because the cementitious matrix displays brittle post-peak behavior and the compressive stress reduces significantly after the peak [126, 163, 169, 172]. Accordingly, the stress equilibrium at the later stage is more difficult to achieve as shown in Figure 8-7 owing to the damage to the specimen. Besides, the surface-to-surface contact between steel bars and specimens may also affect the stress equilibrium condition. It is noted that the end faces of the specimens could not be perfectly parallel to achieve full surface contact despite the use of the automatic surface grinder to smoothen the surface as much as possible. The variation of thickness can be up to 0.5 mm [172], which might cause stress localization. This non-uniform contact would be intensified by the specimen damage. Additionally, the contact between engineered aggregates and steel bars as well as the damage of steel shells outside the ERCSBs may also affect the distribution of stress at the later post-peak stage. Consequently, the distribution of stress would not be uniform, therefore, it is difficult to achieve a perfect stress equilibrium condition in the high-speed dynamic tests after damage to specimen that has occurred. Although the perfect stress equilibrium as shown in Figure 8-7 is hard to achieve after the peak stress, the reported data in this chapter is still acceptable because the primary interest in the test is to investigate the increment in the dynamic strength with the strain rate, the dynamic strength, i.e., the peak stress is obtained when the dynamic equilibrium condition is still satisfied.
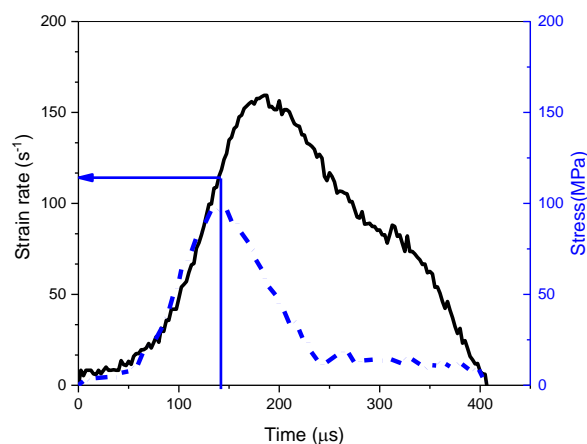
Figure 8-6. Strain rate determination.
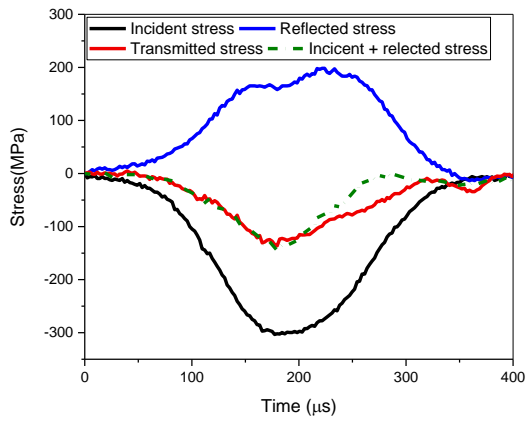
(a) Typical stress equilibrium of SHPB test.
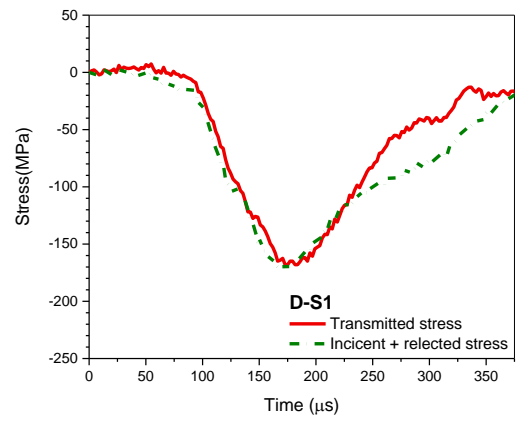
(b) D-S1
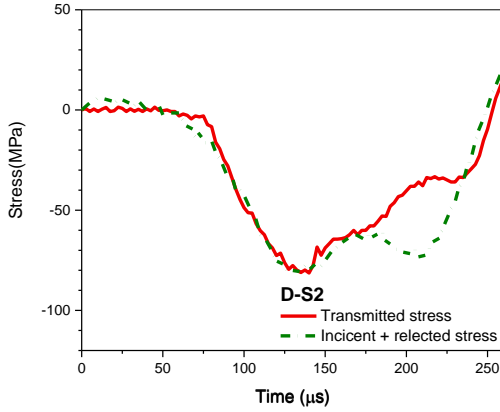
(c) D-S2
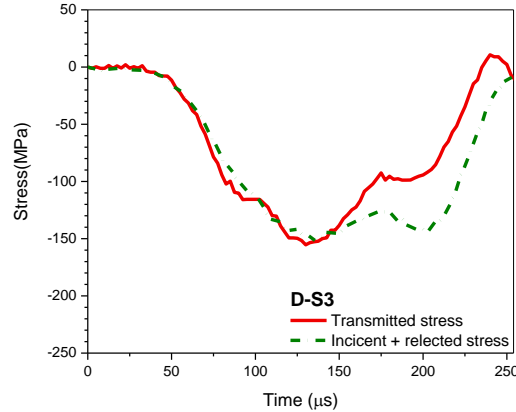
(d) D-S3
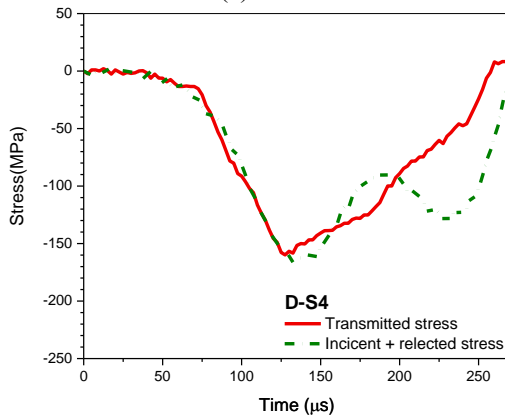
(e) D-S4
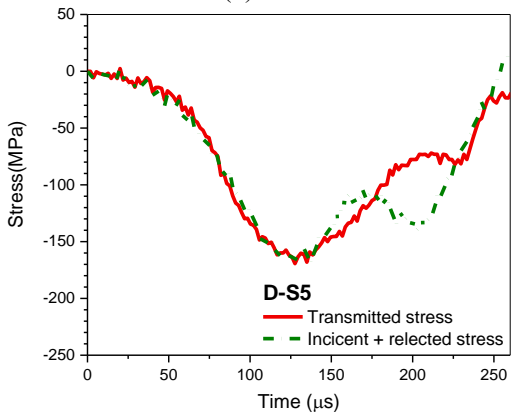
(f) D-S5
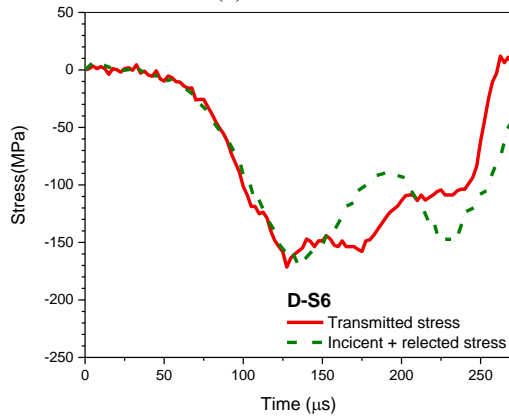
(g) D-S6
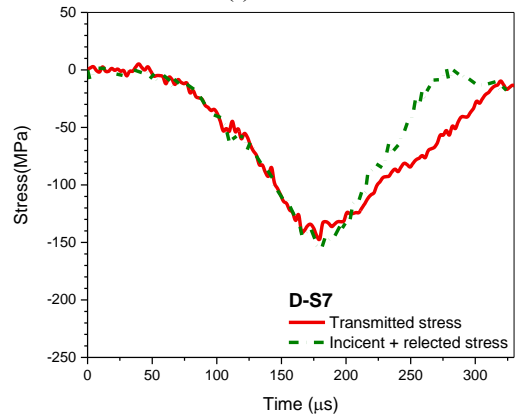
(h) D-S7

Figure 8-7. Illustration of stress equilibrium for each configuration.

173

8.3.3 Failure process

Figure 8-8 depicts the failure process of all types of specimens under strain rates around 120 s^{-1} recorded by a high-speed camera with a frame rate of 12500 frames per second. The image at 0 μs denotes the time instant when the specimen started being stressed. For the plain mortar specimen D-S1 at 80 μs, cracks are initiated at both ends and propagated towards the centre of the specimen, indicating the stress equilibrium [126]. Afterwards, the initial cracks are widened and extended and more cracks have appeared in the specimen. At the same instant, D-S2 exhibits more cracks than plain mortar (D-S1). Figure 8-8(b) shows more than ten cracks developed in D-S2 at 80 μs, while there are three major cracks and four minor cracks in D-S1 (see in Figure 8-8(a). This is because: a) D-S2 has much lower compressive strength and b) the cementitious matrix is vulnerable to damage due to the mismatched modulus of elasticity and deformation capacity between mortar and silicone rubber. Adding a steel shell could slow down the crack development, as observed in D-S3 and D-S4, as shown in Figure 8-8(c) and (d). This is because adding a steel shell enhanced its compressive strength as compared to D-S2.

At 160 μs, more fine cracks are initiated and propagated to the centre of the specimens with some other cracks spreading in different directions for all the specimens. From 160-240 μs, plain mortar and concrete specimens (i.e., D-S1 and D-S5) have several major cracks running almost parallel to the loading direction plus several smaller cracks. More fine cracks are observed in the metaconcrete specimens because of their relatively lower compressive strength. In particular, numerous cracks are observed at the surface edge of D-S2. Although the cracks are inhibited at an earlier stage (<160 μs) for D-S3, numerous fine cracks are found at 240 μs due to the poor bonding between ERCSBs and the mortar matrix at the interfacial transition zone (ITZ), leading to more severe damage. A similar phenomenon is observed for D-S5, D-S6 and D-S7. At 320 μs, all the specimens are almost broken into pieces. The numbers of major cracks are unchanged while the existing cracks are widened. Eventually, all the specimens are shattered into pieces due to the brittle nature of the mortar matrix. It is

observed that the metaconcrete specimens with ERCSBs are shattered into relatively larger pieces than the specimens with RCSBs.
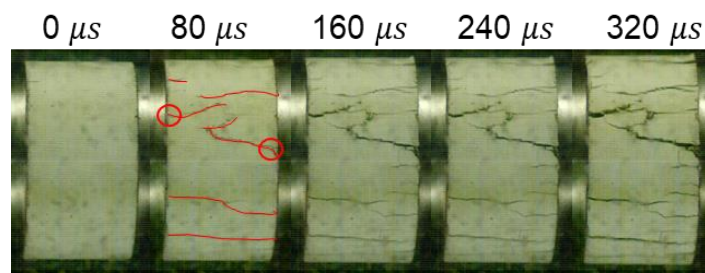
(a) D-S1
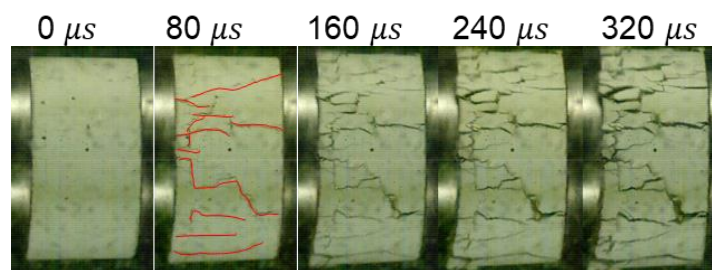
(b) D-S2

(c) D-S3

(d) D-S4

(e) D-S5

(f) D-S6

(g) D-S7
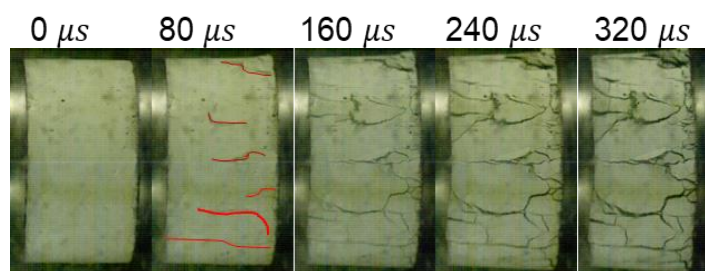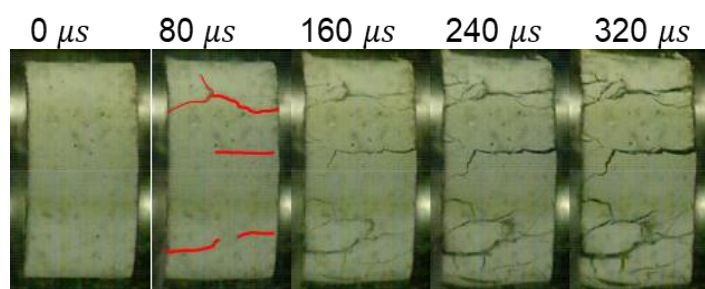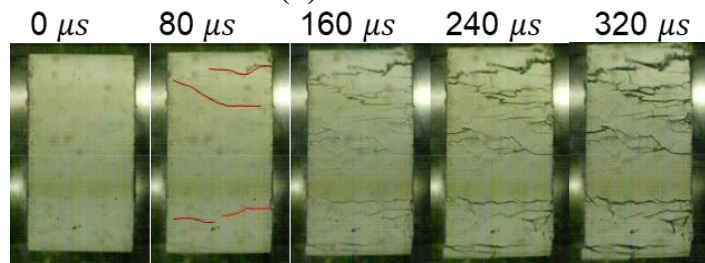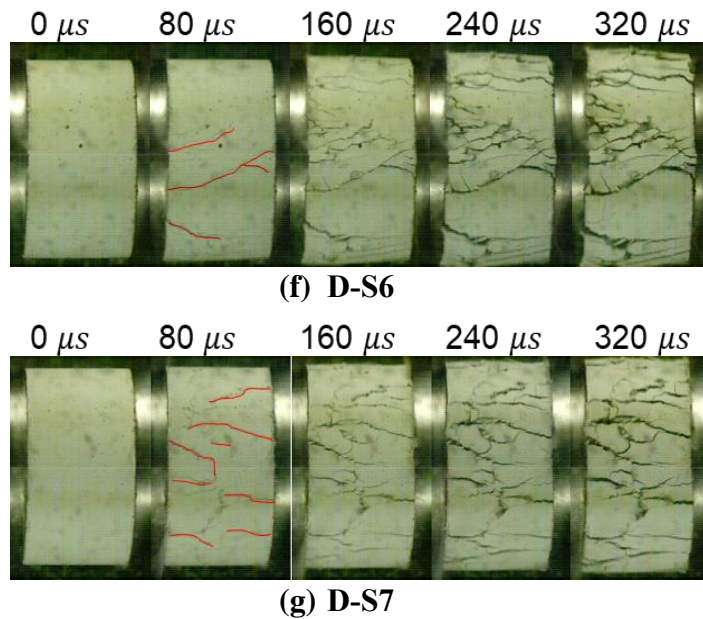
Figure 8-8. Illustration of failure process of representative specimens at the strain rate about 120 s^{-1}.

8.3.4 Failure mode and failure mechanism

Figure 8-9 compares the failure modes of all types of specimens at different strain rates. In general, the damage level is increased with the rising strain rate for all the specimens. The final failure modes for all the specimens can be categorized as: 1) a dominant crack penetrating through the specimen under low to medium strain rate, and 2) crushing into chunks and pulverized in numerous fragments under high strain rate. The fragment size is dependent on the applied strain rates as the fragment size is decreased with the increase of strain rates, consistent with those reported in [179-181]. Under low to medium strain rate around 45.72 ~ 63.54 s^{-1} as shown in Figure 8-9, plain mortar (D-S1) is experienced a major crack cutting through the specimen together with several edge cracks. Plain concrete (D-S5) is failed at the outer edges, in which several chunks are stripped away from the centre part. A similar failure mode is observed for all metaconcrete specimens with ERCSBs (i.e., D-S3, D-S4, D-S6 and D-S7), which are failed from the outer edges and the central part remained intact. Nevertheless, D-S2 is experienced more severe damage and shattered into several chunks. This is mainly because of its lower compressive strength.

At the strain rate of 74.28 ~ 76.12 s^{-1}, the primary difference among the specimens is that cracks start to cut through natural aggregates as shown in concrete-based specimens. When

the strain rate reached 83.32 ~ 96.37 s^{-1}, mortar-based specimens are broken into smaller pieces. With a further increase in strain rate, the fragment size becomes smaller, leading to higher energy absorption during the brittle fracture of the matrix/and or normal aggregates. When the strain rate is 110.71 ~ 119.35 s^{-1}, cracks are developed by cleaving the matrix into even smaller pieces, leading to numerous fragments. All the specimens are drastically pulverized into fragments when the strain rate reached above approximately 140 s^{-1}. For concrete-based metaconcrete specimens (D-S6 and D-S7), the damage is observed in natural aggregates due to cracks cutting through natural aggregates. Besides, the steel shell of ERCSBs is damaged by creating an opening or being detached when the specimen experienced damage beyond a certain strain rate threshold, as shown in Figure 8-9. It is also observed that for ERCSBs with the gap (ERCSBs/15), the steel shell is experienced indentation or deformation due to dynamic crushing.

Meanwhile, the mortar-based specimens containing ERCSBs (i.e., D-S3 and D-S4) demonstrate a better loading resistance than the specimens without the hard shell (i.e., D-S2) under a relatively low strain rate. For instance, at the strain rate of 45.72 s^{-1} ~ 63.54 s^{-1}, the metaconcrete specimens with ERCSBs are suffered less damage than the metaconcrete specimens with RCSBs. This is because the enhanced coating layer of ERCSBs has higher stiffness than rubber coating, which enhances the compressive strength of the metaconcrete specimen. On the other hand, when the strain rate is increased above a certain threshold, i.e., between 106.94 s^{-1} ~ 125.60 s^{-1}, the steel shell outside the ERCSBs starts opening/detaching. With further increasing in strain rate, the steel shell outside the ERCSB is completely detached and the enclosed RCSB is exposed as shown in Figure 8-9. Besides, the number of ERCSBs in metaconcrete specimens that experienced shell damage is increased and the severity of shell damage is positively correlated to the increase in strain rate.

	61.46/s	83.32/s	109.86/s	142.33/s
D-S1 **Plain mortar**				
	63.54/s	86.52/s	106.94/s	152.92/s
D-S2 **Mortar with RCSBs**				
	55.23/s	96.37/s	125.60/s	148.62/s
D-S3 **Mortar with ERCSBs/18**	Edge failure		Shell opening	Shell detaching
	45.72/s	79.54/s	110.01/s	144.35/s
D-S4 **Mortar with ERCSBs/15**			Shell detaching	Shell detaching
	53.12/s	74.61/s	119.35/s	148.36/s
D-S5 **Plain concrete**				
	46.52/s	76.12/s	110.71/s	145.60/s
D-S6 **Concrete with ERCSBs/18**				
	50.09/s	74.28/s	110.85/s	142.16/s
D-S7 **Concrete with ERCSBs/15**			Shell opening Indentation	Detached shells Exposed RCSBs Shell detaching

No shell damage ◄————► With shell damage

Figure 8-9. Comparison of failure modes for each configuration at various strain rates.

It is commonly observed that the failure mechanisms of concrete-like materials can be divided into different stages with the increased strain rates, i.e. matrix cleavage, and cutting or fracture of aggregates [178]. However, the observed failure modes of metaconcrete specimens with engineered aggregates are different from those of normal concrete with natural aggregates. Under a relatively low strain rate, for normal concrete (i.e., left of Figure 8-10(a)), the cracks are developed and propagated inside the matrix without damaging the coarse aggregates. For metaconcrete specimens with RCSBs (i.e., left of Figure 8-10(b)), the

cracks are initiated at the interfacial area between EAs and mortar, then propagated within the matrix. Similarly, this failure mechanism is also observed in the metaconcrete specimens with ERCSBs (i.e., left of Figure 8-10(c) and (d)). Consequently, the specimen is failed into large pieces due to matrix damage. With the increase of the strain rates, the cracks are propagated along the shorter path in the normal concrete, resulting in fracture of stiffer coarse aggregates (i.e., the centre of Figure 8-10(a)). However, this failure mechanism is not observed in metaconcrete specimens with RCSBs. For metaconcrete specimens with RCSBs, more cracks are developed without cutting through RCSBs (i.e., the centre of Figure 8-10(b)) due to the high strength of the solid steel core. For metaconcrete specimens with ERCSBs, the cracks are propagated along a short path and the steel shell started detaching (i.e., centre of Figure 8-10(c) and (d)).
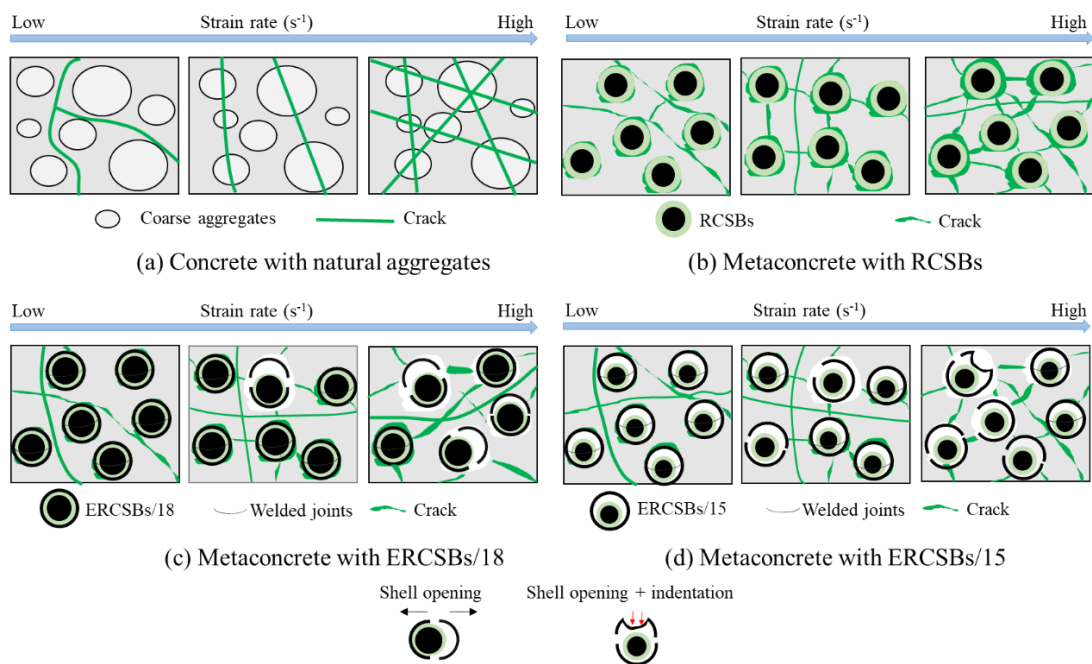
Figure 8-10. Illustration of failure mechanism associated with the specimen in different configurations.

When further increasing the strain rate, larger numbers of cracks are developed, and more coarse aggregates are fractured in the normal concrete (i.e., right of Figure 8-10(a)). For metaconcrete specimens with RCSBs, the matrix is shattered into smaller pieces without damage to RCSBs. For metaconcrete specimens with ERCSBs without gap (i.e., ERCSBs/18), the steel shell is separated into two pieces and severe matrix cracking is observed (i.e., right of Figure 8-10(c)). For ERCSBs with the gap, the increasing numbers of cracks are observed

with the increase in strain rate. Meanwhile, the shell separation in combination with indentation and deformation of the shell wall is also noticed (i.e., right of Figure 8-10(d)). As expected, increasing the loading intensity causes more severe damage to the steel shell outside the ERCSBs.

8.3.5 Comparison of stress-strain relationships

The stress-strain curves for each configuration at the representative strain rates are illustrated in Figure 8-11(a) to (e). As observed, the dynamic compressive strength increases with the increase in strain rates for all the specimens, consistent with the previous findings regarding the strain rate effect on the dynamic compressive properties of concrete-like materials [179-181]. The stress-strain curves also showed that plain mortar (D-S1) and plain concrete (D-S5) have higher dynamic compressive strength than metaconcrete specimens with ERCSBs and metaconcrete specimens with RCSBs under similar strain rate. It is because the static compressive strength of the plain specimens is higher than that of the metaconcrete specimens as shown in Figure 8-4. Specifically, the dynamic compressive strength of the plain mortar (D-S1) increases from 85.89 MPa at 61.46 s^{-1} to 167.19 MPa at 142.33 s^{-1}. The dynamic compressive strength of plain concrete (D-S5) increases from 81.69 MPa at 53.12 s^{-1} to 169.35 MPa at 148.36 s^{-1}. Figure 8-11(b) shows that the dynamic compressive strength of metaconcrete specimens with RCSBs (D-S2) increases from 56.05 MPa at 63.54 s^{-1} to 126.21 MPa at 152.92 s^{-1}, indicating the compressive strength of metaconcrete specimens with RCSBs is highly sensitive to strain rate. Figure 8-11(c) and (d) show that the dynamic compressive strength of metaconcrete specimens with ERCSBs/18 (D-S3) increases from 71.13 MPa at 55.23 s^{-1} to 176.58 MPa at 148.62 s^{-1} and the dynamic compressive strength of metaconcrete specimens with ERCSBs/15 (D-S4) increases from 68.78 MPa at 45.72 s^{-1} to 163.44 MPa at 144.35 s^{-1}. A similar trend is also observed in concrete-based specimens, as shown in Figure 8-11(e)-(g).
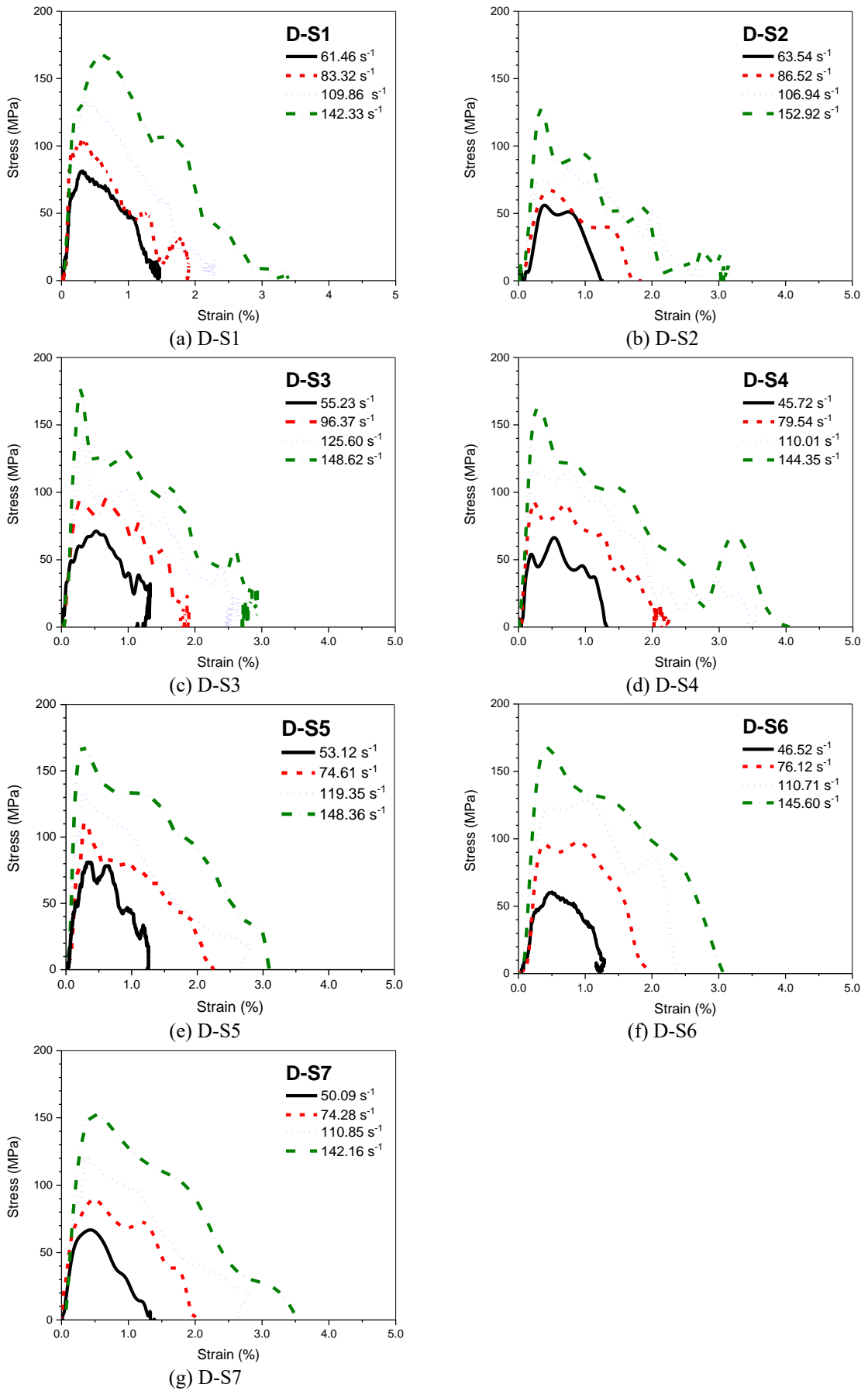
Figure 8-11. Dynamic compressive stress-strain curves.

Moreover, the failure mechanism as discussed in Section 8.3.4 can help to explain the strain rate effect on the dynamic compressive strength of tested specimens. For plain mortar (D-S1), the sand-matrix interfacial transition zone is weaker than the cement pastes and sand particles themselves. Therefore, the cracks are prone to pass these weak spots or air voids at a low strain rate, while the cracks are forced to cut off stiffer sand particles with a rising strain rate. Thus, it causes an increment of the dynamic strength. Similarly, when plain concrete is experienced intensive impact loading, the cracks are prone to propagate along shorter and straighter paths by means of cutting through stronger and stiffer coarse aggregates, leading to a higher strength. For metaconcrete specimens with ERCSBs, the induced cracks tend to cause the breakage or/and deformation of steel shells, resulting in an increase in dynamic strength. Therefore, crack propagation could influence the dynamic compressive strength and energy absorption capacities of the specimen. There are also other mechanisms such as the viscosity effect of free water on cementitious material (e.g., matrix) that could also contribute to the enhancement of the dynamic strength of materials [182, 183].

8.3.6 Strain rate effects on dynamic compressive strength

The conventional approach to calculate the dynamic increase factor (DIF) of the compressive strength is to normalize the dynamic compressive strength with the quasi-static compressive strength [171, 172, 178]. However, as commonly agreed now that some other factors not related to material properties may also result in an increase in the dynamic compressive strength, including lateral inertial confinement and the end friction produced between the impact bars and specimen. This could result in overestimating the DIF, especially under a high strain rate [116, 184]. In this chapter, the end friction is minimized by using grease at both ends of the specimens as well as the attached bars. Meanwhile, the contribution of lateral inertia confinement to the DIF of compressive strength is removed according to the approach suggested in the previous studies [116, 184]. The method has been commonly adopted to eliminate the lateral inertia effect in dynamic tests on the dynamic compressive strength of concrete-like materials [170, 178, 180]. The true DIF (DIF_T) can be obtained based on the

following equation [116, 184]:

$$DIF_T = DIF_E - DIF_i + 1 \qquad\qquad (8\text{-}4)$$

where DIF_E stands for DIF directly obtained from dynamic tests; DIF_i represents the contribution of lateral inertia confinement to the obtained DIF in tests, which can be obtained from numerical simulations without considering strain rate effect as reported in [116, 184].

In this chapter, only 10.6% of engineered aggregates are used in metaconcrete specimens. As a result, the maximum ratio of average density between metaconcrete specimens (e.g., D-S6) and referenced one (D-S5) is only 1.16 as given in Table 8-1, indicating the variation of total weight between concrete specimens and metaconcrete specimens is limited. The empirical formula suggested for normal concrete to remove the lateral inertia confinement effect is therefore approximately adopted to remove the lateral inertia confinement effect on metaconcrete specimens in this chapter. As stated in the previous studies [116, 184], SHPB tests on concrete specimens at different strain rates are numerically simulated by defining the material DIF value as 1.0, namely, the strength increment of the material is purely attributed to the lateral inertia confinement. The suggested empirical formula reported in [116, 184] for estimating the contribution of lateral inertia confinement of $\varnothing 100 \times 50$ mm specimens is then derived. The true DIF (DIF_T) is obtained by Eq. (8-4). Table 8-2 to Table 8-8 give the dynamic compressive strength and compressive strength DIFs of all the specimens at various strain rates. For comparison, Figure 8-12 depicts the relationship of DIF for compressive strength versus strain rates for each configuration. The DIF of compressive strength for all the specimens is sensitive and positively correlated to the strain rate. Specifically, the DIF_T of plain mortar (D-S1) increases from 1.166 at 61.46 s^{-1} to 2.273 at 149.69 s^{-1}. The metaconcrete specimens with RCSBs (D-S2) exhibit the highest sensitivity of dynamic compressive strength to the strain rate and its DIF_T is 1.430 at 54.26 s^{-1} and increased to 3.678 at 152.92 s^{-1}, and it is 61.8 % and 68.4 % higher than that of plain mortar and plain concrete at the similar strain rate, respectively. Besides, DIF_T for metaconcrete specimens with ERCSBs/18 (D-S3) is 1.066 at 47.06 s^{-1} and increases to 2.812 at 148.62 s^{-1}, followed by

metaconcrete specimens with ERCSBs/15 (D-S4) increases from 1.027 at 43.87 s^{-1} to 2.632 at 149.23 s^{-1}. The CEB recommendation [185] for normal concrete is also plotted for comparison, which shows a similar trend as plain concrete (D-S5). For concrete-based specimens, DIF_T for plain concrete (D-S5) increases from 1.093 at 46.87 s^{-1} to 2.183 at 148.36 s^{-1}. DIF_T of metaconcrete specimens with ERCSBs/18 (D-S6) increases from 1.031 at 43.62 s^{-1} to 2.647 at 149.92 s^{-1}, followed by metaconcrete specimens with ERCSBs/15 (D-S7) increases from 1.073 at 42.67 s^{-1} to 2.465 at 149.33 s^{-1}.

Among all the mortar-based specimens, D-S2 displays the highest strain rate sensitivity on the compressive strength. It is then followed by metaconcrete specimens with ERCSBs/18 (D-S3) and then ERCSBs/18 (D-S4), while plain mortar (D-S1) exhibits the lowest strain rate sensitivity. The concrete-based specimens exhibit a similar trend as mortar-based specimens. Metaconcrete specimens with ERCSBs have a higher sensitivity of strain rate on the compressive strength than plain concrete. It is mainly due to different types of failure mechanisms, cracking characteristics and damage modes at different strain rates as discussed in Section 8.3.4. Specifically, the reason that the metaconcrete specimens with RCSBs (D-S2) exhibit the highest strain rate sensitivity on the compressive strength can be explained as follows: 1) D-S2 has the lowest static compressive strength due to the existence of soft coating and thus the similar strength enhancement under dynamic loading could lead to higher DIF; 2) although steel cores of RCSBs in metaconcrete specimens are not damaged under dynamic loading, the damage to the soft coating of RCSBs could dissipate a certain amount of energy. In addition, the crack arresting mechanism of the rubber coating may contribute to the enhanced dynamic strength of rubberized concrete as reported in the previous studies [126, 186]; 3) more cracks are generated at the interface of D-S2 and more wave energy are dissipated, leading to a more pronounced effect on strength enhancement; 4) metaconcrete specimens with 10.6% of engineered aggregates such as RCSBs could lead to higher compressive DIF than normal concrete due to slightly higher inertial effect induced by dense steel core of engineered aggregates. For metaconcrete with ERCSBs, stress wave propagation in ERCSBs causes the deformation or/and damage of steel shell, resulting in the

dissipation of impact energy and the enhancement of dynamic strength. Besides the shell damage, soft coating damage and the contribution of inertia effect from steel inclusion contribute to the enhancement of dynamic strength, resulting in higher strain rate sensitivity. It is worth noting that the dynamic strength of metaconcrete specimens with RCSBs is lower than that of metaconcrete specimens with ERCSBs at a similar strain rate, indicating lower impact resistance, despite the dynamic compressive strength of the metaconcrete specimens with RCSBs being the most sensitive to strain rate.

(a) Mortar-based specimens   (b) Concrete-based specimens
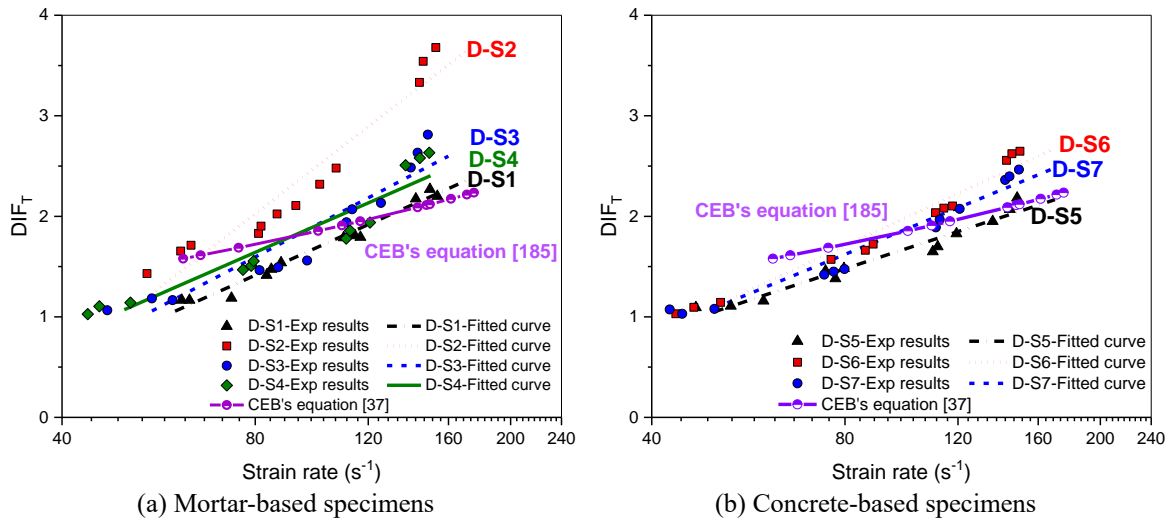
Figure 8-12. Comparison of DIF for the compressive strength under different strain rates.

Based on Figure 8-12, the empirical equations for the best-fit curves between DIF for compressive strength and strain rate ($\dot{\varepsilon}$) of different types of specimens are given as follows.

For D-S1 (Plain mortar):

$$DIF = 2.863\log_{10}(\dot{\varepsilon}) - 4.043 \quad for \ 61.46\,s^{-1} < \dot{\varepsilon} < 153.75\,s^{-1} \ (R^2 = 0.976) \tag{8-5}$$

For D-S2 (Mortar with RCSBs)

$$DIF = 4.931\log_{10}(\dot{\varepsilon}) - 7.359 \quad for \ 54.26\,s^{-1} < \dot{\varepsilon} < 152.92\,s^{-1} \ (R^2 = 0.927) \tag{8-6}$$

For D-S3 (Mortar with ERCSBs/18)

$$DIF = 3.331\log_{10}(\dot{\varepsilon}) - 4.744 \quad for \ 47.06\,s^{-1} < \dot{\varepsilon} < 148.62\,s^{-1} \ (R^2 = 0.895) \tag{8-7}$$

For D-S4(Mortar with ERCSBs/15)

$$DIF = 2.791\log_{10}(\dot{\varepsilon}) - 3.671 \quad for \ 43.87\,s^{-1} < \dot{\varepsilon} < 149.23\,s^{-1} \ (R^2 = 0.898) \tag{8-8}$$

For D-S5 (Plain concrete)

$$DIF = 2.0999\log_{10}(\dot{\varepsilon}) - 2.518 \quad for \ 46.87\,s^{-1} < \dot{\varepsilon} < 148.36\,s^{-1} \ (R^2 = 0.958) \tag{8-9}$$

For D-S6 (Concrete with ERCSBs/18)

185

$$DIF = 2.964\log_{10}(\dot{\varepsilon}) - 3.936 \quad for \ 43.62s^{-1} < \dot{\varepsilon} < 149.92s^{-1} \ (R^2 = 0.965) \tag{8-10}$$

For D-S7 (Concrete with ERCSBs/15)

$$DIF = 2.631\log_{10}(\dot{\varepsilon}) - 3.385 \quad for \ 42.67s^{-1} < \dot{\varepsilon} < 149.33s^{-1} \ (R^2 = 0.960) \tag{8-11}$$

8.3.7 Strain rate effect on energy absorption capability

Energy absorption capacities (W) can be calculated by the enclosed area of stress-strain curves (e.g., Figure 8-11(a) to (g)) through the equations below [171, 172, 178],

$$W = \int_0^\varepsilon \sigma(t)\,d\varepsilon(t) \tag{8-12}$$

$$W^* = \int_0^\varepsilon \sigma(t)\,d\varepsilon(t) / f'c$$

where W denotes the energy absorption capacity, $\sigma(t)$ stands for the time-dependent stress, $\varepsilon(t)$ represents time-dependent strain, W^* is the normalized energy absorption capacity by dividing its corresponding quasi-static compressive strength (f'_c). As shown in Figure 8-13(a) and (c), the energy absorption capacities (W) of all the specimens increase with the rising strain rate. Metaconcrete specimens with ERCSBs/15 have the highest absolute energy absorption capacity among all types of specimens at a similar strain rate, followed by metaconcrete specimens with ERCSBs/18 and plain mortar specimens. Although the compressive strength is reduced when introducing EAs such as ERCSBs to metaconcrete specimens, the energy absorption increases possibly due to the following reasons. Firstly, adding a hard shell outside the RCSBs could prolong the local resonance effect and thus the core vibration of ERCSBs could contribute to the improvement of energy absorption before the damage of the cementitious matrix, which is also observed in the previous impact tests as reported in Chapter 7. Secondly, shell damage (e.g., opening or detaching) could absorb a considerable amount of wave energy. Namely, if the increase in the energy absorption caused by core vibration and shell damage overtakes the loss in the energy absorption due to the reduced strength, metaconcrete material could exhibit an improvement in energy absorption.

Moreover, metaconcrete specimens with RCSBs (D-S2) have the lowest absolute energy absorption capacity. Namely, adding RCSBs to concrete reduces the overall energy

absorption capacity of the specimen due to its lowest compressive strength. However, the increment in the DIF for energy absorption capacities of the metaconcrete specimens with RCSBs (D-S2) is more prominent than that of plain mortar (D-S1).

(a) Absolute energy absorption capacities of mortar-based specimens

(b) Normalized energy absorption capacities of mortar-based specimens

(c) Absolute energy absorption capacities of concrete-based specimens

(d) Normalized energy absorption capacities of concrete-based specimens
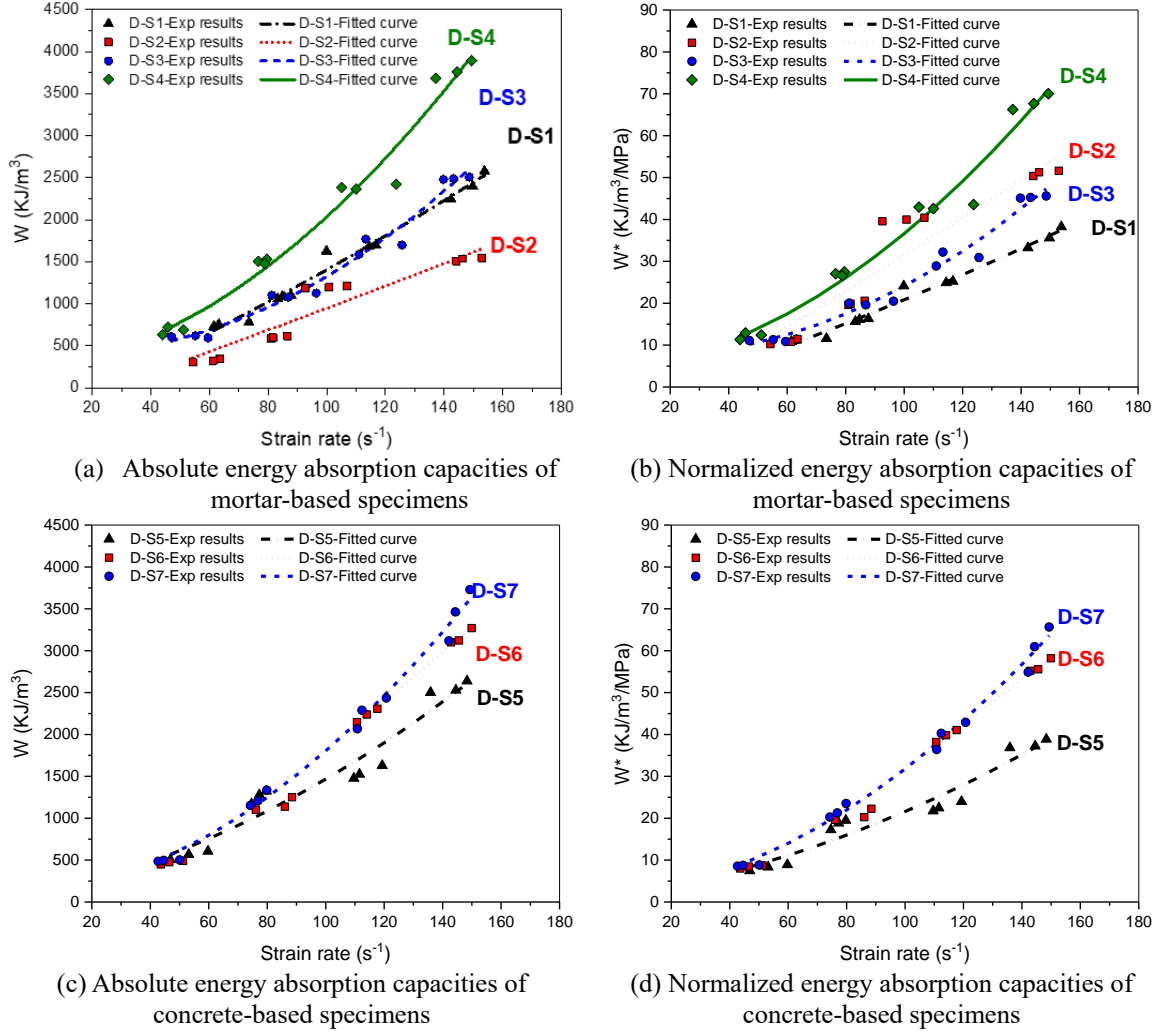
Figure 8-13. Energy absorption capacities of all kinds of specimens under different strain rates.

As shown in Figure 8-13(b) and (d), the energy absorption capacity of all the specimens is normalized with their quasi-static compressive strength for further comparison. The normalized energy absorption capacity (W^*) of metaconcrete specimens with RCSBs (D-S2) is substantially increased and is higher than that of plain mortar. For instance, the normalized energy absorption capacity of metaconcrete specimens with RCSBs (D-S2) is 35.0%~51.5% higher than that of plain mortar at strain rate 144 s^{-1} ~ 153 s^{-1}. For metaconcrete specimens with ERCSBs/15 (D-S4), the value of W^* is respectively 34.4% and 49.5% higher than that of metaconcrete specimens with RCSBs (D-S2) and ERCSBs/18 (D-S3) at strain rate around

144 s^{-1}. This can be explained as follows: a) adding engineered aggregates could trigger local vibration of steel cores besides material failure, which would contribute to the energy absorption; b) steel shell added outside the inner inclusion can be detached and/or damaged under high strain rate loading, so that considerable amount of wave energy can be dissipated by the shell damage. In addition, the experimental results demonstrate a similar trend regarding the strain rate sensitivity for the concrete-based specimens. Specifically, the *W** values for metaconcrete specimens are greater as compared to plain concrete (D-S5) under intensive impact loading. Besides, D-S7 has slightly higher *W** values than D-S6. This may be caused by more significant shell indentation/damage due to the existence of a gap between inner inclusion and shell wall, as well as the movement of RCSB inside the steel shell.

Based on Figure 8-13, the empirical equations for the best-fit curves of energy absorption capacities (W) and strain rate ($\dot{\varepsilon}$) of different types of specimens are given as:

For D-S1(plain mortar):

$$W = 0.0229\dot{\varepsilon}^2 + 15.064\dot{\varepsilon} - 329.37 \quad for \ 61.46\,s^{-1} < \dot{\varepsilon} < 153.75\,s^{-1} \ (R^2 = 0.983) \tag{8-13}$$

For D-S2 (Mortar with RCSBs):

$$W = 0.0032\dot{\varepsilon}^2 + 8.708\dot{\varepsilon} - 225.83 \quad for \ 54.26\,s^{-1} < \dot{\varepsilon} < 152.92\,s^{-1} \ (R^2 = 0.975) \tag{8-14}$$

For D-S3 (Mortar with ERCSBs/18):

$$W = 0.1165\dot{\varepsilon}^2 - 2.7198\dot{\varepsilon} + 431.97 \quad for \ 47.06\,s^{-1} < \dot{\varepsilon} < 148.62\,s^{-1} \ (R^2 = 0.974) \tag{8-15}$$

For D-S4 (Mortar with ERCSBs/15):

$$W = 0.1354\dot{\varepsilon}^2 + 4.957\dot{\varepsilon} + 184.99 \quad for \ 43.87s^{-1} < \dot{\varepsilon} < 149.23s^{-1} \ (R^2 = 0.985) \tag{8-16}$$

For D-S5 (Plain concrete):

$$W = 0.0648\dot{\varepsilon}^2 + 7.405\dot{\varepsilon} + 78.35 \quad for \ 46.87\,s^{-1} < \dot{\varepsilon} < 148.36\,s^{-1} \ (R^2 = 0.940) \tag{8-17}$$

For D-S6 (Concrete with ERCSBs/18):

$$W = 0.0887\dot{\varepsilon}^2 + 10.561\dot{\varepsilon} - 243.05 \quad for \ 43.62s^{-1} < \dot{\varepsilon} < 149.92s^{-1} \ (R^2 = 0.984) \tag{8-18}$$

For D-S7(Concrete with ERCSBs/15):

$$W = 0.12787\dot{\varepsilon}^2 + 4.789\dot{\varepsilon} + 48.309 \quad for \ 42.67s^{-1} < \dot{\varepsilon} < 149.33s^{-1} \ (R^2 = 0.993) \tag{8-19}$$

Table 8-2. Experimental results for D-S1 (plain mortar).

Specimen No.	Strain rate (s-1)	Dynamic compressive strength (MPa)	DIF_E	DIF_T	W (kJ/m3)	W* (kJ/m3 /MPa)
D-S1-1	61.46	85.89	1.273	1.166	732.36	10.85
D-S1-2	63.18	86.07	1.275	1.168	754.93	11.19
D-S1-3	73.46	88.05	1.305	1.188	780.29	11.56
D-S1-4	83.32	105.42	1.562	1.414	1055.77	15.64
D-S1-5	84.75	110.17	1.632	1.477	1087.62	16.12
D-S1-6	87.78	115.34	1.709	1.543	1100.21	16.30
D-S1-7	109.86	134.45	1.992	1.778	1628.31	24.13
D-S1-8	114.40	137.29	2.034	1.811	1680.22	24.90
D-S1-9	116.67	136.47	2.022	1.799	1701.23	25.21
D-S1-10	142.33	167.19	2.477	2.175	2242.00	33.22
D-S1-11	153.75	170.26	2.523	2.203	2580.36	38.23
D-S1-12	149.69	175.31	2.598	2.273	2400.12	35.56

Note: DIF_E denotes the dynamic increase factor (DIF) for compressive strength directly attained from the experiment; DIF_T is the true DIF by removing the contribution of lateral inertial confinement; W represents the energy absorption capacity. W* stands for the normalized energy absorption capacity.

Table 8-3. Experimental results for D-S2 (mortar with RCSBs).

Specimen No.	Strain rate (s-1)	Dynamic compressive strength (MPa)	DIF_E	DIF_T	W (kJ/m3)	W* (kJ/m3 /MPa)
D-S2-1	54.26	46.58	1.554	1.430	307.12	10.24
D-S2-2	63.54	56.05	1.870	1.711	343.44	11.46
D-S2-3	61.23	54.10	1.804	1.654	323.09	10.78
D-S2-4	86.52	67.10	2.238	2.023	617.06	20.58
D-S2-5	80.94	60.51	2.018	1.830	587.08	19.58
D-S2-6	81.68	62.94	2.100	1.902	596.06	19.88
D-S2-7	92.57	70.14	2.340	2.107	1186.35	39.57
D-S2-8	106.94	83.17	2.774	2.480	1211.37	40.41
D-S2-9	100.83	77.52	2.586	2.319	1198.34	39.97
D-S2-10	144.20	113.85	3.797	3.332	1509.63	50.35
D-S2-11	146.18	121.14	4.041	3.542	1536.30	51.24
D-S2-12	152.92	126.21	4.210	3.678	1547.63	51.62

Table 8-4. Experimental results for D-S3 (mortar with ERCSBs/18).

Specimen No.	Strain rate $\dot{\varepsilon}$ (s-1)	Dynamic compressive strength (MPa)	DIF_E	DIF_T	W (kJ/m3)	W* (kJ/m3 /MPa)
D-S3-1	59.48	69.84	1.271	1.164	595.87	10.84
D-S3-2	55.23	71.13	1.294	1.190	620.93	11.30
D-S3-3	47.06	63.38	1.153	1.066	610.37	11.10
D-S3-4	96.37	95.42	1.736	1.560	1125.66	20.48
D-S3-5	86.89	90.88	1.653	1.494	1078.26	19.62
D-S3-6	81.26	88.76	1.615	1.463	1100.33	20.02
D-S3-7	110.99	119.60	2.176	1.941	1587.96	28.89
D-S3-8	113.28	127.65	2.322	2.069	1769.48	32.19
D-S3-9	125.60	132.43	2.409	2.133	1699.24	30.91
D-S3-10	139.78	155.37	2.826	2.485	2479.01	45.10
D-S3-11	143.27	164.89	3.000	2.633	2487.36	45.25
D-S3-12	148.62	176.58	3.212	2.812	2505.90	45.59

Table 8-5. Experimental results for D-S4 (mortar with ERCSBs/15).

Specimen No.	Strain rate $\dot{\varepsilon}$ (s-1)	Dynamic compressive strength (MPa)	DIF_E	DIF_T	W (kJ/m3)	W* (kJ/m3 /MPa)
D-S4-1	45.72	68.78	1.238	1.141	718.39	12.93
D-S4-2	43.87	61.62	1.109	1.027	630.27	11.34
D-S4-3	51.12	66.39	1.195	1.105	689.64	12.41
D-S4-4	76.56	92.36	1.662	1.508	1503.16	27.05
D-S4-5	79.54	95.24	1.714	1.555	1527.07	27.48
D-S4-6	78.82	89.78	1.616	1.468	1478.23	26.60
D-S4-7	105.10	110.79	1.994	1.779	2387.05	42.96
D-S4-8	123.76	121.36	2.184	1.938	2420.36	43.56
D-S4-9	110.01	115.81	2.084	1.858	2366.93	42.59
D-S4-10	137.16	158.33	2.849	2.508	3680.43	66.23
D-S4-11	149.23	167.12	3.007	2.632	3892.12	70.04
D-S4-12	144.35	163.44	2.941	2.580	3760.13	67.66

Table 8-6. Experimental results for D-S5 (plain concrete).

Specimen No.	Strain rate $\dot{\varepsilon}$ (s-1)	Dynamic compressive strength (MPa)	DIF_E	DIF_T	W (kJ/m3)	W* (kJ/m3 /MPa)
D-S5-1	53.12	81.69	1.203	1.108	566.27	8.34
D-S5-2	46.87	80.32	1.183	1.093	504.58	7.43
D-S5-3	59.72	85.78	1.263	1.159	604.63	8.90
D-S5-4	77.32	103.23	1.520	1.381	1278.81	18.83
D-S5-5	79.71	110.95	1.634	1.482	1322.75	19.48
D-S5-6	74.61	108.77	1.601	1.457	1171.02	17.24
D-S5-7	109.65	125.45	1.847	1.649	1475.83	21.73
D-S5-8	119.35	139.76	2.058	1.828	1627.57	23.96
D-S5-9	111.59	129.35	1.904	1.698	1525.16	22.46
D-S5-10	135.88	150.32	2.213	1.950	2499.92	36.81
D-S5-11	148.36	169.35	2.493	2.183	2637.75	38.84
D-S5-12	144.54	160.23	2.359	2.069	2528.37	37.23

Table 8-7. Experimental results for D-S6 (concrete with ERCSBs/18).

Specimen No.	Strain rate $\dot{\varepsilon}$ (s^{-1})	Dynamic compressive strength (MPa)	DIF_E	DIF_T	W (kJ/m^3)	W* (kJ/m^3 /MPa)
D-S6-1	46.52	66.53	1.184	1.095	474.95	8.45
D-S6-2	51.21	69.72	1.241	1.144	490.26	8.73
D-S6-3	43.62	62.53	1.113	1.031	448.76	7.99
D-S6-4	76.12	97.14	1.729	1.571	1101.74	19.61
D-S6-5	86.06	103.29	1.838	1.662	1137.29	20.24
D-S6-6	88.51	107.26	1.909	1.723	1250.34	22.25
D-S6-7	110.71	128.18	2.281	2.035	2146.13	38.19
D-S6-8	114.06	131.26	2.336	2.081	2237.36	39.82
D-S6-9	117.71	132.87	2.365	2.102	2306.14	41.04
D-S6-10	142.84	163.59	2.911	2.556	3100.78	55.18
D-S6-11	145.60	168.04	2.991	2.622	3121.52	55.55
D-S6-12	149.92	169.99	3.025	2.647	3269.45	58.19

Table 8-8. Experimental results for D-S7 (concrete with ERCSBs/15).

Specimen No.	Strain rate $\dot{\varepsilon}$ (s^{-1})	Dynamic compressive strength (MPa)	DIF$_E$	DIF$_T$	W (kJ/m^3)	W* (kJ/m^3 /MPa)
D-S7-1	50.09	66.42	1.169	1.079	501.59	8.83
D-S7-2	42.67	65.78	1.158	1.073	485.71	8.55
D-S7-3	44.62	63.26	1.114	1.027	496.33	8.74
D-S7-4	76.82	90.62	1.595	1.449	1208.37	21.27
D-S7-5	79.87	92.43	1.627	1.476	1335.23	23.50
D-S7-6	74.28	88.64	1.560	1.420	1152.11	20.28
D-S7-7	110.85	120.31	2.118	1.889	2067.79	36.40
D-S7-8	120.75	132.76	2.337	2.074	2435.80	42.88
D-S7-9	112.42	125.42	2.208	1.968	2288.26	40.28
D-S7-10	142.16	152.76	2.689	2.361	3117.80	54.88
D-S7-11	149.33	160.03	2.817	2.465	3730.04	65.66
D-S7-12	144.32	155.21	2.732	2.397	3463.58	60.97

8.4 Summary

This chapter investigates the dynamic compressive properties of metaconcrete material consisting of engineered aggregates, i.e., RCSBs and two types of newly proposed ERCSBs by using the SHPB technique. The failure process, failure mode and dynamic stress-strain curves of the tested specimens are presented and discussed. The strain rate sensitivity on the dynamic compressive strength and energy absorption capacity of metaconcrete material is studied. Empirical formulae of dynamic increase factor (DIF) for compressive strength and energy absorption capacity are proposed. The main findings from this chapter are summarized as follows.

(1) The failure mode of all the specimens under dynamic loading is sensitive to strain rate and the average fragment size reduces with the increasing strain rate. The dynamic compressive strength of metaconcrete material is sensitive to strain rate. The metaconcrete material with conventional engineered aggregates RCSBs (D-S2) exhibits the highest strain rate sensitivity on the compressive strength, which can

reach up to 3.678 at a strain rate of 152.92 s^{-1}, and is 61.8 % and 68.4 % higher than that of plain mortar and plain concrete, respectively.

(2) Metaconcrete material with enhanced engineered aggregates ERCSBs shows higher dynamic strength than metaconcrete material with RCSBs under the tested strain rates, indicating higher impact resistance.

(3) Energy absorption capacities of all the specimens increase with the rising strain rate. Metaconcrete materials with ERCSBs demonstrate a higher strain rate sensitivity on the energy absorption capacity than plain mortar and normal concrete, while metaconcrete materials with RCSBs show a higher strain rate sensitivity on the normalized energy absorption capacity (W^*) only. Metaconcrete material with ERCSBs/15 containing a gap between the RCSB and the external steel shell has the highest strain rate sensitivity on its energy absorption capacity than other types of specimens in the strain rate range tested in this chapter.

(4) The dynamic compressive strength of metaconcrete with conventional engineered aggregates (RCSBs) is substantially lower than that of normal concrete, while that of metaconcrete with enhanced engineered aggregates (ERCSBs) is higher but still slightly lower than that of normal concrete despite its relatively higher energy absorption capacity. To improve the mechanical properties of metaconcrete material with ERCSBs, mechanical or chemical treatment on the EA surface is required to enhance the bond between EA and mortar matrix.

THIS PAGE IS INTENTIONALLY LEFT BLAN

Chapter 9 Conclusions and recommendations for future works

9.1 Main findings

In this thesis, bandgap characteristics and wave attenuation performance of metaconcrete structures, as well as static and dynamic compressive properties of metaconcrete materials, are investigated, in which the results and essential findings are presented in Chapter 3 to Chapter 8. Chapter 3 studies the effects of various geometric and material parameters of engineered aggregates (EAs) such as aggregate shape, size, volume fraction, and material properties on the frequency bandgap associated with the negative effective mass density (NEMD) (e.g., bandwidth and location) of metaconcrete unit cell structure by using finite element software *COMSOL Multiphysics* so that the desired attenuation performance of metaconcrete structures can be achieved through appropriate design of EAs to resist impulsive loading. In Chapter 4, the numerical study is conducted to explore the influences of different EAs on the stress wave attenuation of an example metaconcrete rod structure by using hydrocode LS-DYNA. Meanwhile, a flowchart to design EAs with multiple resonant frequencies for better design of metaconcrete structure with broadband attenuation range is proposed. In Chapter 5, the effectiveness of using engineered aggregates, named *rubber-coated steel ball* (i.e., RCSBs), on mitigation of wave propagation induced by longitudinal impulsive load of an example metaconcrete rod structure is comparatively assessed by carrying out non-destructive tests. In Chapter 6, the damping properties and stress wave attenuation capacity of metaconcrete structures subjected to the transverse impulsive loading are experimentally and numerically studied. In Chapter 7, a new EA by adding a relatively stiff shell named *rubber-coated steel ball with an enhanced coating* (i.e., ERCSBs), to address the issue of strength reduction caused by the soft coating of the traditional EAs (i.e., RCSBs) whilst maintaining its favorable wave attenuation properties, is developed. Static mechanical properties and the effectiveness of using these retrofitted EAs on mitigation of

wave propagation induced by impulsive loading are investigated by conducting standard compression tests, destructive and non-destructive tests. In Chapter 8, the dynamic mechanical properties of metaconcrete material with different types of EAs are experimentally tested and quantified. The main findings from each chapter are summarized as follows.

In Chapter 3, it is demonstrated that the bandgap characteristics such as bandgap location and range depend on the geometric parameters ($R_c t$), core density (ρ_c) and coating modulus ($E_c{'}$). When the Poisson's ratio (ν) of coating material is between 0.4 and 0.5, it can significantly influence the location of the bandgap. The width of the bandgap is highly sensitive to the variation of the core size (D_c), volume fraction (V_a) and coating modulus ($E_c{'}$). It is also observed that the simplified metaconcrete rod structure with purposely designed engineered aggregates can effectively attenuate the blast wave propagation in the desired frequency range.

In Chapter 4, it is found that the attenuation is more prominent when the metaconcrete rod structure with an effective bandgap region coinciding with the primary dominant wave frequency (PDWF) induced by the impulsive loading. Besides, geometric and material parameters of engineered aggregates, e.g., core size, coating thickness, core density and coating modulus could influence the bandgap characteristics and stress wave attenuation performance of a metaconcrete rod structure. It is demonstrated that engineered aggregates with larger core size (D_c) could enhance performance metrics. The performance metrics are sensitive to the change in core density (ρ_c). However, having an over-dense core has no significant improvement on these performance metrics. Furthermore, by using the proposed flowchart, the specimen with multiple resonant aggregates features an enhanced wave mitigation performance than the specimen with uniform inclusion configuration.

Chapter 5 presents the experimental investigation of the performance of cement-based metaconcrete rod structure with conventional EAs (i.e., *rubber-coated steel balls* (RCSBs)) against impulsive loading by considering the effects of inclusion type, and volume fraction

and effective bandgap region. The results show that the volume fraction of RCSBs is an important factor affecting the wave attenuation performance under longitudinal impulsive loading. It is also demonstrated that the specimen with the bandgap covering primary dominant wave frequency (PDWF) leads to more effective wave filtering and better performance in wave mitigation. Besides, the results from the numerical study suggest that the wave mitigation performance in metaconcrete rod structure can be enhanced when subjected to the input longitudinal impulse with a shorter duration or higher amplitude.

Chapter 6 demonstrates the damping properties and response of metaconcrete structures under transverse impulsive loading by conducting a series of non-destructive impact tests. The results demonstrate that the equivalent damping ratio of metaconcrete specimen can substantially increase up to 96% as compared with normal concrete structure. It is also found that the volume fraction, boundary conditions and impact force could affect the attenuation performance of metaconcrete structures. In particular, the attenuation level of the metaconcrete specimen is more prominent as the intensity of excitation force is increased. Furthermore, the bandgap characteristics obtained from the experiment are compared with the numerical prediction using *COMSOL Multiphysics*. From the numerical results, the existence of bandgap in metaconcrete specimens under transverse impulsive loading is observed so that the vibration attenuation of metaconcrete structures can be attributed to the local resonance of EAs.

In Chapter 7, according to the results from the compression test, destructive and non-destructive wave propagation tests, adding a stiffer shell externally to the conventional EAs can significantly improve the mechanical properties of metaconcrete structure while still keeping its good performance in mitigating stress wave propagation under both destructive and non-destructive loading in comparison with metaconcrete specimen with conventional EAs. Moreover, the material used for the enhanced layer outside the retrofitted engineered aggregates (ERCSBs) is suggested to have similar wave impedance to the mortar matrix to ensure the smooth stress transition to the inner heavy core. To further improve the

performance of metaconcrete material with ERCSBs, mechanical or chemical treatment on the enhanced layer of ERCSBs is recommended to improve its bonding strength.

In Chapter 8, dynamic compressive properties of metaconcrete material including failure modes, energy absorption capacities and dynamic increase factors (DIFs) are experimentally assessed. It is found that the metaconcrete specimen with RCSBs has the highest strain rate sensitivity to dynamic compressive strength. Metaconcrete material with ERCSBs shows higher dynamic compressive strength and energy absorption capacity at a similar strain rate. Metaconcrete material containing ERCSBs with the gap between the solid core and steel shell shows the best energy absorption capacity owing to the contribution of steel shell damage.

9.2 Recommendations for future works

In this thesis, the influences of design parameters of engineered aggregates on the bandgap characteristics, stress wave attenuation performance and dynamic compressive properties of metaconcrete structures and materials are investigated and summarized above. Future studies using a similar research framework, numerical modelling approach and experimental method are suggested as follows.

(1) A commonly used concrete model has been used to simulate the behavior of metaconcrete structure by considering material damage when subjected to the selected loading scenarios. It is found that the material damage may cause the change of primary dominant wave frequency (PDWF) of the structure, while this factor is not discussed in depth. Therefore, it is recommended to be considered in future study for better design and analysis of metaconcrete material/structure.

(2) In this thesis, the effect of design parameters on mitigating stress wave propagation of metaconcrete rod structure under impulsive loading is qualitatively studied. However, the threshold value of the parameter (e.g., volume fraction) could be further determined for design purposes in future study.

(3) Moreover, static and dynamic tensile properties of metaconcrete materials are recommended to be further investigated. To improve the tensile strength of metaconcrete, cementitious matrix strengthened by using fibre reinforcement or nanoparticles can be harnessed for better performance, which can also be an interesting topic for further study.

(4) The single-resonant engineered aggregate has been harnessed and studied in this thesis. The metaconcrete material/structure with engineered aggregates in a more complex form such as dual, ternary or higher-architectural-order engineered aggregates in conjunction with the topological optimization is recommended for further work.

(5) Dynamic response and stress wave attenuation performance of structural components (e.g., beam, column and panel) made of metaconcrete material subjected to impulsive loading are suggested to be investigated. In addition, the effect of aggregate volume fraction and distribution as well as using multiple resonant engineered aggregates on the dynamic performance of metaconcrete structures are suggested to be explored in future study.

(6) Metaconcrete material consisting of engineered aggregates with enhanced coating has shown superior performance than metaconcrete material/structure with conventional engineered aggregates. It is also found that the material properties of enhanced coating significantly affect the static and dynamic response of metaconcrete material. However, the steel shell with a smooth surface still causes a reduction of compressive strength due to poor bonding. Meanwhile, engineered aggregates with steel shell as an enhanced coating show a good wave attenuation capability under elastic wave propagation but this might cause serious wave reflection leading to less effective performance. Thus, proper coating material which has a rough surface and a close wave impedance to the surrounding matrix should be suggested for design. Besides, the dynamic performance of metaconcrete containing engineered aggregates with

different enhanced coating candidates under impulsive loading are suggested in future study. Besides, the effects of geometric shapes and material parameters on interfacial damage subjected to intensive impulsive loading are recommended for future study.

References

[1] BBC News. BBC News, 2020. What We Know About The Beirut Explosion. [cited 17 August 2020], Available from: https://www.bbc.com/news/world-middle-east-53668493.

[2] Luccioni BM, Ambrosini RD, Danesi RF. Analysis of building collapse under blast loads. Engineering Structures. 2004;26:63-71.

[3] Ngo T, Mendis P, Gupta A, Ramsay J. Blast loading and blast effects on structures - An overview2007.

[4] Liu Z, Zhang X, Mao Y, Zhu YY, Yang Z, Chan CT et al. Locally Resonant Sonic Materials. Science. 2000;289:1734-6.

[5] Daraio C, Nesterenko VF, Herbold EB, Jin S. Energy Trapping and Shock Disintegration in a Composite Granular Medium. Physical Review Letters. 2006;96:058002.

[6] Yong X, Jihong W, Xisen W. Longitudinal wave band gaps in metamaterial-based elastic rods containing multi-degree-of-freedom resonators. New Journal of Physics. 2012;14:033042.

[7] Yuan B, Humphrey VF, Wen J, Wen X. On the coupling of resonance and Bragg scattering effects in three-dimensional locally resonant sonic materials. Ultrasonics. 2013;53:1332-43.

[8] Matlack KH, Bauhofer A, Krödel S, Palermo A, Daraio C. Composite 3D-printed metastructures for low-frequency and broadband vibration absorption. Proceedings of the National Academy of Sciences. 2016;113:8386-90.

[9] Sharma B, Sun CT. Local resonance and Bragg bandgaps in sandwich beams containing periodically inserted resonators. Journal of Sound and Vibration. 2016;364:133-46.

[10] Pennec Y, Djafari-Rouhani B. Fundamental Properties of Phononic Crystal. In: Khelif A, Adibi A, editors. Phononic Crystals: Fundamentals and Applications. New York, NY: Springer New York; 2016. p. 23-50.

[11] Krushynska AO, Miniaci M, Bosia F, Pugno NM. Coupling local resonance with Bragg band gaps in single-phase mechanical metamaterials. Extreme Mechanics Letters. 2017;12:30-6.

[12] Chang IL, Liang Z-X, Kao H-W, Chang S-H, Yang C-Y. The wave attenuation mechanism of the periodic local resonant metamaterial. Journal of Sound and Vibration. 2018;412:349-59.

[13] Christensen J, Kadic M, Kraft O, Wegener M. Vibrant times for mechanical metamaterials. MRS Communications. 2015;5:453-62.

[14] Zhu R, Yasuda H, Huang GL, Yang JK. Kirigami-based Elastic Metamaterials with Anisotropic Mass Density for Subwavelength Flexural Wave Control. Scientific Reports. 2018;8:483.

[15] Huang HH, Sun CT. Theoretical investigation of the behavior of an acoustic metamaterial with extreme Young's modulus. Journal of the Mechanics and Physics of Solids. 2011;59:2070-81.

[16] Huang HH, Sun CT. Wave attenuation mechanism in an acoustic metamaterial with negative effective mass density. New Journal of Physics. 2009;11:013003.

[17] Zhou X, Liu X, Hu G. Elastic metamaterials with local resonances: an overview. Theoretical and Applied Mechanics Letters. 2012;2:041001.

[18] Ma G, Sheng P. Acoustic metamaterials: From local resonances to broad horizons. Science Advances. 2016;2.

[19] Jensen JS. Phononic band gaps and vibrations in one- and two-dimensional mass–spring structures. Journal of Sound and Vibration. 2003;266:1053-78.

[20] Kirkpatrick DD. 2015. Saudi Arabia Said to Arrest Suspect in 1996 Khobar Towers Bombing. [cited 2021 December 10], Available from: https://www.nytimes.com/2015/08/27/world/middleeast/saudia-arabia-arrests-suspect-khobar-towers-bombing.html.

[21] Buth CE, Williams WF, Brackin MS, Lord D, Geedipally SR, Abu-Odeh AY. Analysis of large truck collisions with bridge piers: phase 1, report of guidelines for designing bridge piers and abutments for vehicle collisions. Texas Transportation Institute; 2010.

[22] BBC News, 2003. 1993: IRA bomb devastates City of London. [cited 2021 December 10], Available from: http://news.bbc.co.uk/onthisday/hi/dates/stories/april/24/newsid_2523000/2523345.stm.

[23] Karson Y, Morgan W. 2018. Death toll rises to 9 in earthquake that toppled buildings in Taiwan. [cited 2021 December 10], Available from: https://abcnews.go.com/International/rescuers-scramble-find-dozens-people-trapped-earthquake-kills/story?id=52901523.

[24] BBC News, 2011. New Zealand quake: Workers embark on delicate rescue. [cited 2021 December 10], Available from: https://www.bbc.com/news/world-asia-pacific-12555559.

[25] Mitchell SJ, Pandolfi A, Ortiz M. Metaconcrete: designed aggregates to enhance dynamic performance. Journal of the Mechanics and Physics of Solids. 2014;65:69-81.

[26] Mitchell SJ, Pandolfi A, Ortiz M. Investigation of elastic wave transmission in a metaconcrete slab. Mechanics of Materials. 2015;91:295-303.

[27] Mitchell SJ, Pandolfi A, Ortiz M. Effect of Brittle Fracture in a Metaconcrete Slab under Shock Loading. Journal of Engineering Mechanics. 2016;142:04016010.

[28] Briccola D, Ortiz M, Pandolfi A. Experimental Validation of Metaconcrete Blast Mitigation Properties. Journal of Applied Mechanics. 2016;84:031001--6.

[29] Briccola D, Tomasin M, Netti T, Pandolfi A. The Influence of a Lattice-Like Pattern of Inclusions on the Attenuation Properties of Metaconcrete. Frontiers in Materials. 2019;6.

[30] Briccola D, Cuni M, De Juli A, Ortiz M, Pandolfi A. Experimental Validation of the Attenuation Properties in the Sonic Range of Metaconcrete Containing Two Types of Resonant Inclusions. Experimental Mechanics. 2020.

[31] Kettenbeil C, Ravichandran G. Experimental investigation of the dynamic behavior of metaconcrete. International Journal of Impact Engineering. 2018;111:199-207.

[32] Cormie D, Mays G, Smith P. Blast Effects on Buildings - (2nd Edition). ICE Publishing.

[33] Ou J, Liu T, Li J. Dynamic and seismic property experiments of high damping concrete and its frame models. Journal of Wuhan University of Technology-Mater Sci Ed. 2008;23:1-6.

[34] Wagner PR, Dertimanis VK, Antoniadis IA, Chatzi EN. On the feasibility of structural metamaterials for seismic-induced vibration mitigation. International Journal of Earthquake and Impact Engineering. 2016;1:20-56.

[35] Zhang C, Gholipour G, Mousavi AA. Nonlinear dynamic behavior of simply-supported RC beams subjected to combined impact-blast loading. Engineering Structures. 2019;181:124-42.

[36] Shi Y, Wang J, Cui J. Experimental studies on fragments of reinforced concrete slabs under close-in explosions. International Journal of Impact Engineering. 2020;144:103630.

[37] Long WJ, Li HD, Mei L, Li W, Xing F, Khayat KH. Damping characteristics of PVA fiber-reinforced cementitious composite containing high-volume fly ash under frequency-temperature coupling effects. Cement and Concrete Composites. 2021;118:103911.

[38] Chi L, Lu S, Yao Y. Damping additives used in cement-matrix composites: A review. Composites Part B: Engineering. 2019;164:26-36.

[39] Palermo A, Marzani A. Control of Love waves by resonant metasurfaces. Scientific Reports. 2018;8:7234.

[40] Palermo A, Krödel S, Marzani A, Daraio C. Engineered metabarrier as shield from seismic surface waves. Scientific Reports. 2016;6:39356.

[41] Liu Z, Chan CT, Sheng P. Three-component elastic wave band-gap material. Physical Review B. 2002;65:165116.

[42] Milton GW, Willis JR. On modifications of Newton's second law and linear continuum elastodynamics. Proceedings of the Royal Society A: Mathematical, Physical and Engineering Science. 2007;463:855-80.

[43] Dodin IY, Fisch NJ. Positive and negative effective mass of classical particles in oscillatory and static fields. 2007.

[44] Huang HH, Sun CT, Huang GL. On the negative effective mass density in acoustic metamaterials. International Journal of Engineering Science. 2009;47:610-7.

[45] Khan MH, Li B, Tan KT. Impact load wave transmission in elastic metamaterials.

International Journal of Impact Engineering. 2018;118:50-9.

[46] Li B, Liu Y, Tan K-T. A novel meta-lattice sandwich structure for dynamic load mitigation. Journal of Sandwich Structures & Materials. 2017;0:1099636217727144.

[47] Yao S, Zhou X, Hu G. Experimental study on negative effective mass in a 1D mass–spring system. New Journal of Physics. 2008;10:043020.

[48] Yao S, Zhou X, Hu G. Heterogeneous Structures with Negative Effective Mass. Dordrecht: Springer Netherlands; 2013. p. 257-67.

[49] Yin J, Ruzzene M, Wen J, Yu D, Cai L, Yue L. Band transition and topological interface modes in 1D elastic phononic crystals. Scientific Reports. 2018;8:6806.

[50] Baravelli E, Carrara M, Ruzzene M. High stiffness, high damping chiral metamaterial assemblies for low-frequency applications. SPIE Smart Structures and Materials + Nondestructive Evaluation and Health Monitoring: SPIE; 2013. p. 10.

[51] Achaoui Y, Ungureanu B, Enoch S, Brûlé S, Guenneau S. Seismic waves damping with arrays of inertial resonators. Extreme Mechanics Letters. 2016;8:30-7.

[52] Manimala JM, Huang HH, Sun CT, Snyder R, Bland S. Dynamic load mitigation using negative effective mass structures. Engineering Structures. 2014;80:458-68.

[53] Ma G, Fu C, Wang G, del Hougne P, Christensen J, Lai Y et al. Polarization bandgaps and fluid-like elasticity in fully solid elastic metamaterials. Nature Communications. 2016;7:13536.

[54] Fang X, Wen J, Bonello B, Yin J, Yu D. Ultra-low and ultra-broad-band nonlinear acoustic metamaterials. Nature Communications. 2017;8:1288.

[55] Xin L, Siyuan Y, Harry L, Minghui L, Yanfeng C. Topological mechanical metamaterials: A brief review. Current Opinion in Solid State and Materials Science. 2020;24:100853.

[56] Chan CT, Li J, Fung KH. On extending the concept of double negativity to acoustic waves. Journal of Zhejiang University-SCIENCE A. 2006;7:24-8.

[57] Ding Y, Liu Z, Qiu C, Shi J. Metamaterial with Simultaneously Negative Bulk Modulus and Mass Density. Physical Review Letters. 2007;99:093904.

[58] Liu XN, Hu GK, Huang GL, Sun CT. An elastic metamaterial with simultaneously negative mass density and bulk modulus. Applied Physics Letters. 2011;98:251907.

[59] Mei J, Ma G, Yang M, Yang J, Sheng P. Dynamic Mass Density and Acoustic Metamaterials. In: Deymier PA, editor. Acoustic Metamaterials and Phononic Crystals. Berlin, Heidelberg: Springer Berlin Heidelberg; 2013. p. 159-99.

[60] Marco M, Anastasiia K, Federico B, Nicola MP. Large scale mechanical metamaterials as seismic shields. New Journal of Physics. 2016;18:083041.

[61] An L-q, Zhang X-c, Wu H-x, Jiang W-q. In-plane dynamic crushing and energy absorption capacity of self-similar hierarchical honeycombs. Advances in Mechanical

Engineering. 2017;9:1687814017703896.

[62] Chen YY, Barnhart MV, Chen JK, Hu GK, Sun CT, Huang GL. Dissipative elastic metamaterials for broadband wave mitigation at subwavelength scale. Composite Structures. 2016;136:358-71.

[63] Yousefzadeh B, Phani AS. Energy transmission in finite dissipative nonlinear periodic structures from excitation within a stop band. Journal of Sound and Vibration. 2015;354:180-95.

[64] Tan KT, Huang HH, Sun CT. Blast-wave impact mitigation using negative effective mass density concept of elastic metamaterials. International Journal of Impact Engineering. 2014;64:20-9.

[65] Xin F, Jihong W, Bernard B, Jianfei Y, Dianlong Y. Wave propagation in one-dimensional nonlinear acoustic metamaterials. New Journal of Physics. 2017;19:053007.

[66] Maldovan M. Sound and heat revolutions in phononics. Nature. 2013;503:209.

[67] Shamonina E, Solymar L. Metamaterials: How the subject started. Metamaterials. 2007;1:12-8.

[68] Alamri S, Li B, Tan KT. Dynamic load mitigation using dissipative elastic metamaterials with multiple Maxwell-type oscillators. Journal of Applied Physics. 2018;123:095111.

[69] Chen JS, Sharma B, Sun CT. Dynamic behaviour of sandwich structure containing spring-mass resonators. Composite Structures. 2011;93:2120-5.

[70] Li T, Su Q, Kaewunruen S. Seismic metamaterial barriers for ground vibration mitigation in railways considering the train-track-soil dynamic interactions. Construction and Building Materials. 2020;260:119936.

[71] Zhang B, Zhang Y, Liao W, Ma H. Locally resonant meta-composite for sound-proof of building envelops: Analytical model and experiment. Construction and Building Materials. 2018;164:792-8.

[72] Li Z, Yang Q, Fang R, Chen W, Hao H. Origami metamaterial with two-stage programmable compressive strength under quasi-static loading. International Journal of Mechanical Sciences. 2021;189:105987.

[73] Ren T, Li F, Chen Y, Liu C, Zhang C. Improvement of the band-gap characteristics of active composite laminate metamaterial plates. Composite Structures. 2020;254:112831.

[74] An X, Lai C, Fan H, Zhang C. 3D acoustic metamaterial-based truss-lattice structures for low-frequency and broadband vibration attenuation. International Journal of Solids and Structures. 2020.

[75] Xu X, Barnhart MV, Li X, Chen Y, Huang G. Tailoring vibration suppression bands with hierarchical metamaterials containing local resonators. Journal of Sound and Vibration. 2019;442:237-48.

[76] Hu J, Yu TX, Yin S, Xu J. Low-speed impact mitigation of recoverable DNA-inspired double helical metamaterials. International Journal of Mechanical Sciences. 2019;161-162:105050.

[77] Chen Y, Hu G, Huang G. A hybrid elastic metamaterial with negative mass density and tunable bending stiffness. Journal of the Mechanics and Physics of Solids. 2017;105:179-98.

[78] Jiang W, Yin M, Liao Q, Xie L, Yin G. Three-dimensional single-phase elastic metamaterial for low-frequency and broadband vibration mitigation. International Journal of Mechanical Sciences. 2020:106023.

[79] Shi HYY, Tay TE, Lee HP. Numerical studies on composite meta-material structure for mid to low frequency elastic wave mitigation. Composite Structures. 2018.

[80] An X, Lai C, He W, Fan H. Three-dimensional chiral meta-plate lattice structures for broad band vibration suppression and sound absorption. Composites Part B: Engineering. 2021:109232.

[81] Kim E, Yang J, Hwang H, Shul CW. Impact and blast mitigation using locally resonant woodpile metamaterials. International Journal of Impact Engineering. 2017;101:24-31.

[82] Mitchell S, Pandolfi A, Ortiz M. Engineered aggregates for metamaterials. Google Patents; 2016.

[83] Liu Y, An X, Chen H, Fan H. Vibration attenuation of finite-size metaconcrete: Mechanism, prediction and verification. Composites Part A: Applied Science and Manufacturing. 2021;143:106294.

[84] Sridhar A, Liu L, Kouznetsova VG, Geers MGD. Homogenized enriched continuum analysis of acoustic metamaterials with negative stiffness and double negative effects. Journal of the Mechanics and Physics of Solids. 2018;119:104-17.

[85] Cheng Z, Shi Z. Novel composite periodic structures with attenuation zones. Engineering Structures. 2013;56:1271-82.

[86] Cheng Z, Shi Z. Composite periodic foundation and its application for seismic isolation. Earthquake Engineering & Structural Dynamics. 2018;47:925-44.

[87] Mitchell SJ. Metaconcrete: Engineered aggregates for enhanced dynamic performance. California Institute of Technology2016.

[88] Jin H, Hao H, Hao Y, Chen W. Predicting the response of locally resonant concrete structure under blast load. Construction and Building Materials. 2020;252:118920.

[89] Jin H, Hao H, Chen W, Xu C. Spall Behaviors of Metaconcrete: 3D Meso-Scale Modelling. International Journal of Structural Stability and Dynamics. 2021:2150121.

[90] Jin H, Hao H, Chen W, Xu C. Effect of enhanced coating layer on the bandgap characteristics and response of metaconcrete. Mechanics of Advanced Materials and Structures. 2021:1-14.

[91] Sharma B, Sun CT. Impact load mitigation in sandwich beams using local resonators. Journal of Sandwich Structures & Materials. 2015;18:50-64.

[92] Barnhart MV, Xu X, Chen Y, Zhang S, Song J, Huang G. Experimental demonstration of a dissipative multi-resonator metmaterial for broadband elastic wave attenuation. Journal of Sound and Vibration. 2018.

[93] Sharma B, Sun C. Impact load mitigation in sandwich beams using local resonators. Journal of Sandwich Structures & Materials. 2016;18:50-64.

[94] Briccola D, Pandolfi A. Analysis on the Dynamic Wave Attenuation Properties of Metaconcrete Considering a Quasi-Random Arrangement of Inclusions. Frontiers in Materials. 2021;7.

[95] LSTC. LS-DYNA Version 971 Keyword User's Manual. Livermore Software Technology Corporation. 2010;22:p49-51.

[96] Randers-Pehrson G, Bannister KA. Airblast Loading Model for DYNA2D and DYNA3D. DTIC document: US Army Research Laboratory; 1997.

[97] US Army. Structures to resist the effects of accidental explosions, UFC3-340-02. The US Department of Army Washington, DC; 2008.

[98] Kinney GF, Graham KJ. Explosive Shocks in Air. Berlin, Heidelberg: Springer Berlin Heidelberg; 1985.

[99] COMSOL. MA, USA: COMSOL Inc; 2019.

[100] Wang X, Zhang M, Jivkov AP. Computational technology for analysis of 3D meso-structure effects on damage and failure of concrete. International Journal of Solids and Structures. 2016;80:310-33.

[101] Zhou XQ, Hao H. Modelling of compressive behaviour of concrete-like materials at high strain rate. International Journal of Solids and Structures. 2008;45:4648-61.

[102] Krushynska AO, Kouznetsova VG, Geers MGD. Towards optimal design of locally resonant acoustic metamaterials. Journal of the Mechanics and Physics of Solids. 2014;71:179-96.

[103] Wang C, Liu Z, Gao L, Xu D, Zhuang Z. Analytical and numerical modeling on resonant response of particles in polymer matrix under blast wave. Computational Materials Science. 2017;140:70-81.

[104] Ashby M, Shercliff H, Cebon D. Materials : Engineering, Science, Processing and Design. Oxford, UNITED KINGDOM: Elsevier Science & Technology; 2007.

[105] Bo Z, Li Z. New Analytical Model for Composite Materials Containing Local Resonance Units. Journal of Engineering Mechanics. 2011;137:1-7.

[106] Xu Z, Hao H, Li HN. Mesoscale modelling of fibre reinforced concrete material under compressive impact loading. Construction and Building Materials. 2012;26:274-88.

[107] An X, Lai C, He W, Fan H. Three-dimensional meta-truss lattice composite structures with vibration isolation performance. Extreme Mechanics Letters. 2019;33:100577.

[108] Chen G, Hao Y, Hao H. 3D meso-scale modelling of concrete material in spall tests. Materials and Structures. 2015;48:1887-99.

[109] Samiee A, Amirkhizi AV, Nemat-Nasser S. Numerical study of the effect of polyurea on the performance of steel plates under blast loads. Mechanics of Materials. 2013;64:1-10.

[110] Hanifpour M, Petersen CF, Alava MJ, Zapperi S. Mechanics of disordered auxetic metamaterials. The European Physical Journal B. 2018;91:271.

[111] Liao Y, Shi S, Liu Z, Liang C. Study on shock resistance of steel plate reinforced with polyurea–woven fiberglass mesh composite under shock wave. International Journal of Protective Structures. 2018;9:248-66.

[112] Chicot D, Mendoza J, Zaoui A, Louis G, Lepingle V, Roudet F et al. Mechanical properties of magnetite (Fe_3O_4), hematite (α-Fe_2O_3) and goethite (α-FeO·OH) by instrumented indentation and molecular dynamics analysis. Materials Chemistry and Physics. 2011;129:862-70.

[113] Jacobsen SD, Reichmann HJ, Kantor A, Spetzler HA. A gigahertz ultrasonic interferometer for the diamond anvil cell and high-pressure elasticity of some iron-oxide minerals. In: Chen J, Wang Y, Duffy TS, Shen G, Dobrzhinetskaya LF, editors. Advances in High-Pressure Technology for Geophysical Applications. Amsterdam: Elsevier; 2005. p. 25-48.

[114] Lu Y, Yang Y, Guest JK, Srivastava A. 3-D phononic crystals with ultra-wide band gaps. Scientific Reports. 2017;7:43407.

[115] Wu H, Zhang Q, Huang F, Jin Q. Experimental and numerical investigation on the dynamic tensile strength of concrete. International Journal of Impact Engineering. 2005;32:605-17.

[116] Hao Y, Hao H. Numerical Evaluation of the Influence of Aggregates on Concrete Compressive Strength at High Strain Rate. International Journal of Protective Structures. 2011;2:177-206.

[117] Hao Y, Hao H, Zhang XH. Numerical analysis of concrete material properties at high strain rate under direct tension. International Journal of Impact Engineering. 2012;39:51-62.

[118] Li J, Wu C, Hao H, Su Y, Li Z. A study of concrete slabs with steel wire mesh reinforcement under close-in explosive loads. International Journal of Impact Engineering. 2017;110:242-54.

[119] Xu PB, Xu H, Wen HM. 3D meso-mechanical modeling of concrete spall tests. International Journal of Impact Engineering. 2016;97:46-56.

[120] Malvar LJ, Crawford JE, Wesevich JW, Simons D. A plasticity concrete material model for DYNA3D. International Journal of Impact Engineering. 1997;19:847-73.

[121] Cui J, Hao H, Shi Y. Discussion on the suitability of concrete constitutive models for high-rate response predictions of RC structures. International Journal of Impact Engineering. 2017;106:202-16.

[122] Hao H, Hao Y, Li J, Chen W. Review of the current practices in blast-resistant analysis and design of concrete structures. Advances in Structural Engineering. 2016;19:1193-223.

[123] Hao Y, Hao H. Numerical Investigation of the Dynamic Compressive Behaviour of Rock Materials at High Strain Rate. Rock Mechanics and Rock Engineering. 2013;46:373-88.

[124] Davco Australia. Davco lanko 701 duragrout data sheet. 2020.

[125] Sreenilayam Raveendran RK, Azarian MH, Morillo C, Pecht MG, Kida K, Santos EC et al. Comparative evaluation of metal and polymer ball bearings. Wear. 2013;302:1499-505.

[126] Pham TM, Chen W, Khan AM, Hao H, Elchalakani M, Tran TM. Dynamic compressive properties of lightweight rubberized concrete. Construction and Building Materials. 2020;238:117705.

[127] Pai PF, Peng H, Jiang S. Acoustic metamaterial beams based on multi-frequency vibration absorbers. International Journal of Mechanical Sciences. 2014;79:195-205.

[128] Landis E, Shah S. Frequency-Dependent Stress Wave Attenuation in Cement-Based Materials. Journal of Engineering Mechanics-asce - J ENG MECH-ASCE. 1995;121.

[129] Xu C, Chen W, Hao H. The influence of design parameters of engineered aggregate in metaconcrete on bandgap region. Journal of the Mechanics and Physics of Solids. 2020:103929.

[130] Zhou R, Song Z, Lu Y. 3D mesoscale finite element modelling of concrete. Computers & Structures. 2017;192:96-113.

[131] Lee K. Effects on the various rubber fenders of a tripod offshore wind turbine substructure collision strength due to boat. Ocean Engineering. 2013;72:188-94.

[132] Clough R, Penzien J. Dynamics of Structures: Computers & Structures, Inc.; 2003.

[133] Yuan W, Jin J, Guo Z, Wu Y. Theoretical Analysis of Longitudinal Wave Attenuation in a Stressed Rock With Variable Cross-Section. Frontiers in Earth Science. 2019;7.

[134] Cheng Y, Song Z, Jin J, Wang J, Wang T. Experimental study on stress wave attenuation and energy dissipation of sandstone under full deformation condition. Arabian Journal of Geosciences. 2019;12:736.

[135] Lougou KG, Boudaoud H, Daya EM, Azrar L. Vibration modeling of large repetitive sandwich structures with viscoelastic core. Mechanics of Advanced Materials and Structures. 2016;23:458-66.

[136] Hamdaoui M, Ledi KS, Robin G, Daya EM. Identification of frequency-dependent viscoelastic damped structures using an adjoint method. Journal of Sound and Vibration.

2019;453:237-52.

[137] Mead DM. wave propagation in continuous periodic structures: research contributions from Southampton, 1964–1995. Journal of Sound and Vibration. 1996;190:495-524.

[138] Xiao Y, Wen J, Yu D, Wen X. Flexural wave propagation in beams with periodically attached vibration absorbers: Band-gap behavior and band formation mechanisms. Journal of Sound and Vibration. 2013;332:867-93.

[139] Chesnais C, Boutin C, Hans S. Effects of the local resonance on the wave propagation in periodic frame structures: generalized Newtonian mechanics. Journal of the Acoustical Society of America. 2012;132:15p.

[140] Liu Y, Yu D, Li L, Zhao H, Wen J, Wen X. Design guidelines for flexural wave attenuation of slender beams with local resonators. Physics Letters A. 2007;362:344-7.

[141] Yu D, Liu Y, Zhao H, Wang G, Qiu J. Flexural vibration band gaps in Euler-Bernoulli beams with locally resonant structures with two degrees of freedom. Physical Review B. 2006;73:064301.

[142] Wang T, Sheng M-P, Qin Q-H. Multi-flexural band gaps in an Euler–Bernoulli beam with lateral local resonators. Physics Letters A. 2016;380:525-9.

[143] Doyle JF. Wave propagation in structures: an FFT-based spectral analysis methodology: Springer, New York, NY; 2012.

[144] Silva CWd. Vibration Fundamentals and Practice, Second Edition. 2nd Edition ed. Boca Raton: Taylor & Francis Group; 2006.

[145] He H, Fan H. Explosion vibration mitigation of meta-plate with mass–spring metastructures. Extreme Mechanics Letters. 2021;42:101108.

[146] Pan Z, Feng KN, Gong K, Zou B, Korayem AH, Sanjayan J et al. Damping and microstructure of fly ash-based geopolymers. Journal of Materials Science. 2013;48:3128-37.

[147] Cui Y, Hao H, Li J, Chen W. Effect of Adding Methylcellulose on Mechanical and Vibration Properties of Geopolymer Paste and Hybrid Fiber-Reinforced Geopolymer Composite. Journal of Materials in Civil Engineering. 2020;32:04020166.

[148] Song W, Zou D, Liu T, Teng J, Li L. Effects of recycled CRT glass fine aggregate size and content on mechanical and damping properties of concrete. Construction and Building Materials. 2019;202:332-40.

[149] Raghavan L, Phani AS. Local resonance bandgaps in periodic media: Theory and experiment. The Journal of the Acoustical Society of America. 2013;134:1950-9.

[150] Guo Z, Sheng M, Pan J. Effect of boundary conditions on the band-gap properties of flexural waves in a periodic compound plate. Journal of Sound and Vibration. 2017;395:102-26.

[151] Xu C, Chen W, Hao H, Bi K, Pham TM. Experimental and numerical assessment of stress wave attenuation of metaconcrete rods subjected to impulsive loads. International Journal of Impact Engineering. 2022;159:104052.

[152] Xu C, Chen W, Hao H, Jin H. Effect of engineered aggregate configuration and design on stress wave attenuation of metaconcrete rod structure. International Journal of Solids and Structures. 2021;232:111182.

[153] Xu C, Chen W, Hao H, Pham TM, Bi K. Damping properties and dynamic responses of metaconcrete beam structures subjected to transverse loading. Construction and Building Materials. 2021;311:125273.

[154] ASTM C29 / C29M-07. Standard Test Method for Bulk Density (Unit Weight) and Voids in Aggregate. West Conshohocken, PA: ASTM International; 2007.

[155] Kim KM, Lee S, Cho JY. Effect of maximum coarse aggregate size on dynamic compressive strength of high-strength concrete. International Journal of Impact Engineering. 2019;125:107-16.

[156] Gagnon L, Morandini M, Ghiringhelli GL. A review of particle damping modeling and testing. Journal of Sound and Vibration. 2019;459:114865.

[157] Masri SF, Ibrahim AM. Response of the impact damper to stationary random excitation. The Journal of the Acoustical Society of America. 1973;53:200-11.

[158] Salueña C, Pöschel T, Esipov SE. Dissipative properties of vibrated granular materials. Physical Review E. 1999;59:4422-5.

[159] Lu Z-Q, Zhao L, Ding H, Chen L-Q. A dual-functional metamaterial for integrated vibration isolation and energy harvesting. Journal of Sound and Vibration. 2021;509:116251.

[160] ASTM C192/C192M-19. Standard Practice for Making and Curing Concrete Test Specimens in the Laboratory. West Conshohocken, PA: ASTM International; 2019.

[161] ASTM C39/C39M-21. Standard Test Method for Compressive Strength of Cylindrical Concrete Specimens. West Conshohocken, PA: ASTM International; 2021.

[162] ASTM C469/C469M-14e1. Standard Test Method for Static Modulus of Elasticity and Poisson's Ratio of Concrete in Compression. West Conshohocken, PA: ASTM International; 2014.

[163] Chen X, Wu S, Zhou J. Experimental and modeling study of dynamic mechanical properties of cement paste, mortar and concrete. Construction and Building Materials. 2013;47:419-30.

[164] McVay MK. Spall damage of concrete structures. Waterways Experiment Station, Vicksburg, Miss: Army Corps of Engineers; 1988.

[165] Wang L. Foundations of stress waves. Amsterdam: Elsevier Science Ltd; 2007.

[166] Brara A, Camborde F, Klepaczko JR, Mariotti C. Experimental and numerical study of

concrete at high strain rates in tension. Mechanics of Materials. 2001;33:33-45.

[167] Khosravani MR, Wagner P, Fröhlich D, Weinberg K. Dynamic fracture investigations of ultra-high performance concrete by spalling tests. Engineering Structures. 2019;201:109844.

[168] Klepaczko JR, Brara A. An experimental method for dynamic tensile testing of concrete by spalling. International Journal of Impact Engineering. 2001;25:387-409.

[169] Pham TM, Liu J, Tran P, Pang V-L, Shi F, Chen W et al. Dynamic compressive properties of lightweight rubberized geopolymer concrete. Construction and Building Materials. 2020;265:120753.

[170] Li Z, Chen W, Hao H, Khan MZN, Pham TM. Dynamic compressive properties of novel lightweight ambient-cured EPS geopolymer composite. Construction and Building Materials. 2021;273:122044.

[171] Pham TM, Renaud N, Pang V-L, Shi F, Hao H, Chen W. Effect of rubber aggregate size on static and dynamic compressive properties of rubberized concrete. Structural Concrete. 2021;n/a.

[172] Pham TM, Davis J, Ha NS, Pournasiri E, Shi F, Hao H. Experimental investigation on dynamic properties of ultra-high-performance rubberized concrete (UHPRuC). Construction and Building Materials. 2021;307:125104.

[173] Ha NS, Marundrury SS, Pham TM, Pournasiri E, Shi F, Hao H. Effect of grounded blast furnace slag and rice husk ash on performance of ultra-high-performance concrete (UHPC) subjected to impact loading. Construction and Building Materials. 2022;329:127213.

[174] Huang Z, Chen W, Hao H, Aurelio R, Li Z, Pham TM. Test of Dynamic Mechanical Properties of Ambient-Cured Geopolymer Concrete Using Split Hopkinson Pressure Bar. Journal of Materials in Civil Engineering. 2022;34:04021440.

[175] Lv T, Chen X, Chen G. Analysis on the waveform features of the split Hopkinson pressure bar tests of plain concrete specimen. International Journal of Impact Engineering. 2017;103:107-23.

[176] Lindholm U. Some experiments with the split hopkinson pressure bar∗. Journal of the Mechanics and Physics of Solids. 1964;12:317-35.

[177] Ravichandran G, Subhash G. Critical Appraisal of Limiting Strain Rates for Compression Testing of Ceramics in a Split Hopkinson Pressure Bar. Journal of the American Ceramic Society. 1994;77:263-7.

[178] Chen W, Shaikh F, Li Z, Ran W, Hao H. Dynamic compressive properties of high volume fly ash (HVFA) concrete with nano silica. Construction and Building Materials. 2021;301:124352.

[179] Zhang M, Wu H, Li Q, Huang F. Further investigation on the dynamic compressive strength enhancement of concrete-like materials based on split Hopkinson pressure bar tests.

Part I: Experiments. International Journal of Impact Engineering. 2009;36:1327-34.

[180] Wang C, Chen W, Hao H, Zhang S, Song R, Wang X. Experimental investigations of dynamic compressive properties of roller compacted concrete (RCC). Construction and Building Materials. 2018;168:671-82.

[181] Hao Y, Hao H. Dynamic compressive behaviour of spiral steel fibre reinforced concrete in split Hopkinson pressure bar tests. Construction and Building Materials. 2013;48:521-32.

[182] Li N, Long G, Li W, Ma C, Zeng X, Xie Y et al. Designing high impact-resistance self-compacting concrete by addition of asphalt-coated coarse aggregate. Construction and Building Materials. 2020;253:118758.

[183] Yan Z-W, Bai Y-L, Ozbakkaloglu T, Gao W-Y, Zeng J-J. Rate-dependent compressive behavior of concrete confined with Large-Rupture-Strain (LRS) FRP. Composite Structures. 2021;272:114199.

[184] Hao Y, Hao H, Li Z-X. Numerical Analysis of Lateral Inertial Confinement Effects on Impact Test of Concrete Compressive Material Properties. International Journal of Protective Structures. 2010;1:145-67.

[185] CEB-FIP Model Code. Design code. Comité Euro-International du Béton, Bulletins d'Information 203-205, Lausanne, Switzerland. 1993.

[186] Najim KB, Hall MR. Mechanical and dynamic properties of self-compacting crumb rubber modified concrete. Construction and Building Materials. 2012;27:521-30.

Appendix I Statement of contribution of co-authors

To whom it may concern,

I, Cheng Xu, conducted experimental, numerical and theoretical investigations, data processing and analysis, and wrote the manuscripts of the papers entitled as follows, which are reviewed and edited by the co-authors. They also provided insights on conceptual design, experimental preparation, data processing and data analysis.

1. The influence of design parameters of engineered aggregate in metaconcrete on bandgap region.

2. Effect of engineered aggregate configuration and design on stress wave attenuation of metaconcrete rod structure.

3. Experimental and numerical assessment of stress wave attenuation of metaconcrete rods subjected to impulsive loads.

4. Damping properties and dynamic responses of metaconcrete beam structures subjected to transverse loading.

5. Static mechanical properties and stress wave attenuation of metaconcrete subjected to impulsive loading.

6. Dynamic compressive properties of metaconcrete materials. (Under review)

Cheng Xu   ………………………………………..

I, as a co-author, endorse that this level of contribution by the candidate indicated above is appropriate.

A/Prof. Wensu Chen   ………………………………………….

Prof. Hong Hao   ………………………………………….

Dr. Thong M. Pham   ………………………………………….

A/Prof. Kaiming Bi   ………………………………………….

Dr. Hexin Jin   …………….………..............................

Mr. Zhixing Li   ………………………………………….

Appendix II Copyright Clearance

The proof of the rights, granted by publisher for the publications that form the chapters of this thesis are attached below.

Xu C, Chen W, and Hao H., *The influence of design parameters of engineered aggregate in metaconcrete on bandgap region*. Journal of the Mechanics and Physics of Solids, 2020. 139: 103929.

Xu C, Chen W, Hao H and Jin H., *Effect of engineered aggregate configuration and design on stress wave attenuation of metaconcrete rod structure.* International Journal of Solids and Structures, 2021. 232: 111182.

Xu C, Chen W, Hao H, Bi K, and Pham TM., *Experimental and numerical assessment of stress wave attenuation of metaconcrete rods subjected to impulsive loads*. International Journal of Impact Engineering, 2022. 159: 104052.

Xu C, Chen W, Hao H, Pham TM and Bi K., *Damping properties and dynamic responses of metaconcrete beam structures subjected to transverse loading*. Construction and Building Materials, 2021. 311:125273.

Xu C, Chen W, Hao H, Pham TM, Bi K., *Static mechanical properties and stress wave attenuation of metaconcrete subjected to impulsive loading*. Engineering Structures, 2022. 263: 114382.